TIME-LAPSE MULTICOMPONENT GEOPHONE AND DAS VSP PROCESSING AND ANALYSIS

by

Whitney H. Schultz

A thesis submitted to the Faculty and the Board of Trustees of the Colorado School of Mines in partial fulfillment of the requirements for the degree of Master of Science (Geophysics).

Golden, Colorado

Date _____

Signed: _____
Whitney H. Schultz

Signed: _____
Dr. Jim Simmons
Thesis Advisor

Golden, Colorado

Date _____

Signed: _____
John Bradford
Professor and Head
Department of Geophysics

ABSTRACT

Various geophone and distributed acoustic sensing (DAS) vertical seismic profile (VSP) datasets acquired in south central Texas are processed for P-wave and PS-wave imaging. The surveys acquired and analyzed in this project were time-lapse zero-offset and walkaway recorded on both geophones and DAS, and a 3D survey recorded only by DAS. This project focuses on reprocessing and analyzing the various datasets to evaluate the differences between the geophone and DAS VSP surveys and to analyze the time-lapse changes from hydraulic fracturing. The DAS performs comparably to the geophones and records PS-waves well enough to be processed and interpreted. DAS fiber has significant advantages over geophones in large VSP surveys due to the larger receiver depth aperture. DAS receiver spacing is also denser than geophone arrays, but DAS records only the particle motion parallel to the fiber whereas geophones can record three-components.

A P-wave velocity model is developed from the first-break picks of the zero-offset geophone VSP and used in the processing of various other datasets. Using the Vp/Vs ratio from sonic logs, the corresponding shear wave velocity model is developed. The velocity models are used as an input to the walkaway and 3D VSP processing. The 1-D model has limitations, but is a useful starting point toward development of an integrated 3-D velocity that can be used to processes various surface seismic and microseismic datasets. While converting the zero-offset DAS to geophone response, noise is smeared across the gather and the higher frequencies are lost. Aggressive 2D median filtering is necessary, but the result ties well to the geophone zero-offset gather.

Imaging of the time-lapse geophone and DAS walk-away surveys is completed using the 1-D velocity models and ray tracing for the VSP reflection traveltime correction and common reflection point (CRP) binning. Unfortunately, the receiver aperture for the geophone time-lapse survey is limited to 1500 ft. The radial component contains the most P and PS-wave

energy and is probably the most useful component for this survey. The limited receiver aperture also limits the offset from the well which can be imaged to $\sim$ 2500 ft. When compared to the microseismic data, it becomes apparent that this survey is not imaging a significant portion of the well, and even less for the PS image ($\sim$ 1000 ft). Since the hydraulic fracturing occurred in Well A and the geophones are located in Well B, the time-lapse response is expected to be minimal. Currently, the time-lapse response is noisy and further processing is probably necessary to produce a conclusive time-lapse response.

The DAS walkaway survey contains a much larger receiver aperture (full length of the well) which improves the ability to cross-equalize the datasets using strong reflections located in the overburden. The fiber images the P-wave reflections very well and also records enough PS energy to image. Overall, the DAS walkaway is comparable to the vertical component for the geophone data, with a much improved receiver aperture. When compared to the microseismic, there is a potential time-lapse response, however, the image is noisy and would benefit from further time-lapse processing.

The 3D DAS VSP is imaged using the same ray tracing method and velocity model as the walkaway survey. The PS-wave reflections are recorded on the fiber and produce very good CRP mapping results. Even with potential lateral velocity variations within the survey area, the 1-D velocity model is valid to the first order. The results tie well to the dataset after a few velocity model modifications. Additionally, the 3D DAS VSP is sectioned off into 4 azimuth lines in order to perform both a reverse time migration (RTM) and a least-squares RTM in order to compare the migrations to the stacked results. The migrations are too computationally intensive to run on the full 3D dataset. The least-squares migration performs better than the RTM, but both migrations do not provide as clear an image as the CRP stacking performed on the same azimuth lines. The migrated images are negatively impacted by the irregular source spacing along the azimuth lines and the resulting gaps in reflection points.

TABLE OF CONTENTS

LIST OF FIGURES

LIST OF TABLES

LIST OF ABBREVIATIONS

Barrels (of oil)	Bbl
Common Reflection Point	CRP
Distributed Acoustic Sensing	DAS
Thousand Cubic Feet	MCF
Million Cubic Feet	MMcf
Normal Moveout	NMO
Reservoir Characterization Project	RCP
Source 1, Inline direction	SlIL
Source 2, Crossline direction	S2XL
Time-frequency Domain	TFD
Total Organic Content	TOC
Vertical Seismic Profile	VSP
Automatic Gain Control	AGC
One-way Time	OWT
Two-way Time	TWT

ACKNOWLEDGMENTS

First and foremost, I would like to thank my family: parents, sister, grandparents, and aunts. You have all been consistent supporters throughout my education and without your continuous love, support, and encouragement none of this would have been possible.

Thank you Dr. Ali Tura and Sue Jackson for admitting me into the RCP program. This has been an amazing, and difficult, experience for which I will be forever grateful. I give special thanks to Sue for her support and guidance these last couple years. I used to be terrified of presenting in front of an audience and thanks to you, and the many, many presentations I gave while in RCP, it's still not my favorite thing to do, but I'm confident in my ability to make and present quality presentations.

To my advisor, Dr. Jim Simmons. Thank you for your advice and guidance over the last couple years. I have enjoyed our research discussions over handfuls of pistachios and I'm still waiting for you to prove to me that you are really "King of Core." Your passion for research and teaching is clear and the excitement and energy you bring to the lab everyday made this experience way more enjoyable. I don't think I could have asked for a better advisor.

Thank you, to the students of RCP, for the community and support we have with each other. Without this amazing team, the research, as well as the endless days in the computer lab, would be bland and boring.

To my friends at Mines and elsewhere, you helped me stay composed and remind me of life outside of research. Our evenings at breweries and the climbing gym have helped me stay sane and more relaxed than I would be otherwise.

For those that shall follow after.

CHAPTER 1

INTRODUCTION

1.1 Project Background

This project is part of Phase XVII of the Reservoir Characterization Project (RCP), otherwise known as the Eagle Ford Project. Comprehensive geophysical, geological, geomechanical, completions, and production datasets are provided by Devon Energy Corporation. Analysis of these data could give insights into the design of a permanent reservoir monitoring program, enhance understanding of the value of different technologies, and lead to improvements and discovery of new technologies and methods to solve important problems in unconventional reservoirs.

The focus of this project is reprocessing and analyzing the time-lapse multicomponent geophone and DAS VSP data to evaluate the time-lapse changes induced by hydraulic fracturing, and to compare VSP data quality between the geophone and DAS datasets. Time-lapse changes are compared with results from microseismic to comprehensively analyze changes detected in the reservoir induced by hydraulic fracturing.

VSP surveys using DAS fiber are acquired in much the same way as with traditional geophones except that the receivers, being the fiber, is cemented in the borehole casing and is a permanent fixture in the well. DAS fiber is a relatively new technology and, as such, its utility in borehole geophysics is being extensively researched. Various studies have compared conventional geophone VSP to DAS VSP: Mateeva *et al.* (2014), Willis *et al.* (2016), Cai *et al.* (2016). Others have discussed methods to convert the DAS recorded strain rate to geophone recorded particle motion: Bakku (2015), Daley *et al.* (2015), Bóna *et al.* (2017), Correa *et al.* (2017). These studies focus on comparing the data quality, such as the signal-to-noise ratio and frequency content, as well as converting to a geophone response, primarily on zero-offset datasets. They discuss that the DAS fiber is useful for acquiring VSP data even though, in

earlier models, the DAS fiber has a poorer signal to noise ratio than the geophones. Different conversion methods have had success in properly matching the amplitude and phase recorded by the geophones and newer studies report better signal-to-noise ratios.

This study compares geophone to DAS responses for single shot gathers as well as common reflection point (CRP) stacked images, from the time-lapse walkaway surveys. The final stacked images comparing geophone to DAS of a walkaway survey has not yet been published, so this is an important contribution of this study. The time-lapse repeatability of these data is compared and discussed as well. Overall, this project does not compare geophone to DAS datasets in the same depth and detail as studies mentioned above, however, the comparison is broader and compares multiple types of survey designs.

1.2 Study Area

This project is located near the San Marcos Arch in Lavaca County, South Central Texas (Figure 1.1). The primary reservoir targets in this area are the Austin Chalk and the underlying Lower Eagle Ford Shale. This package of rocks has an elongated trend from northeast to southwest that stretches over 400 miles across Texas and into Mexico. The formations dip towards the southeast causing differing levels of maturity and changes in fluid type. The RCP study area is located in the volatile oil window in the transition zone between oil and gas.

1.3 Available Data

Located in the center of the study area are two wells (A and B) which are the focus of this study (Figure 1.2). The data were acquired in a time-lapse sense (baseline and monitor surveys) centering around the hydraulic fracturing of Well A. The VSP geophone array is located within Well B, while the DAS fiber is encased within Well A. Since the tools are located in different wells, the comparison between the datasets cannot be exact and careful considerations must be taken while analyzing the two datasets together. Multiple VSP surveys where shot for each well. These surveys include zero-offset, walkaway, vertical incident,

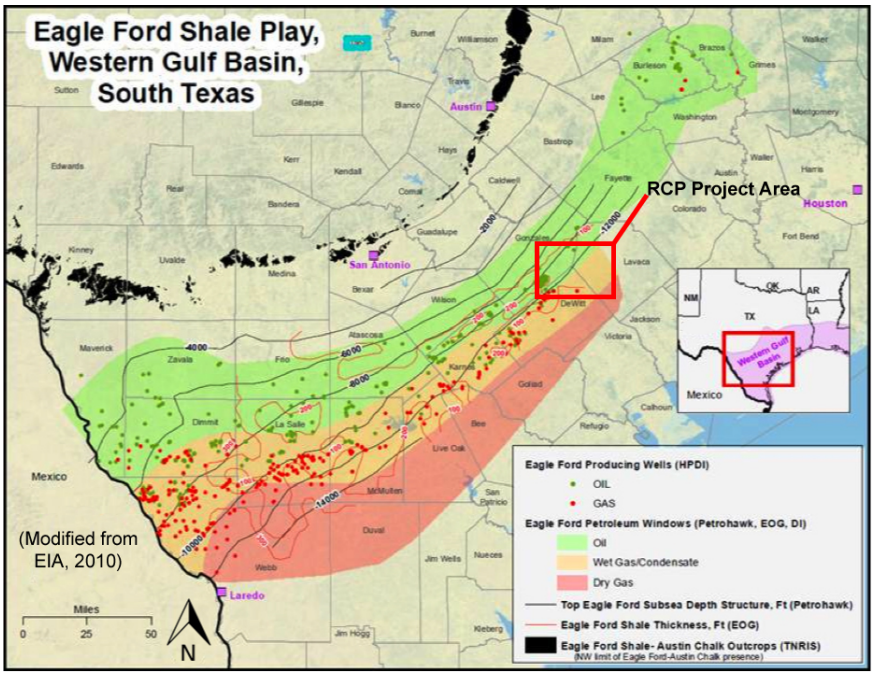

Figure 1.1 Location of RCP study area in Eagle Ford Basin, South Central Texas (Modified from EIA, 2010)

a small arc, and post frac 3D recorded by DAS. The time-line for the VSP acquisition is found in the following table (Table 1.2). The zero-offset and arc surveys were acquired with three-component sources (vertical and two horizontal), the walkaway and 3D were acquired with only a vertical source.

With the plethora of available data, decisions about what datasets to focus on had to be made. The zero-offset, walkaway, and 3D surveys were determined to be the most useful in resolving the reservoir properties and had the best survey design qualities. The small arc survey was considered to be less useful because of its small extent. It does not cover a full 90 degrees to gather a complete picture of the azimuthal variations.

1.3.1 Goal of VSP Processing

Vertical seismic profiles can be a useful tool in reservoir monitoring and is best used along with other data such as surface seismic, sonic logs, and other well logs. These data have better resolution than surface seismic surveys because the reflection travel-path is less than that of

Table 1.1 Pre-frac acquisition time-line

Day 1	Day 2	Day 3
Well A - DAS		
Arc, Walkaway	Walkaway	Zero-offset
Well B - Geophone		
Arc	Walkaway	Zero-offset

Table 1.2 Post-frac acquisition time-line

Day 1	Day 2	Day 3	Day 4	Day 5
Well A - DAS				
Walk-away, Zero-offset	Walkaway Zero-offset	Walkaway, Offset	Walkaway, Offset, Walkaway	Walkaway
Well B - Geophone				
Walkaway, Zero-offset	Walkaway, Zero-offset	Walkaway, Arc	Walk-above, Arc	

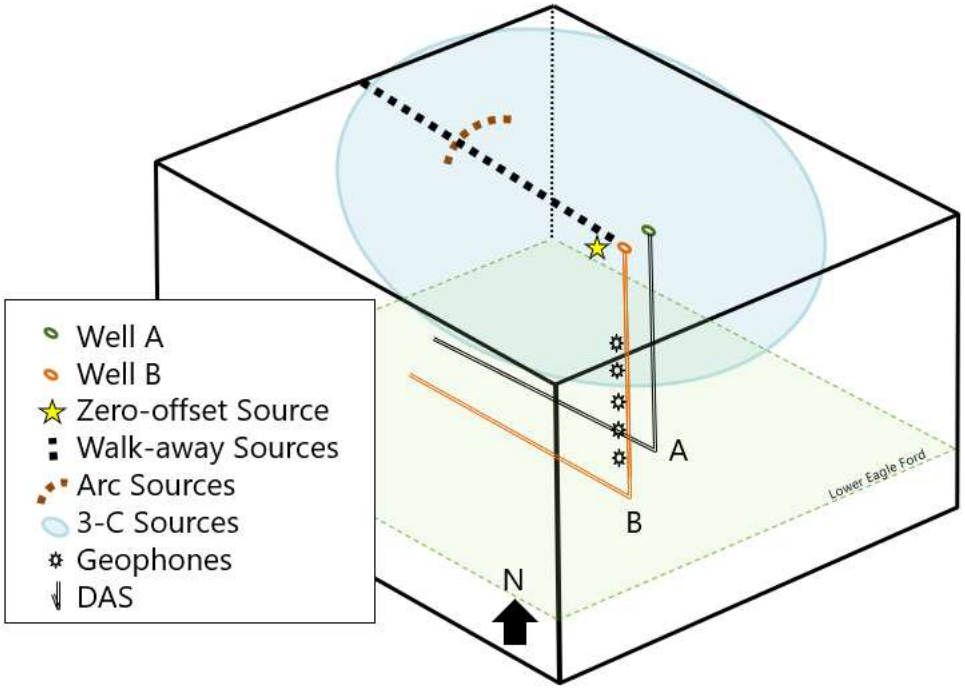

Figure 1.2 3D diagram of VSP surveys acquired as part of this project.

surface seismic data because the receivers are at depth. This allows for higher frequencies to be less attenuated and for better signal-to-noise ratios at those higher frequencies. VSP surveys have less resolution than sonic logs but are not as prone to errors from fluid invasion and other borehole effects and thus are useful in determining velocities when the sonic log has errors. The known placement of geophones in depth allows for exact time-to-depth calculations and thus are useful in calibrating velocity models and tying major reflectors across well logs and surface seismic.

1.3.2 3C Geophone VSP

Deploying a string of geophones is the traditional method of acquiring VSP. The geophones are deployed to their deepest level and then successively pulled up higher in the well. Each source point must be repeated at every tool level. There are 20 receiver levels per string with 50 ft spacing for this project. This becomes a tedious process when acquiring a walkaway line so only a small number of tool placements are used. Unfortunately, this also

makes acquiring a 3D survey unrealistic for a tool with only 20 levels. One large advantage that geophones have over DAS fiber are three-component receivers. Recording particle motion (z,x,y) allows for shear-wave processing and interpretation which can add a lot of value when in anisotropic media. Three-component receivers are necessary when performing shear-wave splitting analysis using the Alford rotation method (Alford, 1986) and determining shear wave velocities using the direct arrival from a shear source zero-offset VSP. The single component of DAS cannot be used for these calculations, however, PS converted waves can be recorded so shear wave information can still be gathered.

The geophone details are listed in Table 1.3 below and the source parameters for both the geophone and DAS surveys is listed in Table 1.4.

Table 1.3 Geophone Parameters

Downhole Receivers	
Type	ASR
Sensor Pack	3-Component Fixed
Time Sampling	2 ms
Number of Levels	Dependent on Survey
Level Spacing	50 ft
Geophone Locations	Vertical section of well (dependent on survey)

Table 1.4 Source Parameters

Source Type	**P Source**	**S Source**
Number of Vibes	2	2
Sweep Period	16000 ms	32000 ms
Record Length	2200 ms	44000 ms
QC Data Length	6000 ms	12000 ms
Start Frequency	4 Hz	2 Hz
End Frequency	96 Hz	44 Hz
Sweep Description	Linear	Linear
Surveys	Zero-offset, Arc, Walkaway, 3D	Zero-offset, Arc

It is important to note that the shaking directions of the two shear vibroseis sources are not oriented as inline and crossline relative to the well. The sources are shaking in the directions of the interpreted maximum (S1) and minimum (S2) regional stress, presumably, in order to compare the fast and slow shear wave propagation directions. All three sources are also located along different azimuths relative to the well (Figure 1.3). This survey design poses some unique challenges when attempting to orient the receivers. These challenges and the solutions are discussed in detail in Chapter 2.

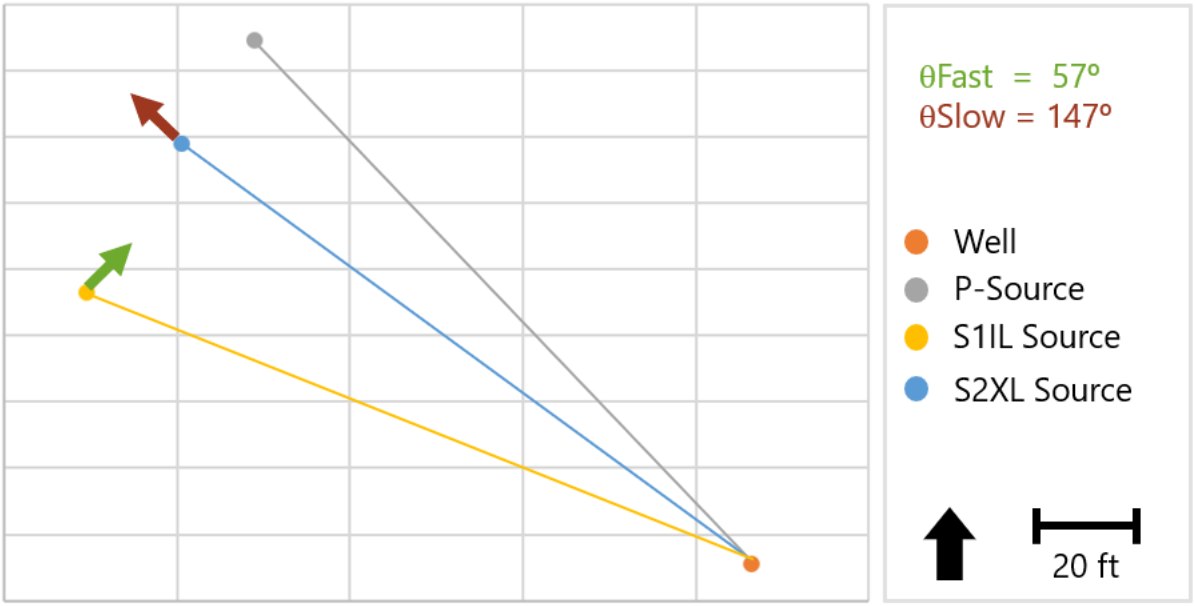

Figure 1.3 Map view of the pre-frac zero-offset VSP survey.

1.3.3 DAS VSP

The fiber optic (DAS) cable is cemented behind the casing of Well A. The DAS VSP surveys were recorded concurrently with geophone VSP surveys. While the sources were acquired for the geophone VSP surveys described above, the DAS was recording. The geometries can be seen in Figure 1.4 and Figure 1.5.

The basic concept of how DAS measurements are recorded are as follows. Laser pulses are sent along the fiber in the well by a DAS interrogator unit. Small random heterogeneities

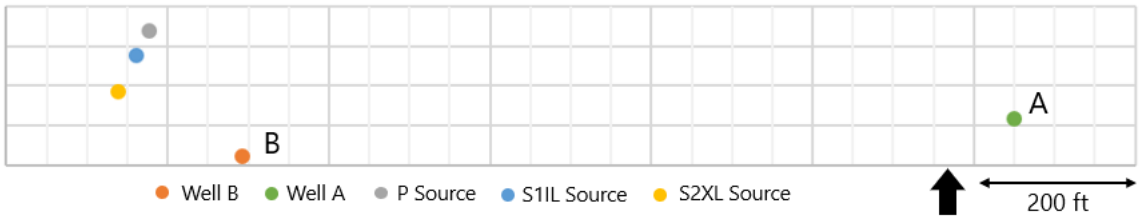

Figure 1.4 Map view of Well A and Well B in relation to the pre-frac zero-offset sources.

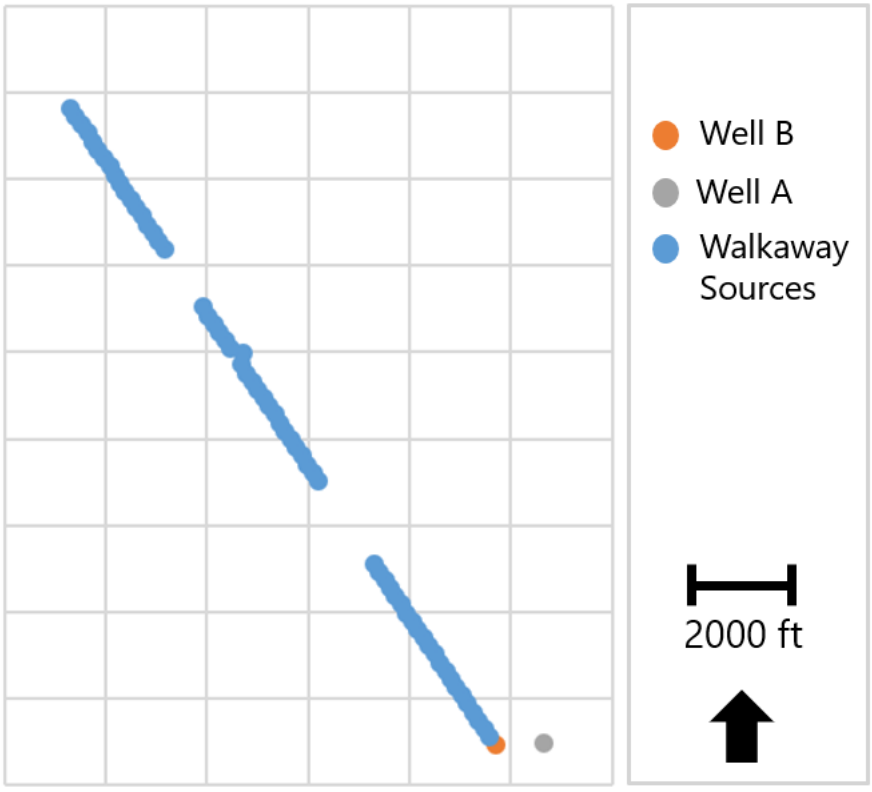

Figure 1.5 Map view of walkaway line. Walkaway sources are vertical sources only.

naturally present in the fiber cause a small fraction of the laser light to backscatter (Rayleigh Scattering). When a seismic wave deforms the fiber, changes in the Rayleigh back-scattered pattern occur and these changes are translated into seismic measurements. This most basic form of DAS measurements are only capable of measuring seismic intensity, and so, is not useful for seismic measurements that require accurate representation of waveforms in terms of amplitude and phase (Mateeva *et al.*, 2014). Newer generations of DAS systems, including the one used in this project, utilize a pair of laser pulses with a known separation called gauge length. This system provides seismic displacement measurements (strain over gauge length) based on the changes between the two pulses. This technology is changing rapidly and since these data were acquired, significant improvements to data quality have been achieved (Daley *et al.* 2015, Munn *et al.* 2017 Chen *et al.* 2018).

This technology has a few advantages over traditional geophones for VSP acquisition. DAS can be deployed along the full length of the well, providing full well coverage for each VSP shot and at a much finer receiver spacing. Geophones, however, have limited aperture and require multiple tool placements to image the length of the well. The full coverage and non-intrusiveness of the DAS fiber improves the safety, logistics, and cost of performing a VSP survey (Mateeva *et al.*, 2014). The slim cables also allow VSP to be performed on wells that geophones cannot access such as injectors, producers, and ultra-slim observation wells (Mateeva *et al.*, 2014). DAS also has better receiver spacing compared to geophones (1ft vs 50ft) and is generally less responsive to tube wave energy (Willis *et al.*, 2016). The main disadvantage to DAS is that it can only record a single component of particle motion because it is only sensitive to particle motion that is parallel to the fiber. This makes processing for shear waves difficult, but not impossible. DAS will only record shear waves at incident angles having "significant" particle motion in the direction of the fiber.

DAS fiber has a few sources of noise that are unique to itself. There are faded channels seen as vertical noise, and common mode noise seen as horizontal noise caused by the interrogator unit. These will be discussed further in Chapter 3.

1.3.4 Differences Between Geophone and DAS Recordings

There are a number of important differences between geophone and DAS recordings. The signal to noise ratio for geophones is higher than that for DAS (Mateeva *et al.*, 2014). This is true for this experiment and other older systems however, newer systems are significantly improving the signal to noise ratio. A simple way to improve this is to increase the number of sweeps to stack together, although this method of improving signal to noise is not unique to DAS. As interrogator units improve, the signal to noise ratio is likely to increase. The angles of sensitivity also differ. DAS is sensitive to particle motion arriving parallel to the fiber and insensitive to perpendicular particle motion. It also has a maximum sensitivity to S-waves at incidence angles of 45° (Bakku, 2015). Additionally, unlike geophones, polarity doesn't change with angle of incidence so both the upgoing and downgoing waves have the same polarity on DAS, while they have the opposite polarity on geophones (Bakku 2015, Mateeva *et al.* 2014). DAS also does not distinguish between the direction of propagation of shear waves. Geophones would record different polarities (Bakku, 2015).

1.4 VSP Imaging: Common Reflection Point Mapping Versus Stacking VS Reverse Time Migration

One of the major processing steps for the walk-away and 3D surveys are traveltime (moveout) correction and common reflection point (CRP) mapping. The two step process uses a code developed by Dr. James Simmons in RCP and begins with one-dimensional ray tracing using isotropic velocity models (Vp and Vs). Ray tracing computes the travel time corrections and the reflection-point locations needed for the CRP mapping. Next, the common reflection points are mapped using the traveltime-corrected shot gathers. The ray tracing produces traveltime corrections and common-reflection points as a function of vertical traveltime and spatial position $(t_0, crossline, inline)$. The traces in the traveltime corrected shot gathers are mapped to their corresponding common-reflection points using a specified bin size. The benefit to this process is that it is fast and produces accurate results. If there are missing reflection points caused by the acquisition geometry, there is a gap in the final

image. This is very useful in interpretation to ensure that noise smeared across a reflection point gap, as occurs in prestack migration, is not interpreted as signal.

Two migrations were used to process 2-D lines from the 3-D VSP dataset, reverse time migration (RTM), and least-squares reverse time migration (LSRTM). While a conventional migration propagates the data downward through a velocity model into the earth, the RTM propagates events both downward and upward though a velocity model. This type of a migration can handle more complex geology and propagation paths than conventional migration algorithms. The LSRM improves this process by updating each shot gather of the migration image separately and producing and ensemble prestack image along with the common image gathers (Dai & Schuster, 2013). This method increases the computational cost but can provide higher quality images. For a more detailed description of the migration methods used in this project and how they are implemented to DAS data please see Lim (2019).

1.4.1 Other Data

Other data provided by Devon Energy Corporation for the Eagle Ford Project include a time-lapse 3-D 3-C surface seismic survey, microseismic, well logs, completion, and production information. Additional well logs in the study area are provided by Penn Virginia Corporation.

Wells A and B are located roughly in the center of the 3-D 3-C surface seismic grid. Tying to the seismic data is an important quality control step and products from the VSP processing can be used to help interpret and depth convert the surface seismic.

Microseismic was acquired with various receiver geometries (Figure 1.6) including scattered 3-component surface receivers (same receivers as surface seismic), 1-component radial and patch arrays, downhole geophones (Well B), and fiber optic DAS (Well A). When processing microseismic events it is important to have a correct velocity model. The VSP can help improve the velocity model that is used. Additionally, the locations of the microseismic events can indicate where time-lapse changes in the VSP should be if they are observable.

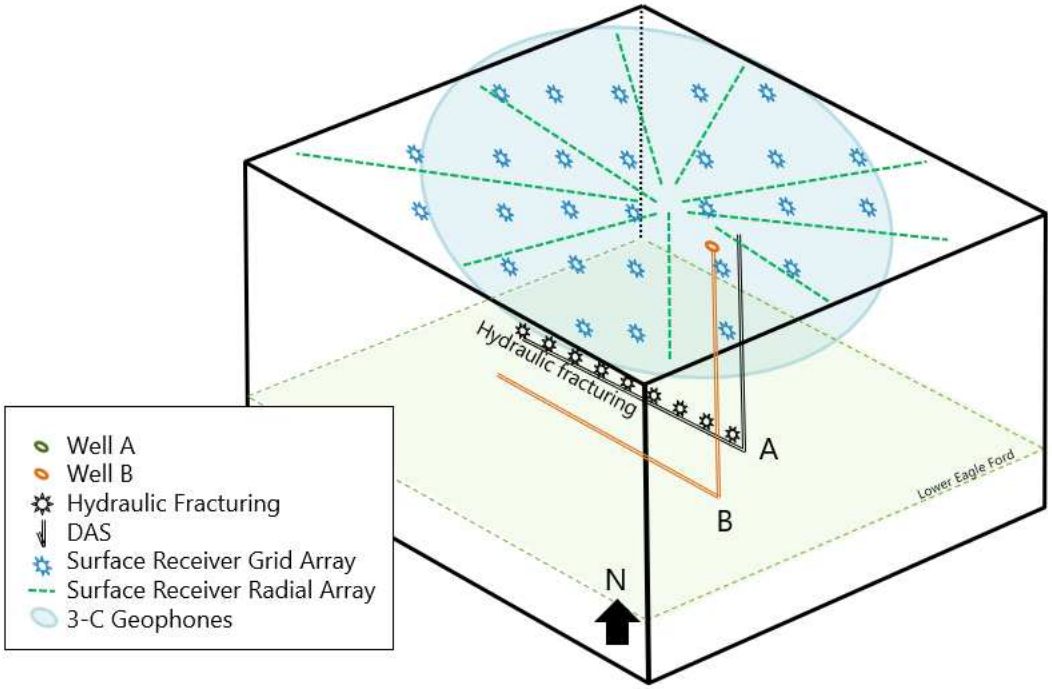

Figure 1.6 3D diagram of microseismic acquisition.

Conventional processing of the surface seismic, microseismic, and VSP data is done independently. Different vendors processed each data set separately, each deriving a different velocity model to satisfy their processing. This is concerning because it can lead to uncertainties when attempting to integrate the various datasets. One goal of the Eagle Ford Project is to use information from these three datasets to ultimately create a single unified velocity model. The VSP can provide a one-dimensional velocity model to be used as a starting point for more complex (and anisotropic) velocity models.

1.5 Geologic Background

Since production began in 2008, the Eagle Ford Formation and overlying Austin Chalk have been one of the top producing plays in the United States. The production hit a peak in 2015 producing over 1,196,000 Bbl and 6,000 MMCF of gas per day (Craddick *et al.*, n.d.). During this time Devon has been one of the top gas operators in the region producing 131,776,923 MCF total gas as of 2016 (Craddick *et al.*, n.d.). Although production has

declined in recent years, the Eagle Ford is still a young play with lots of potential.

1.5.1 Depositional Environment

The Austin Chalk and the Eagle Ford Shale consist of organic carbon enriched mudstones and chalks (Robison, 1997). Both formations are Late Cretaceous in age and usually contact each other unconformably (Montgomery, 1991). They were deposited into the Western Interior Seaway during a period of high sea levels and low oceanic oxygen levels, creating an ideal environment for the preservation of organic matter (Phelps *et al.*, 2014). The deposition took place mostly in a low energy environment which was episodically interrupted by higher-energy events (Harbor, 2011). In the eastern part of the play (our study area), Eagle Ford rocks have more shale and carbonates and less sandstone than the time-equivalent rocks on the western side. This is due to the fact that in the late Cretaceous Period, the eastern part of the play subsided less than the western side (Dyman & Condon, 2006).

1.5.2 Petroleum System

The Eagle Ford Shale generally exhibits greater organic contents and larger quantities of oil-prone kerogen than the Austin Chalk (Robison, 1997). The TOC content in the Eagle Ford ranges from 1.7% to 7.2% with and average of 3.9% (Chalmers & Bustin, 2017). In both the Eagle Ford Shale and the Austin Chalk, type 2 and type 3 kerogen is present. Type 2 kerogen contains mostly hydrogen-enriched kerogen such as florescent amorphous material, alginite, and exinite. Type 3 kerogen contains mostly hydrogen-pure humic organic matter such as vitrinite and oxidized amorphous material (Robison, 1997). There are higher levels of kerogen and TOC in the central portion of the Eagle Ford shale and the organic rich kerogen in the dry-gas window is post-mature (Dyman & Condon, 2006).

There is a change of fluid type across the play due to the beds regionally dipping to the southeast. To the northwest, there is predominately oil, but this transitions to volatile oil, wet gas, and then dry gas towards the southeast. The study area lies mostly in the volatile oil area of the transition zone (Figure 1.1). The oil window is more quartz rich in the lower

Eagle Ford than in the dry-gas and wet gas windows, which are more carbonate and clay rich (Dyman & Condon, 2006). The percentage of calcite is also greater in the oil window and many of the other occurring minerals are consistent in the different windows. The carbonate content in the Eagle Ford varies widely from 9-90% but averages at 56% (Harbor, 2011).

During the expulsion phase of hydrocarbon generation the migration of Eagle Ford hydrocarbons was primarily along bedding planes. In the areas absent of traps, the hydrocarbons migrated updip, or north, to where vertical fractures were encountered (Martin *et al.*, 2011). The fractures are associated with regional fault trends and this is how the hydrocarbons migrated into the highly fractured Austin Chalk. Both stratigraphic and structural traps are found in current Eagle Ford exploration areas.

1.6 Scope of Work

The work presented in this thesis include the processing of multicomponent geophone and DAS zero-offset VSP, time-lapse walkaway VSP, and DAS 3D VSP. The processing steps are described in detail and their utility and affect on the data are discussed. The DAS and geophone data undergo the same processing steps up until the DAS is converted to a geophone response. The final processing results are shown and the limitations of the data are addressed. The zero-offset and walkaway processing for the geophone and DAS data is discussed in Chapters 2 and 3, respectively. Chapter 4 addresses the processing of the 3D DAS VSP dataset. A brief time-lapse analysis on the walk-away survey is performed and compared with the microseismic results in Chapter 5. Finally, while this is a broad project, it is by no means comprehensive, recommendations for future work and improvements are discussed in Chapter 6.

CHAPTER 2

MULTICOMPONENT GEOPHONE DATA PROCESSING

This chapter discuses all the Geophone VSP datasets. Beginning with the zero-offset survey, the processing steps are outlined and examples provided. Most of the processing steps use the vertical geophone component as an example, unless otherwise stated. The P-wave vertical component is processed through to the corridor stack and tied to seismic. A one dimensional P-wave velocity model is created and is used in ray tracing on the walkaway and 3D datasets. Then the shear-wave and horizontal component processing is addressed. Next, the walkaway processing is discussed, starting with the ray tracing to correct travel times and map reflection points. Statics and filters are tested to improve the final image.

2.1 Zero-offset Vertical Source

Zero-offset VSP is a simple but important survey. The sources are located close to the well in order for the energy to travel essentially vertically downward, simulating a normal incidence seismic experiment. The known receiver depths allow for accurate time-depth relationships and, thus, accurate velocity calculations. The correction from one-way time (OWT) to two-way time (TWT) is simple and important when tying to surface seismic.

Figure 2.2 illustrates the pre-frac survey in map view and the parameters are listed in Table 2.1. There are no offset P-sources to help orient the geophones, so the zero-offset source will be used. This survey design imposes some unique challenges when rotating the horizontal geophones, which will be discussed later in this chapter. The geophones for this survey are located along the whole vertical portion of the well, a $12,000$ ft aperture, at 50 ft receiver spacing.

The post-frac (monitor) zero-offset survey design is slightly different Figure 2.3. There is no zero-offset P-source and both shear sources are located at the S1IL source location. This survey was operated concurrently with the post-frac walk-away so there are multiple

offset P-sources to chose from to orient the geophones. The number of receiver locations is significantly limited for this survey compared to the baseline with an aperture of only 2000 ft at 50 ft spacing. The geophones are concentrated near the base of the well. The receiver differences can be seen in (Figure 2.4).

The general processing flow used for this survey is listed in Figure 2.1. These processing steps will be discussed in this chapter.

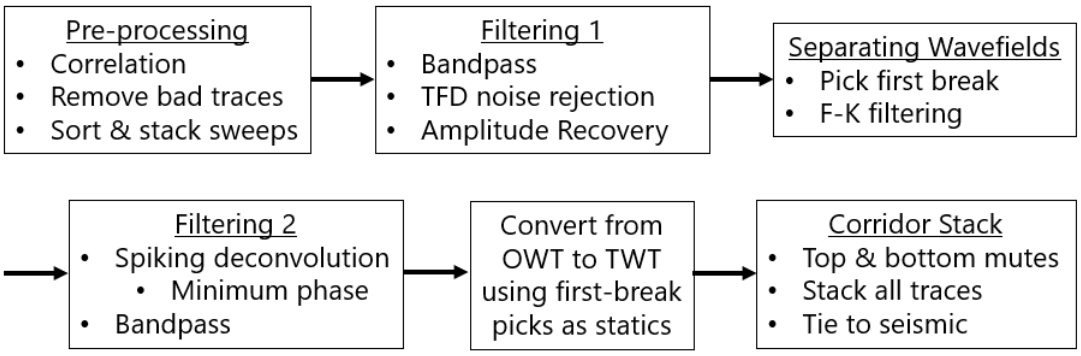

Figure 2.1 Generalized processing flow for zero-offset survey.

Table 2.1 Zero-Offset Source Locations Relative to Well and Shaking Directions

	P-Source	S1IL-Source	S2XL-Source
Offset	195 ft	174 ft	183 ft
Azimuth	-36°	-61°	-46°
Shaking direction	Vertical	57deg	147 deg

2.1.1 Vibroseis Correlation

The first processing step performed is vibroseis correlation. The sweep signal is crosscorrelated with the recorded vibroseis record to produce the correlated shot record (Figure 2.5). This figure shows one shot record into 19 receiver depths with 3 components/channels each. The last channel in both images is the recorded vibroseis sweep. After the correlation, the traces are much shorter in time and the first-breaks for the P-wave and S-wave can be seen.

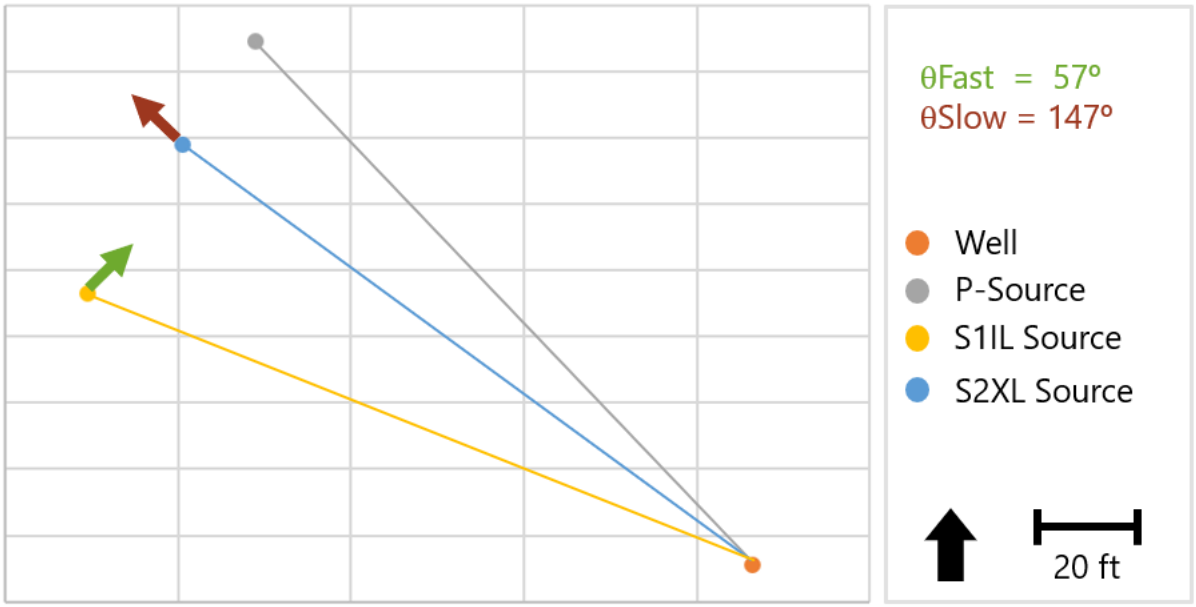

Figure 2.2 Map view of the pre-frac zero-offset VSP survey. The shaking directions of the shear sources are indicated by the red and green arrows. Lines are drawn connecting the source points to the well location (orange) to help visualize the different azimuths of the sources.

Next the vertical and horizontal components are separated and the shots are stacked together before finally sorting into a single shot gather.

2.1.2 Noise Attenuation

A space,time-frequency dependent (TFD) 2-D median filter is applied to attenuate noise bursts. This is a filtering method which removes high amplitude isolated noise (existing on a single trace or few traces) over a limited frequency range. Anomalous amplitudes are replaced with the amplitudes from adjacent traces using a median filter. Occasionally, there are traces with anomalous amplitudes which have a frequency spectrum similar to that of the rest of the data. A bandpass filter can not remove this noise but a TFD filter efficiently removes this type of noise (Figure 2.6).

To account for the loss of amplitude due to wavefront spreading and attenuation a simple time-power amplitude correction is applied in the form of the following equation: $g(t) =$

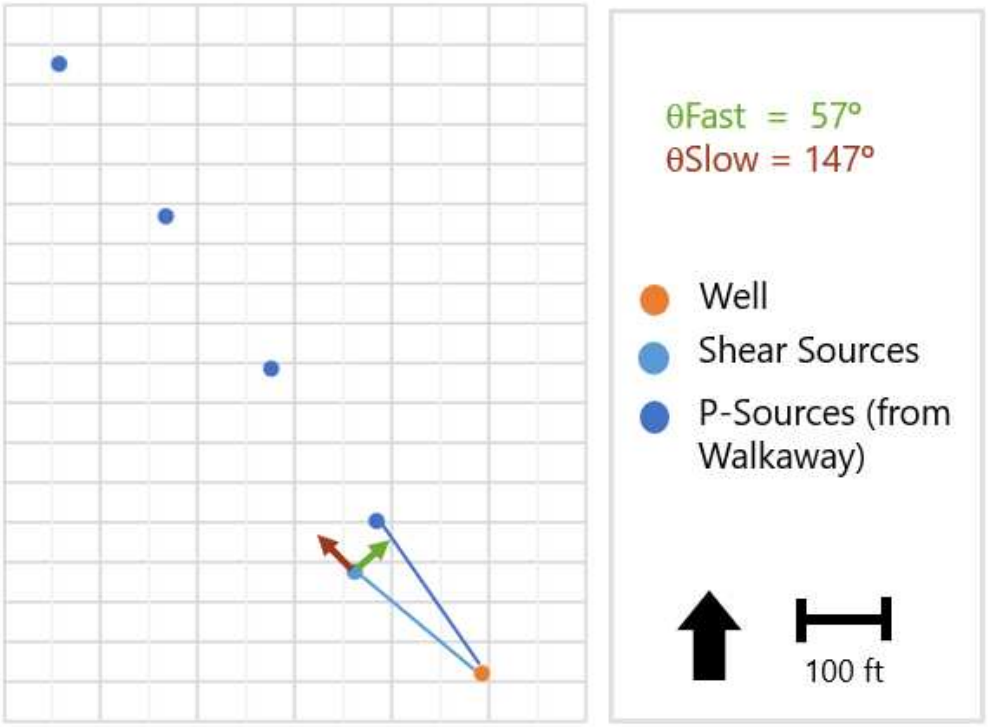

Figure 2.3 Map view of the post-frac zero-offset VSP survey.

t^{power}, where power=2. This increases the amplitudes of the deeper reflections (Figure 2.7).

Now that the initial filtering has been performed, high frequency noise and anomalous large amplitude noise is removed and the amplitudes have been corrected. The important elements in this P-source zero-offset VSP record will now be discussed using Figure 2.8.

The downgoing P-wave is highlighted in red and dipping from left to right, also known as the direct arrival or first-break. This is used for the first-break picks which are used for calculating the P-wave velocities and for connecting the data from one-way time to two-way time, which flattens the upgoing reflections. Upgoing P-wave reflections, dipping opposite the downgoing waves from right to left, are seen in orange. Highlighted in green is the tube wave. A tube wave is an interface wave which travels down the well along the interface between the wall of the wellbore and the fluid of the wellbore. It has a near constant velocity, and so, is easily removed by a median filter if desired. For the purposes of this study, only the direct arrival and the reflections near the direct arrival are of interest so the tube wave

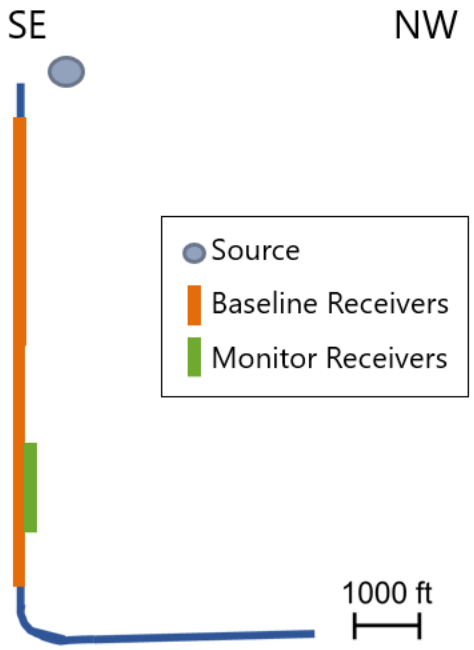

Figure 2.4 Geophone levels for the baseline survey (orange) and the monitor survey (green).

is ignored.

Now that the noise in the data are sufficiently attenuated, P-wave first-breaks are picked. The time-depth pairs are used to convert the zero-offset survey from one-way time to two-way time which "flattens" the reflections. Also, a one dimensional velocity model is created using these time-depth pairs that is used in processing of the other VSP datasets and can help the processing of surface seismic and microseismic.

The typical procedure for producing a time-depth curve used to calculate the 1-D velocity model starts with picking the first arrivals. Since there is a small amount of offset from the source to the well head, the travel times need to then be corrected from the slanted time to vertical time. Then the velocity can be calculated by: $v = dz/dt$.

2.1.3 F-K Filter

In order to separate the upgoing from downgoing wavefields an F-K filter, based on their dips, is applied. Two tools are used for this process, F-K Analysis and F-K Filter. The

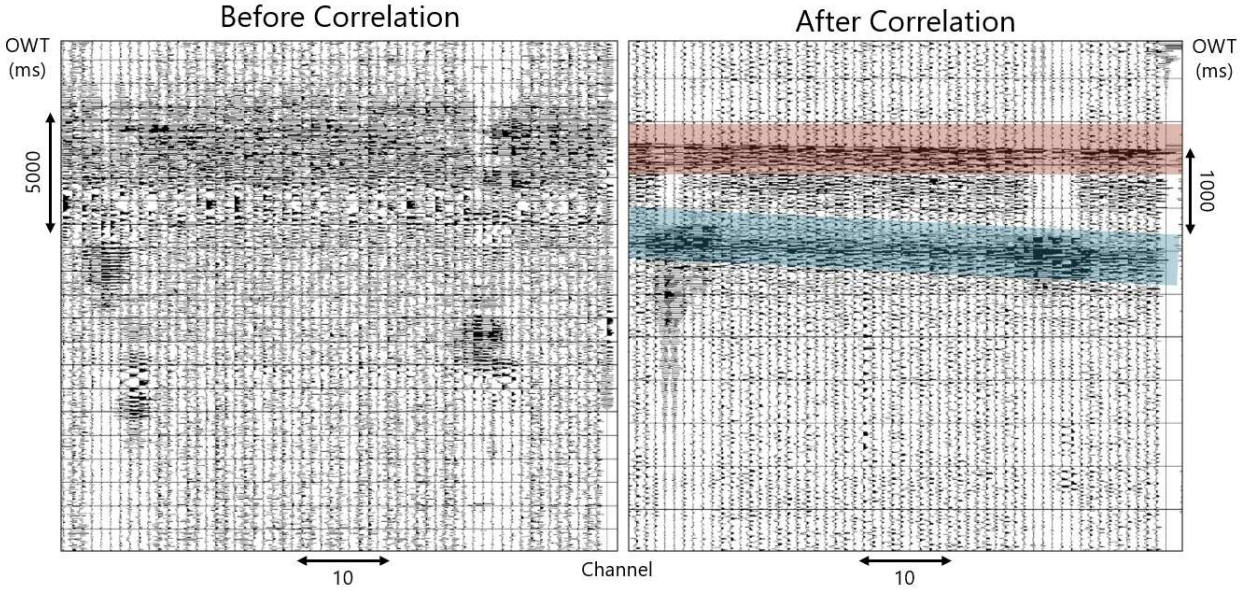

Figure 2.5 Raw P-source zero-offset geophone VSP before and after vibroseis correlation. The red shaded area highlights the P-wave arrival and the blue highlights the shear-wave arrival. Neither are visible before correlation.

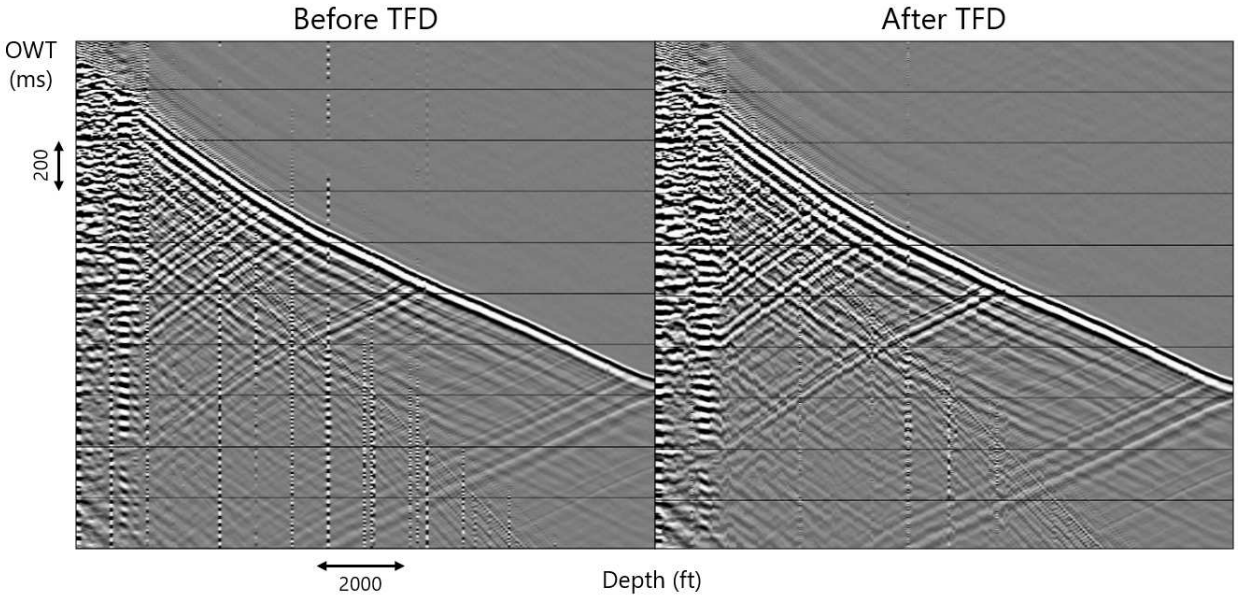

Figure 2.6 Zero-offset geophone VSP before and after TFD noise rejection.

analysis tool converts the data from time and space (T-Z) to the frequency and wavenumber domain (F-K) using a two dimensional Fourier Transform. The data are displayed in F-

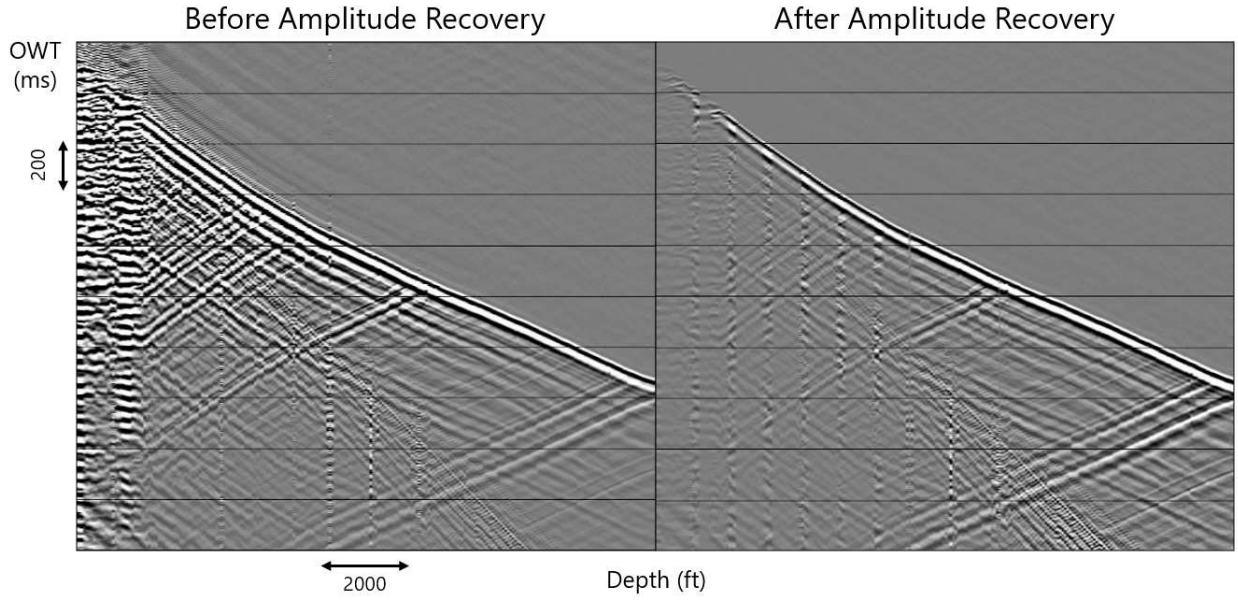

Figure 2.7 P-source zero-offset vertical component geophone VSP before and after amplitude recovery.

K space and the filter can be manually picked (Figure 2.9). Since all downgoing energy must be removed, all energy with a positive wavenumber (downgoing energy), as well as aliased energy, is included in the filter. Everything within the filter is rejected and the data are converted back into T-Z space for further processing (Figure 2.10). An automatic gain control (AGC) is applied before the F-K filter and removed afterwards. Since the filter is based on dips, the AGC helps see the dipping energy in F-K space. The results of using F-K filtering to separate the wavefields is seen in Figure 2.11. The wavefields are clearly separated, but the upgoing wavefield contains remnants of the tube wave energy.

When the F-K filter encounters a discontinuity, such as the first break, artifacts are created. This shows up as a smearing across the first breaks that needs to be excluded from the final corridor stack. Evidence of this can be seen in Figure 2.11(b). A top mute removes this noise. Another method for removing the downgoing energy is using a 2D spatial filter once the upgoing waves are converted to two-way time. This method passes the flattened energy and effectively minimizes all the energy that is not flat.

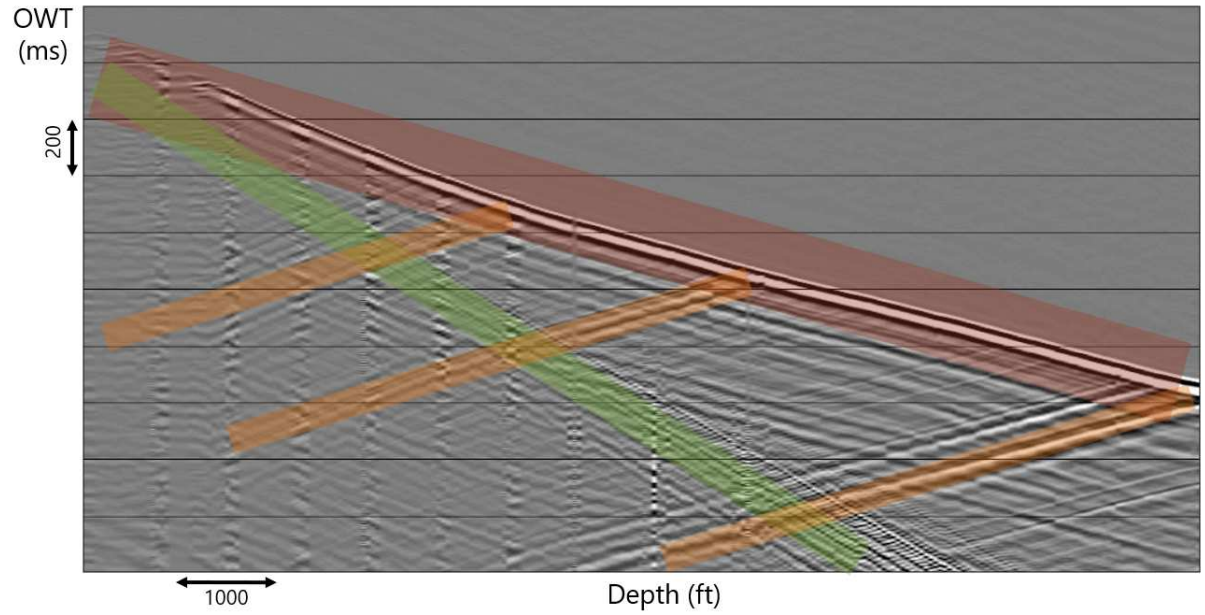

Figure 2.8 Initial filtering of vertical source zero-offset z-component. (Red) First break, (Orange) Reflections, (Green) Tube wave.

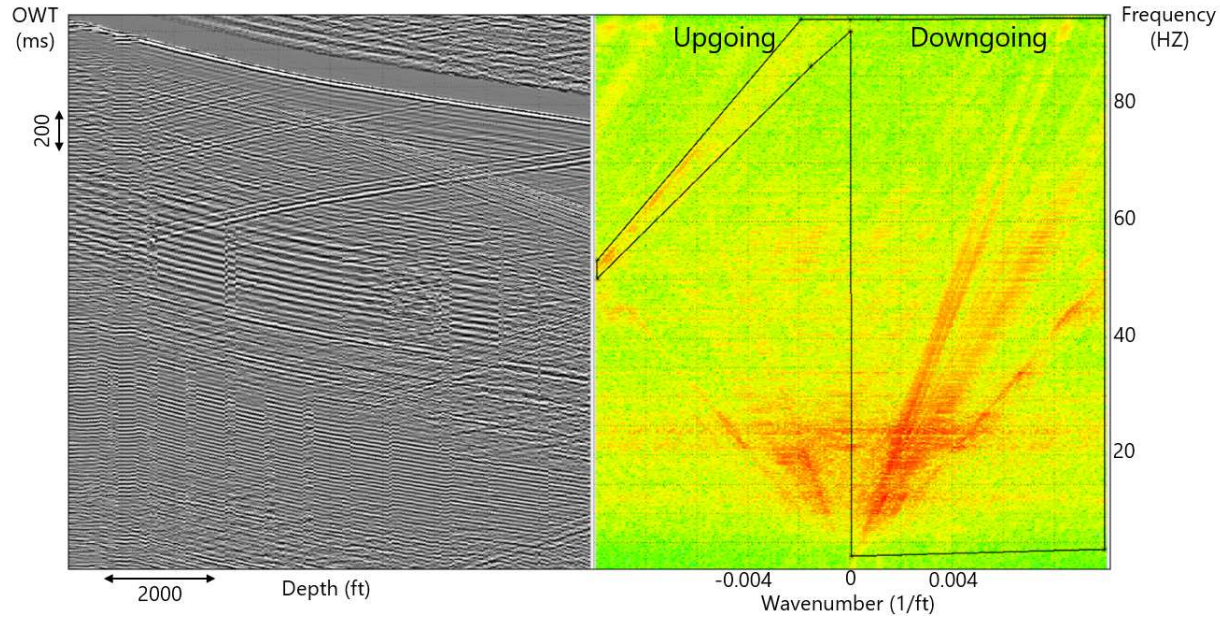

Figure 2.9 Before F-K filter is applied. Automatic gain correction (AGC) is applied to increase energy visibility in plots. (Left) Zero-offset VSP in T-Z space. (Right) Zero-offset VSP in F-K space. Filter is outlined in black. All positive wavenumbers as well as aliased energy (seen in top left) will be removed.

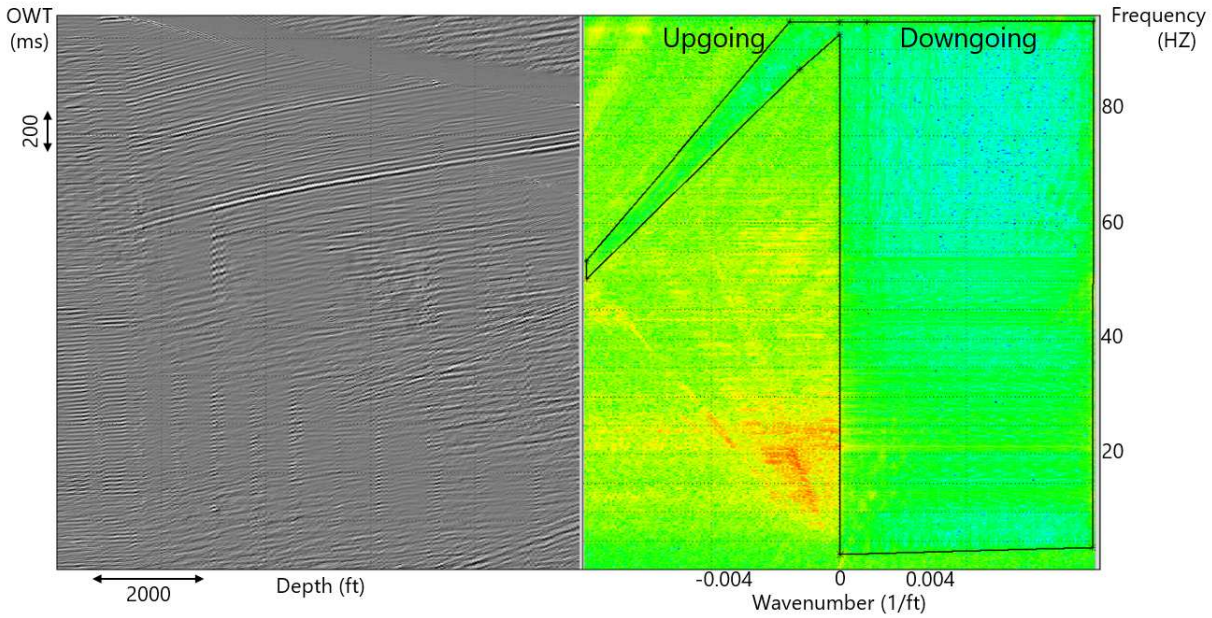

Figure 2.10 After F-K filter is applied. Automatic gain correction (AGC) is applied to increase energy visibility in plots. (Left) Zero-offset VSP in T-Z space. (Right) Zero-offset VSP in F-K space. Filter is outlined in black. All positive wavenumbers as well as aliased energy (seen in top left) is removed.

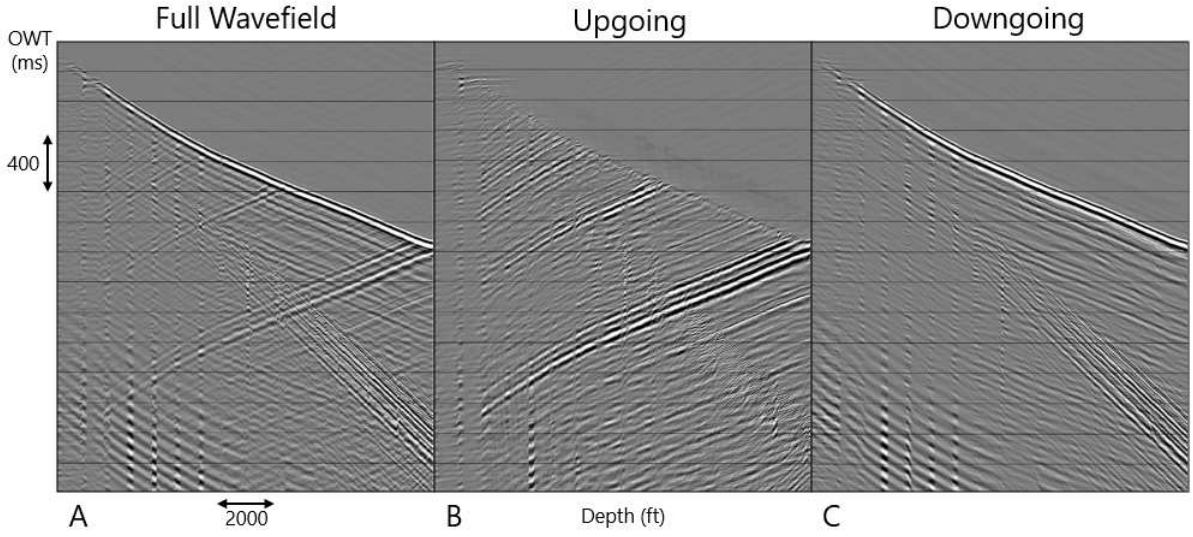

Figure 2.11 (A)Zero-offset VSP before wavefield separation (FK filtering), (B) resulting upgoing wavefield or reflected waves, (C) resulting downgoing wavefield.

2.1.4 Spiking Deconvolution

The objective of spiking deconvolution is to compress the wavefield to a spike which whitens the frequency spectrum. The specific type of deconvolution applied is minimum phase spiking which applies a traditional Wiener-Levinson spiking deconvolution (Lines & Ulrych, 1977). It assumes minimum phase data, so first, the data must be converted to minimum phase. To do this a synthetic vibroseis sweep is generated using the source parameters specified in the acquisition report. This sweep is autocorrelated and then used to create a minimum phase filter to be applied to each trace.

Next, the spiking deconvolution filter is generated by specifying a filter design window (example in Figure 2.12). Then, the average auto-correlation within the design window is taken and used to design the minimum phase spiking deconvolution filter. The filter is then applied to the data. A bandpass filter must be applied after the filter because this process can amplify frequencies that have low signal to noise ratio.

The results of the spiking deconvolution is shown in Figure 2.12. The reflections deeper in the section are brighter and more defined. Some additional detail has been added with the higher frequencies. The middle of the section looks more noisy than before the spiking deconvolution, but the area of interest is at the deeper reflections and will not affect the final stack. This noise is the result of remnant tube wave energy and a few "slightly" noisy traces.

As previously stated, the goal of spiking deconvolution is to sharpen the wavefield into a spike which whitens the frequency content. Figure 2.13 shows the amplitude spectrum of the zero-offset VSP before spiking deconvolution and Figure 2.14 shows the amplitude spectrum after spiking deconvolution. Before, the amplitudes peak around 20 Hz but the spiking deconvolution increases the higher and lower frequencies to about the same power as the 20 Hz frequencies. A bandpass filter of $8-12-65-70$ Hz was applied directly after the deconvolution because frequencies much higher than that have a low signal to noise ratio.

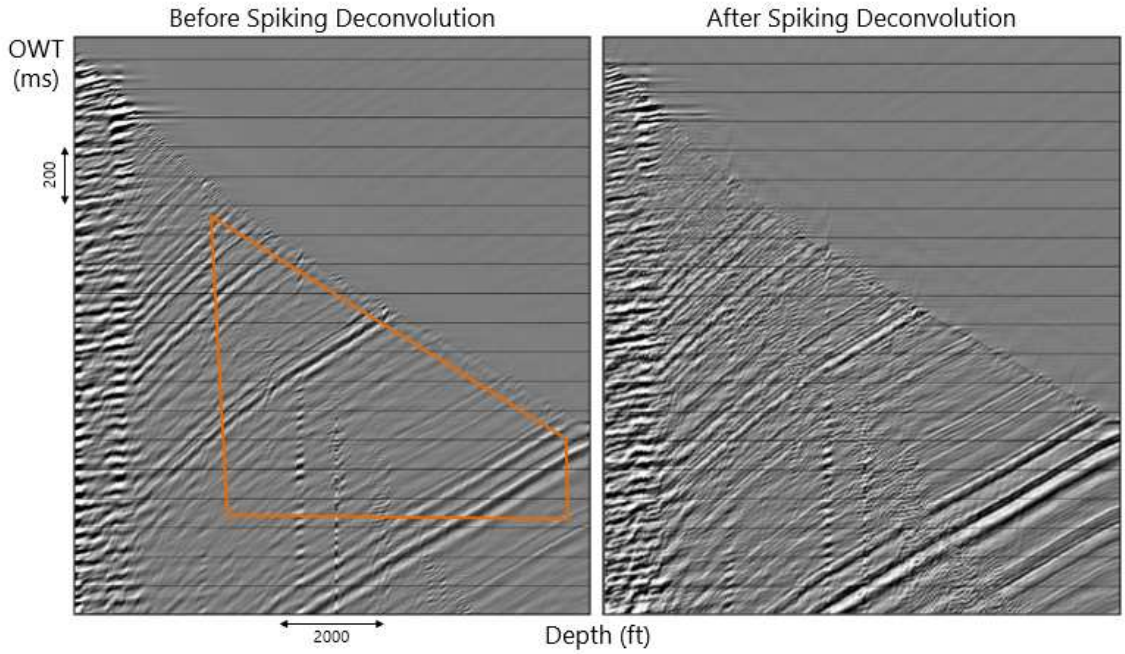

Figure 2.12 Zero-offset geophone VSP before and after spiking deconvolution

Looking at the frequency-depth plots in both Figure 2.13 and Figure 2.14, it is clear where those high frequencies are concentrated in the seismic. High frequencies attenuate faster than lower frequencies, so it is to be expected that the deeper section does not contain the same amount of high frequency energy. The deconvolution does a good job at increasing the high frequencies at depth.

2.1.5 Horizontal Receiver Components

The horizontal components (H1, H2) can have an arbitrary azimuthal orientation at each depth level. The goal of hodogram analysis is to maximize the P-wave first arrival energy on one of the horizontal components, radial (R), which consequently minimizes it on the transverse component (T).

Hodogram analysis starts by using a specified window around the first break (Figure 2.15 A&C) and cross plots the amplitudes of the horizontal components (Figure 2.15 B&D). There is generally a defining trend which indicates the angle of rotation which maximizes the energy to the R component.

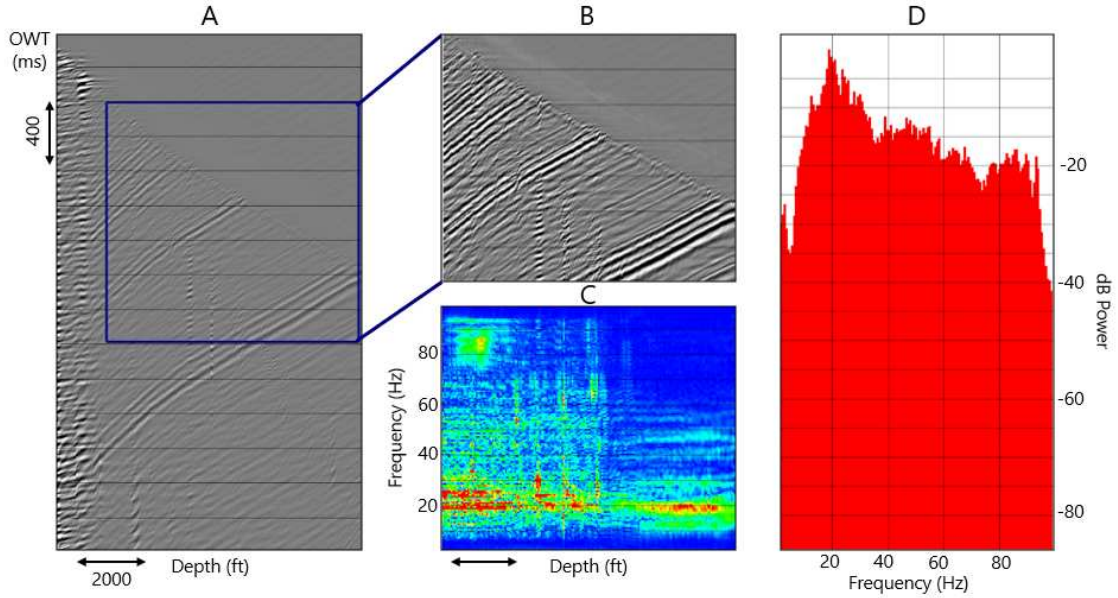

Figure 2.13 Amplitude analysis before spiking deconvolution. (A) Zero-offset VSP gather with window for amplitude analysis. (B) Zoomed in view of window shown in A. (C) Frequency-depth plot. (D) Amplitude spectrum

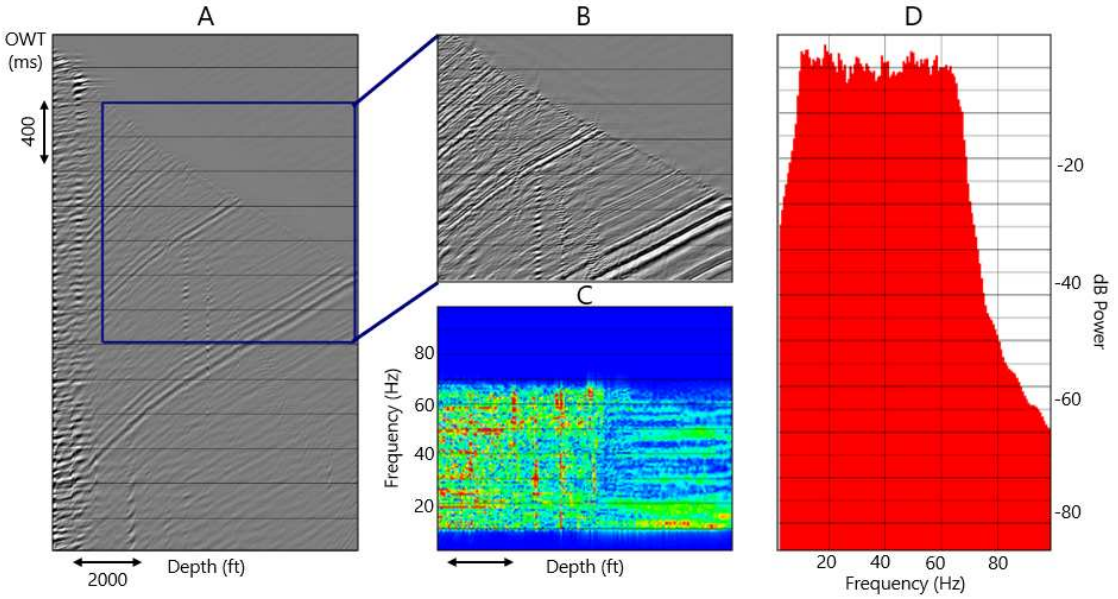

Figure 2.14 Amplitude analysis after spiking deconvolution(A) Zero-offset VSP gather with window for amplitude analysis. (B) Zoomed in view of window shown in A. (C) Frequency-depth plot. (D) Amplitude spectrum

The vertical source is used for this analysis and, generally, there is an offset vertical source in order to get a high angle of incident where there is a large horizontal component of the downgoing P-wave particle motion. As seen in Figure 2.15, there is very little p-wave energy recorded on the horizontal components. Sometimes there is sufficient energy to get a decisive determination (Figure 2.15 B) while other times it is not so decisive (Figure 2.15 C). The level of uncertainty increases as the receiver depth increases and the incidence angle decreases (Figure 2.16).

Results of the geophone rotation are seen in Figure 2.17. The p-wave direct arrival should be concentrated on the radial (R) component. These results could be improved with an offset vertical source. As seen in Figure 2.16, the angle of incidence is very small for the deeper sections of the well. This limits the amount of P-wave energy that the horizontal receivers register, which then limits the quality of the geophone orientations. The amplitudes on the H1 and H2 components are very weak which suggests that these estimated rotation values may not be reliable. With an offset vertical source, more P-wave energy would be recorded on the horizontal components, and the hodogram analysis more robust.

2.1.6 Alternate Geophone Rotation Method

In addition to hodogram analysis, a separate rotation code was tested on the zero-offset survey and used for the other geophone datasets. This code first generates a 2 by 2 covariance matrix using the H1 and H2 trace amplitudes. Then, it directly solves for the optimal horizontal rotation angle which maximizes the energy on the H1 component. This component, once rotated, becomes the radial component. The rotation angles are then exported as a separate file in case precise editing is required, and then re-imported and applied to each trace to complete the rotations. There were a few instances in both the zero-offset and walkaway surveys which required an edit to the rotation angles: one or two geophones which had reverse polarity after rotation.

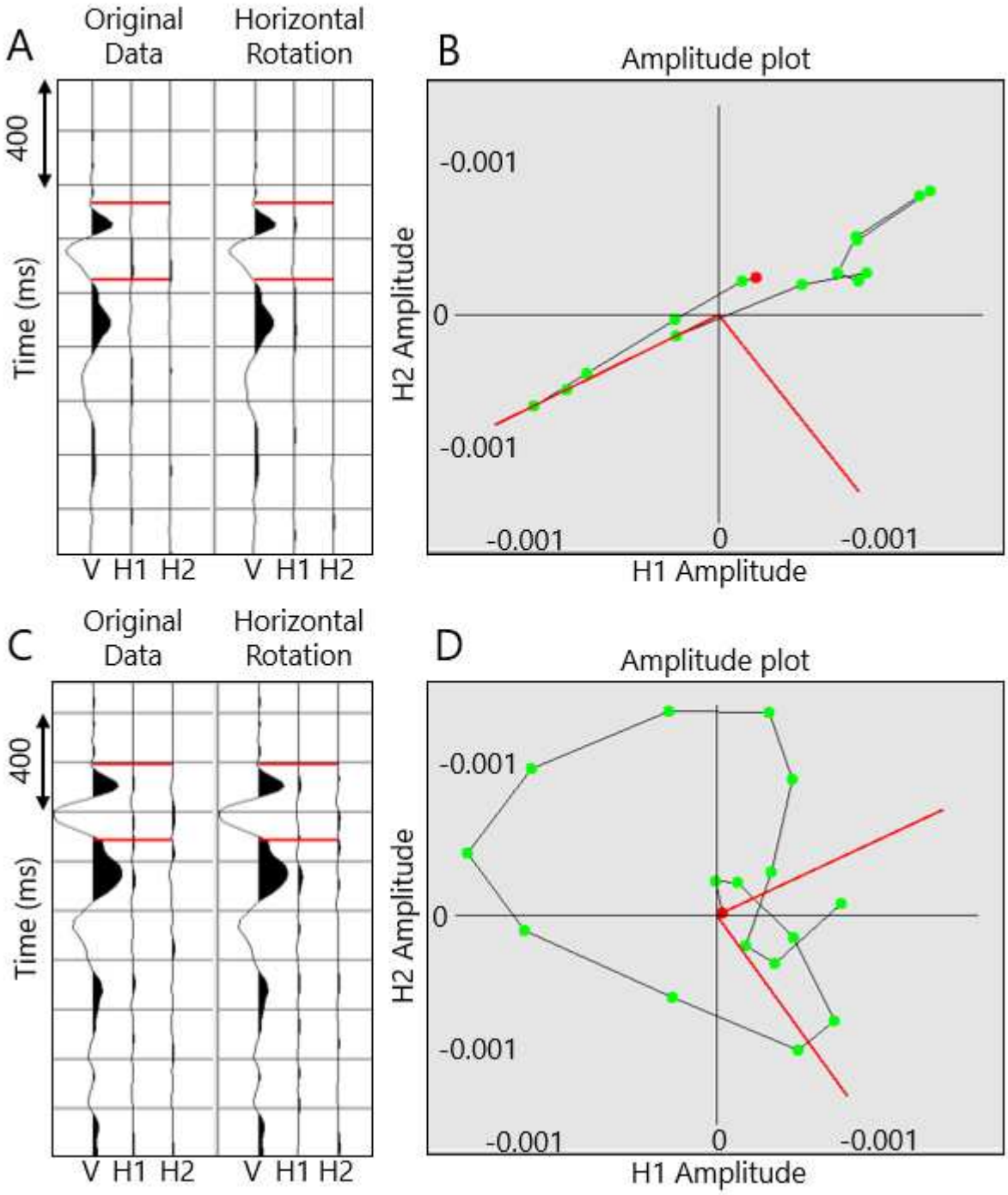

Figure 2.15 (A & C) Original traces (left) and rotated traces (right). Traces in A are from a shallower receiver than traces in C. The red lines indicated the time window used for the analysis. (B & D) Amplitudes of the original H1 and H2 traces plotted together. (Top row) example of geophone with decisive orientation, (Bottom row) example of geophone with indecisive orientation.

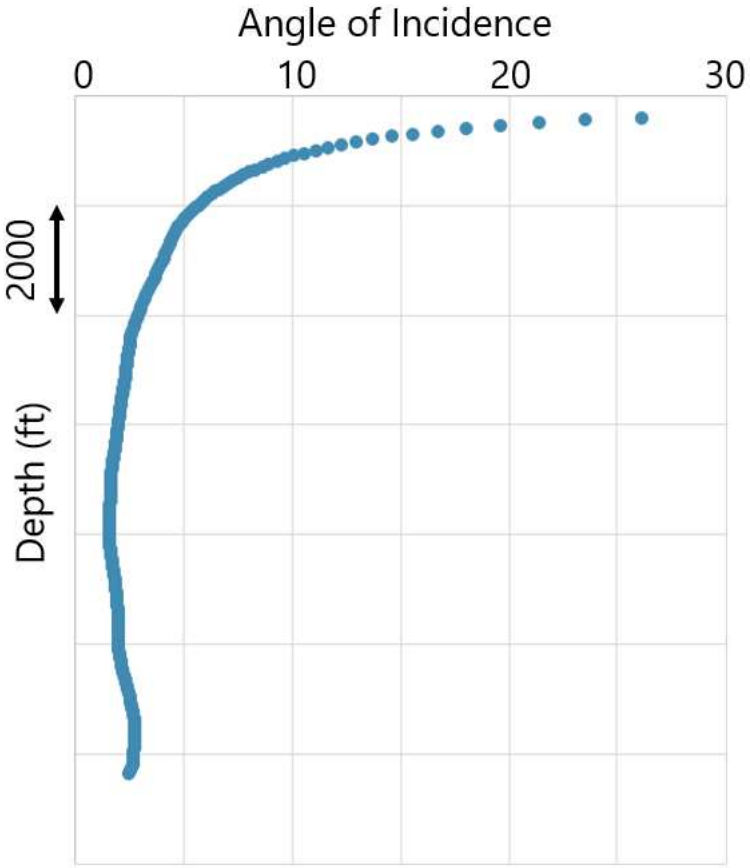

Figure 2.16 P-wave angle of incidence as a function of receiver depth.

2.1.7 Corridor Stack

Before the reflections can be stacked together to create the final corridor stack, the upgoing wavefields must be converted to two-way time by using the first-break pick times applied as static corrections. The times are added as a time-shift for each trace. The reflected waves are now flattened and the resulting gather is in two-way time (Figure 2.18).

Selective mutes are now applied to remove everything that is not directly surrounding the first-break (Figure 2.19). A top mute is used to remove all the noise before the direct arrival, such as the smearing caused by the F-K filter, and the bottom mute is used to remove the tube wave, if needed, and potential multiple reflections (multiples). Multiples are easily distinguished and removed in zero-offset VSP data. This is important to note when tying to

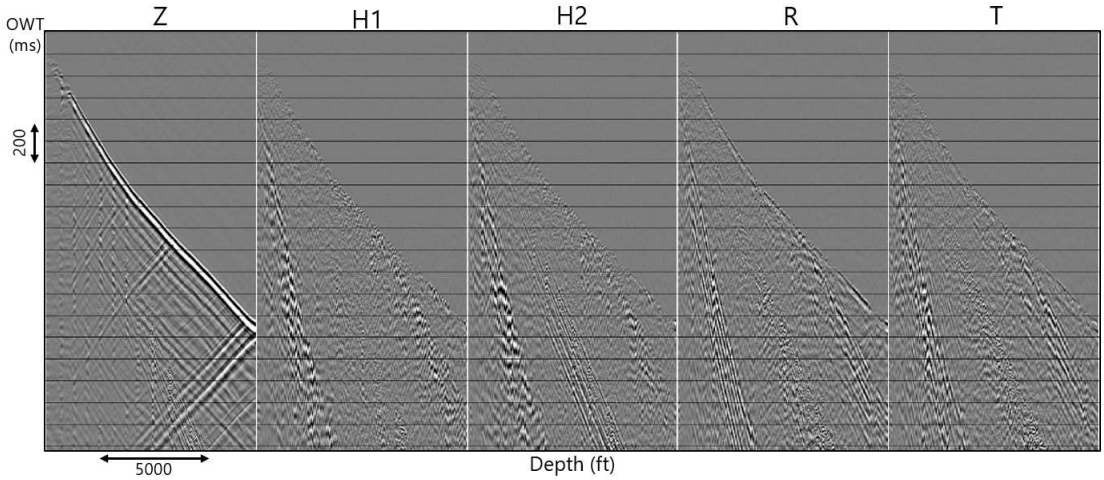

Figure 2.17 Results of geophone rotations. Z is the vertical component, no rotations necessary. H1 and H2 are the unrotated horizontal components. R is the radial horizontal component that is rotated to point towards the source. T is the transverse horizontal component rotated orthogonal to the source.

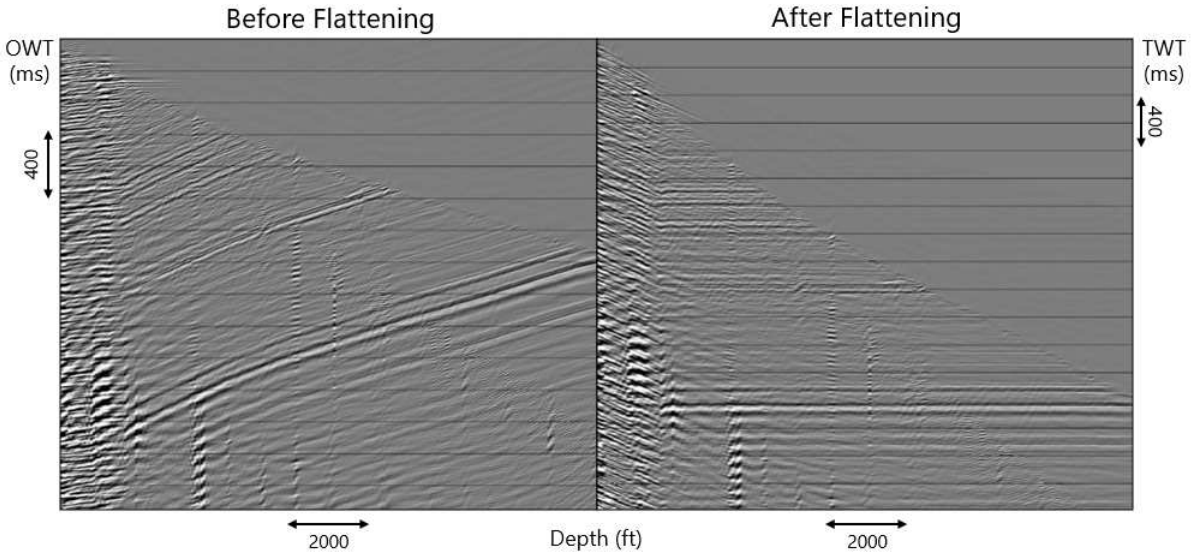

Figure 2.18 Before and after reflected waves are flattened.

the surface seismic, which may still have multiples that were not removed. The remaining data are stacked together to create a single trace (corridor stack) and replicated to help visualization.

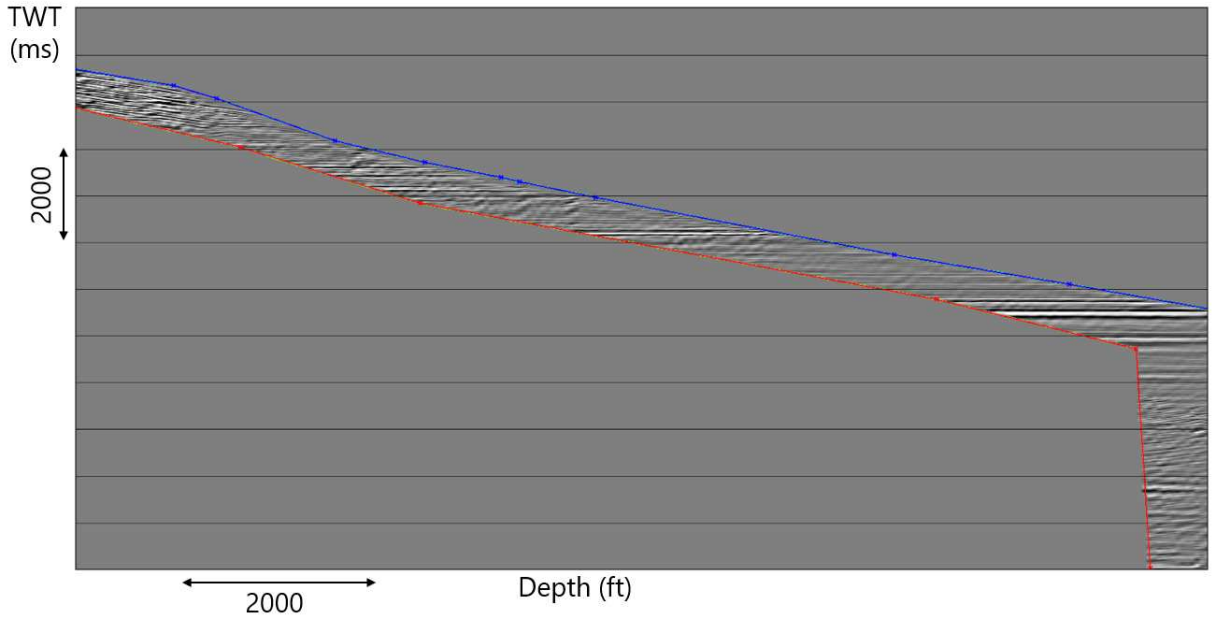

Figure 2.19 Flattened reflected energy with top (blue) and bottom (red) mutes applied.

The VSP traces can now be correlated to traces from the surface seismic data. This is an important step in validating both datasets. High amplitude reflections should be seen in both and should appear at the same times. The VSP naturally has a higher frequency content than the seismic, which can be seen in Figure 2.20, but for comparison purposes it has also been filtered to match the frequency spectrum of the seismic (Figure 2.21). The VSP, after a time-shift to account for the different datums (VSP referenced to Kelly Bushing = 485 m, surface seismic referenced to 500 m above mean sea level), ties to the surface seismic very well and the major horizons correlate across the datasets.

Now that the important horizons have been correlated across the VSP and seismic, the exact depths of the horizons are known and any depth converted seismic can be validated in this location.

2.1.8 Horizontal Components

Although the results of the geophone orientation is ambiguous given the absence of a far offset P-wave shot, there is one interesting feature that stands out. In Figure 2.22

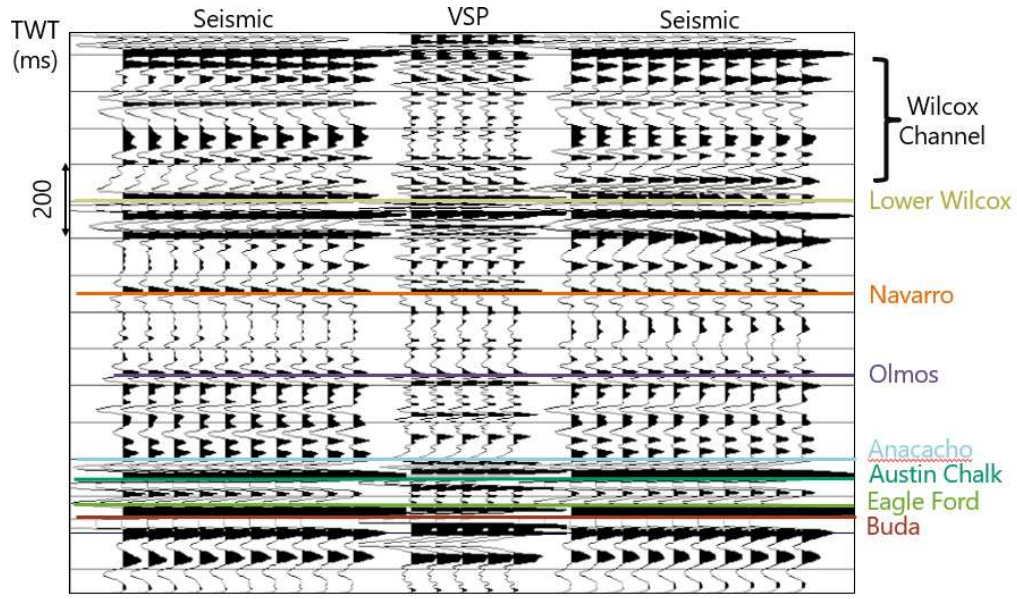

Figure 2.20 Results of the VSP corridor stack compared to a short cross section of seismic traces at Well B. Data are zero-phase so interfaces are located at zero crossings. Major reflections mapped in the 3D surface seismic are labeled and align with VSP reflections.

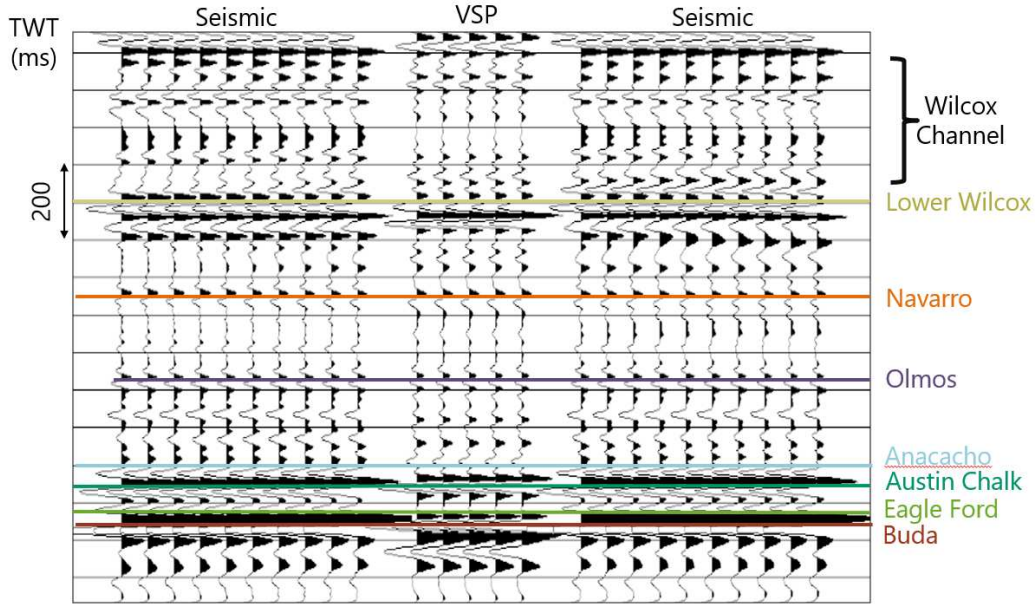

Figure 2.21 Results of the VSP corridor stack compared to a short cross section of seismic traces at well. The VSP has been bandpass filtered to match the frequency spectrum of the surface seismic. Data are in zero-phase so interfaces are located at zero crossings. Major reflections mapped in 3D surface seismic are labeled and align with VSP reflections.

highlighted in blue is a downgoing PS converted wave. This is a strong event that can be seen clearly on both horizontal components. Ideally, the energy would be concentrated on the radial component and any shear wave splitting energy would be recorded on the transverse component. A steeply dipping event is needed to generate a PS converted wave for a zero-offset survey, since downgoing PS converted waves should not be generated from a vertical force source on a zero-offset VSP. If this were a simple downgoing PS converted wave in a simple flat-layered earth, the event would appear on the Z and R components. The event highlighted in blue of Figure 2.22, is not observed on the vertical receiver.

To verify this observation, two surface seismic cross sections centered on the well are analyzed (Figure 2.23). Outlined in the red box is the approximate depth at which this PS conversion occurs. As expected, there is a dipping reflector, seen clearly in the left panel. The reflector is most likely the base of the Wilcox Channel which cuts across the study area.

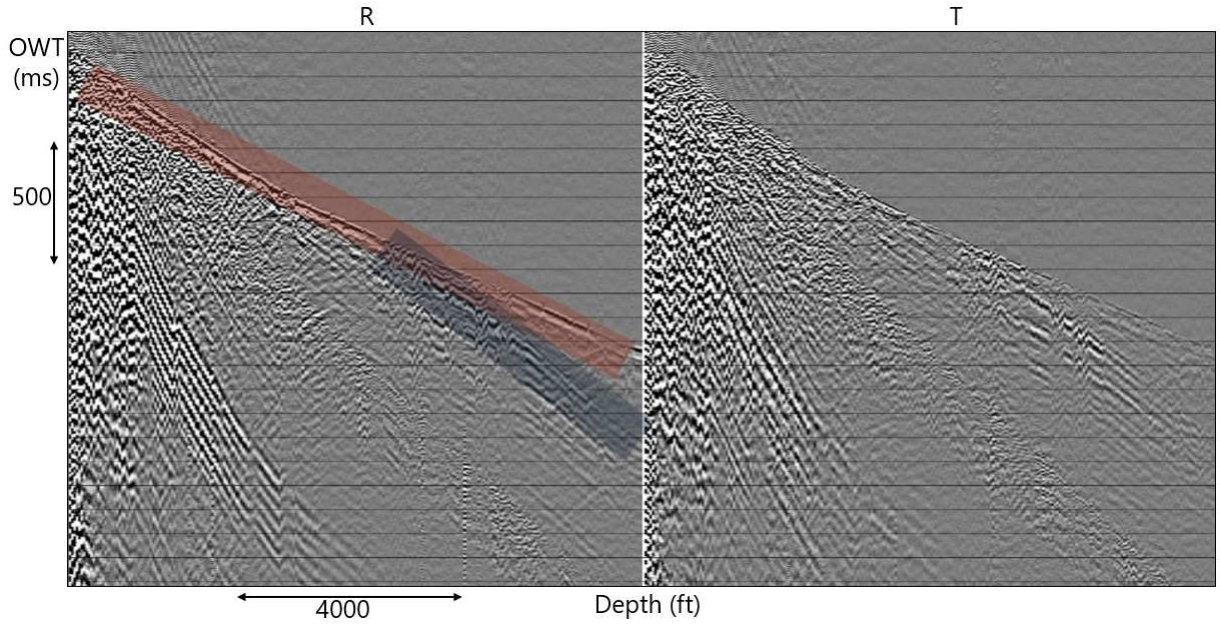

Figure 2.22 Vertical source zero-offset VSP horizontal components with best attempt at rotations. (Red) downgoing P-wave, (Blue) downgoing PS converted wave.

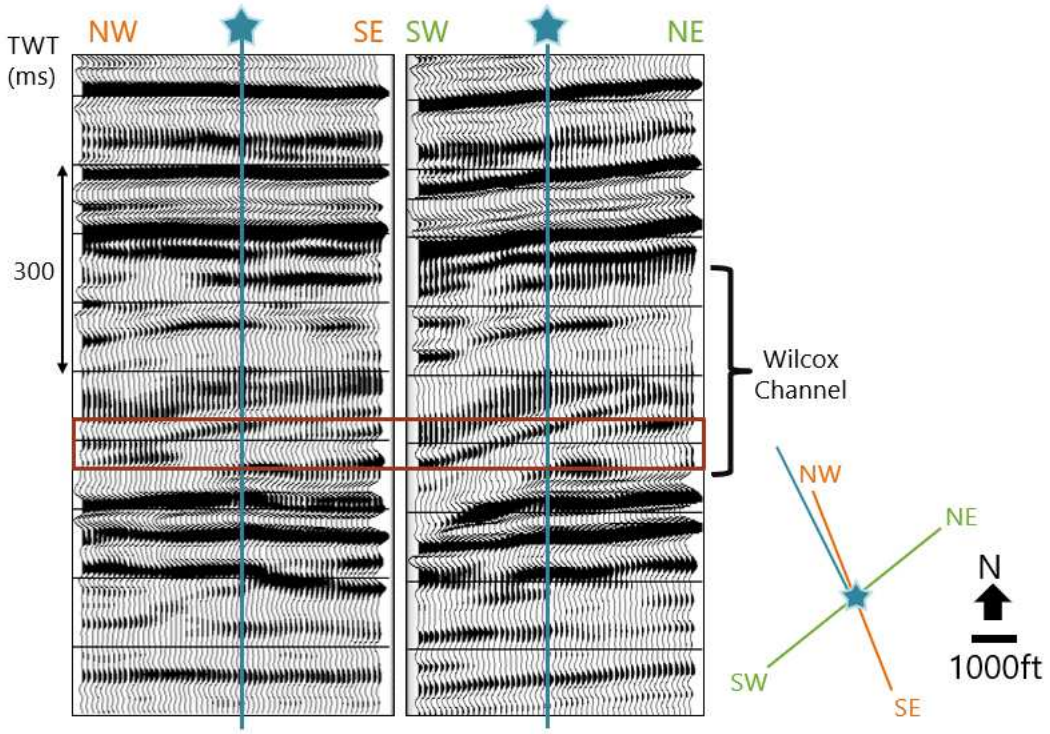

Figure 2.23 Cross sections from the surface seismic going through the well. The approximate location of the PS conversion is outlined in red.

2.2 Shear-source Zero-offset VSP

Shear source zero-offset VSP surveys are useful in determining the vertical shear-wave velocity, with exact time-depth relations, and fast and slow shear-wave directions. These data can then be used to tie to the surface seismic and assist with P-S and S-S seismic processing and interpretation. Like the P-source VSP, the shear-source VSP also contains higher frequencies than does the surface seismic. The vertical vibroseis source is generally thought of as a P-source, but it also generates Sv waves. Shear-wave data are also used for shear-wave splitting analysis which can indicate the presence of anisotropy.

2.2.1 Rotating Geophones

In order to apply shear wave splitting analysis on these data the radial-transverse co-ordinate system must used. Conventionally, orthogonal shear-source zero-offset VSPs are

acquired as follows: (1) both shear sources are located at the same vibe pad location; (2) the radial source shakes toward the receiver well (radial direction); (3) the transverse source shakes perpendicular to this azimuth (transverse direction); (4) H1 and H2 receivers have been rotated to (R,T) using the P-wave first-arrival from a far-offset P-wave source.

This coordinate system maximizes the SV-wave energy on the radial component ($S_R R_R$ or RR) and the SH wave on the transverse component ($S_T R_T$ or TT), while other coordinate systems cannot separate out these wave fields (Simmons & Backus, 2001). In flat, isotropic media the reflection energy should be maximized on the RR and TT and minimized on the crossterm components, RT and TR. If there is a large difference in the shear-wave first-arrival times between the SV and SH there could be media with strong transverse anisotropy with a vertical axis of symmetry (VTI) and coherent energy on the crossterm components suggests the presence of azimuthal anisotropy in the form of shear-wave splitting (Simmons & Backus, 2001).

There are two aspects to this survey that makes rotating the geophones very difficult.

(1) The shear sources are not located along the same azimuth. Since the P-source is used to orient the geophones, they are oriented along that azimuth and an extra step is needed to then rotate them to both shear source azimuths. This raises another question as well: will it be possible to directly relate the data from each shear source?

(2) The shaking directions for the shear sources are not radial and transverse to the well. Instead, they are oriented with the interpreted fast and slow velocity azimuths relating to the presumed maximum and minimum stress directions. This also happens to be the dip direction of the underlying formations and the inline/crossline directions of the surface seismic survey. The inline source shakes parallel to the fast azimuth but roughly transverse to the well. While the crossline source shakes parallel to the slow velocity direction and roughly radial to the well. The azimuth of the P-source to the well aligns with the slow velocity direction, so if the shear sources were along the same azimuth they would be oriented radially and transversely to the well and would be easy to orient.

The combination of the varying source azimuths and shaking directions adds immense difficulty to correctly orient the geophones to a radial-transverse coordinate system. Even if rotating the geophones properly is possible, the fact that the shaking directions of the shear sources are not properly oriented to radial and transverse with respect to the well, raises the question: is it even possible to isolate the SV and SH-waves using the radial and transverse coordinate system?

Below, Figure 2.24 and Figure 2.25 show the unrotated and rotated shear source zero-offset gathers, respectively. The incoherence and similar energy levels seen in the unrotated gathers is to be expected. The horizontal geophones were rotated using the same angles which were used to rotate the P-source zero-offset survey. The P-source orientations are imperfect, but acceptable. In a typical zero-offset survey design, these angles could be applied to the shear sources and achieve an acceptable result. However, Figure 2.25 clearly demonstrates that this is not the case for this survey design. The shear-wave first-breaks are incoherent and the energy levels are consistent across the board. In this coordinate system, the energy should be focused on the RR and TT components. This clearly indicates that the geophones are not properly oriented and more work must be done in order to do so. The different azimuths of the shear-sources along with the shaking directions not pointing radially and transversely relative to the well are the source of these errors. Unfortunately, within the scope of this project the horizontal receivers could not be properly oriented.

2.2.2 Previous Rotations by Production Processing

Turning to the previously processed data and the processing report compiled by Baker Hughes could potentially shed some light on this issue. Figure 2.26 shows the rotated data in the R-T coordinate system. The reflections are more coherent, but the energy levels are consistent on every component. If properly rotated, the energy would only be on RR and TT. Clearly there were the same issues rotating these data. A close-up image of the rotated traces at a shallow, middle, and deep receivers is seen in Figure 2.27. This figure further illustrates that each component has the same amplitudes on the first breaks, outlined in the

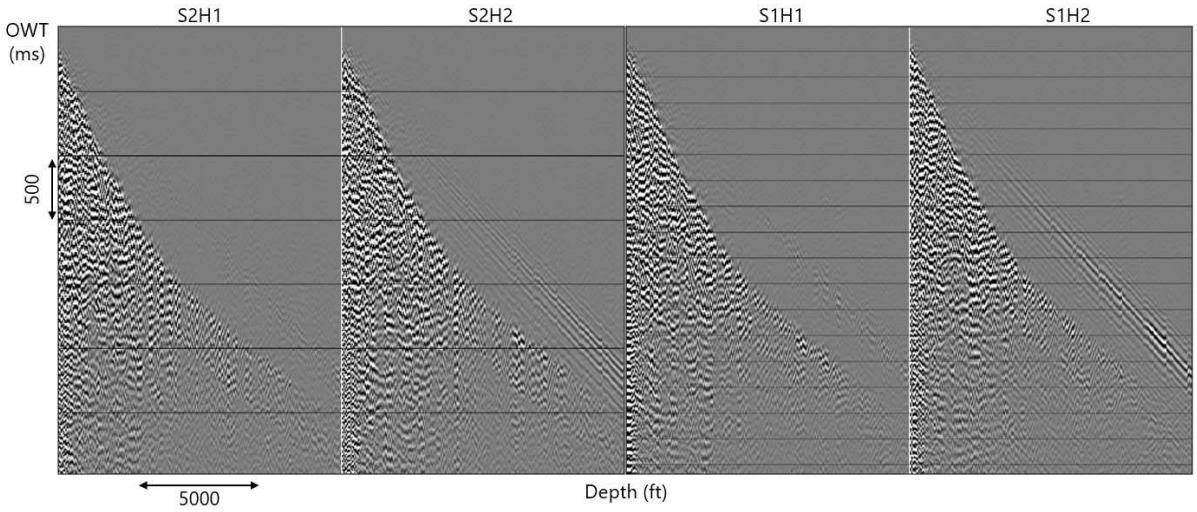

Figure 2.24 Unrotated horizontal components (H1 and H2) from both shear sources (S1 and S2).

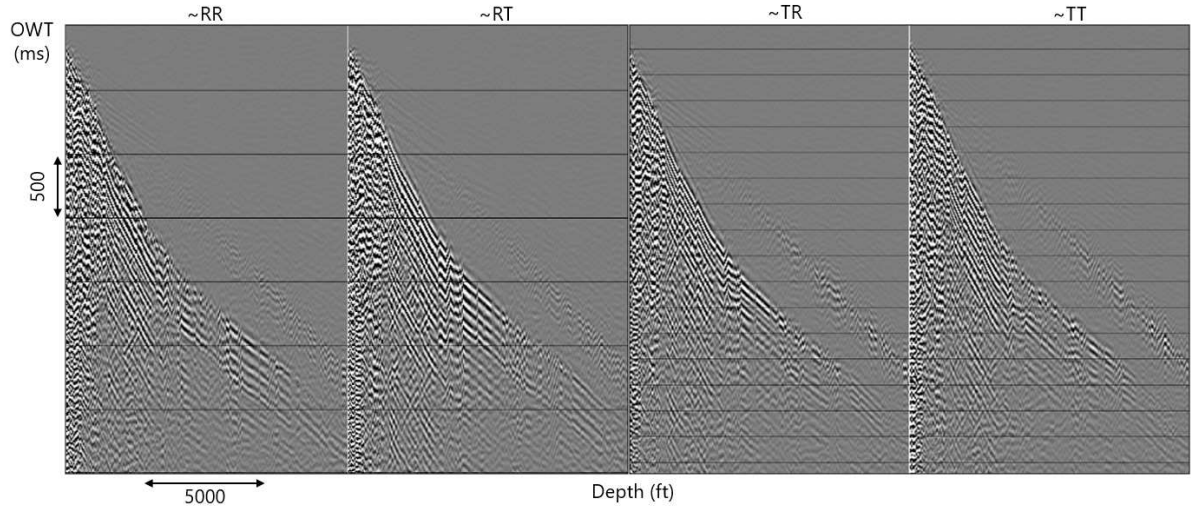

Figure 2.25 Results from geophone rotation using same angles calculated to rotate the P-source zero-offset VSP seen previously.

red box.

During production processing shear-wave splitting analysis was not performed on this dataset, but the shear-wave first breaks were picked and a velocity model derived from these picks. Shear-wave first breaks were not picked on the data processed in this study due to the incoherence of the first breaks. The shear-wave velocities were, instead, derived from the

Vp/Vs ratio from the well logs. The P-wave velocity was derived from the vertical source zero-offset VSP first break picks. The comparison between the two shear-wave velocities is shown in Figure 2.28. The previous velocity model has not been smoothed at all but the two velocities follow the same trends. The previous model has a limited vertical extent due to poor quality first break picks at the top and bottom of the well.

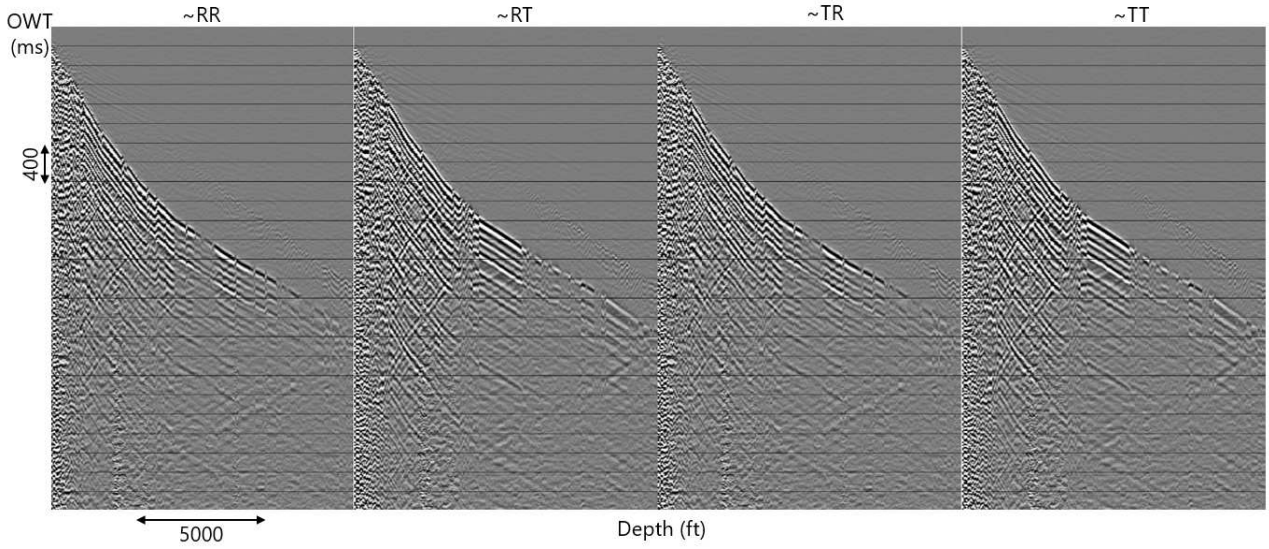

Figure 2.26 Baseline zero-offset VSP shear source rotations done by Baker Hughes

The monitor shear zero-offset survey was not rotated in this study due to similar survey geometry complications. Even though, the shear sources are located at the same position in the monitor survey, the different azimuth from the P-source and the shaking directions complicate the rotation process.

Baker Hughes, however, were able to overcome the geometry challenges for this survey. Figure 2.29 shows the data rotated into the R-T coordinate system. Most of the energy is now focused on the RR and TT components with much smaller amplitudes on the RT and TR components. Looking more closely at the trace-by-trace comparison in Figure 2.30, these rotations are clearly improved from the baseline data. However, the RT and TR components are still not correct. These components should be identical in order to reliably perform the Alford rotations used to calculate shear-wave splitting (Alford, 1986). Energy from the RT

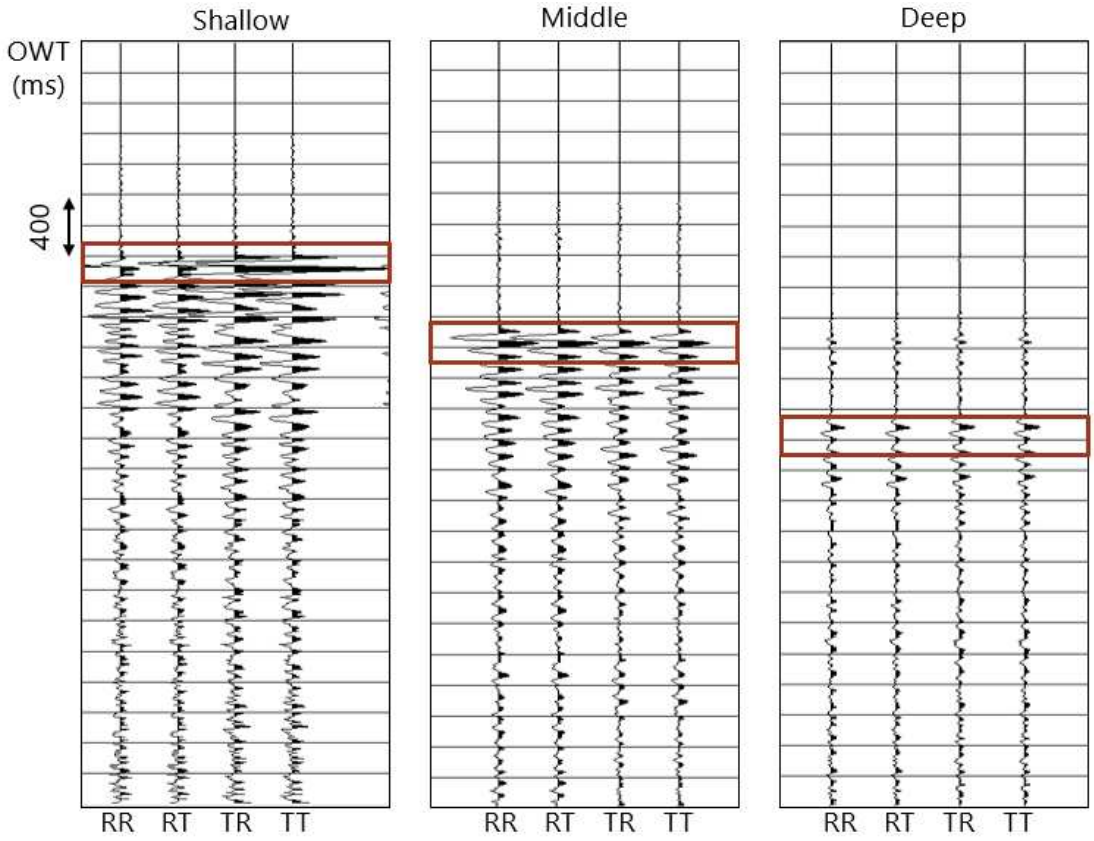

Figure 2.27 Trace by trace view of RR, RT, TR, and TT components for each receiver level.

and TR components are rotated onto the RR and TT components, respectively, during the Alford rotation process. The angle which minimizes the energy on the crossterms indicates the azimuth of the isotropy plane. The RR and TT components will now be separated into fast and slow shear-waves. Cross-correlation of the two estimates the time delay related to shear-wave splitting. The fact that the crossterms are not equal will have an impact on these results.

2.3 Walkaway

The walkaway line starts near the well head and extends over the horizontal section of the well and continues for several thousand feet (Figure 2.31). Sources are the vertical vibrator only and the receiver depths are greatly limited compared to the zero-offset (Figure 2.32). The receivers are located near the heel of the well and the distribution differs between the

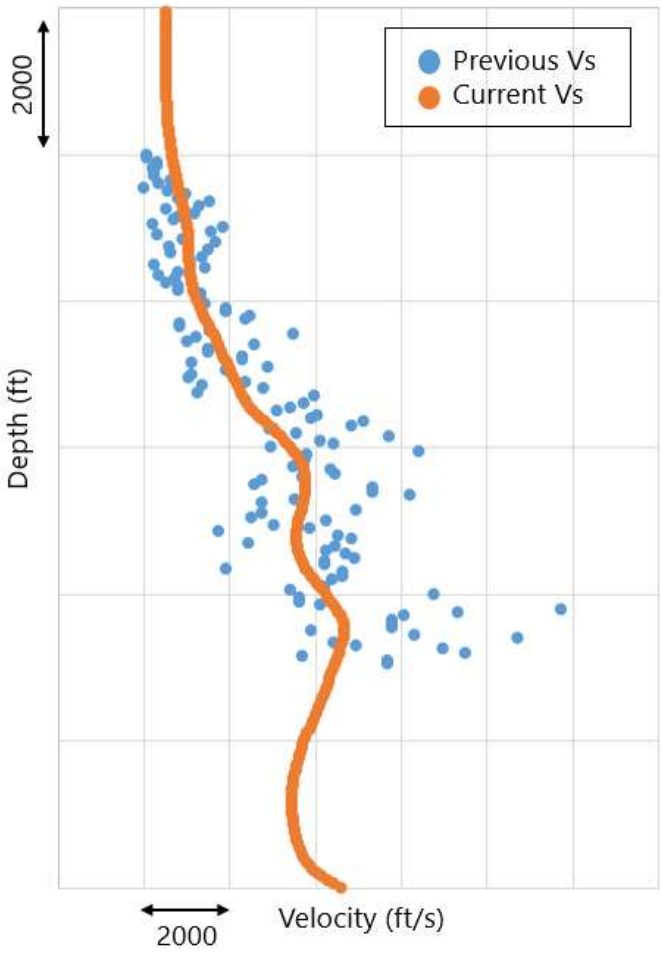

Figure 2.28 Shear wave velocities calculated by Baker Hughes using shear wave first break picks (blue) and shear wave velocities calculated from Vp/Vs ratio from well logs and P-wave first break picks (orange).

monitor and the baseline surveys. There are 38 receiver levels in the baseline survey and 68 in the monitor, both with 50 ft spacing. The narrow receiver depth aperture limits what can be imaged in this survey. Only reflections that occur deeper than the receivers can be imaged. The spatial extent of the image is also limited because of the receiver placement. Reflection points close to the heel of the well will be imaged. Additionally, the differences in the receiver placement will limit the scope of the time-lapse monitoring that is possible. The images in this section will be taken from the baseline survey.

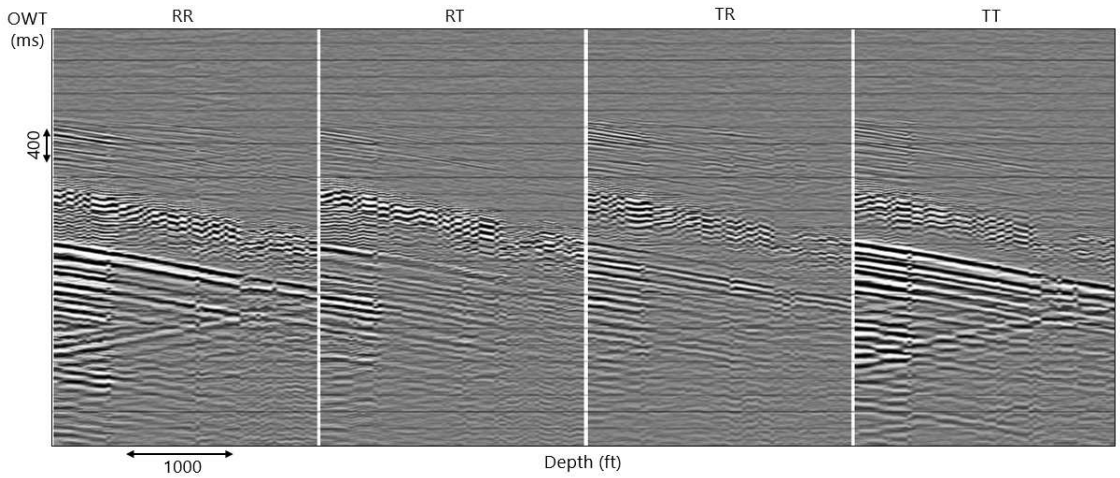

Figure 2.29 Monitor zero-offset VSP geophone rotations cone by Baker Hughes

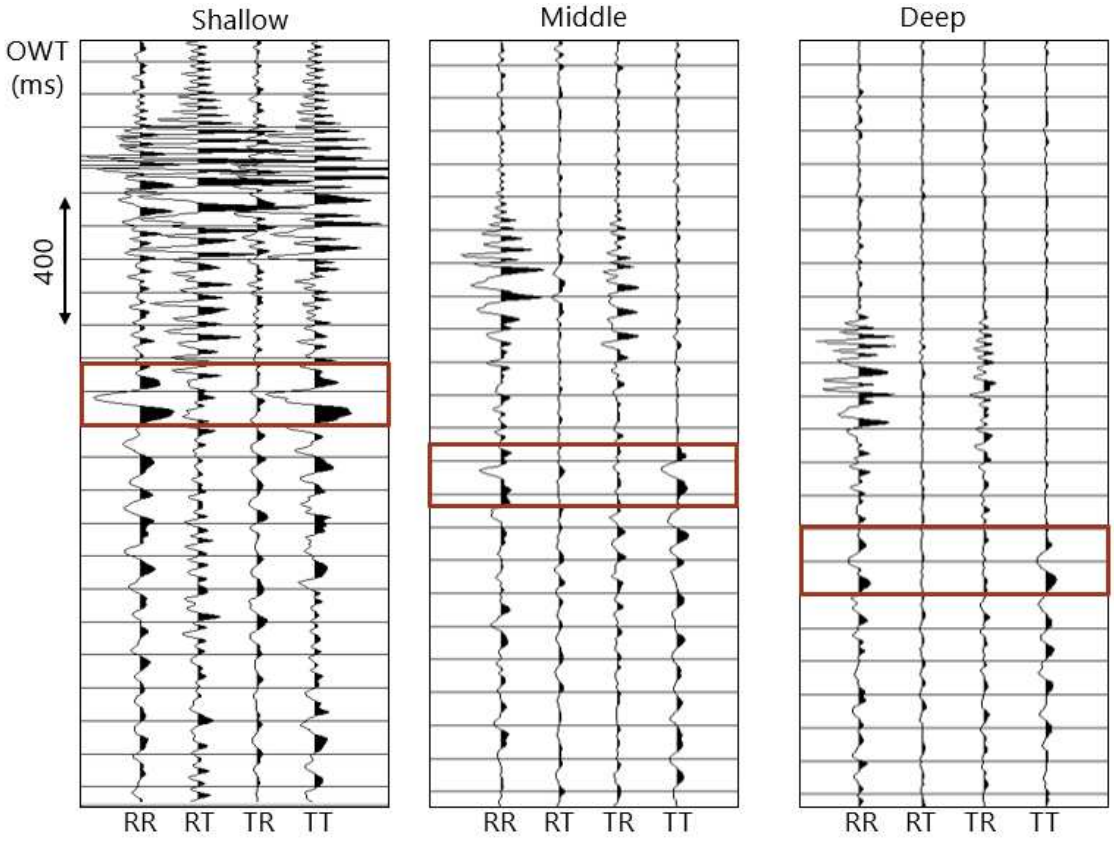

Figure 2.30 Trace by trace view of RR, RT, TR, and TT components for each receiver level.

The initial processing of these data follows that of the zero-offset VSP. Filtering includes a TFD median filter, and an amplitude recovery using a time-power of 2, the same as the

zero-offset. The wavefields are again separated using an FK filter and spiking deconvolution is performed. For the horizontal components, the spiking deconvolution filter is designed on the R-component and applied to both R and T components. After deconvolution, a bandpass filter is applied. Careful steps were taken to ensure that the baseline and monitor surveys were processed the same with no time-varying processes.

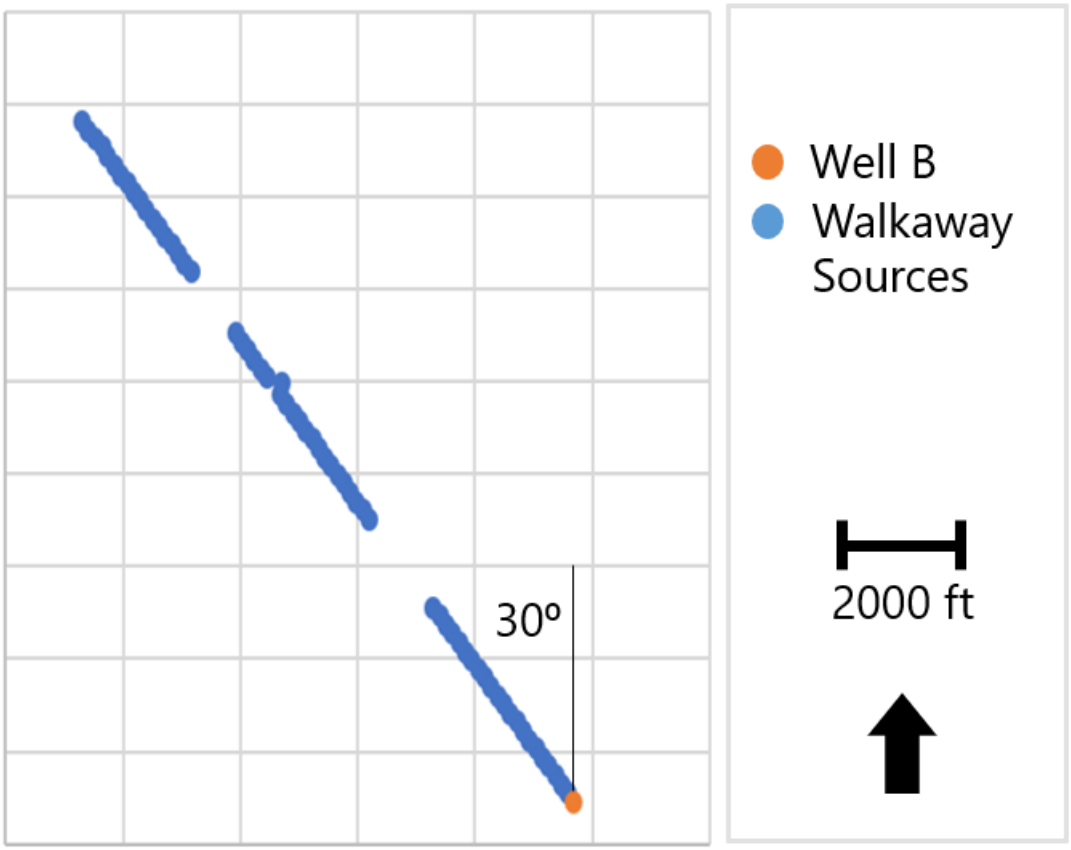

Figure 2.31 Map view of the Walk-away survey

Orientation of the horizontal geophones is now much more straight forward since there are P-sources at larger offsets along the same azimuth. Only one source is needed to rotate the geophones and, unlike the zero-offset survey, there are plenty of offset sources to choose from. This makes the rotation more robust because the direct downgoing P-wave has substantial horizontal particle motion. Figure 2.33 shows the three components before rotation (V, H1, H2) and the rotated components (R and T). The horizontal components begin with

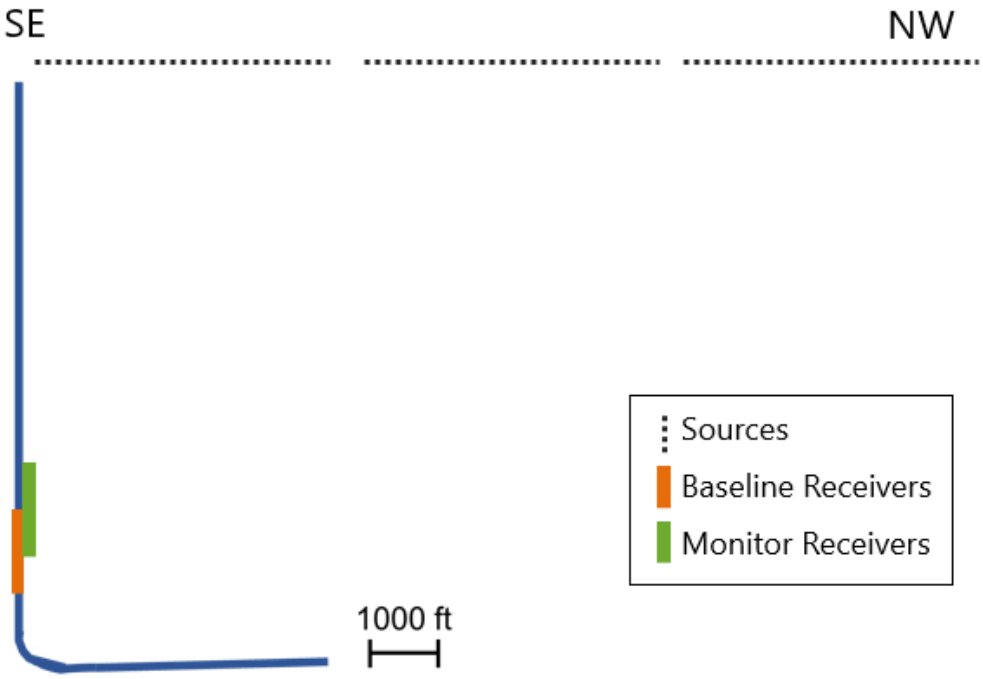

Figure 2.32 Cross section view of the Walk-away survey

incoherent energy that cannot be interpreted, and after rotation, the reflections are coherent. As expected, the radial component contains most of the energy while much less energy is seen on the transverse component.

The event highlighted in blue on the radial and transverse components in Figure 2.33 is potentially a downgoing Sh wave. If this is true, it could be indicative of overburden shear-wave splitting. Any Sh wave, upgoing or downgoing, will polarize energy onto T if that S-wave propagates through the media with horizontal transverse isotropy (HTI). If this is in the overburden (shallower than the shallowest receiver), this effect will not be observable on reflections.

2.3.1 Ray Tracing

Figure 2.35 illustrates how the downgoing waves propagate through the subsurface. The first figure shows only the direct downgoing P and PS-waves. The P-waves, highlighted in red, travel directly from the source and are recorded on both the Z and the R-components.

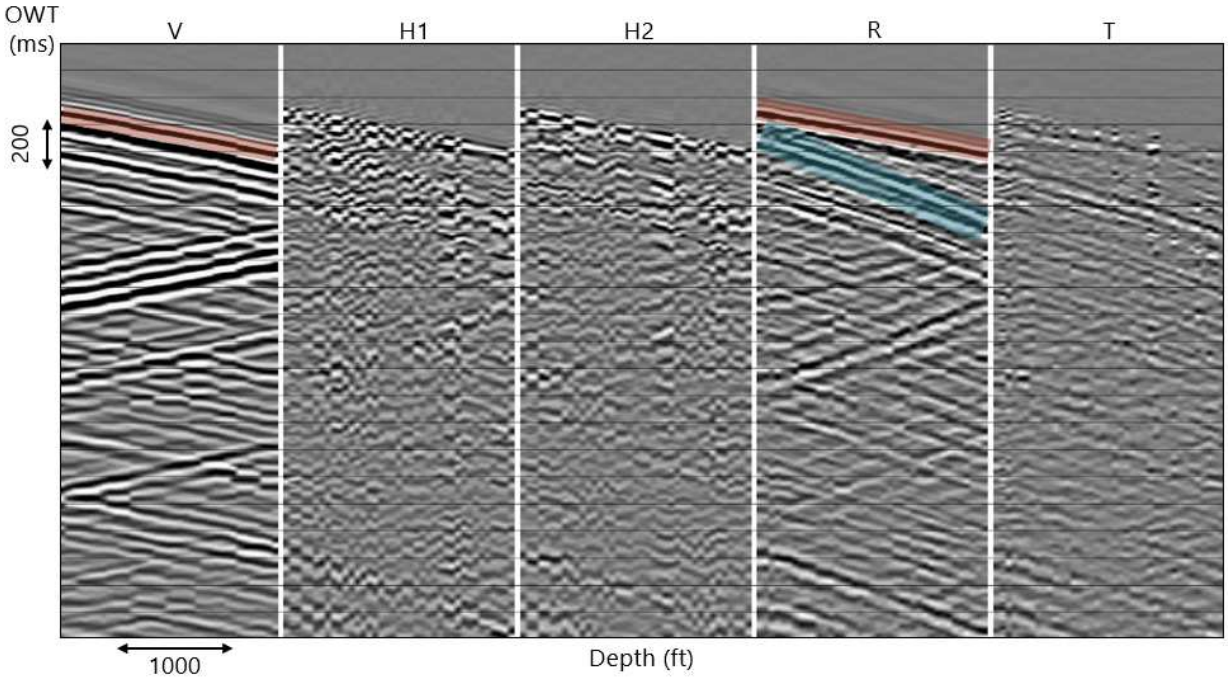

Figure 2.33 A shot gather from the walk-away survey. (v) vertical receiver, (H1 & H2) unrotated horizontal components, (R) radially oriented component, (T) transversely oriented component. The red box highlights the downgoing P-wave and the blue box highlights downgoing the PS-converted wave.

The P-waves get stronger on R at further offsets because the particle motion has a larger horizontal component at these offsets than at the near offsets, where there is mostly vertical particle motion. For the PS-wave to exist, it must convert from a P-wave to an Sv-wave at some horizon. The PS-wave energy is polarized in the radial direction so most of the particle motion will be detected by the R-component, but in general, will appear on both Z and R components. At further offsets, there is more vertical particle motion that is detected by the Z-component. There is a small amount of PS energy detected by the T-component suggesting some level of shear-wave splitting in the overburden.

Figure 2.36 shows a diagram illustrating the concept of ray tracing to map reflection points. The upgoing P-waves are highlighted in red and the upgoing PS-waves are highlighted in blue. The reflections, which are seen at the deeper receiver levels, occur very close to the well, while the shallower receivers see reflections which occur further away from the well.

The offset of the source also changes where these reflection points are located. As the source offset increases, the reflection points for a given reflector depth recorded at a particular receiver moves further away from the well. Additionally, for any given receiver and a set offset, as the reflector depth increases, the reflection points move further away from the well.

The last major processing steps for the walk-away survey are traveltime (moveout) correction and common reflection point (CRP) mapping. This step uses ray tracing code previously mentioned in the introduction. The two step process begins with one-dimensional ray tracing using isotropic velocity models (Vp and Vs) (Figure 2.34). The Vp velocity model was calculated from the P-wave first arrival in the zero-offset VSP. The raw velocity calculations are in light blue and the smoothed version used for ray tracing is in dark blue. The Vs velocity model was calculated from the smoothed Vp velocity using the Vp/Vs ratio determined by the sonic logs. Ray tracing computes the travel time corrections and the reflection-point locations needed for the CRP mapping.

The initial results of P-wave ray tracing can be viewed as source gathers in Figure 2.37. This figure shows near ($\sim$ 700 ft), middle ($\sim$ 9,000 ft), and far offset ($\sim$ 13,700 ft) shot gathers to demonstrate the effectiveness of the ray tracing at various offsets. The three components are also shown to better understand the energy distribution of the wavefields on each receiver components. The P-wave has been flattened and is highlighted in red. The PS converted wave, seen mainly on the R-component, is highlighted in blue.

Looking first at the Z-component, the near offset P-wave reflections are flattened well. This indicates that the velocity model derived from the zero-offset survey is correct. The middle offset reflections are also flattened well and hints of the SV reflections dipping from right to left can also be seen. At the far offsets, however, the ray tracing algorithm starts to break down. The P-wave reflection seems to "split", with one part dipping up, and the other part dipping down. At these far offsets, there are most likely lateral velocity variations or moveout stretch created by ray tracing and the low velocity zones A, B, and C in Figure 2.34, for which, the 1D velocity model cannot account. This effect can be seen on all the far offset

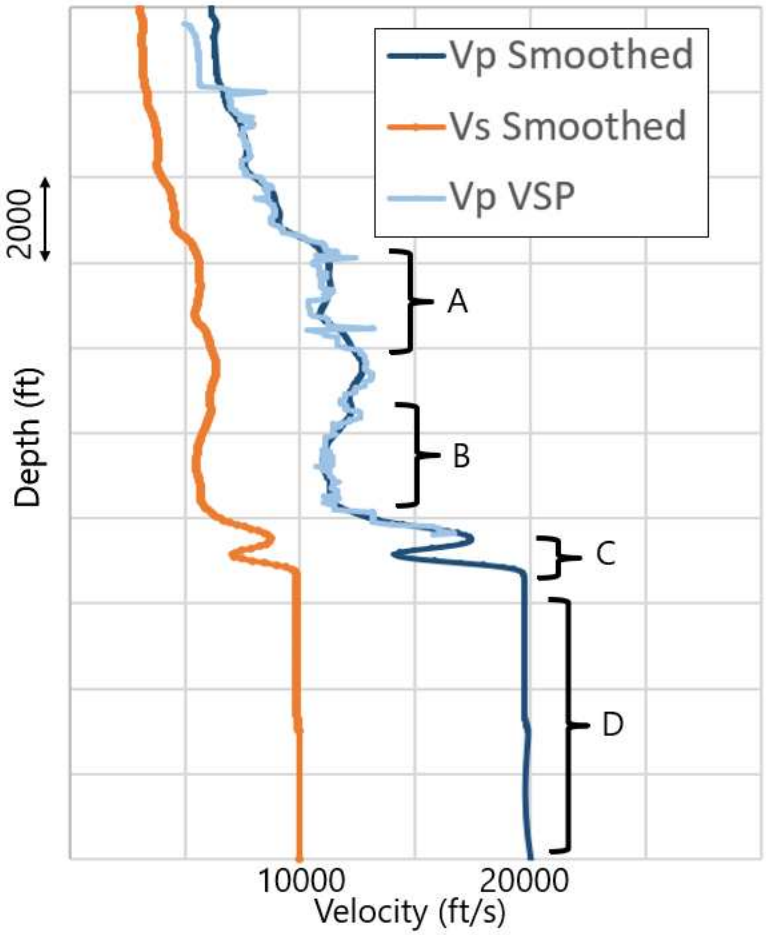

Figure 2.34 Comparison between the P-wave and S-wave velocity models used for traveltime corrections. A, B, and C indicate slower velocity zones which could impact the ray tracing results. C also indicates a part of the velocity model which was filled in using the sonic logs. D indicates the portion of the model which was extrapolated in order to image reflections below the well.

source gathers in both the geophone and DAS recordings.

Next, looking at the radial component (R) from the same figure, Figure 2.42, the P-wave, seen in red, is again flattened. This component records much more SV-wave energy, in blue. The near and middle offsets show flattened P-wave energy, but again in the far offset, the P-wave is 'splitting" which is not a geologic phenomena, but a limitation in the ray tracing.

The last row of the image is the transverse component (T). This component should not have any P-wave energy and should only have shear-wave reflected energy if the wave has

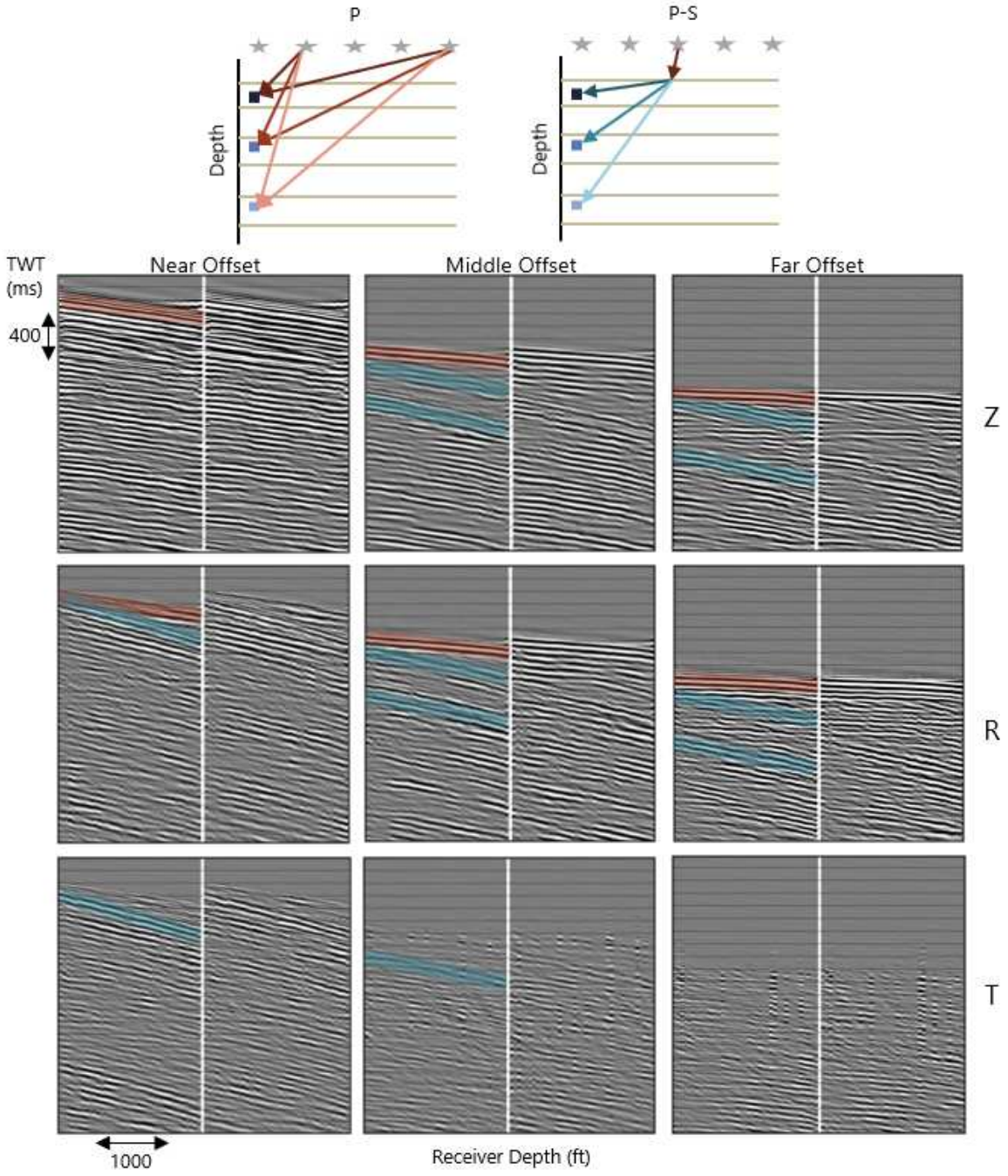

Figure 2.35 Downgoing wavefields, vertical (Z) and radial (R) components. Downgoing P-waves are in red. Downgoing SV-waves generated from a downgoing P-wave to a downgoing SV-wave are in blue.

been polarized by shear wave splitting. Most of the signal seen on this component is noise, but there is a small amount of dipping SV-wave energy seen in the near offsets.

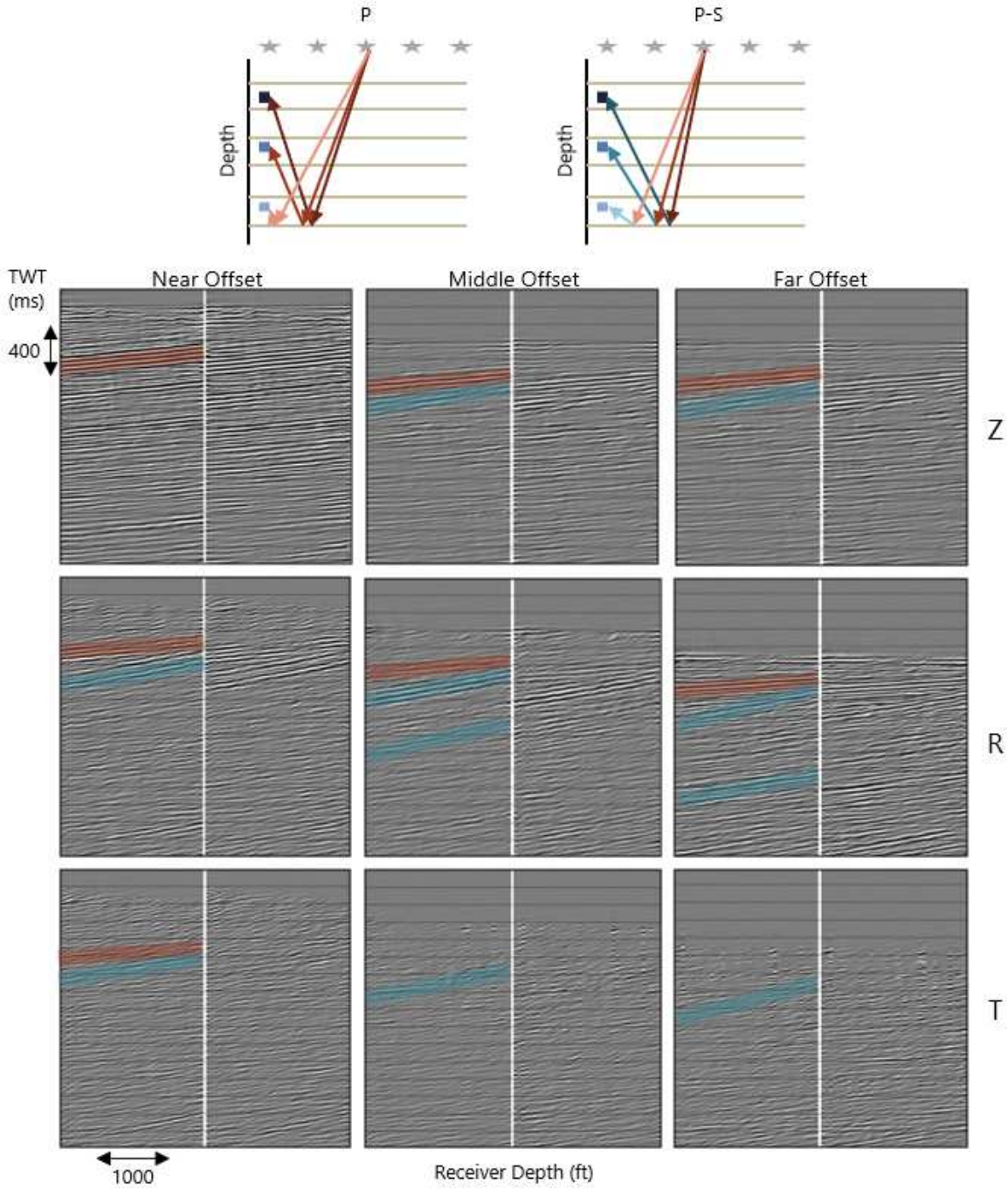

Figure 2.36 Upgoing (reflected) wavefields, vertical (Z) and radial (R) components. Upgoing P-waves are in red. Upgoing SV-waves generated from a downgoing P-wave to a downgoing SV-wave are in blue

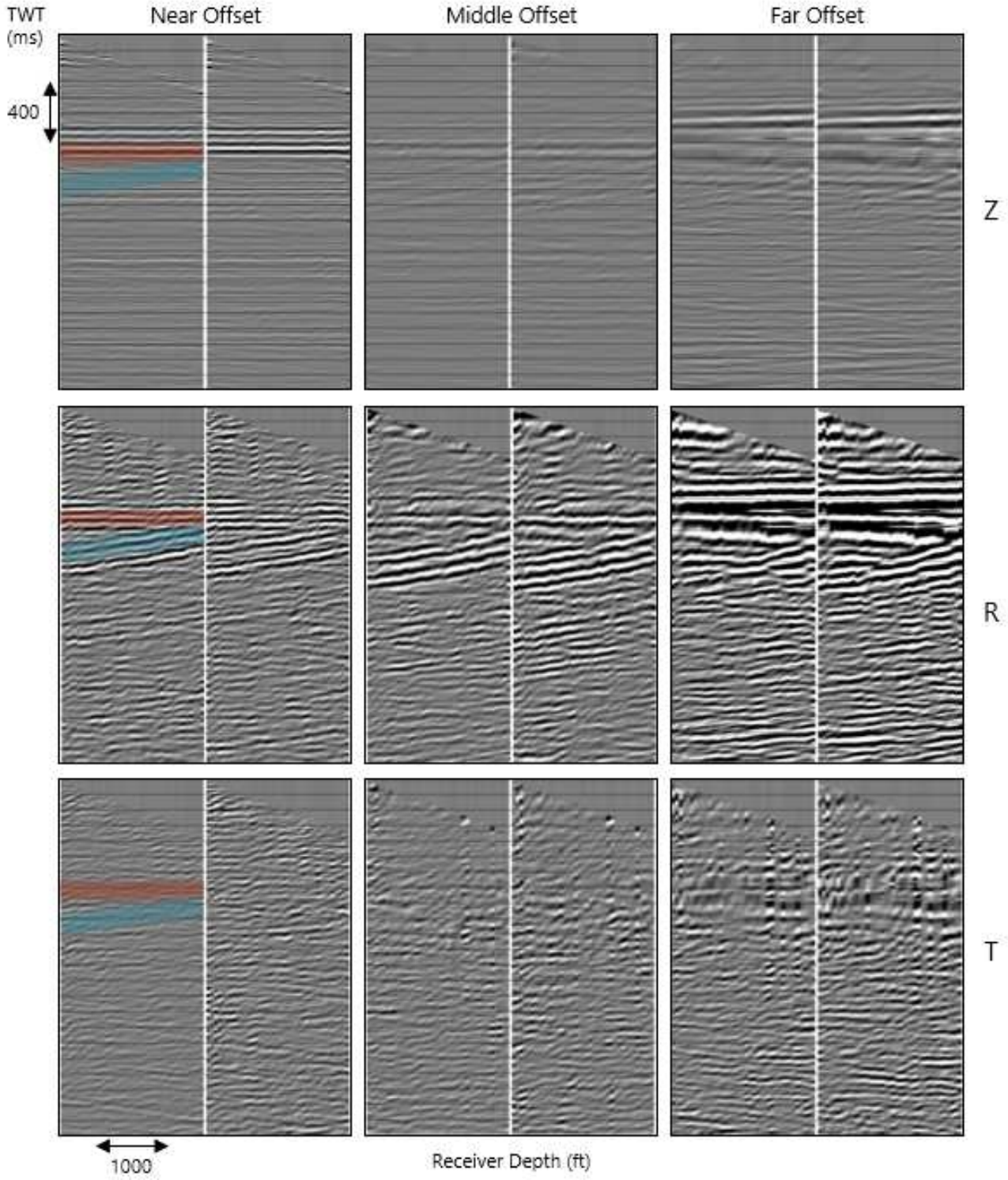

Figure 2.37 Shot gathers at near, middle, and far offsets after moveout correction for P-wave velocity. Flattened P-wave highlighted in red, converted wave highlighted in blue.

2.3.2 Post Traveltime Correction Filtering

There are multiple processes that can be used to improve the image just before and after the traveltime correction. Methods used are 2D median filtering, source static correction, and trim statics. The next three images will illustrate the effects of these processes.

Once the reflections have been flattened, a 2D median filter was used to smooth across the flattened energy. This method must be used carefully because it has the ability to smooth across noise spikes as well as coherent signal. A small number of traces were used to mitigate this effect. The results are shown in Figure 2.38. The P-wave reflections are smoother than the previous example without the filter which had small fluctuations in the reflections.

The first static correction used is a source static correction. This corrects for elevation changes between sources. It is a simple trace math operation, in which, the time shift applied to the trace is represented by the following equation: $T_{shift} = (Src_E - D)/V_r$. Where T_{shift} is the time shift applied to each trace, Src_E is the source elevation, D is the datum elevation, and V_r is the replacement velocity. There is not much elevation variation in this survey so the results of this static correction are very subtle (Figure 2.39).

The other static correction used is trim statics. The reflections are not yet completely flat and to achieve the best possible CRP stack in the next step, these reflections must be flat. This process first stacks all traces in a gather to create a pilot trace. Then, each trace is cross-correlated with the pilot trace over a series of time gates. From the correlations, pick times are assigned to the gate center times. Time pick values are linearly interpolated between gate center times. This gives a variable time correction at each sample for every input trace. The time corrections are applied to the input data and this process is repeated. The time corrections from the second iteration are applied to the output data. This is a time variant process, and so, cannot be used as a processing step when performing a time-lapse analysis. However, this seems to improve the image quality, so will be used as a processing step outside of time-lapse analysis in Chapter 5.

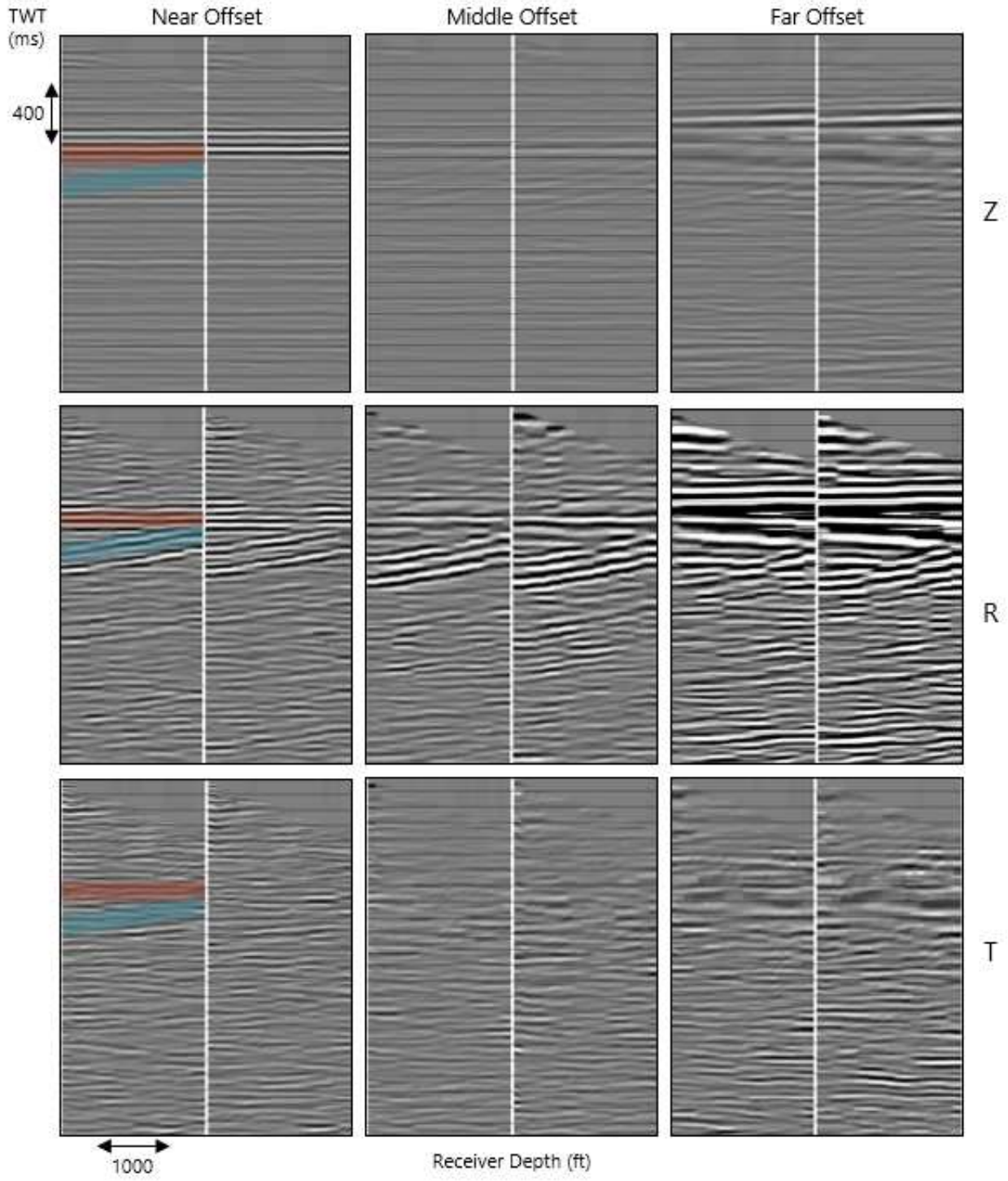

Figure 2.38 Shot gathers at near, middle, and far offsets after moveout correction for P-wave velocity. A 2D median filter is applied. Flattened P-wave highlighted in red, converted wave highlighted in blue.

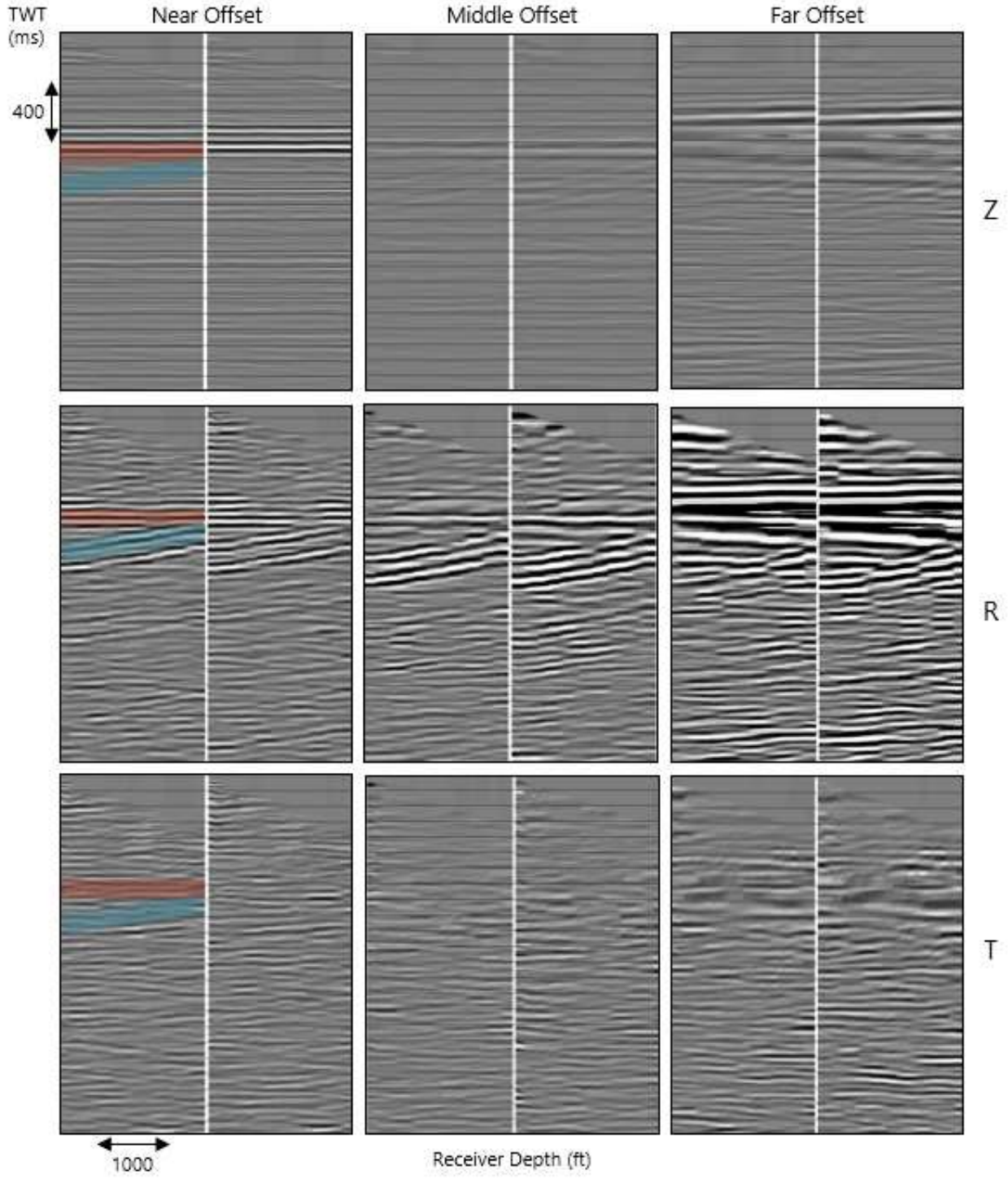

Figure 2.39 Shot gathers at near, middle, and far offsets after moveout correction for P-wave velocity and 2D median filter. Gathers are source static corrected. Flattened P-wave highlighted in red, converted wave highlighted in blue.

This process has a much more dramatic effect than the source statics. Seen in Figure 2.40, the P-wave reflections are now perfectly flat across all offsets. The SV-wave has also been flattened. The maximum time-shift allowed in the trim statics algorithm is 20 ms which means that when a dipping reflection, such as the SV-wave, is flattened it results in a stair step looking result which generally follows the dip of the reflection. The "splitting" reflections at the far offsets are also flattened. This is a concern, because this now looks like two separate reflections. Ideally, a window around the important reflections would be specified and flattened, while data outside the window would be interpolated to compensate for the time-shifts. This would mitigate the flattening of dipping energy. Unfortunately, this could not be done in this project. The initial trim statics method is still used, but its effects are closely monitored and considered during interpretations.

Another consideration with trim statics is focused on the R and T components. The trim statics operator should be designed on the R component and then applied to both R and T components. This would ensure that noise in the T component would not be treated as a reflection and flattened.

Next, source statics and trim statics are used in combination Figure 2.41. The result is clearly dominated by the trim statics.

The traveltime corrections are also used for the PS-converted wave reflections. Now, instead of using only the P-wave velocity model, the S-wave velocities are also used to calculate the PS traveltimes. The same filtering and statics examples will be shown as in the P-wave processing.

The first example (Figure 2.42), are the source gathers from near, middle, and far offsets for each component after traveltime correcting for the SV-wave and without any filtering or static corrections. The P-wave, in red, is now dipping from the left to right and the SV-wave, in blue, is now flat indicating correct velocities. The near offsets in the R-component have flattened reflections, but the middle and far offsets show the same "splitting" phenomena described for the P-wave. The transverse component does not show much flattened coherent

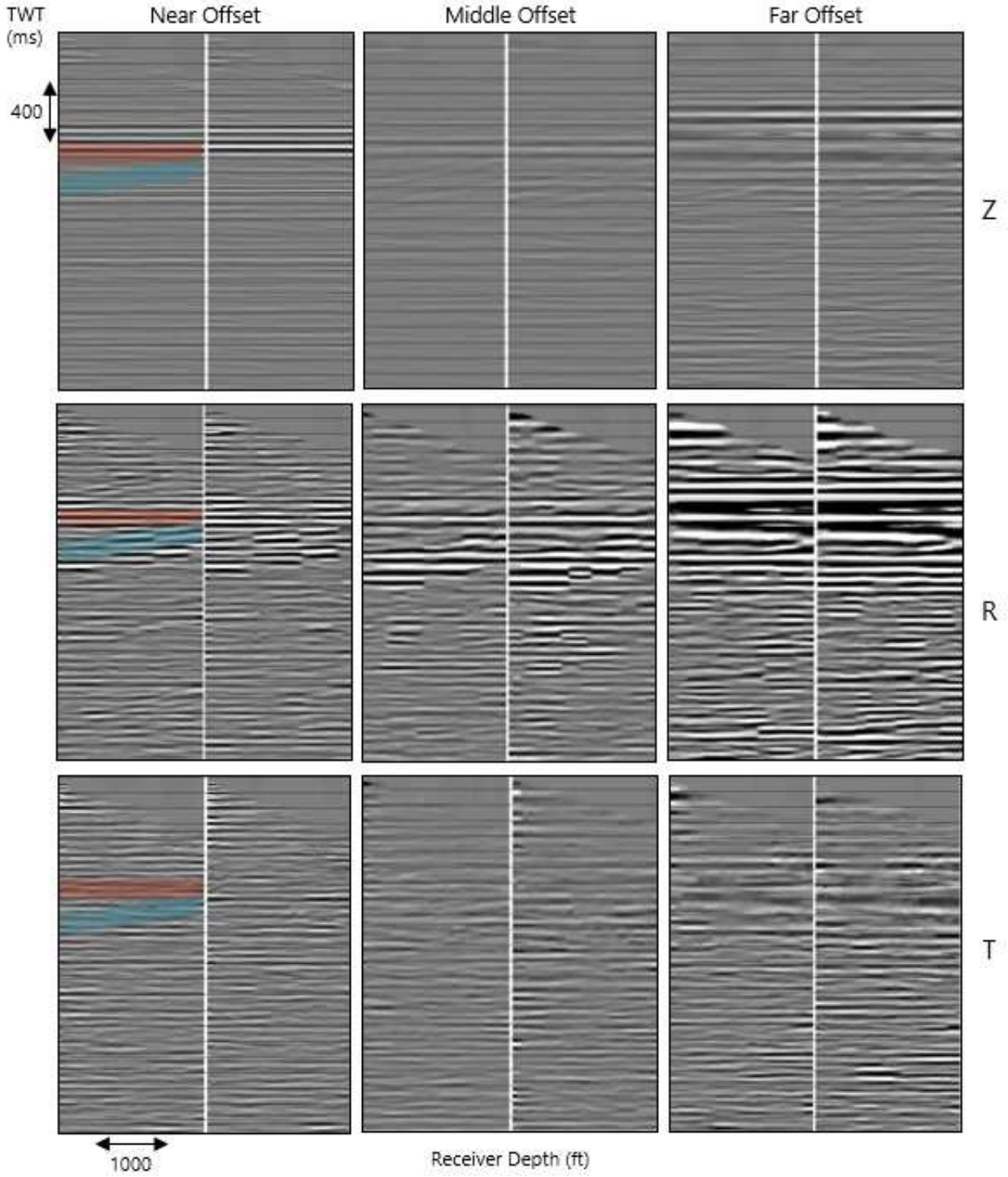

Figure 2.40 Shot gathers at near, middle, and far offsets after moveout correction for P-wave velocity and 2-D median filter. Trim statics are applied. Flattened P-wave highlighted in red, converted wave highlighted in blue.

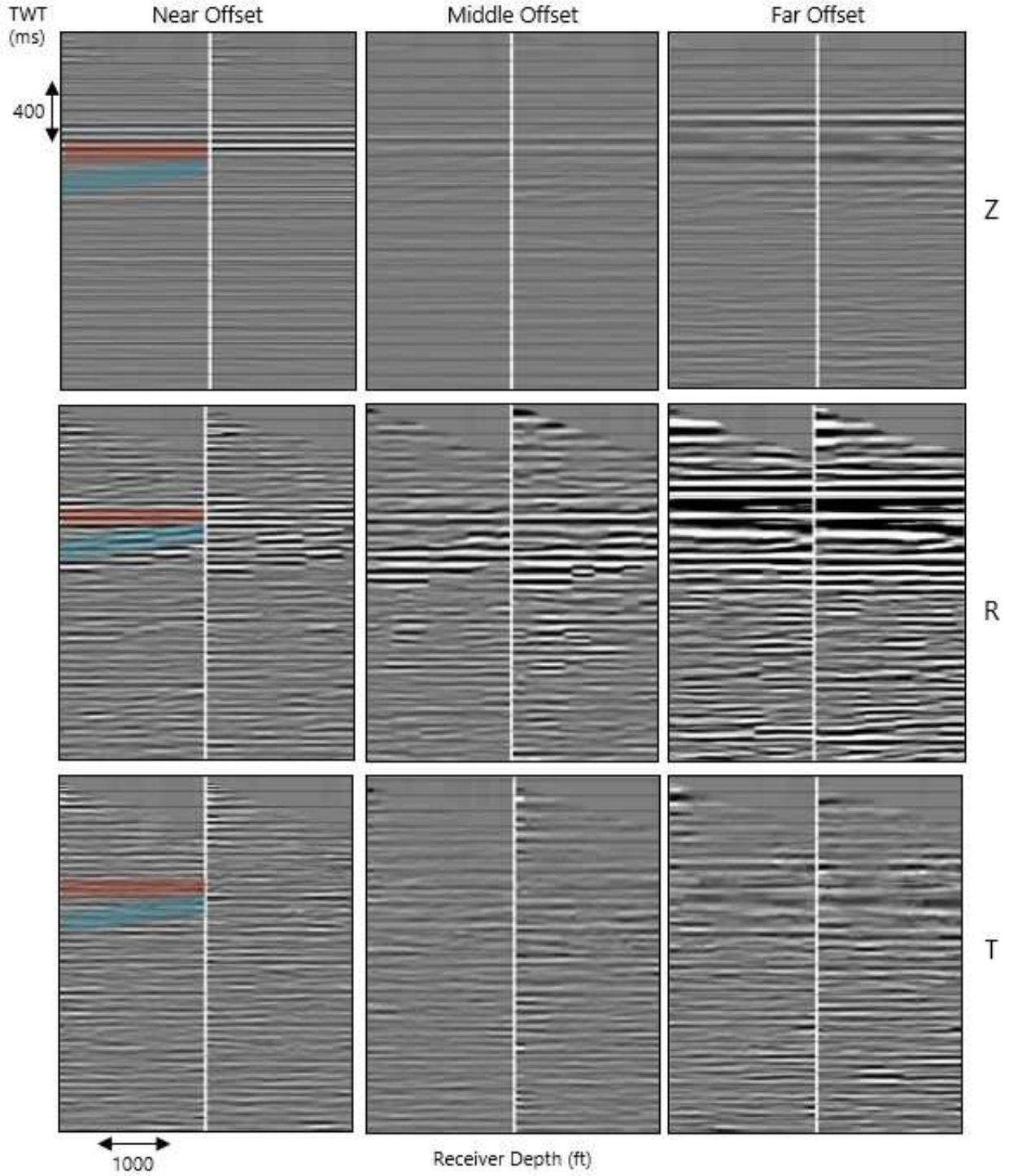

Figure 2.41 Shot gathers at near, middle, and far offsets after moveout correction for P-wave velocity and 2D median filter. Both source statics and trim statics are applied. Flattened P-wave highlighted in red, converted wave highlighted in blue.

energy.

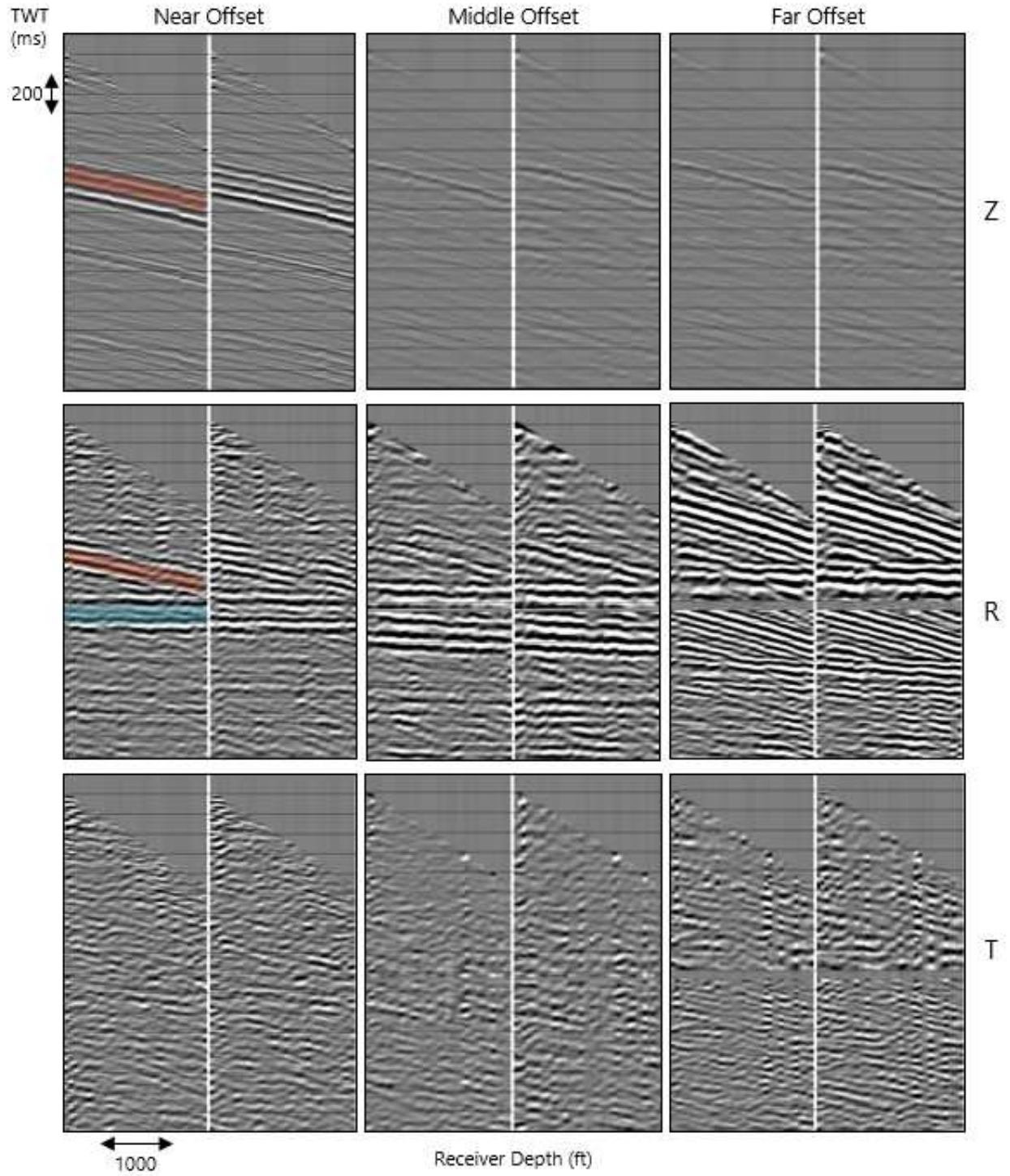

Figure 2.42 Shot gathers at near, middle, and far offsets after moveout correction for PS-wave velocity. P-wave highlighted in red, flattened converted wave highlighted in blue.

A 2D median filter was again used to improve the continuity of the flattened energy (Figure 2.43). Source statics were also applied with similar results as the previous example (Figure 2.44). The last example in this series is again the combination of both source and trim statics (Figure 2.46). The trim statics dominate the result.

Trim statics again has the most dramatic effect (Figure 2.45). The flattening of the dipping P-wave results in the same stair step looking reflections as seen in the previous example. Arguably, the most dramatic result of the trim statics is the appearance of two flat reflections in the transverse component at the middle and far offsets. Before this process was applied, these features were all but invisible. Interpretation should be done with skepticism, but the top reflection is consistent across all four gathers suggesting that it is more than noise.

The last example in this series is again the combination of both source and trim statics (Figure 2.46). The trim statics dominate the result.

2.3.3 Common Reflection Point Mapping

Next, the common reflection points must be mapped using the traveltime-corrected shot gathers. The ray tracing produces traveltime corrections and common-reflection points as a function of vertical traveltime and spatial position $(t_0, crossline, inline)$. The traces in the traveltime corrected gathers are mapped to their corresponding common-reflection points using a specified bin size. A bin represents a space in x and y, in which, the reflection points mapped to that bin are stacked. The larger the bin size, the more traces are stacked together. A bin size of 82.5 ft was specified for the walkaway survey. This bin size is the same used for the surface seismic processing so that they can be merged together more easily. Figure 2.47 compares the results of the CRP mapping using the different static corrections discussed previously. All examples have the 2D median filter applied before CRP mapping.

The prominent reflections in the top half of the images is the area of interest. The Austin Chalk reflection is indicated by the green arrow, the Eagle Ford by blue. These reflections appear near the top of the image because the receivers are placed just above these formations

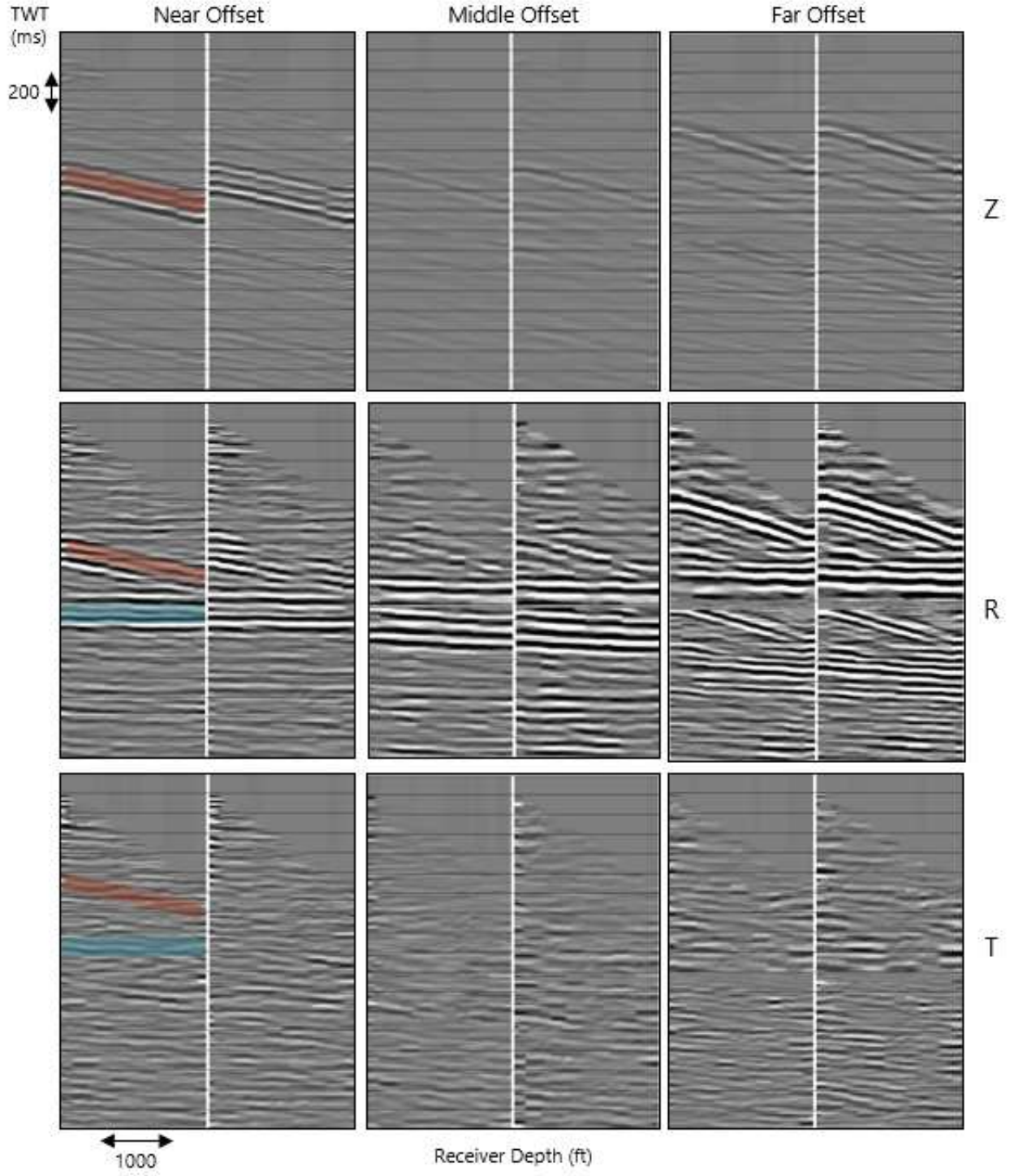

Figure 2.43 Shot gathers at near, middle, and far offsets after moveout correction for PS-wave velocity. A 2D median filted is applied. P-wave highlighted in red, flattened converted wave highlighted in blue.

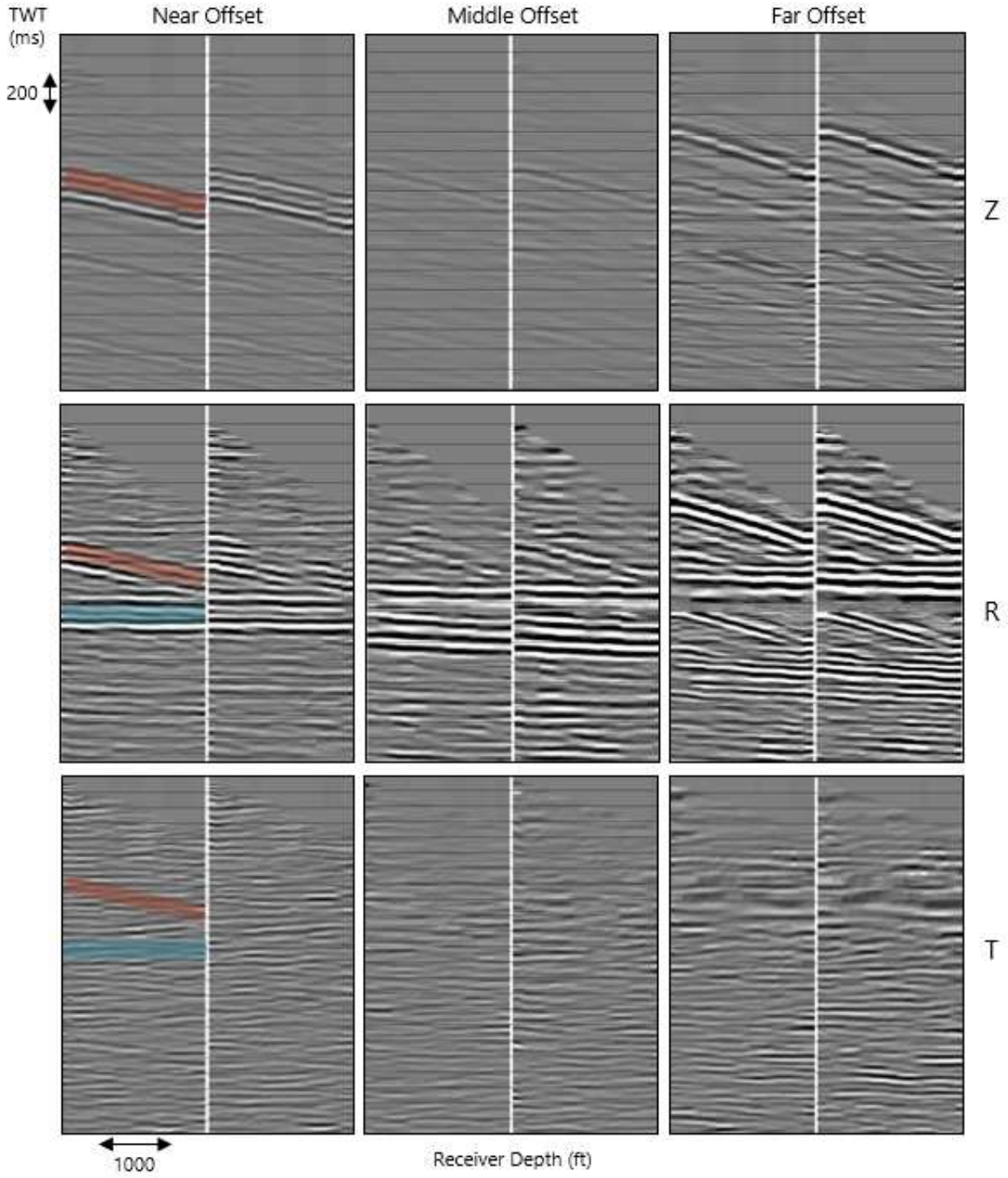

Figure 2.44 Shot gathers at near, middle, and far offsets after moveout correction for PS-wave velocity and 2D median filter. Gathers are source static corrected. P-wave highlighted in red, flattened converted wave highlighted in blue.

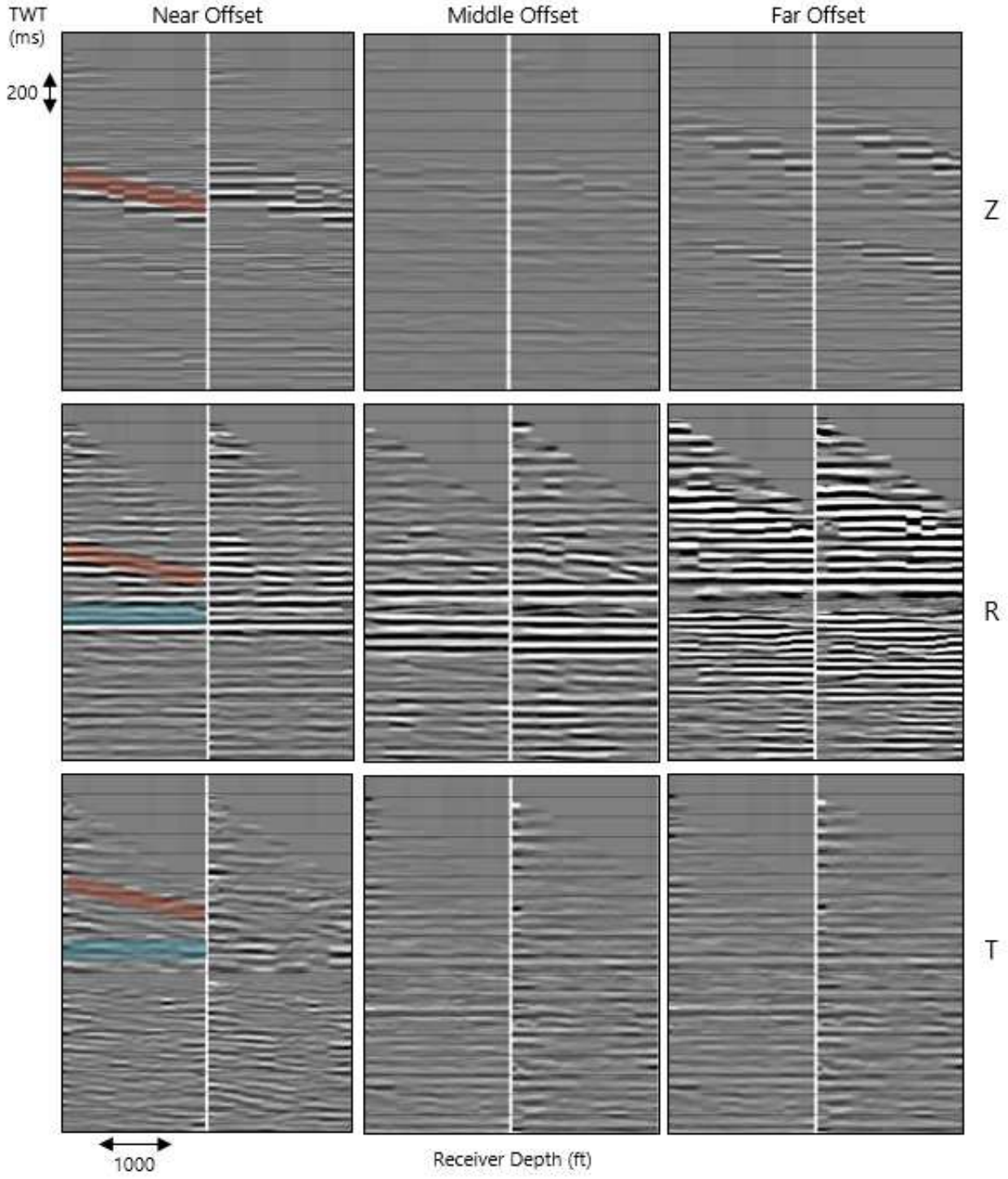

Figure 2.45 Shot gathers at near, middle, and far offsets after moveout correction for PS-wave velocity and 2D median filter. Trim statics are applied. P-wave highlighted in red, flattened converted wave highlighted in blue.

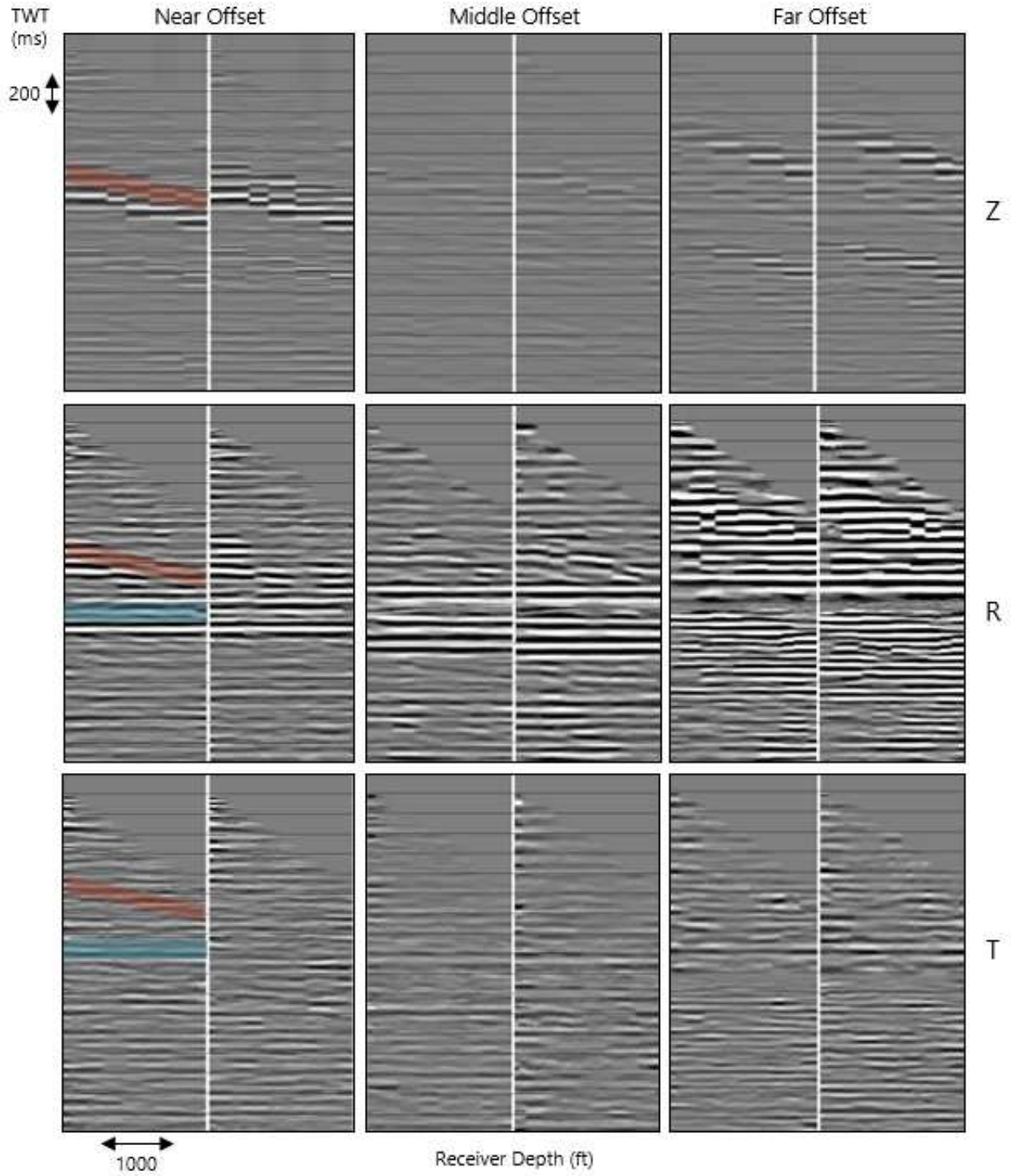

Figure 2.46 Shot gathers at near, middle, and far offsets after moveout correction for PS-wave velocity and 2D median filter. Both source statics and trim statics are applied. P-wave highlighted in red, flattened converted wave highlighted in blue.

and nothing above the receivers can be imaged. Other prominent reflectors like the top of the Wilcox (seen in the Zero-offset VSP) cannot be imaged by this survey, but are imaged in the DAS walkaway survey discussed in the next chapter, illustrating the value of DAS VSP recordings.

The vertical gaps in the reflection points are due to the gaps in the sources Figure 2.31. If there were no gaps in the source points, these gaps would not exist.

Similar to the shot gathers after traveltime correction, the CRP gathers without statics and with source statics are very similar. The near offsets are mapped very well and as the offset increases, the reflections start to "stretch" slightly and in the middle offsets the reflections seem to split. The stretching is similar to NMO stretch seen in surface seismic and most of the stretching has been muted out. The reflection splitting was previously illustrated in the source gathers after traveltime corrections. When trim statics are applied, the split reflections become more prominent because they were flattened after the traveltime corrections and are better mapped in the CRP mapping.

Two different bin sizes were tested in Figure 2.48: 82.5 ft and 165 ft. The larger the bin size, the more traces can be stacked together in each bin. If many reflection points do not have multiple traces imaging them, the resulting image will deteriorate and have gaps. A larger bin size will improve the signal to noise ratio and close the gaps in reflection points. In this walk-away survey, however, there is sufficient coverage using the 82.5 ft bin size and the 165 ft bins unnecessarily smooth the image and the amplitude of some reflections are diminished as well.

The results of CRP mapping the PS reflections are shown in Figure 2.49. A more aggressive mute was applied because the reflections started stretching at nearer offsets. The extent of the reflection point mapping is more limited than when mapping the P-wave reflections due to the geometry of the reflections. The PS-wave reflects at a higher angle (more vertical) than the P-wave reflections. The reflections must occur closer to the well in order for the receivers to record them. The energy is also focused on the radial component and nearly

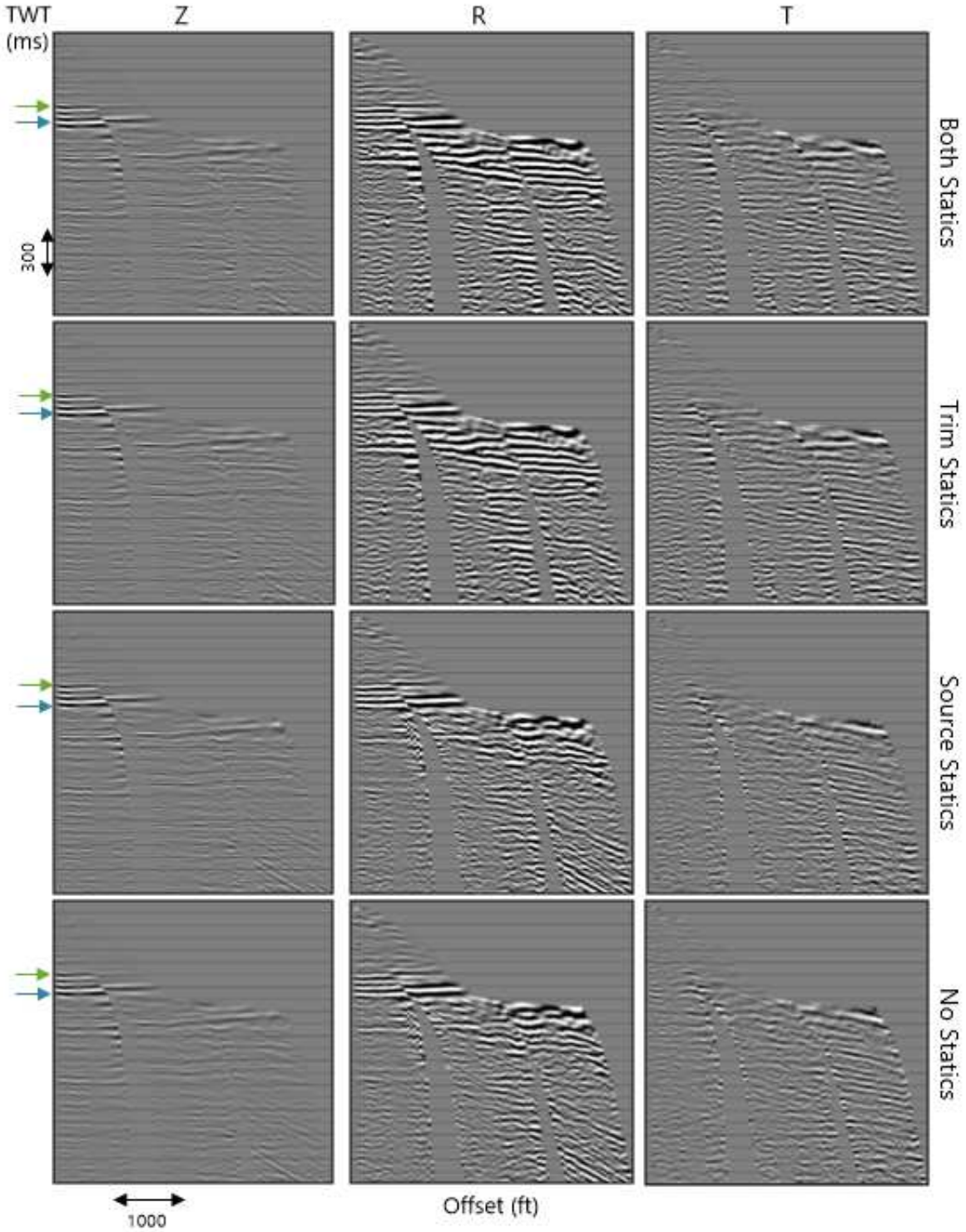

Figure 2.47 P-wave reflection point mapping. Comparison between static corrections. Columns compare different statics and the rows compare the different components.

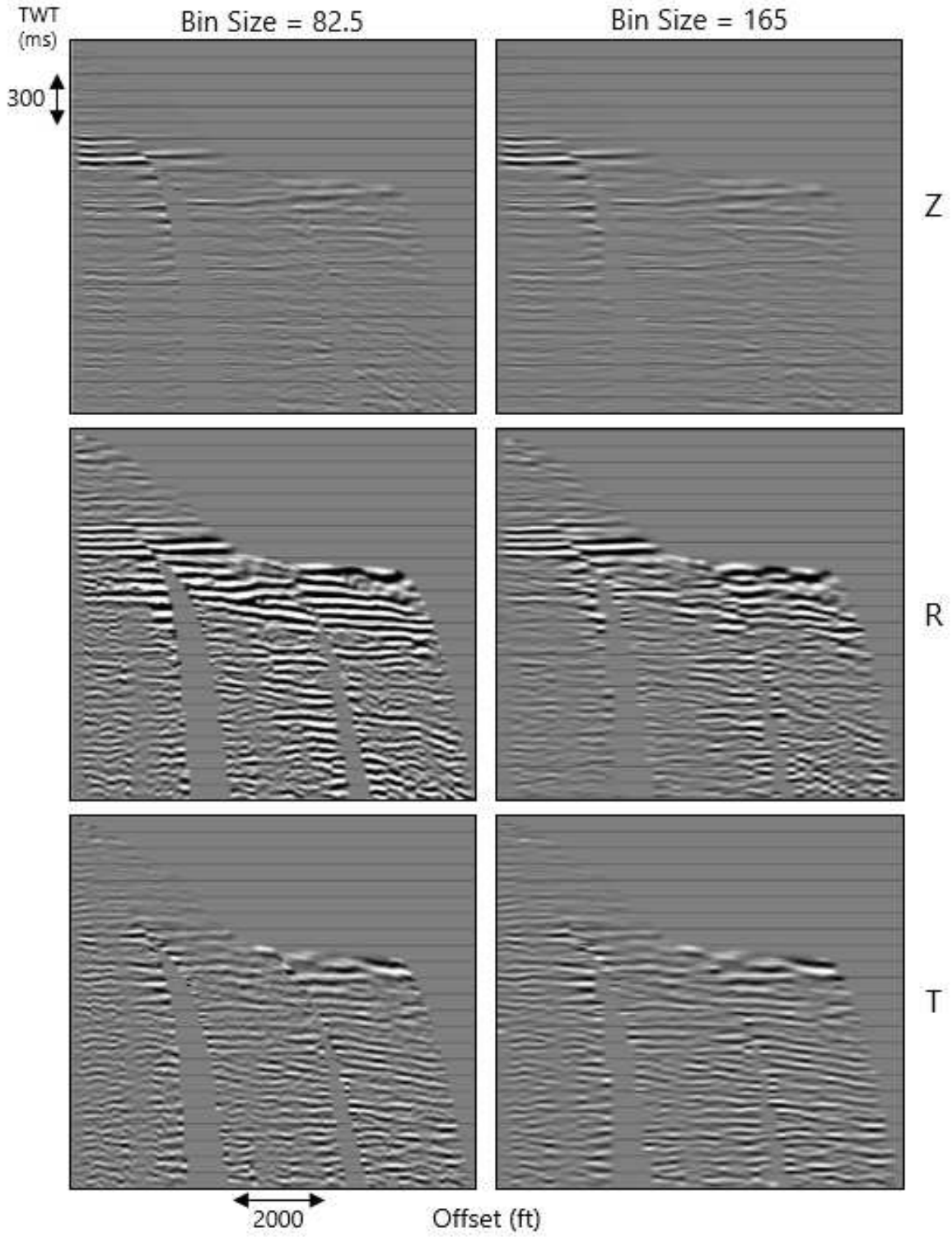

Figure 2.48 P-wave reflection point mapping. Comparison between bin sizes.

no energy is recorded on the other two components. The Eagle Ford and Austin Chalk reflections can be seen in the center of the images.

Again, the effect of the trim statics is the most dramatic. Shallower reflections come into focus with this correction and again in the transverse component there are slight reflections from the the area of interest.

Two bin sizes were again tried with the SV CRP mapping (Figure 2.50). The larger bin size smooths out the reflections and slightly closes the gap at the bottom of the section. The extra smoothing, in this case, is unnecessary so the 82.5 bin size will be used to tie to the seismic.

The final step for this walk-away survey would be to tie in the CRP stack to the surface seismic. The azimuth of this line (30°) does not align with the inline and cross-line directions of the seismic ($-45°$ and 45°). This means that interpolation is needed to properly align the walkaway bins to the surface seismic bins. It is possible to do this, however, it could not be done within the confines of this project. The 3D DAS VSP survey discussed in Chapter 4 was successfully tied to the surface seismic.

Trim statics is demonstrated in this chapter to be potentially misleading and dangerous, especially for the PS processing. Since most of the recorded energy on this walkaway survey is from P-waves and this energy is flattened on the traveltime corrected shot gathers, trim statics potentially improves the final result. However, the PS reflections are much weaker and P-wave energy is still very strong on the traveltime corrected PS shot gathers, so trim statics negatively impacts the final results. Trim statics on the PS gathers can lead to the flattening of P-wave energy which could be mistakenly mapped to reflection points and interpreted as real signal. In further processing of these data for time-lapse analysis, trim statics is not used for either P or PS imaging. The images with trim statics are included as a demonstration of how the interpretation may change based on this late processing step.

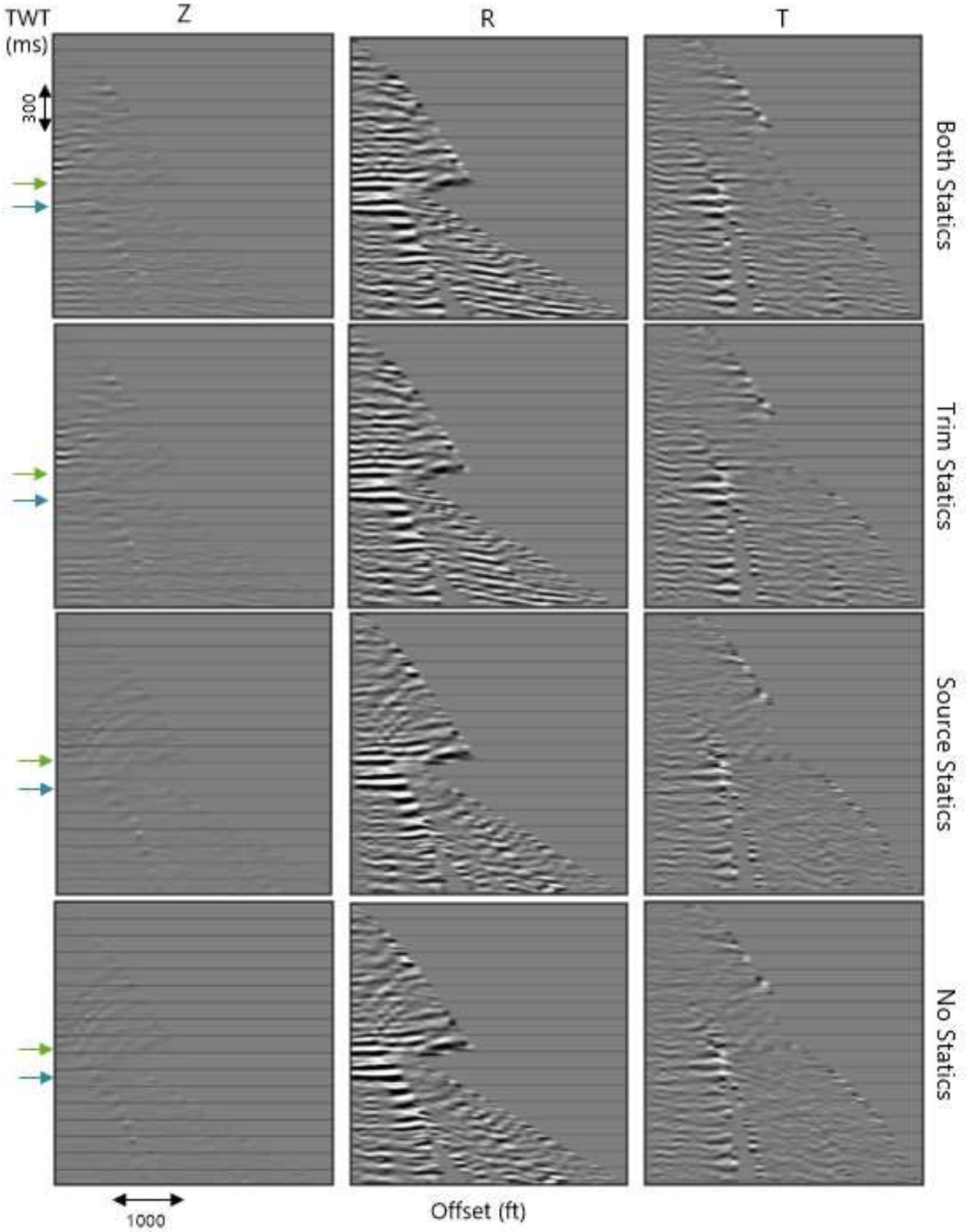

Figure 2.49 P-SVwave reflection point mapping. Comparison between static corrections.

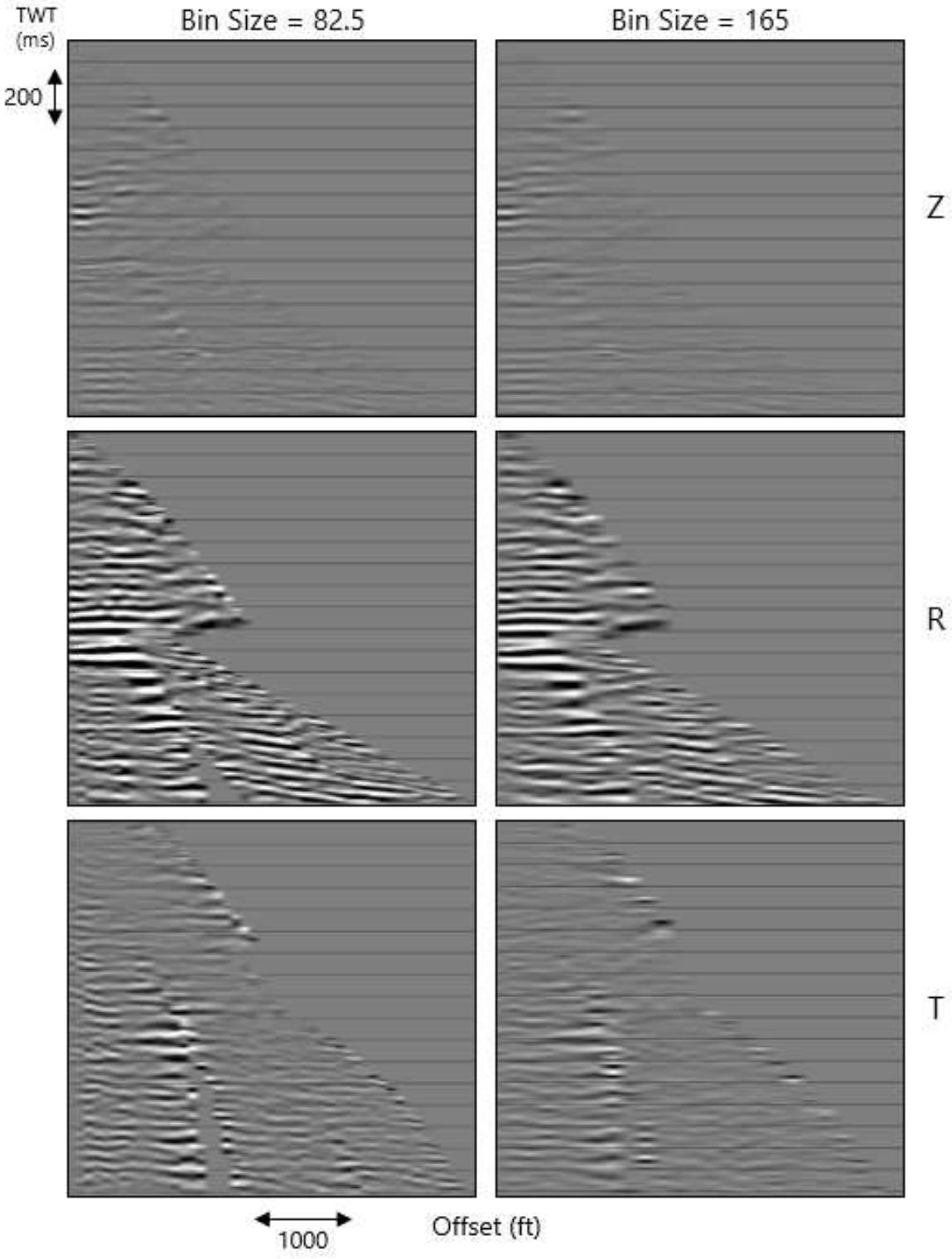

Figure 2.50 P-SVwave reflection point mapping. Comparison between bin sizes.

CHAPTER 3

DAS VSP PROCESSING

This chapter discusses the processing of the DAS VSP for both the zero-offset and the walkaway surveys. The structure is very similar to the previous chapter. First, the zero-offset is processed and then compared to the geophone response once it it is converted to two-way time. The walk-away processing is then discussed using the same ray tracing, filtering, and static corrections as with the geophone survey.

3.1 Zero Offset

The zero offset DAS VSP survey is expected to have much the same utility as the zero offset geophone VSP survey, minus the multicomponent capability. It is a useful exercise to compare the results from these surveys to gain understanding of the advantages and disadvantages. Due to the multicomponent aspect of the geophones, more shear-wave information is expected, but the much denser receiver intervals in the DAS fiber can provide much higher spatial resolution. A direct comparison between the surveys cannot be made because the surveys were not completed in the same well, but in adjacent wells (about 1000 ft apart). There are no major geologic changes over this scale so the surveys should be comparable in that respect.

Additionally, this is not a true zero-offset survey, because the sources are the same ones used for the zero-offset survey into Well B with the geophones (Figure 3.1). The DAS fiber was recording during the geophone zero-offset acquisition so there is about one thousand feet of offset.

DAS fiber has a few sources of noise that are unique to itself. First, the optoelectronic components of the interrogation system generates random noise which is best removed by stacking multiple sweeps together. However, the background noise is still higher than traditional geophones. Second, common mode noise (horizontal noise) is caused by sound entering

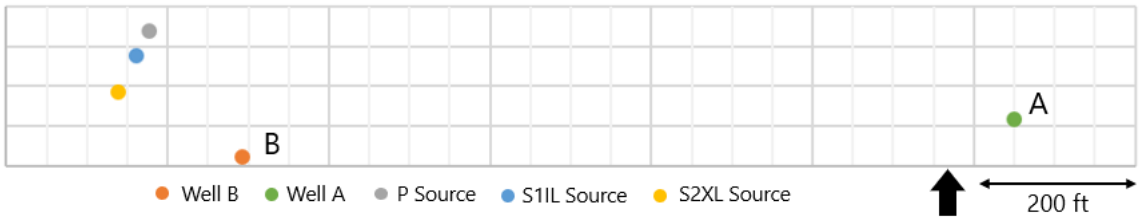

Figure 3.1 Zero-offset VSP survey into the DAS receivers.

the DAS interrogator unit (Figure 3.2). The sound contaminates all channels of the recorded data with an identical set of noise (Willis *et al.*, 2016). This type of noise is easily removed with a simple 2D median filter. In newer generations, this interrogator noise has been significantly reduced. Third, faded channels or vertical noise are locations along the fiber where the optical backscatter signal is very weak. This is created when the ensemble sum of the backscattered light in a particular region of the fiber interfere with one another destructively (Willis *et al.*, 2016). Vertical noise can be removed using a TFD (Time-Frequency Domain) noise rejection filter which replaces traces with anomalous amplitudes with the median amplitude of adjacent traces (Figure 3.3).

The raw DAS data provided was already correlated so the first processing step is removing the horizontal interrogator noise. This time-variant noise is unique to each shot. A simple 2D median filter effectively removes this noise (Figure 3.2). Next, the vertical noise, seen in Figure 3.3 A, B, & C must be removed. When analyzing separate shot gathers, three different types of noise stood out. In Figure 3.3 (A) there is a high amplitude, low frequency trace around 5000ft. This noise was seen in multiple gathers and occurred most commonly at this channel. Similar noise is seen in the geophone data. Another common type of vertical noise is seen in Figure 3.3 (B). In this example there is faint vertical striping across the entire gather. The last type of noise identified is stronger striping, generally concentrated in the shallower channels (Figure 3.3 C). The specific sources of these types of noise is unclear and is beyond the scope of this project. Whatever the cause of this noise, it is simple to remove. Much of the striping can be removed by stacking (Figure 3.3 D), and what remains can be

easily filtered out by using a combination of a bandpass filter and TFD Noise Rejection, very similar to that used to filter noisy traces from the geophone data in the previous chapter (Figure 3.3 E). These examples are all from near offset shots but similar noise is seen in the far offsets and are removed with the same methods.

Once the DAS specific noise is removed, the processing is exactly the same as the vertical geophone component zero-offset processing. The wavefields are separated using F-K filtering, spiking deconvolution is applied, and the traces are corridor stacked.

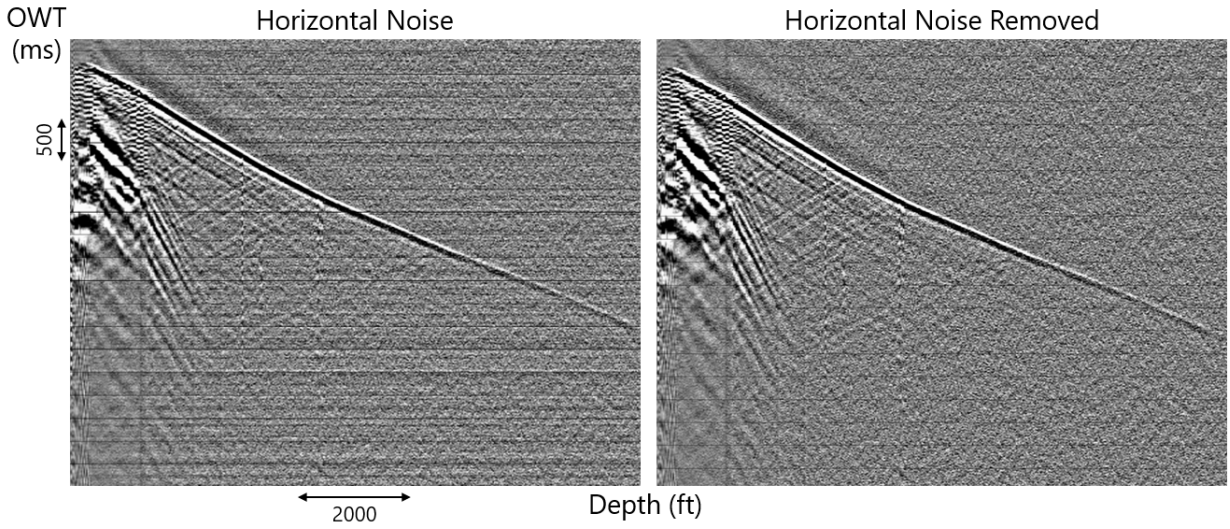

Figure 3.2 Example of the horizontal noise caused by the interrogator unit in a single shot (left). Same shot with noise removed (right).

3.1.1 Converting to Geophone Response

DAS records the strain rate along the fiber (Parker *et al.*, 2017), so in order to accurately compare to the geophone zero-offset survey, it must be converted to particle motion. There are multiple techniques to convert the DAS strain rate response to the geophone particle velocity response (Bakku (2015); Daley *et al.* (2015); Bóna *et al.* (2017); Correa *et al.* (2017)). In this study, one of the more simple methods was used, which is integrating along depth. This method, while not perfect, mostly corrects for the phase and polarity of the reflections.

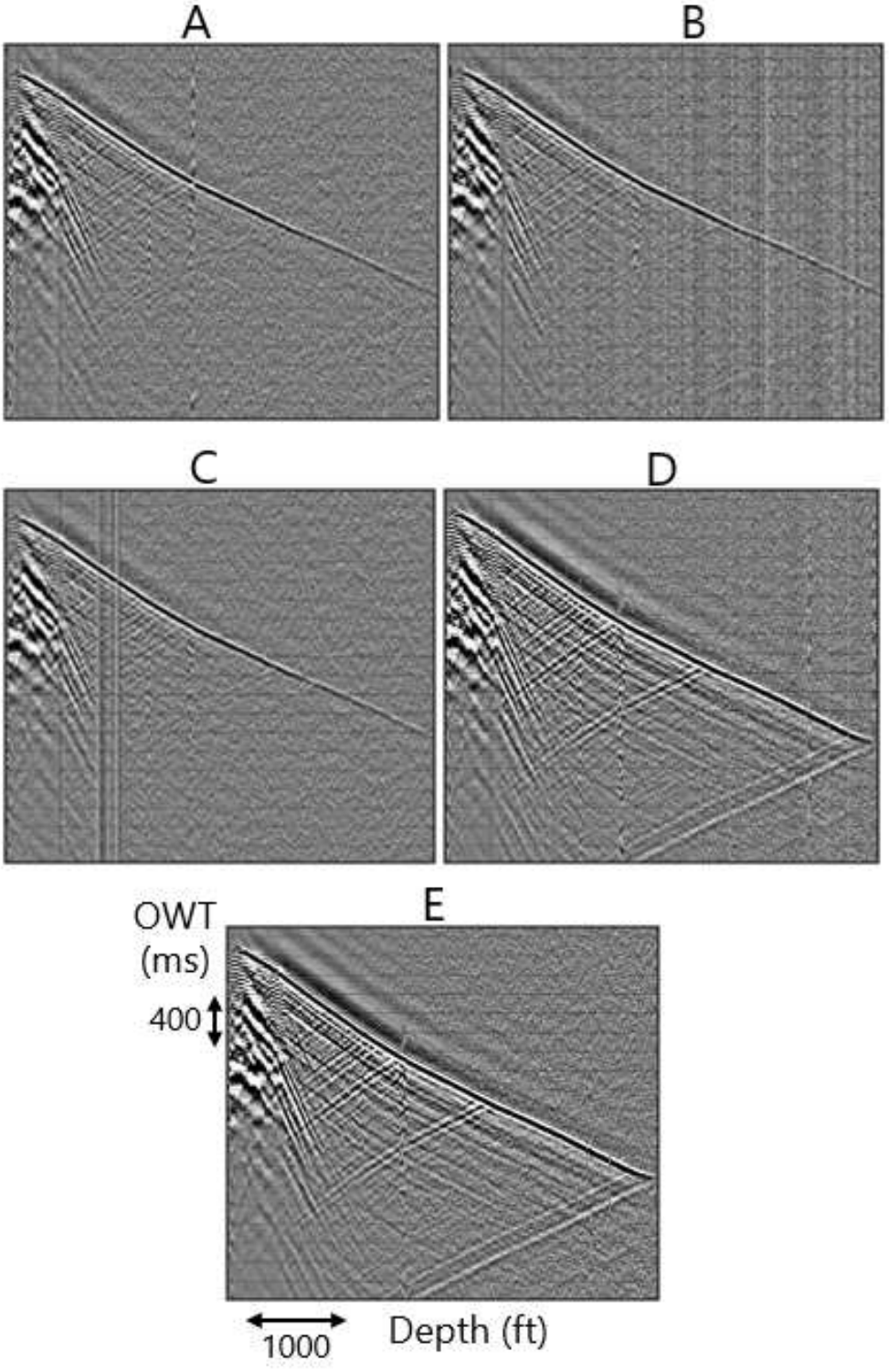

Figure 3.3 Examples of vertical noise. (A) high amplitude, low frequency noisy trace. (B) Faint vertical striping. (C) Strong striping concentrated in shallow channels. (D) Shots stacked together removes most of noise. (E) TFD noise rejection removes the rest of the noise.

Before the reflections are flattened, an integration along the length of the fiber in the frequency domain is performed. Unfortunately, this process will amplify and smear noise across the gather (Figure 3.4). After the conversion, no signal can be seen though the horizontal banding resulting from the integration. An aggressive 2-D median filter is applied to remove this. The image is greatly improved but some of this horizontal noise remains. So, the reflections are flattened by applying the first break picks as a static correction and another 2-D median filter is applied to smooth across the reflectors and remove the non-horizontal energy.

The results from the conversion compared to the geophone data are presented in Figure 3.5. A 512 ms static shift is applied to the DAS data to account for the differences in source locations relative to the well. This time-shift aligns the large reflectors near the bottom of the gathers but does a poor job aligning those above. This is because the DAS zero-offset survey, as previously mentioned, is not a true zero-offset. The P-waves recorded by the fiber travel a large horizontal distance, and so, are subject to more of the horizontal P-wave velocity. These velocities are slightly different, so when comparing the geophone to the DAS zero-offset surveys, they will not perfectly align. This is also the reason for the slight downward dip in reflectors at the shallow receiver depths. To avoid this, ray tracing would be a more correct method to traveltime correct this shot gather.

The converted DAS gather compares well with the geophone data. Of the main reflectors near the bottom of the section, the peaks and troughs line up well but the converted DAS does not contain the same frequency content as the geophone data. This is supported by (Figure 3.6). Some mis-ties between the datasets may be attributed to the differences in frequency content. Before integration, the DAS contains a similar frequency content as the geophone data. This is to be expected because they both underwent nearly an identical processing flow which contained the same bandpass filter after spiking deconvolution. After integration, the frequencies above about 20 Hz lose a lot of their energy. This is unfortunate because one of the benefits of VSP is that it generally contains higher frequencies than surface

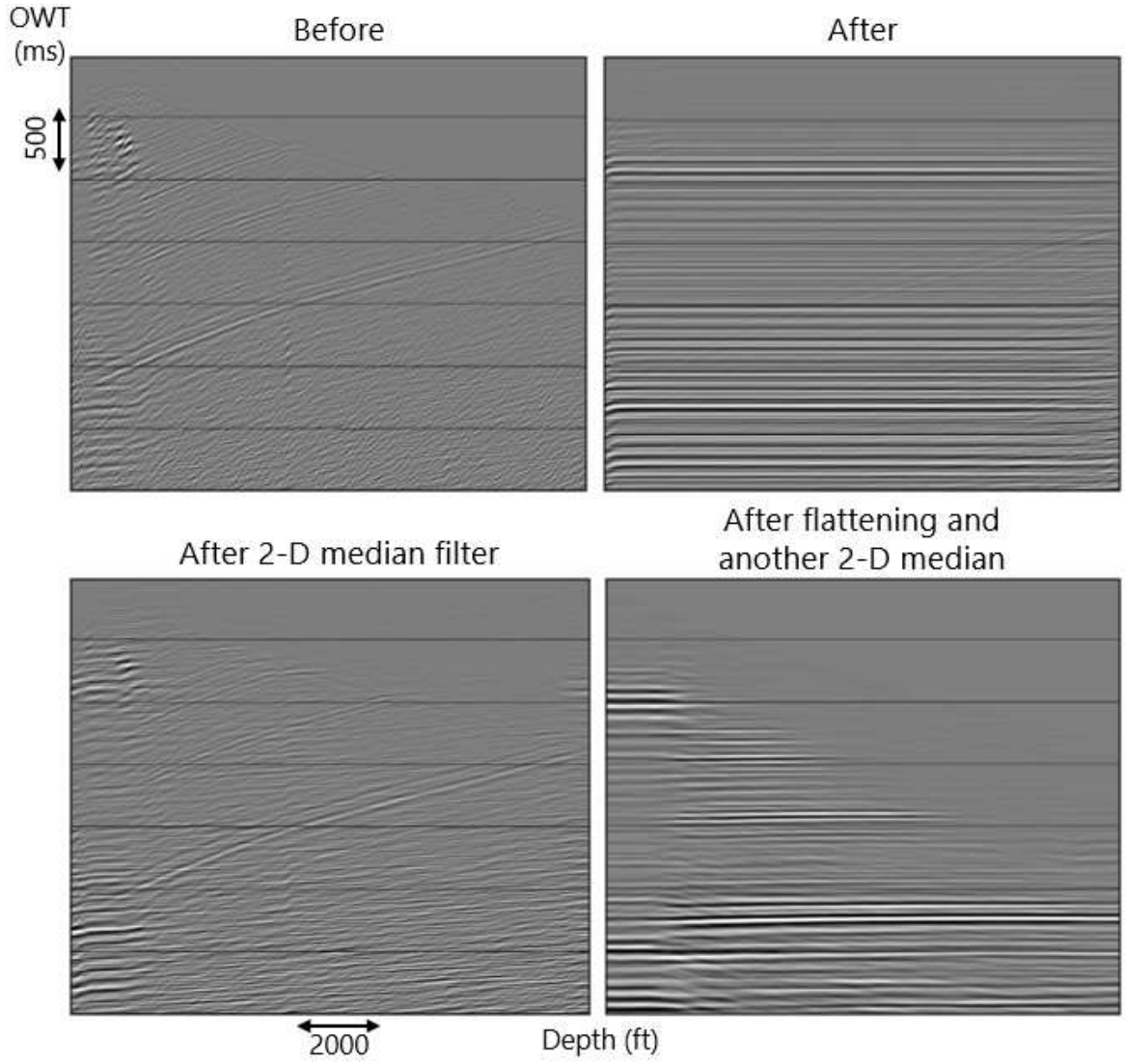

Figure 3.4 Comparison between the zero-offset DAS, the converted DAS and the zero-offset geophone data.

seismic. However, interpretations can still be made on the higher frequency unconverted DAS data, it just cannot be directly compared with geophone data and the interpreter must be aware that interpretations are of strain rate instead of particle motion.

3.1.2 Shear-source Zero-offset

The DAS zero-offset VSP also has shear sources which are the same as the geophone zero-offset survey. Figure 3.7 is an example of these data. This image has been filtered to

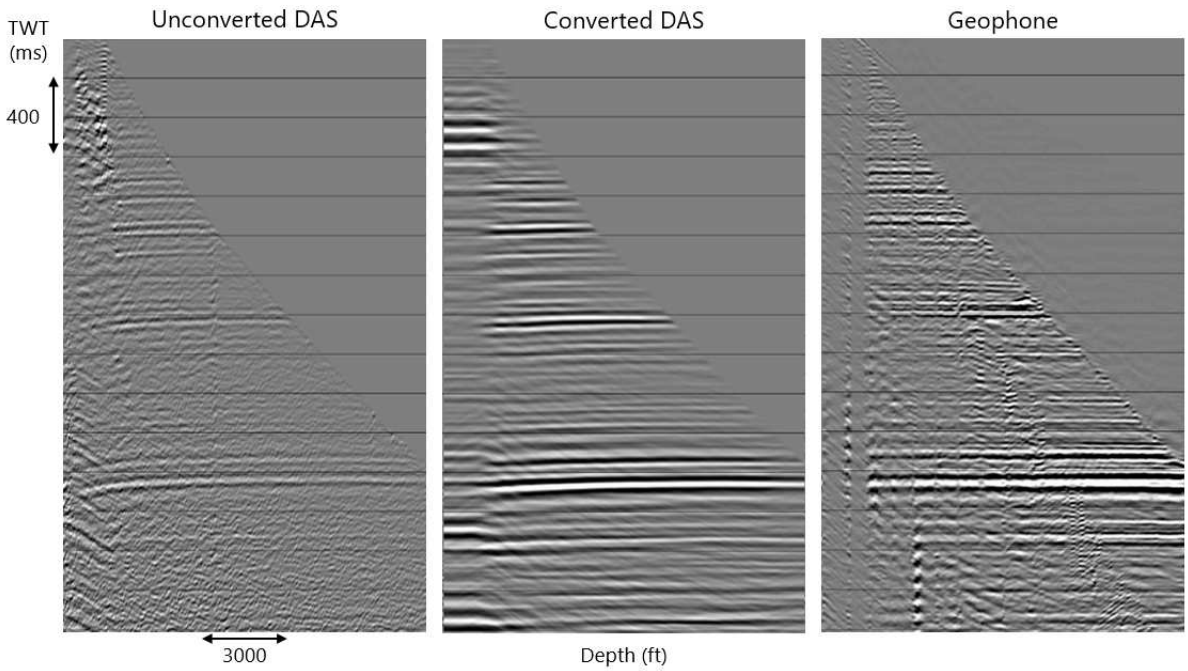

Figure 3.5 Comparison between the zero-offset DAS, the converted DAS and the zero-offset geophone data.

remove both the horizontal and vertical noise, described in the previous section, and the amplitudes have been corrected for wavefield spreading.

In this figure, the shear-wave direct arrival is clearly seen as the bright amplitude and steeply dipping wavefield. The dimmer P-wave arrival can also be seen with the shallower dip. The shear-wave is prominent in these data because of the 1000 ft offset from the source to the well. The shear-waves from this offset have sufficient vertical particle motion to be recorded by the fiber. If this were a true zero-offset survey, the shear-wave would not be present in these data because the shear-wave particle motion would be perpendicular to the fiber.

The first-breaks in these images are very clear and require no rotations like the geophone data. The first-breaks were picked in an attempt to calculate shear-wave velocities for use in ray tracing. Unfortunately, because of the amount of offset and the degree to which the shear-waves travel diagonally through the subsurface, the velocities were incorrect and could not be used for ray-tracing. This dataset was not processed any further. In principal,

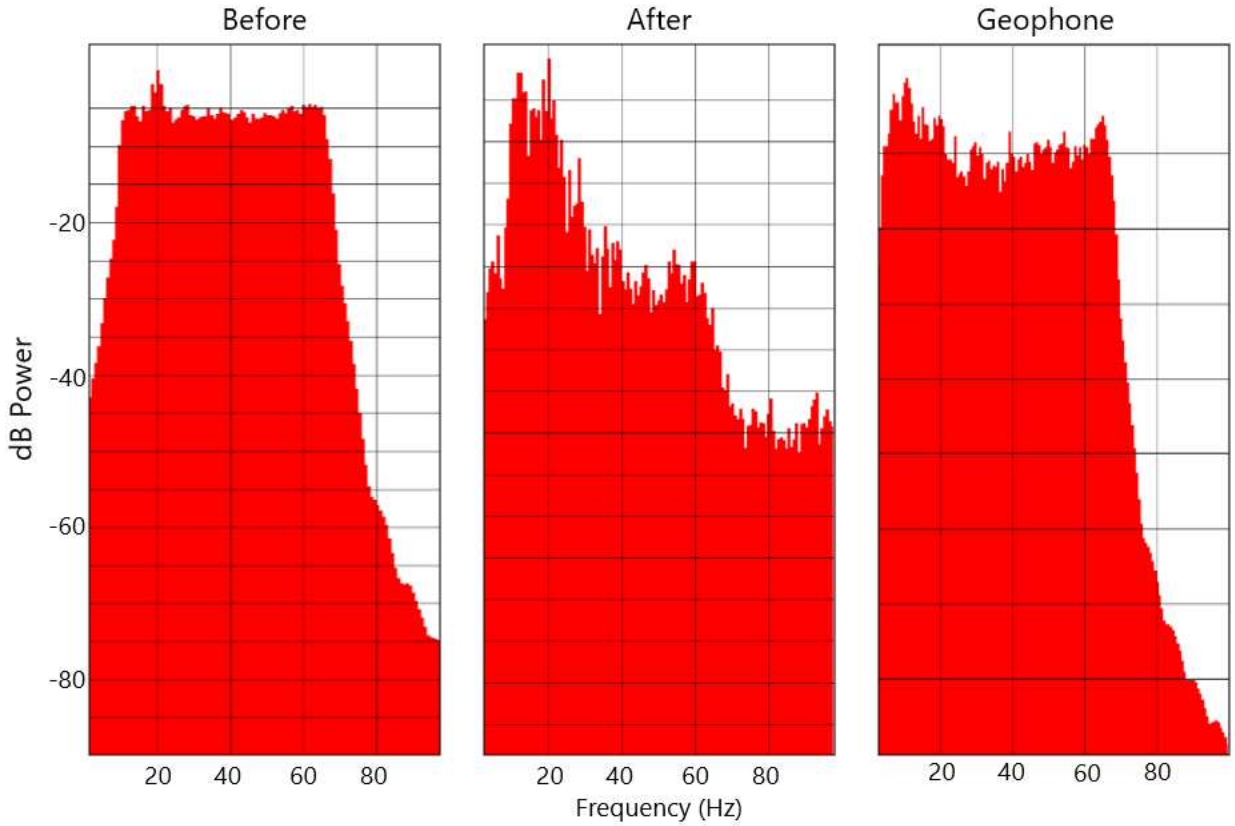

Figure 3.6 Comparison between the frequency spectrum of the unconverted DAS, converted DAS and geophone zero-offset datasets.

though, the S-wave direct arrivals can be inverted to help constrain the shallow S-wave velocity model.

3.2 Walk-away

The DAS walkaway survey was acquired in the same manner as the previous DAS surveys. The DAS fiber was recording while the walkaway survey for Well B was being acquired. The map view of this geometry is seen in Figure 3.8. The same pre-processing used for the geophone walkaway was used for this dataset.

Shot gathers at three different offsets can be seen in Figure 3.9. The wavefields recorded by the fiber are more complex at the middle and far offsets with multiple instances of upgoing and downgoing PS-converted waves. These gathers are comparable to shot gathers from the

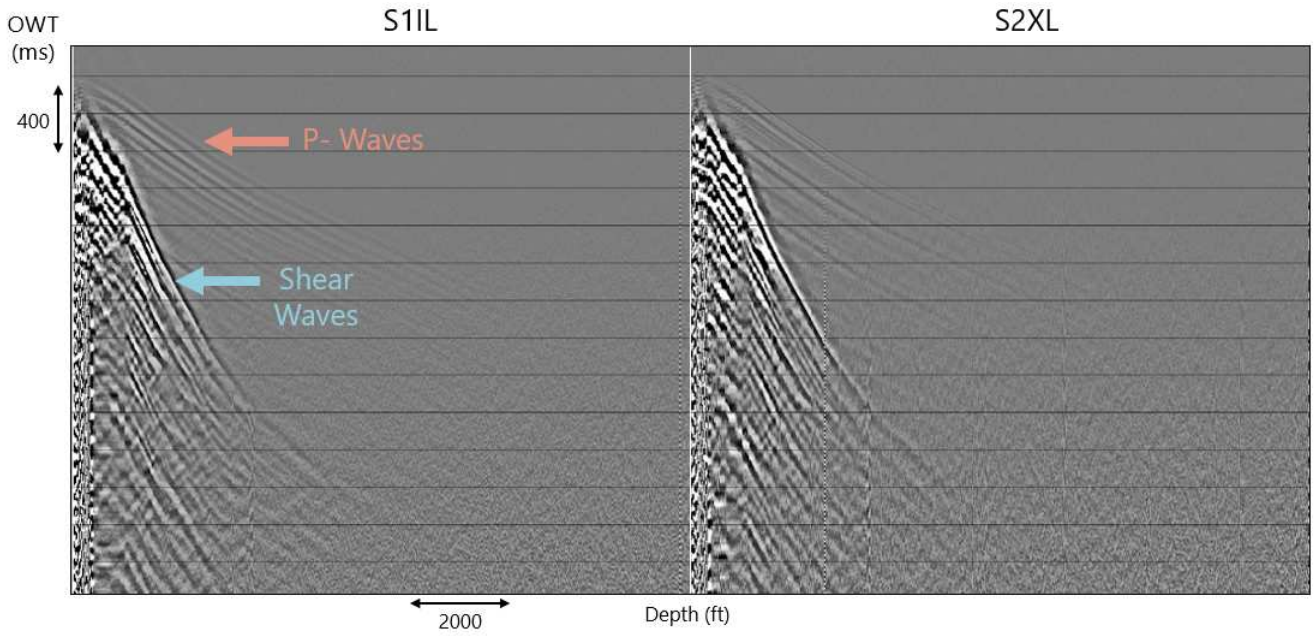

Figure 3.7 Shear source zero-offset DAS VSP. Data are filtered to remove DAS specific noise and amplitude corrected. The S1IL source is the source oriented inline to the V_{fast} direction (57°) and S2Xl is orthogonal to that (147°).

vertical component for the geophone data except with a much larger receiver aperture so much more of the wavefields can be recorded. The origins of the PS-converted waves can be seen. The geophones, with the limited receiver aperture, could not see this.

3.2.1 Ray Tracing

The process of traveltime corrections and common reflection point mapping for the DAS survey is the same as that used for the geophone walkaway survey. The larger vertical extent of the DAS fiber greatly expands the area that can be imaged. This next section will discuss the same filtering and static corrections which were used on the geophone walkaway data. The near offsets are about $1,400$ ft, the middle are about $9,500$ ft, and the far about $14,100$ ft.

Figure 3.10 compares the initial traveltime corrected shot gathers at different offsets with the gathers which have undergone a 2D median filter. The filter smooths across the flattened reflections and improves their continuity. At the near offsets, the P-wave reflections

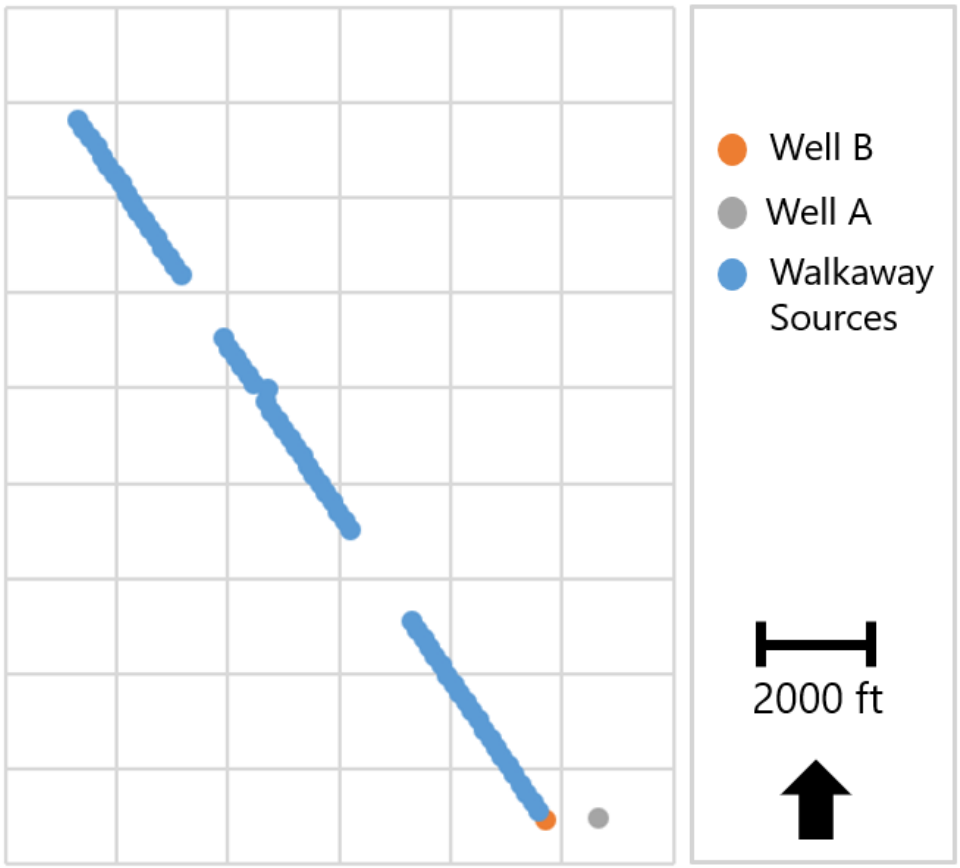

Figure 3.8 Map view illustration of Walkaway DAS survey geometry.

are flattened and near the top of the section, faint SV-waves can bee seen dipping from right to left.

Next, source statics and trim statics were used (Figure 3.11). Again, since the source elevations are relatively consistent, there is not much change after the source statics. The trim statics have the more dramatic changes. At the near offsets, the statics improve the gather by further flattening the reflections. The noise at the bottom of the gather is also flattened and now looks like legitimate reflections. The reflections below the ones highlighted red are not important in this study, but it is important to be aware of these effects of trim statics. At the middle offsets, more shear wave energy is seen and the statics seem to smooth through the reflections and still improve the image. The trim statics on the far offsets affects

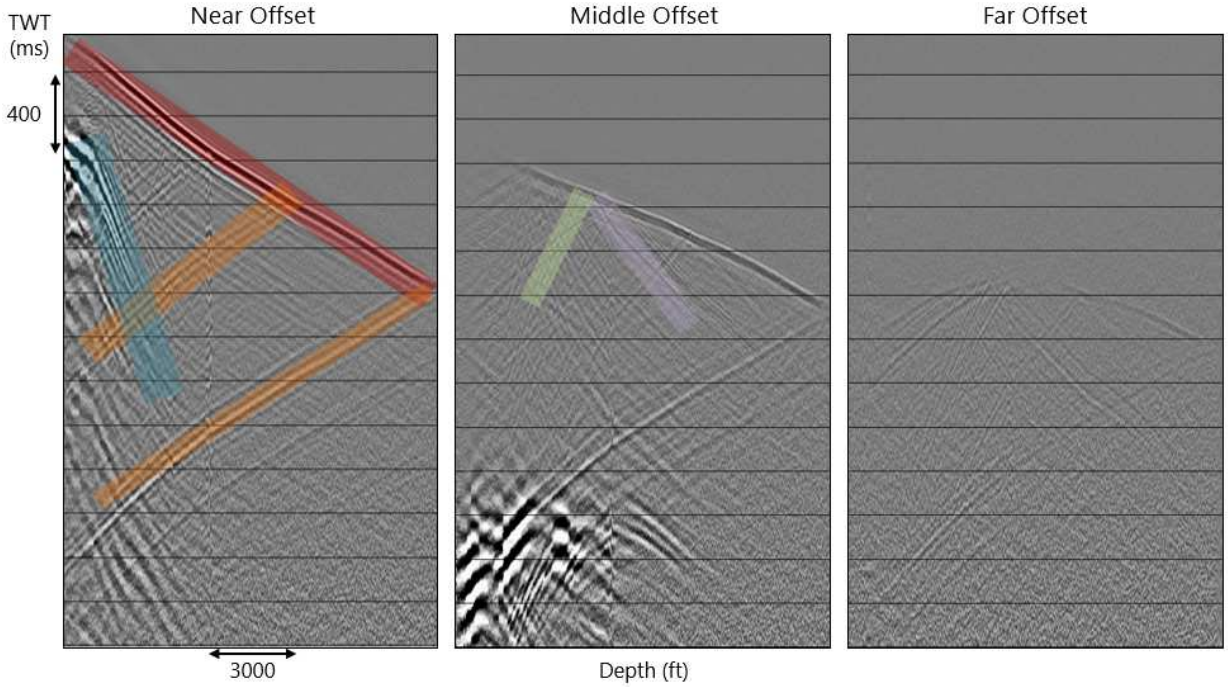

Figure 3.9 Shot gathers from near offset (1400 ft), middle offset (5000 ft), and far offset (9000 ft). Wavefields seen in this figure: downgoing P-wave (red), downgoing shear-wave (blue), upgoing P-wave (orange), downgoing PS (purple), upgoing PS (green).

the gathers substantially, specifically at the deeper receiver levels. The reflections start to swing up. An improved velocity model might be able to mitigate the swing, but a one dimensional model cannot account for lateral velocity changes. The trim statics attempts to flatten these reflections within the limited time window, but the swing is larger than the time window so trim statics flattens these reflections as two separate reflectors.

The PS reflections were flattened using both the P-wave and S-wave velocities in the ray tracing. The same velocities used for the geophone processing. Figure 3.12 compares the result of traveltime correction before and after a 2-D median filer. Near offsets have minimal shear-wave energy because the SV-wave particle motion is perpendicular to the fiber, and so is not recorded. Some shallow reflections are present, but nothing from the reservoir interval deeper in the section. The P-wave particle motion at these offsets is mostly vertical (parallel to the fiber) so the P-wave reflections dominate. Middle offsets start to record more PS reflections. These reflections are mostly flattened, but there is room for improvement for the

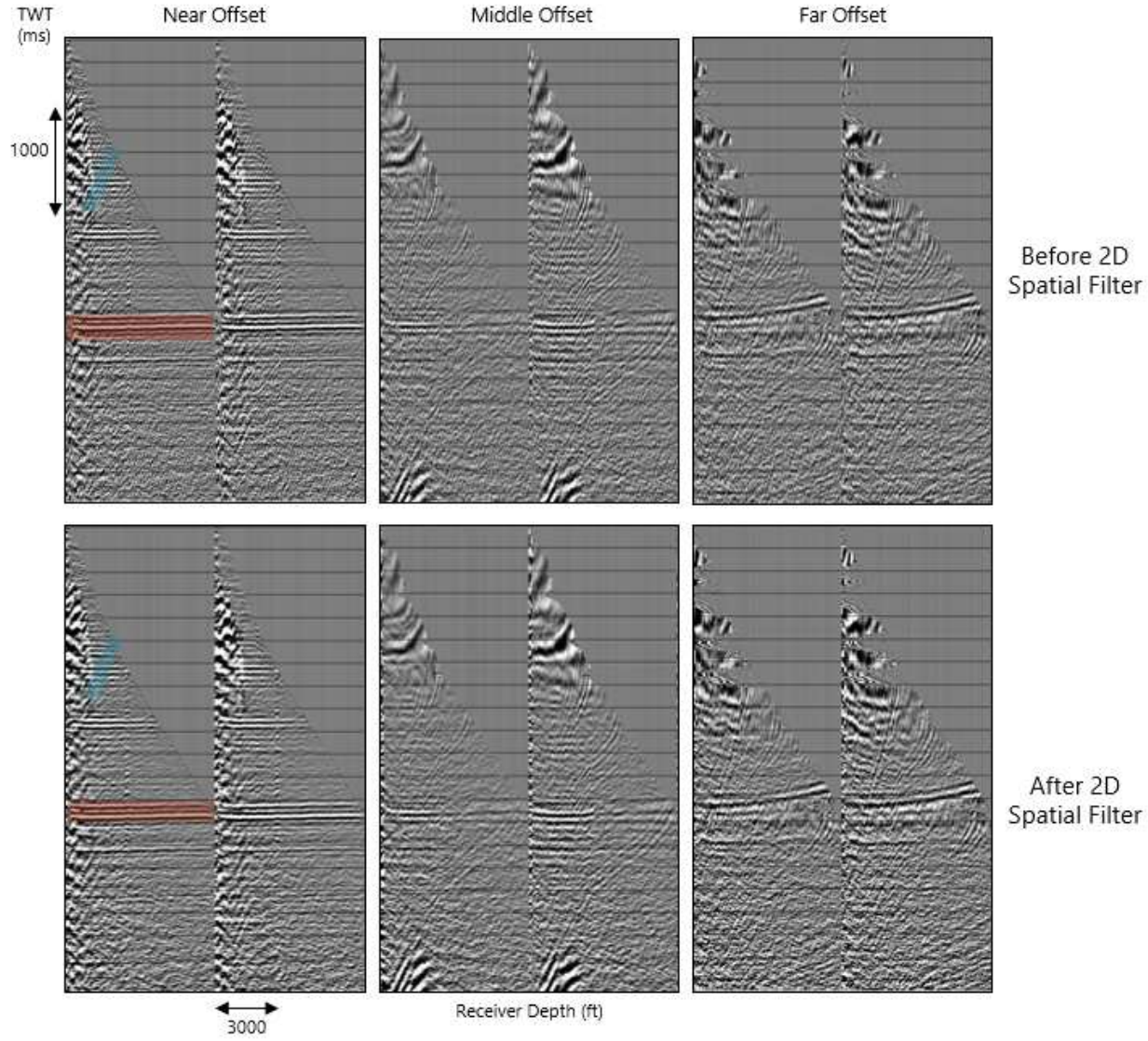

Figure 3.10 Shot gathers at different offsets (near = 1,400 ft, middle = 9,300 ft, far = 14,000 ft) displaying results of the traveltime correction for P-wave. Before and after application of a 2D median filter. P-wave reflections are highlighted in red, PS-waves are highlighted in blue.

velocity model. The reflections wobble in the middle of the section and start to dip down for the deeper reflections, indicating that the deeper velocity model is too slow and needs to be increased to flatten the deeper reflections. Specifically, the shear velocity model needs improvement to reduce these residual moveout errors. The shallow part of the image is also beginning to degrade and no coherent reflections are visible. This is removed by a mute

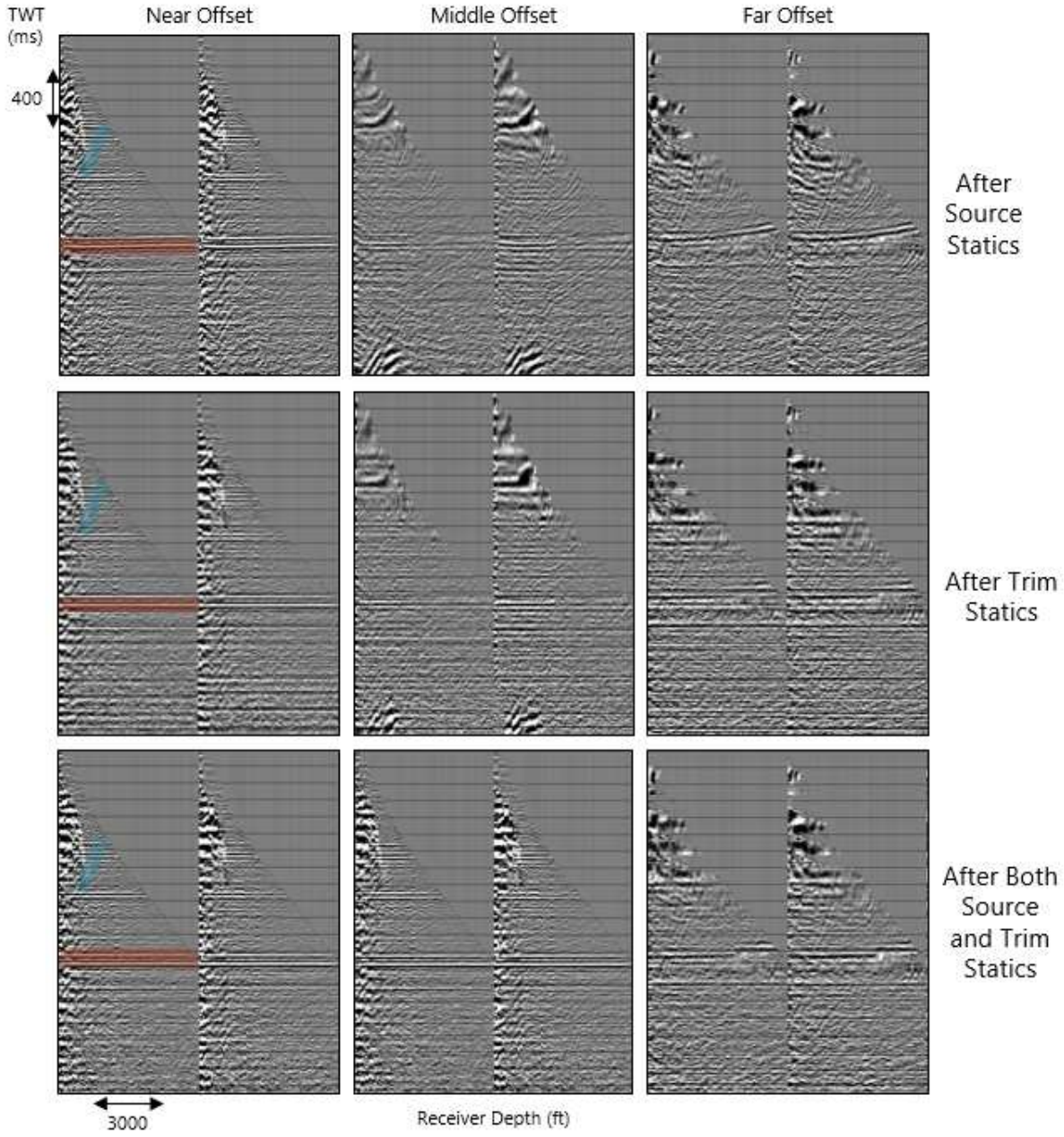

Figure 3.11 Comparison of source gathers after traveltime correction for P-wave with different static corrections applied. 2D median filter is applied to all. P-wave reflections are highlighted in red, PS-waves are highlighted in blue. Near offset = 1,400 ft, middle offset = 9,300 ft, far offset = 14,000 ft)

before mapping reflection point. The image at the further offsets starts to degrade further, but PS reflections are still present and the P-wave reflections are less prominent. For all offsets, the median filter helps smooth across the reflection and break up dipping energy.

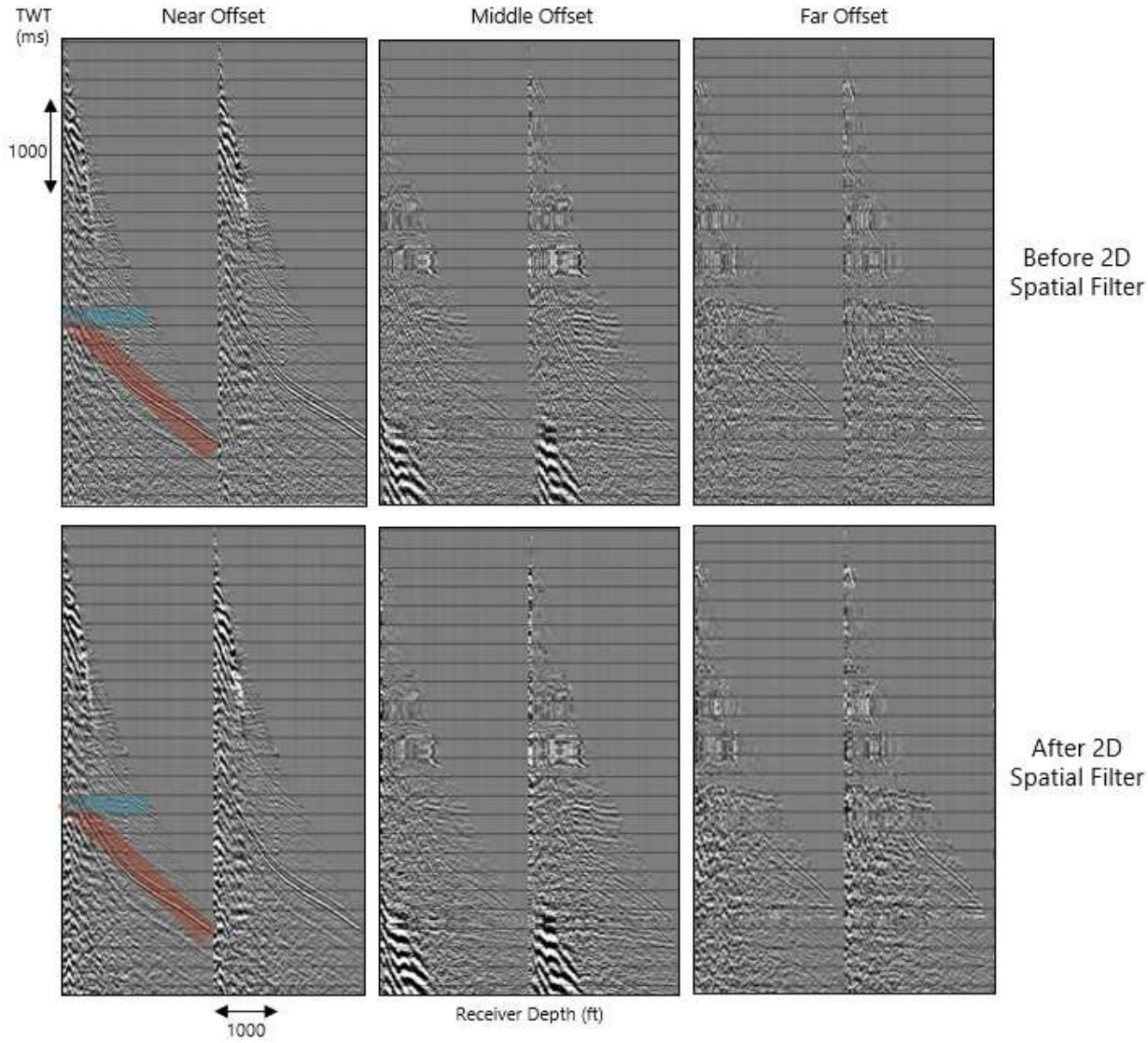

Figure 3.12 Source gathers at different offsets (near = 1,400 ft, middle = 9,300 ft, far = 14,000 ft) displaying results of the traveltime correction for P-SV wave. Comparison between no filters and 2D median filter. P-wave reflections are highlighted in red, PS-waves are highlighted in blue.

Figure 3.13 compares the same source and trim statics which were used previously on the P-wave reflections. Again, source statics does not make a noticeable difference because the sources only had small changes in elevation. The trim statics have a very large impact on these gathers, though. It does a good job at flattening the PS-wave reflections, but it also flattens all of the P-wave reflections as well. This creates a stair-step looking effect which

follows those reflectors highlighted in red. The noise on the inside of the gather (shallow receiver levels) is also flattened. At the near offsets, this noise occurs in the earlier times and the very shallow receivers. Even though the trim statics flattened all the energy, there is no obvious PS reflection, which further confirms the earlier statement that little to no PS-reflections are recorded at the near offsets. The noise in the middle offsets is concentrated near the bottom of the gather at the late times. and could potentially interfere with the signal around the reservoir so this could be problematic. The far offset gathers are noisier than the other offsets shown and much of this noise has been flattened in trim statics. The true PS-reflections are flattened, but they are hard to distinguish due to the noise.

One last step before mapping to common reflection points is to perform an inside mute (Figure 3.14). At all offsets, there is little energy from the PS-reflections seen on the shallow receivers. This is to be expected because reflections recorded at shallow receivers must have a large incident angle and these angles are too large to generate a PS reflection. At deeper reflectors, the angle of incidence is smaller and conducive for generating both P and PS reflections. Additionally, the particle motion of PS-waves at these shallow receivers has a large horizontal component. Due to this lack of signal at the shallow receiver depths, an inside mute is used so the noise is not mapped to reflection points with the reflections.

3.2.2 Common Reflection Point Mapping

The common reflection point mapping for the DAS data is performed the same way as with the geophones. The images look very different because of the larger receiver aperture provided by the DAS fiber. Overall, the common reflection points imaged are extended further away from the well as well as at shallower depths.

The first CRP image Figure 3.15 compares all of the static corrections which were compared previously in the flattened shot gathers for the P-wave reflections. As expected from the shot gathers there is not much difference between the no statics image and the source statics image. The big changes are from the trim statics. The major reflectors are flatter now but the linear features at the bottom of the image are most likely noise which was flattened.

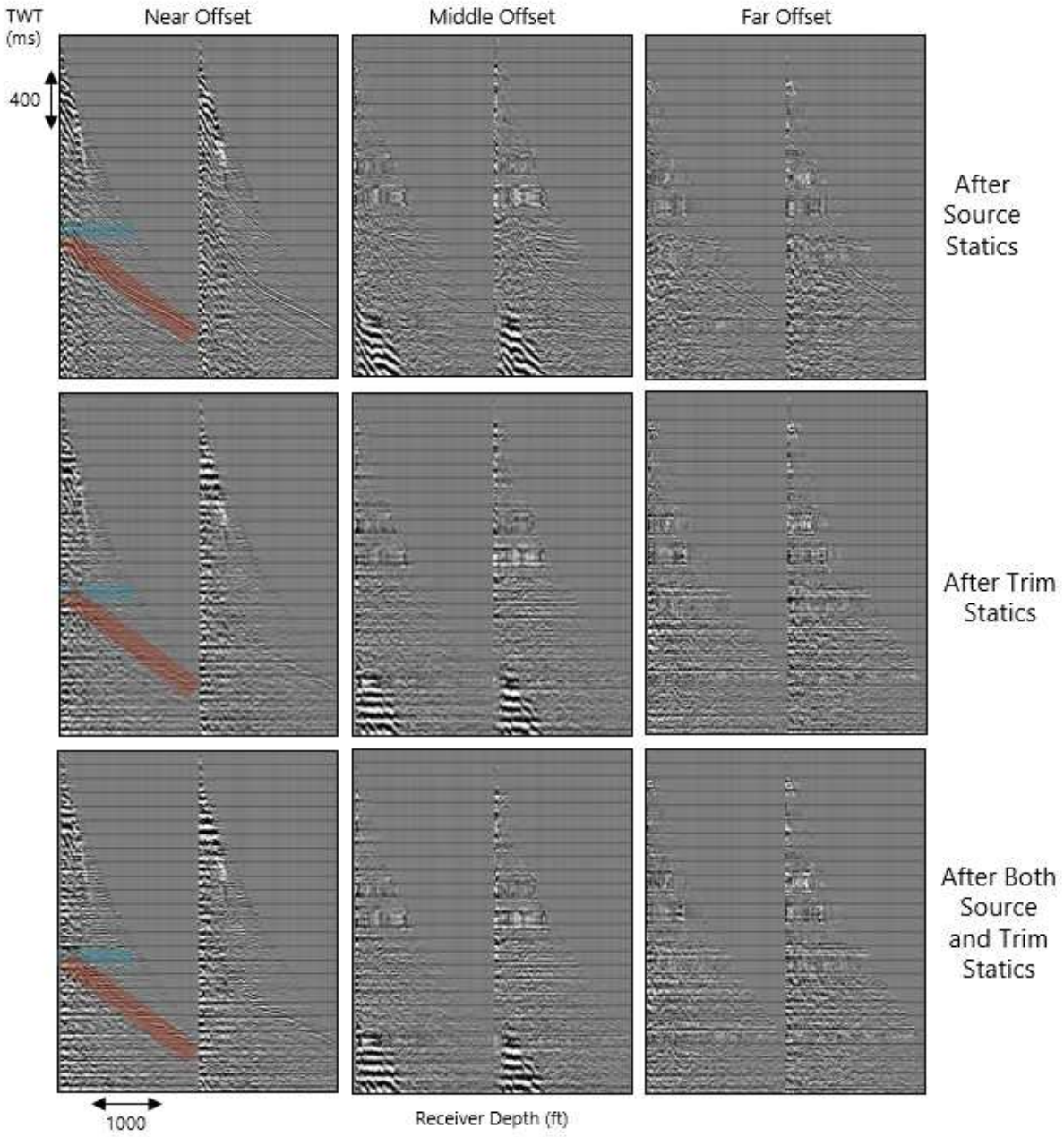

Figure 3.13 Comparison of source gathers after traveltime correction for P-SV wave with different static corrections applied. 2D median filter is applied to all. P-wave reflections are highlighted in red, PS-waves are highlighted in blue. Near offset = 1,400 ft, middle offset = 9,300 ft, far offset = 14,000 ft.

This deep section of the image should not be interpreted.

A prominent feature in all of these CRP images is the dipping and aliased energy which starts at the top left corner and continues to the bottom middle of the images. This could be

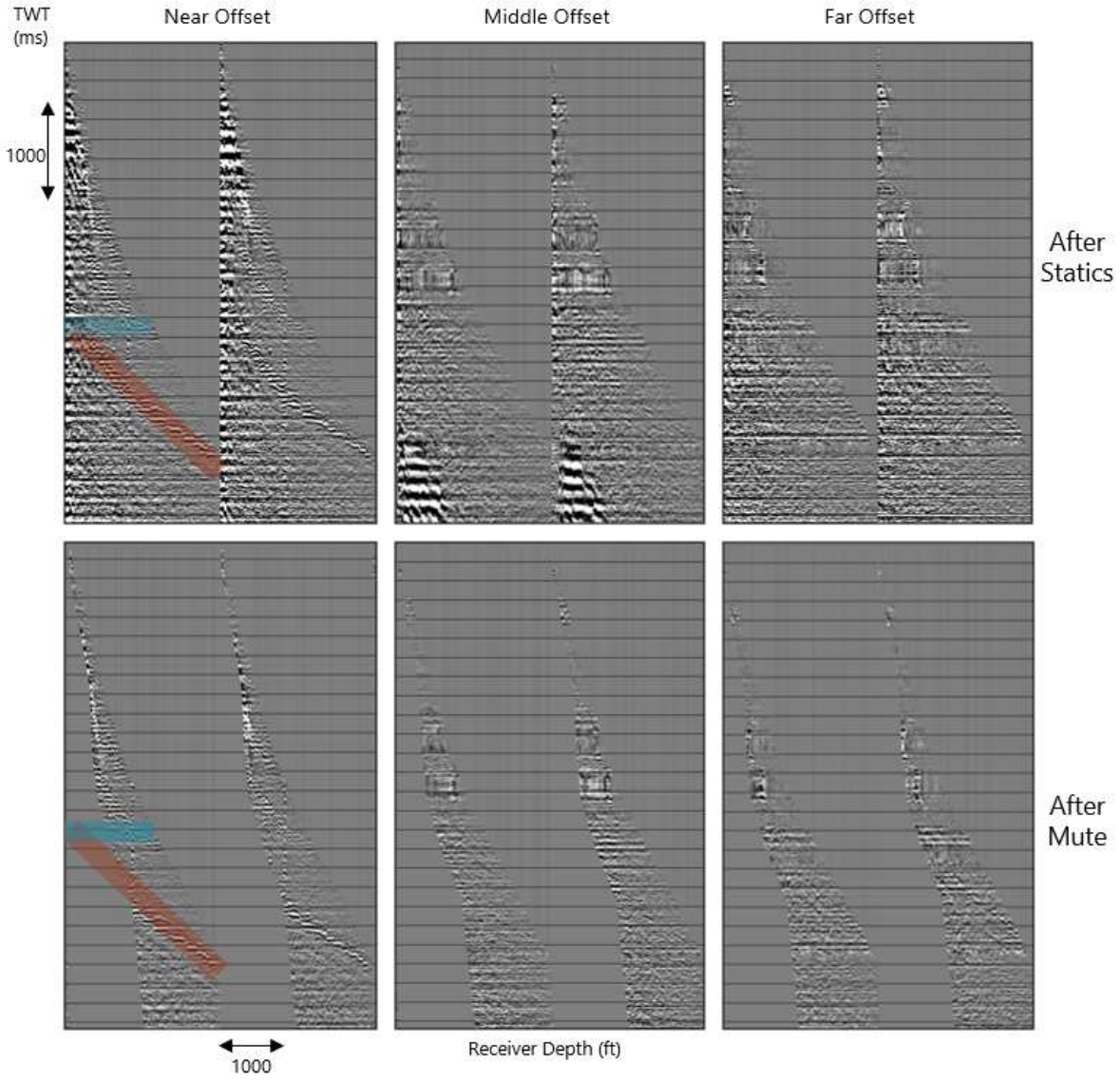

Figure 3.14 Source gathers after traveltime correction for SV-wave before and after inside mute is applied. P-wave reflections are highlighted in red, PS-waves are highlighted in blue. Near offset = 1,400 ft, middle offset = 9,300 ft, far offset = 14,000 ft.

the result of the noise present in the shallow receivers at the near and middle offsets in the source gathers. This noise occurs at the early times in the near offsets and at later times in the middle offsets. It is probably direct shear waves generated by the vertical force source. While this noise only interferes with the prominent reflections of interest in a limited area, it is distracting and attempts were made to remove it.

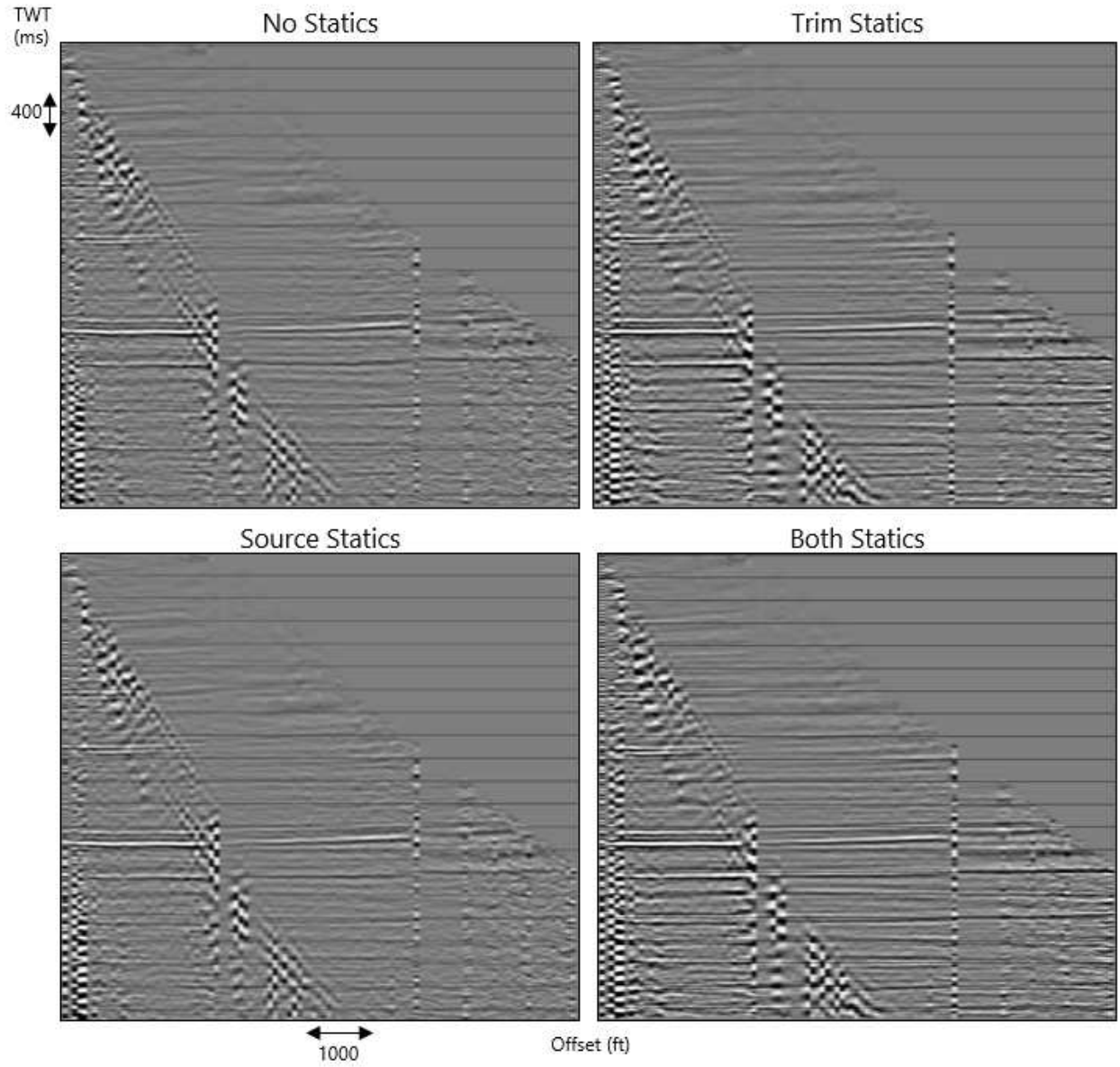

Figure 3.15 P-wave reflection point mapping. Comparison between different static corrections.

An FK filter was used to remove the noise because the dips of the noise and signal are different. The reflections are now flat (a wavenumber of zero) and the noise is dipping (a non-zero wavenumber). Figure 3.16 shows the filter which was used. The noise is mapped in the FK spectrum as a low frequency band across all wave numbers. The signal is mapped around the low wave numbers with varying frequencies. The filter is designed to remove all

the energy except for that which clustered around the low wave numbers. The results of this filter is shown in Figure 3.17. The three panels show the CRP gather without the FK filter and without statics (left), with the FK filter and without statics (center) and with both the FK filter and statics. Some of the dipping noise remains in the image, but it is greatly reduced. The filter also removed some of the random noise present in the image. The noise which remains could not be removed because it mapped to low wave numbers in FK-space. It could not be removed without also removing signal.

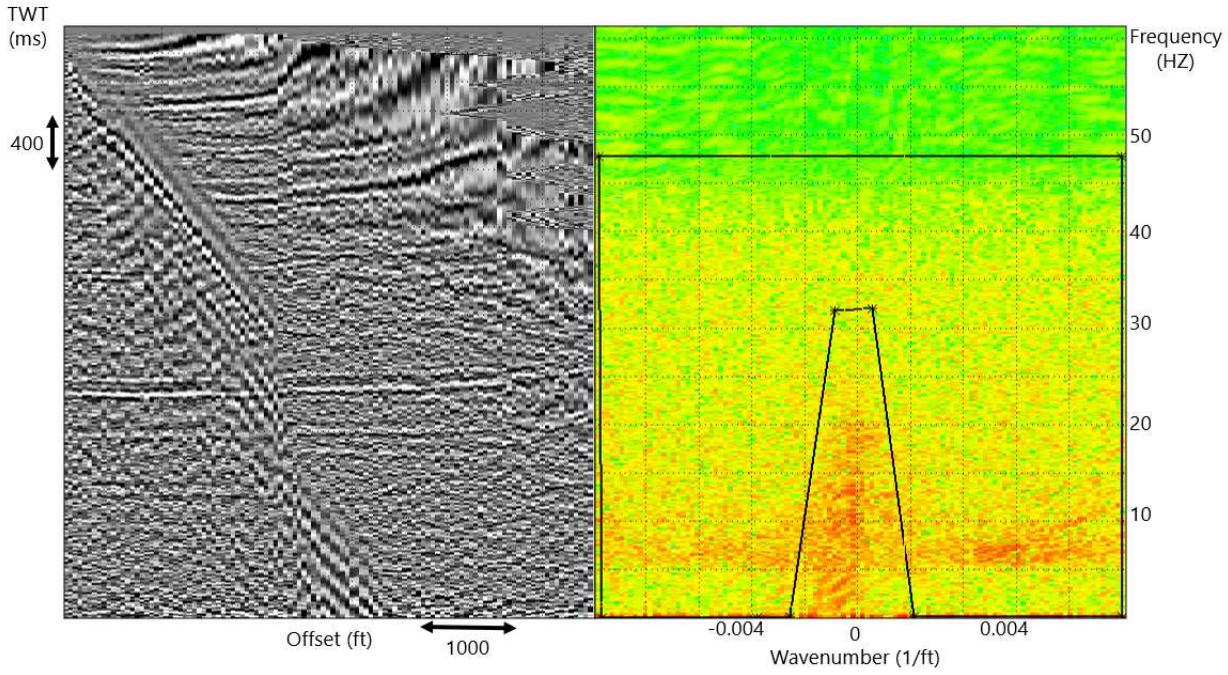

Figure 3.16 FK filter used to remove dipping noise. The passed data is within the tall trapezoid.centered around a wavenumber of 0.

Different bin sizes were tested to determine which one offered the best image. Same as with the geophone survey, bin sizes of 82.5 ft and 165 ft were tested because they correspond to the surface seismic bin size or double the bin size (Figure 3.18). This makes it easier to eventually tie to the surface seismic data.

The larger bin size incorporates more traces into each bin so the effect is a smoother image. In the case of this survey, there are not any large gaps in common reflection points

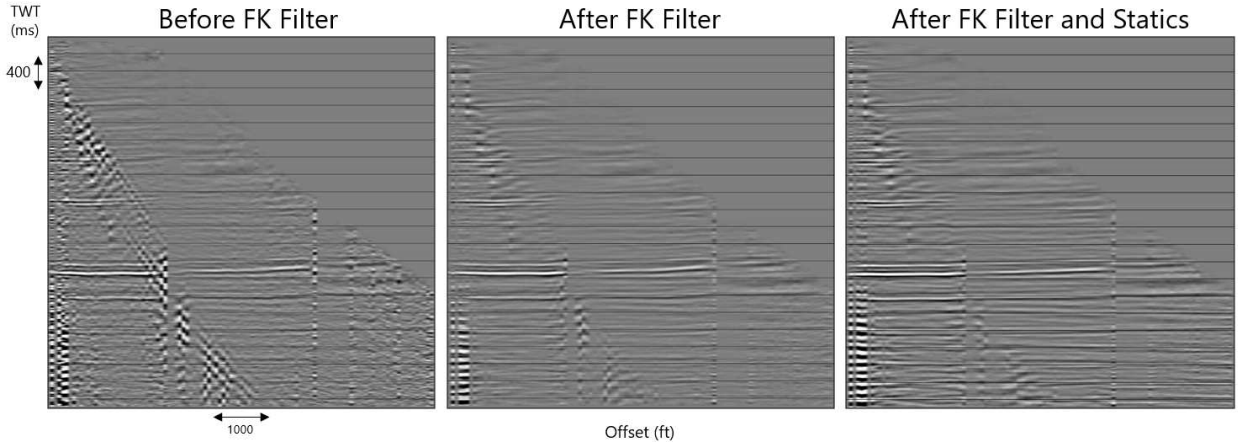

Figure 3.17 P-wave reflection point mapping, offset from wellhead. Comparisons before and after FK filter with and without static corrections.

so the 82.5 ft bin size works well. The larger bin size in this case smooths across a lot of detail that could be of interest.

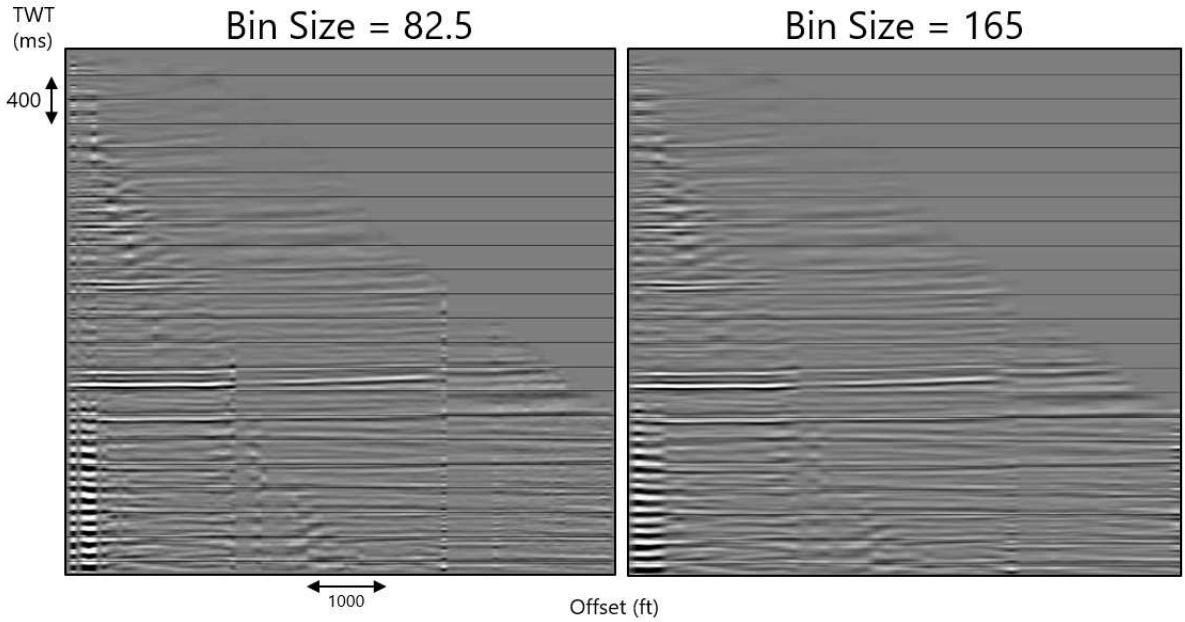

Figure 3.18 P-wave reflection point mapping. Comparisons between bin sizes.

The common reflection points were then mapped for the PS reflections. Figure 3.19 has four panels comparing results from using the inside mute discussed previously (left column vs. right column) and using the static corrections or not (top row vs. bottom row). The first

observation is that the images without the inside mute applied are very noisy. Arguably, no reflections can be observed through this noise. The images with the mute applied are significantly improved. The image without the static corrections has dipping noise caused by the P-wave reflections. This makes it difficult to distinguish between the noise and the flattened PS reflections. The static corrections appear to improve the image, however, some of the reflections may be flattened noise. Or, at the far offsets, a reflection which was flattened into two separate reflections by trim statics. It is useful to view both these CRP gathers together since neither is without its limitations.

Another important observation for the PS reflection mapping is that the lateral extent is much smaller than the P-wave reflection point mapping. The PS-waves reflect at a smaller angle than P-waves, so the reflection point is closer to the well, and the upgoing SV particle motion is perpendicular to the vertical fiber.

Bin sizes were again tested for the PS CRP gathers as well (Figure 3.20). The larger bin size has a dramatic smoothing effect for this gather. The dipping P-wave reflections which are still moderately visible are canceled and are now indistinguishable from the PS reflections.

Overall, in this chapter, the DAS fiber records both P and S-wave energy well and the larger receiver aperture is a huge advantage over traditional geophones. DAS can be processed the same as geophone data after the initial vertical and horizontal noise filtering. Converting DAS strain rate to geophone particle motion smears across noise and reduces the frequency content but corrects for the phase and polarity of the reflections. The walkaway results are promising and it is possible to process for PS-wave reflections even with the single component. With the large receiver aperture, the P-wave walkaway survey, especially, is able to image much larger offsets away from the well.

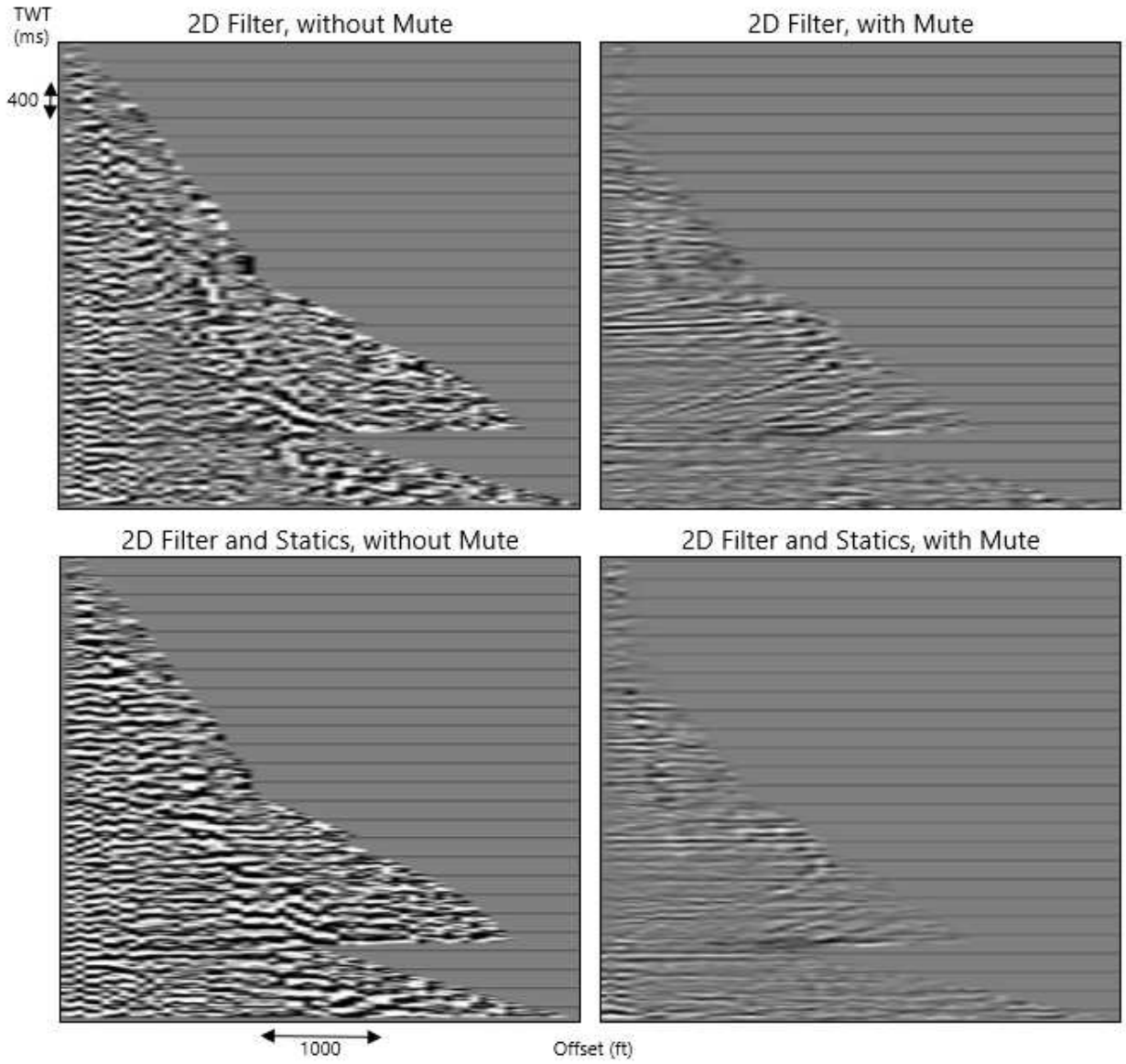

Figure 3.19 SV-wave reflection point mapping. Comparisons with and without inside mute, with and without static corrections.

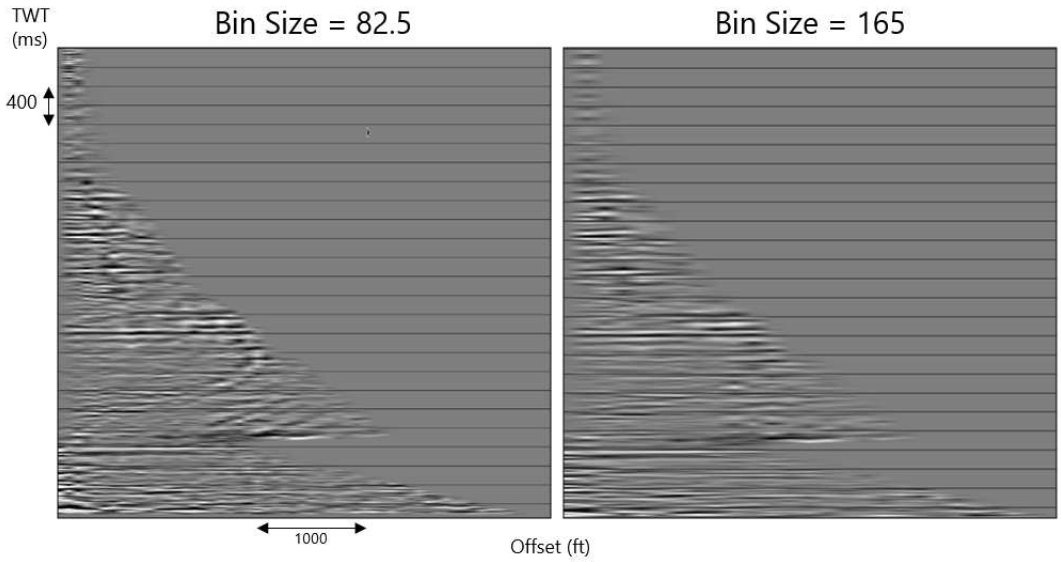

Figure 3.20 SV-wave reflection point mapping. Comparisons between bin sizes.

CHAPTER 4

3D DAS VSP

This chapter discusses the processing of the 3D DAS VSP survey. The initial processing is the same as in the previous chapters and ray tracing with the same velocity model is used. This chapter mainly discusses the final cross sections from the CRP stacked volume and additional processing steps to improve the final image. Two different migration results (RTM and least-squares RTM) are also compared to the CRP stacking along four different azimuths. The migrations perform well but are limited by the inconsistent shot spacing and lack of near offset shots.

4.1 Benefits and Goals of 3D DAS VSP

A 3D VSP survey can provide a detailed image of the formations immediately surrounding the well. Azimuthal information can also be gained by this type of survey. Ideally, there would be both a baseline and monitor survey to track the time-lapse changes. In this study we only have one survey. Even so, valuable information concerning the velocity model, azimuthal variations, and practicality of DAS fiber for this type of survey can be gained.

The source locations for this survey were not specifically designed for a 3D VSP. Instead, the sources are the same as the monitor surface seismic survey and the DAS fiber was recording during the surface seismic acquisition. The map of source locations can be seen in Figure 4.1 and the DAS fiber is located in well A indicated by the green star. The geometry leads to gaps in the common reflection points. Examples of this can be seen later in this chapter.

One goal from this 3D VSP is to image the channel which cuts across the study area. Figure 4.2 illustrates where this channel is located. The yellow line represents the boundary or where it is cutting into older formations and increasing in thickness. Channel sediments are thinnest towards the north east and gradually thicken while cutting into underlying

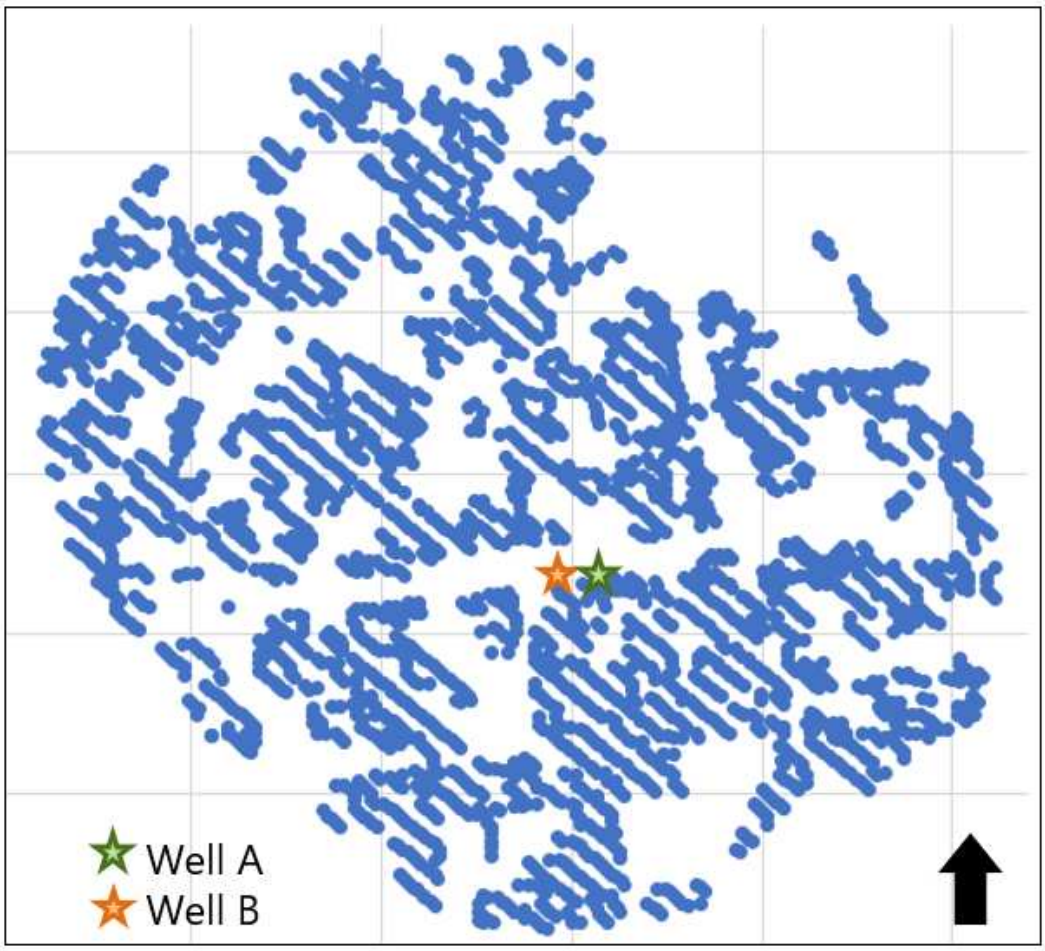

Figure 4.1 Map view of the 3D DAS VSP survey. Blue dots are the source locations. Well A contains the DAS fiber.

formations towards the south west. The other boundary of the channel is not seen in this survey. This feature will be visible when the VSP is tied to the surface seismic. The channel is likely the cause of the largest lateral velocity variations across the survey area. The velocity model used for processing this dataset is the same as previously used in the walkaway surveys. A one dimensional velocity model cannot possibly handle the variations which are expected but it will be an interesting study to see how well it holds up.

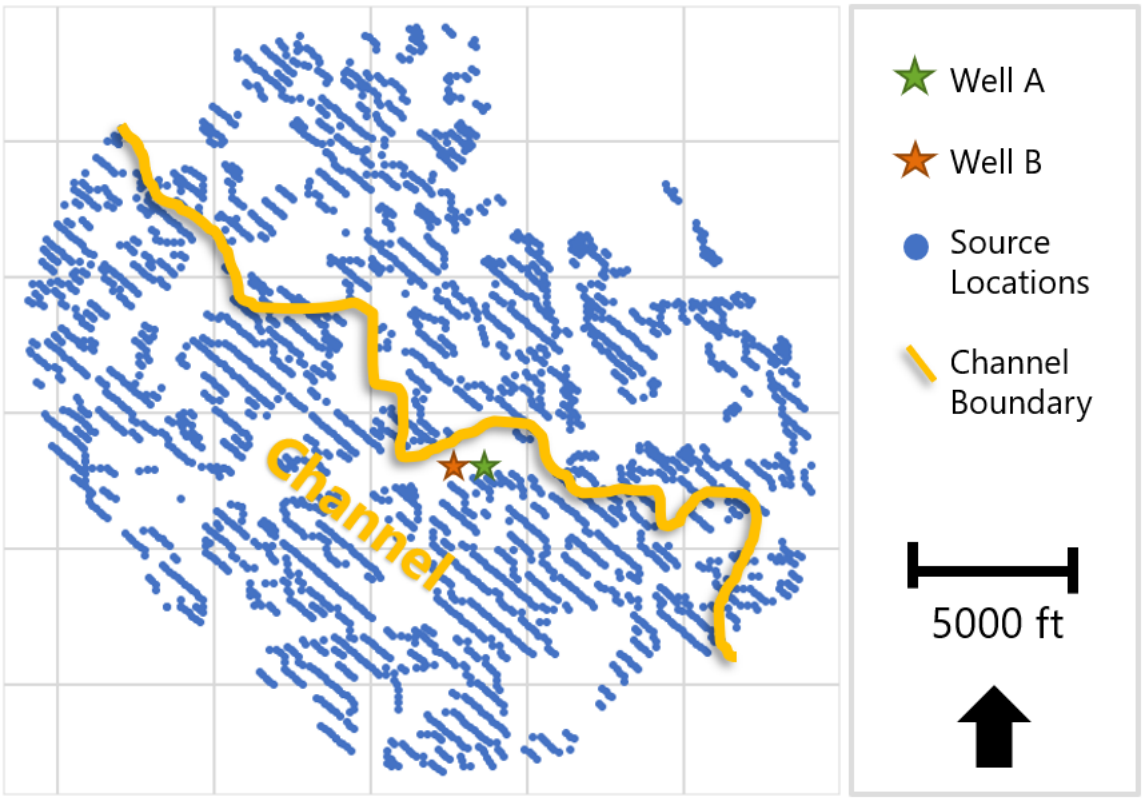

Figure 4.2 Location of edge of channel relative to 3D source locations. Channel increases in thickness towards the southwest.

4.2 Ray Tracing

The pre-processing for the 3D VSP is the same as the other DAS VSP datasets. The horizontal interrogator noise and vertical noise is removed first. F-K filtering is used to separate the wavefields and spiking deconvolution, followed by a bandpass filter, is used to whiten the frequency spectrum. The same method of ray tracing is applied to correct for traveltimes and map common reflection points. Further processing such as static corrections, muting, and TFD filtering are experimented with before and after CRP binning. This section details the results of the ray tracing and various post-processing applications.

After the reflections are traveltime corrected for P-wave reflections, source and trim statics are applied. The top row of Figure 4.3 shows the shot gathers at three different offsets along a single azimuth line after source statics has been applied. As with the previous

datasets, source statics does not significantly improve the gathers so the gather before source statics is not included. The P-waves are well flattened at all offsets and at the middle and far offsets the PS converted waves are again apparent. The trim statics further flattens the main reflections but at the late times the noise is also flattened, creating unreal coherent reflections. Fortunately, most of this is below the area of interest. The last row in this figure illustrates the top mute which was applied to remove the NMO stretch that becomes more apparent at further offsets. Little to no mute is needed for near offsets, but as the offset increases, the top part of the gathers become more stretched and need to be muted to improve the CRP binning.

Figure 4.4 illustrates the CRP gathers with and without the mutes just discussed. In these gathers only source statics has been applied. The edges of the cross-sections at early times are completely incoherent. These shallow receivers are removed for the migrations discussed later in this chapter. Towards the center, some coherent reflections are seen. The near offset sources, which do not need to be muted, contribute to this coherent signal. The bottom row demonstrates the improvement of the cross-sections once muting is applied. Applying the mute greatly improves the image and the edges of the mapped reflections are clearly seen. Similar to the walk-away surveys, the aperture of reflection points increases with increasing two-way time.

Next, the muted CRP stacks are improved further. The results of trim statics is shown in the top row of Figure 4.5. The main reflections are flattened and appear smoother than the cross-section without the static correction. Automatic gain control (AGC) is then applied to increase the shallow reflection amplitudes. There are a few traces throughout the volume that have anomalous high amplitudes, so a TFD filter is applied to remove those amplitudes. The final result is shown in the bottom row of the image. The main reflections look properly traveltime corrected and CRP mapped and most of the noise has been diminished.

Different bin sizes were tested to determine which provided the best image. The bin sizes are the same as those tested for the walkaway surveys to be consistent across VSP surveys

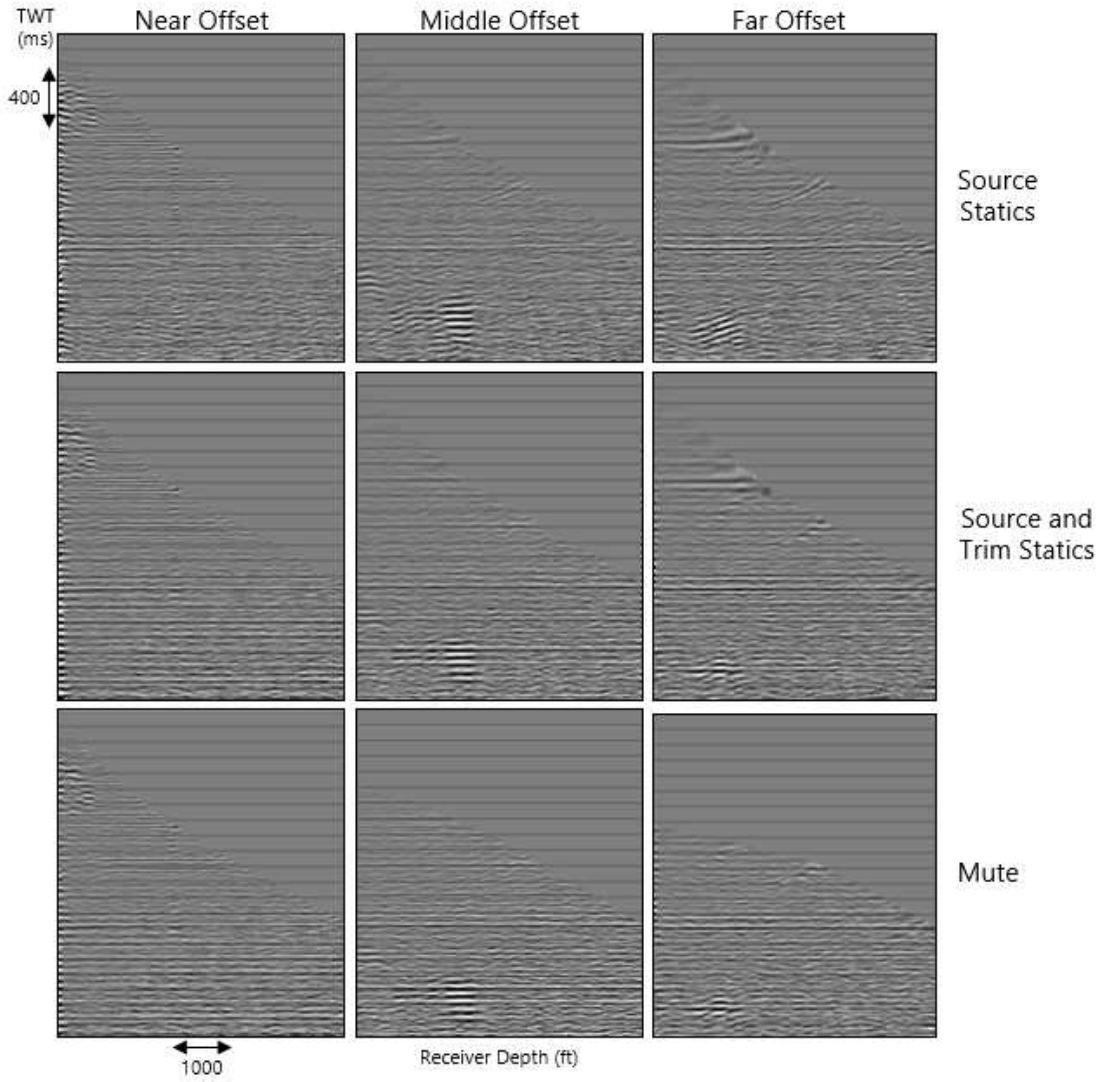

Figure 4.3 Shot gathers from three different offsets along the same azimuth. Reflections are flattened, source and trim static corrections are compared. A top mute is applied to remove the effects of NMO stretch.

and the surface seismic. The surface seismic bin size is 82.5 so the bin sizes tested are 82.5 ft and 165 ft (Figure 4.6). The larger bin size looks better in this case, it removes some of the incoherent noise seen in the smaller bin size cross sections. The irregularity of the sources in this survey leads to irregularity of reflection points that are mapped. The larger bins stack more traces together to create a stronger signal and mitigate the effects of missing reflection points.

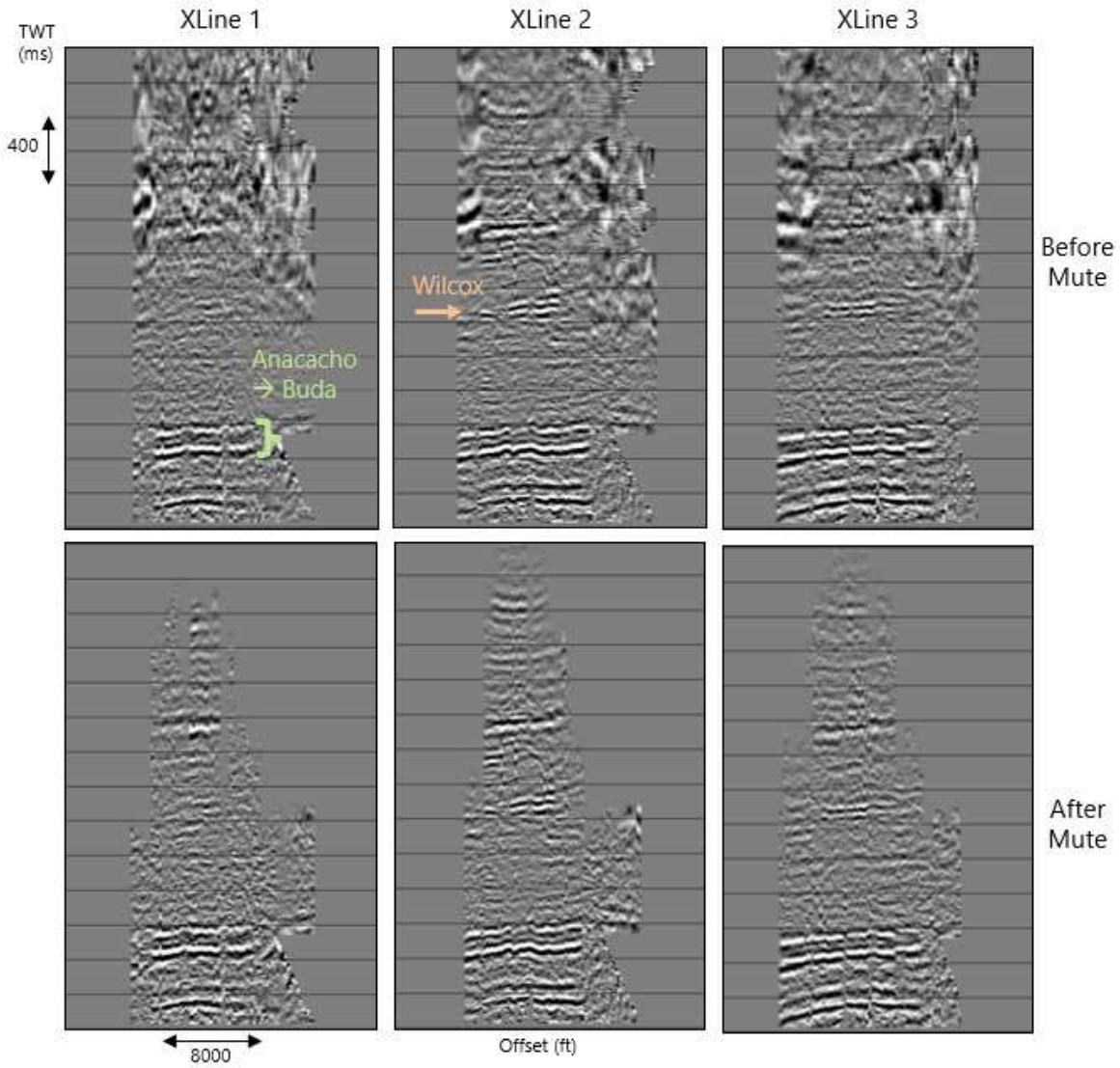

Figure 4.4 Cross-sections from the CRP mapped 3D volume before and after a top mute is applied to shot gathers. The cross-sections are from crosslines centered around the well and about $1,500$ ft apart.

After the P-wave reflections are mapped, the PS-wave reflections are mapped using the same methods. Source and trim statics are are tested in the first two rows of Figure 4.7. The PS reflections are weak compared to the P-wave reflections. Like in the walkaway survey PS energy is recorded best at the middle offsets. The shallow receivers are largely recording the P-wave and noise and no PS energy is recorded. At the far offsets, the ray tracing starts to break down again and the early times must be muted. The trim statics in this case

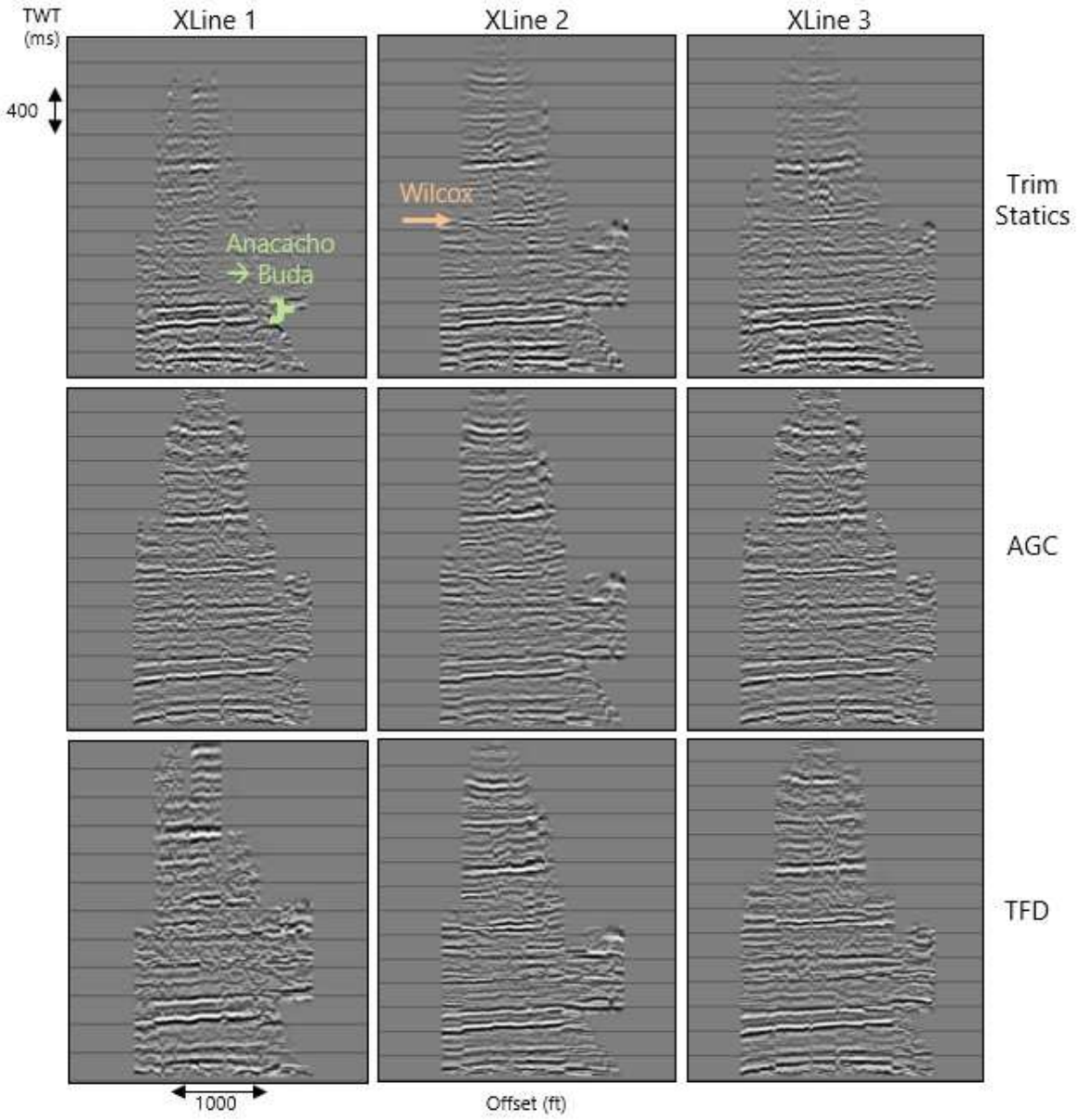

Figure 4.5 Cross-sections from the CRP mapped 3D volume after trim statics, AGC, and TFD filters were applied successively. The cross-sections are from cross-lines centered around the well and about $1,500$ft apart.

completely overpower the signal. It is extremely difficult to separate the flattened PS signal from the flattened noise. The last row in this image shows the mutes that are applied before CRP stacking. A top mute is applied for the same reason as with the P-wave processing, there is NMO stretching that needs to be removed before stacking. The same inside mute

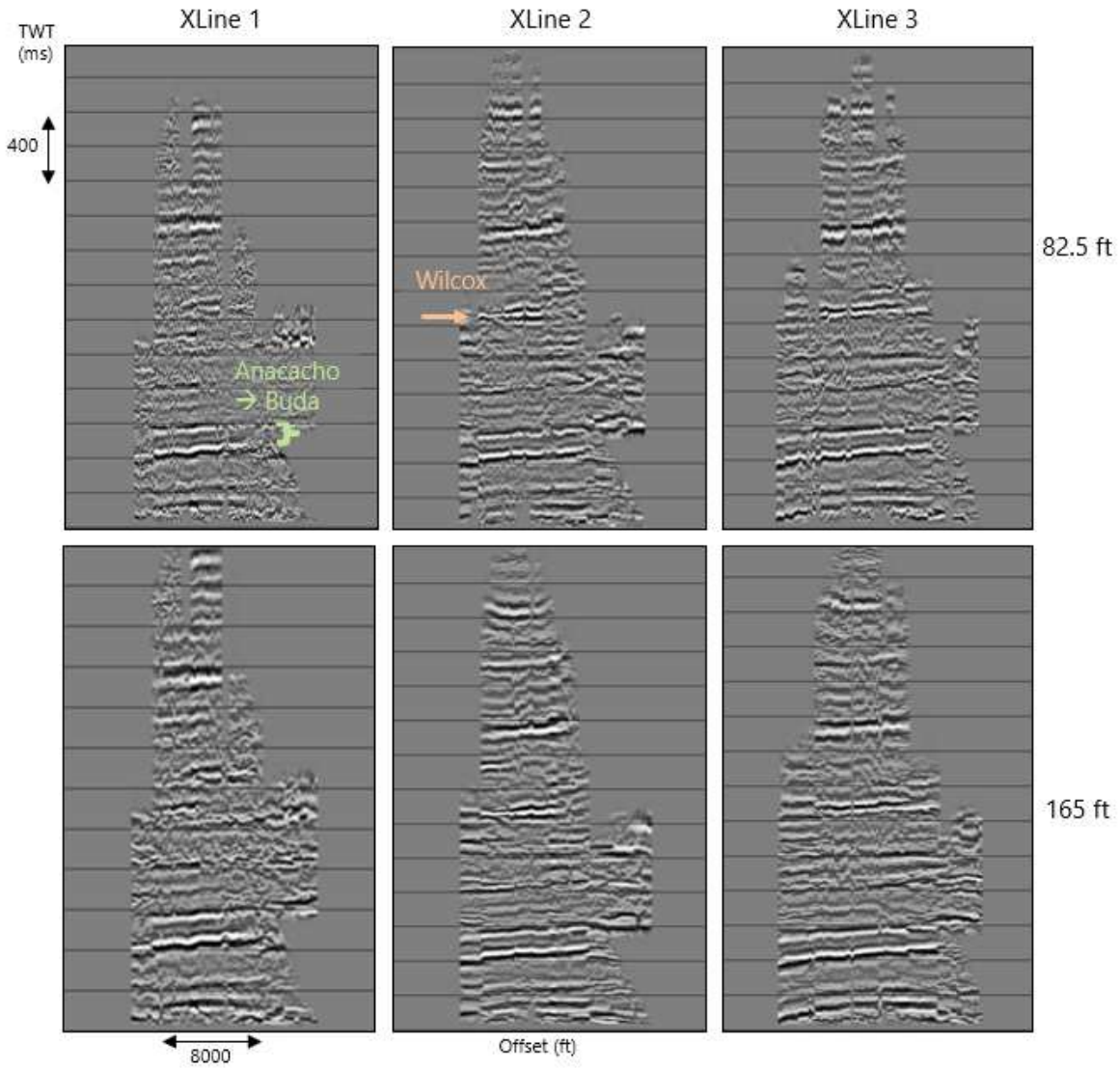

Figure 4.6 Cross-sections from the 3D volume testing two different bin sizes.

is used as in the walkaway processing in order to remove the portions of the data which do not record any PS signal. With the mutes applied, it is clear how little signal the far offsets contribute to the CRP binning process. Much of the gather has been muted and even then, the signal which is left does not contain much flattened PS reflections.

The next step in the ray tracing process is CRP mapping. The same statics and mutes just discused are tested with CRP mapping and shown in three different cross sections to illustrate their effectiveness (Figure 4.8). The first row depicts the cross sections with only

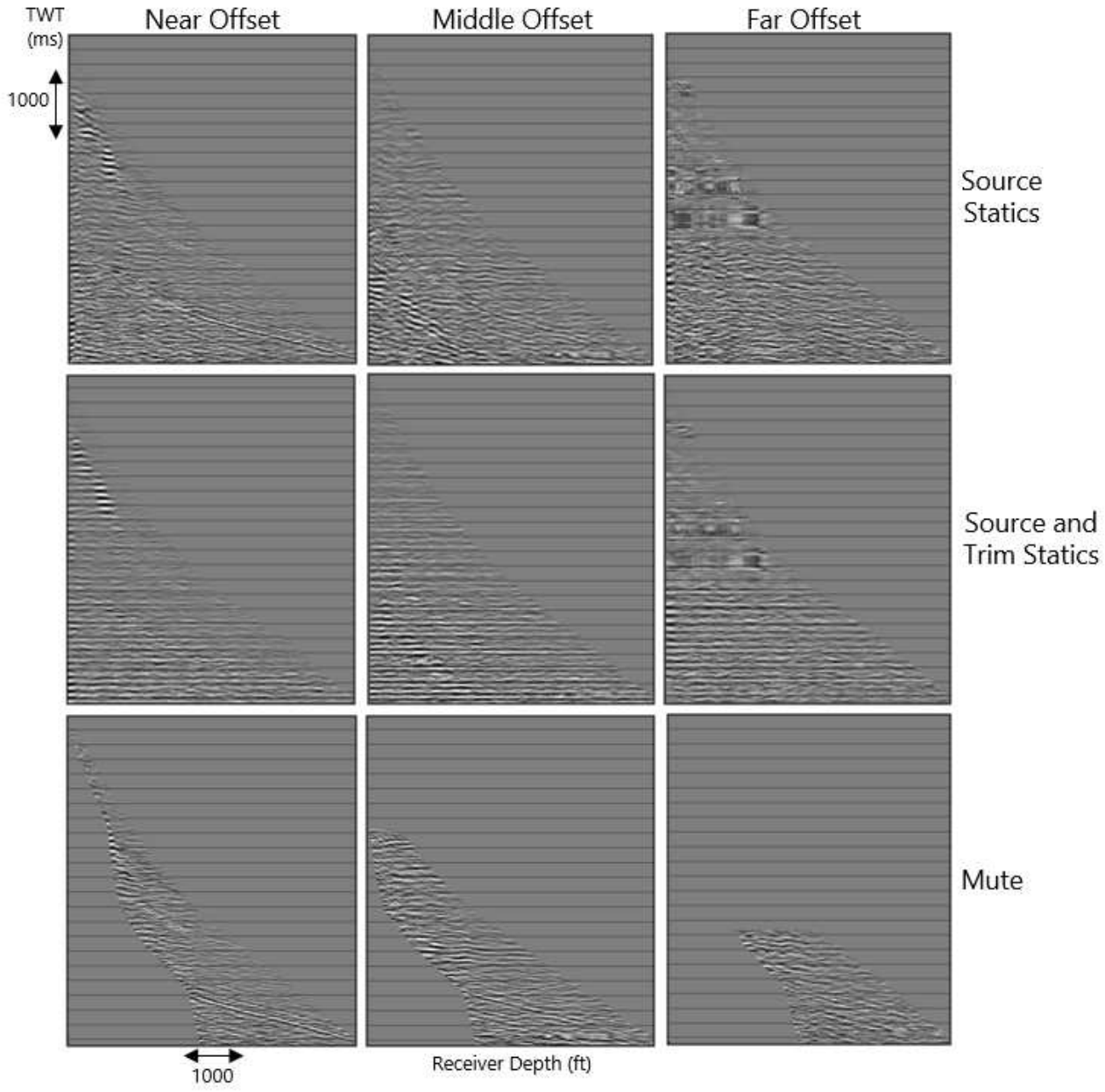

Figure 4.7 Source gathers after the reflections have been flattened using PS-wave traveltimes. Source and trim statics are tested and a top and inside mute is applied.

source statics applied. It is difficult to see any signal except for directly in the middle of each gather. The cross sections in the middle row had source statics and the mutes applied. This significantly improves the image. The noise at the shallow receivers was completely overpowering much of the signal. The reflections at the bottom of the image are relatively

flat, while the reflections in the middle swing up at the edges. The bottom row shows the results if both source and trim statics are applied with the mute. The image is completely degraded by the trim statics and so will not be used further in the PS ray tracing process.

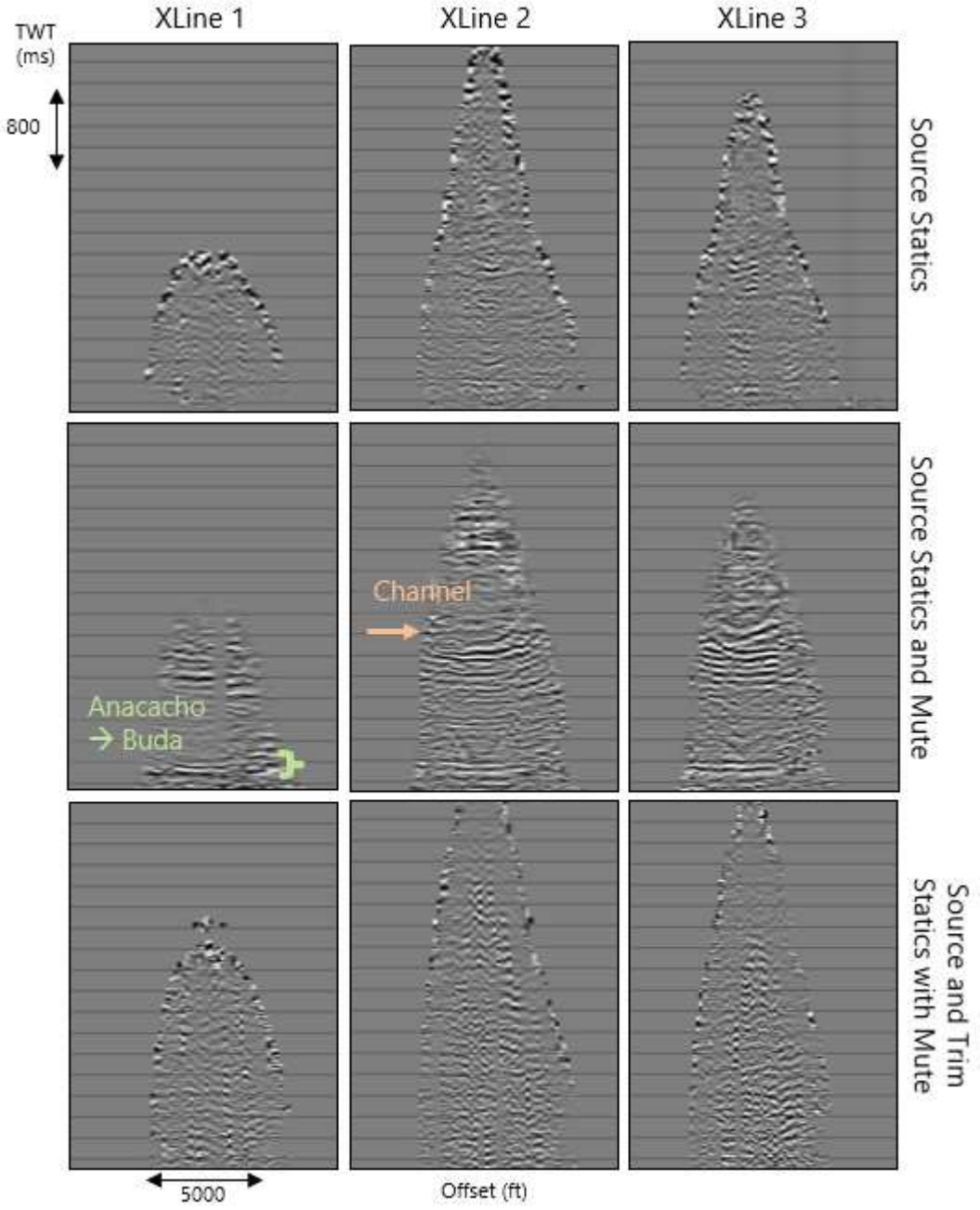

Figure 4.8 CRP mapping of PS reflections. Source and trim statics are tested as well as the mutes.

As with the P-wave CRP stacking, different post-processing filters are tested. First ACG is applied to equalize the amplitudes across the sections (Figure 4.9). The reflections in the middle of the section are higher amplitude than the deeper reflections and AGC corrects for this so the amplitudes are roughly equal. Then, TFD is applied. This filter is not needed in this dataset as much as with the P-waves. However, there are a few noise spikes throughout this volume that are removed with the filter.

Bin sizes are again tested for the PS-wave CRP mapping. The PS reflection points are more limited than the P-waves so the larger bin size greatly increases the quality of the image and closes some reflection point gaps that appear with the smaller bin size (Figure 4.10).

4.2.1 Tying to Seismic

The P-wave CRP stack is then tied to the surface seismic. The result is shown in Figure Figure 4.11. Prior to comparing to seismic a 2D median filter is applied to improve the image for comparison.

The orange arrows point to two prominent reflectors that match up very well. The peaks and troughs align in time and the amplitudes are comparable. These reflectors indicate the top and bottom of the channel which runs through this study area and contributes to large lateral velocity variations. The reflections in the reservoir interval below do not match up as well, indicated by the yellow arrows. It is possible that the velocity model could be updated to improve the tie at this depth. For ray tracing, the known velocities from the zero-offset VSP are extrapolated downward to extend beneath the well and it appears that these velocities are too fast. In an attempt to correct this, the deep velocities were slowed by 5% and 10%. This did not improve the tie. The most likely cause of the mis-tie is a combination of phase and velocity. The DAS 3D CRP stack has not been corrected to a geophone response, so it is understandable, and even expected, that the phases do not align properly.

The PS-wave CRP stack is also compared to the PS surface seismic data, however, this result does not tie as well to the surface seismic as the P-wave CRP stack. Overall, the main

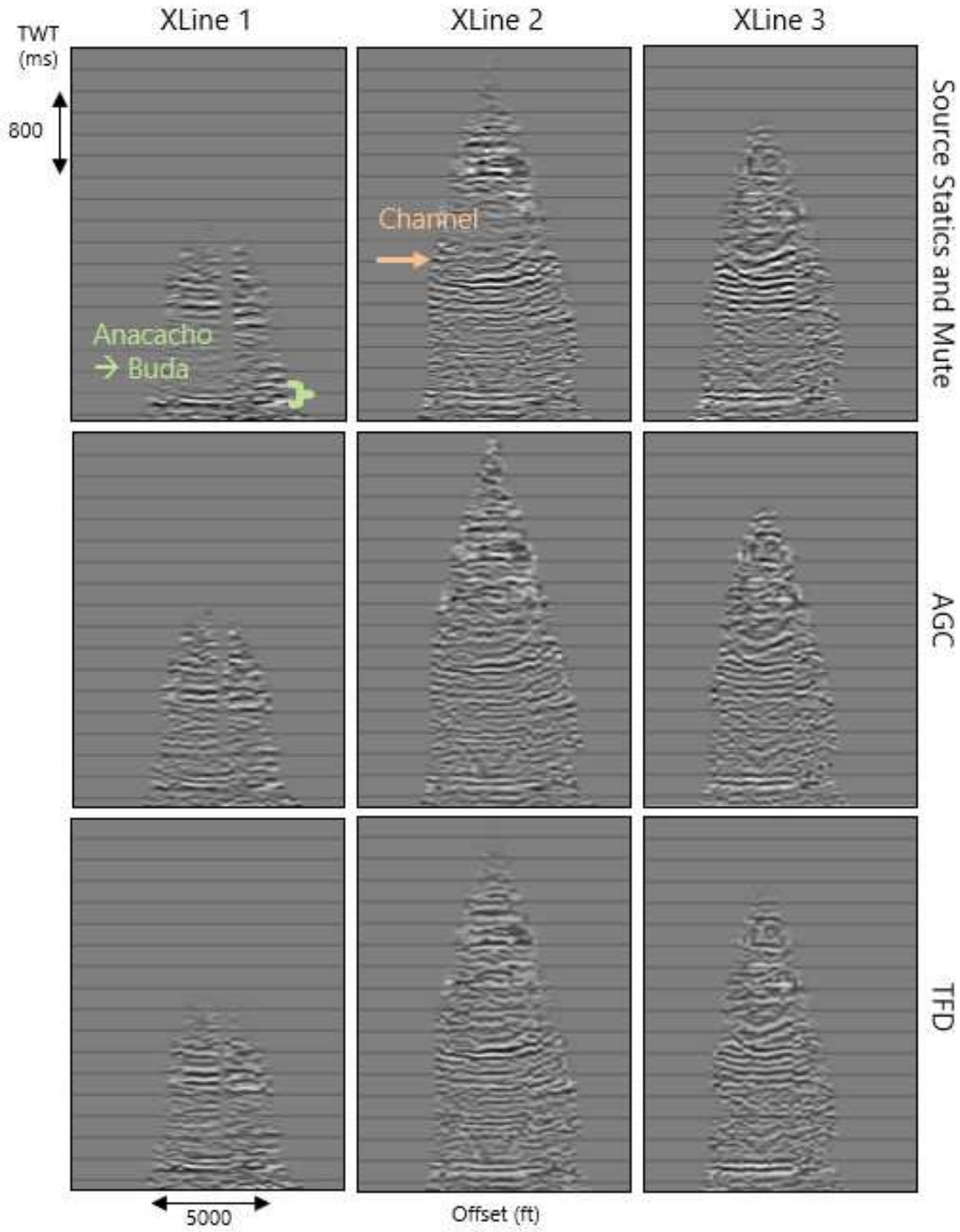

Figure 4.9 CRP mapping of PS reflections. AGC and TFD filters are tested to improve the final image.

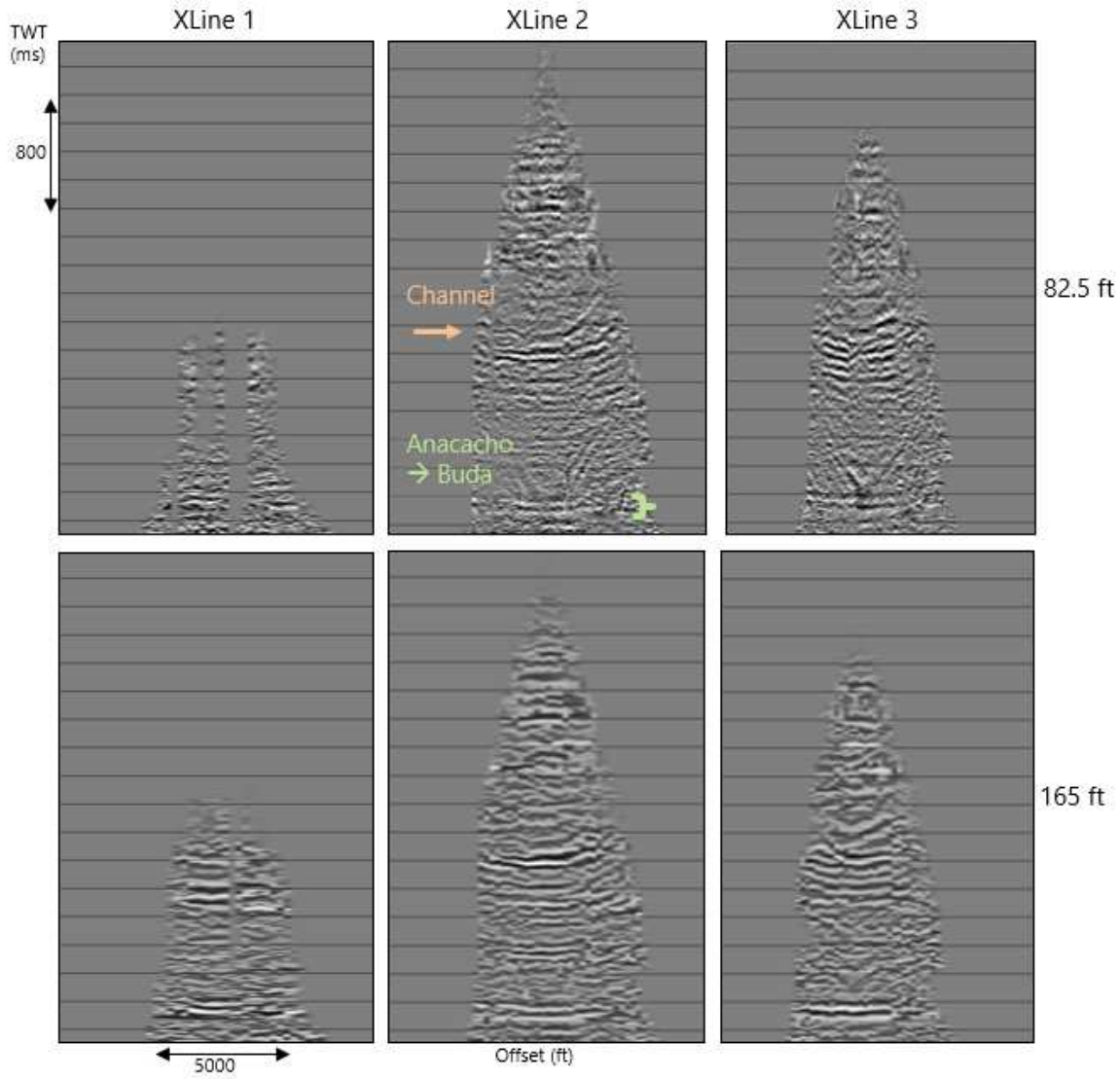

Figure 4.10 CRP mapping of PS reflections. Bin sizes of 82.5ft and 165ft are tested.

reflections are being mapped (as seen in the cross sections), but they are not aligning properly. This means that the P-wave model is most likely correct and the shear-wave velocity model needs improvement. In order to improve the velocity model, PP-PS registration with the surface seismic is performed to update the Vp/Vs ratios used to calculate the shear-wave velocities. This is discussed further in Appendix A.

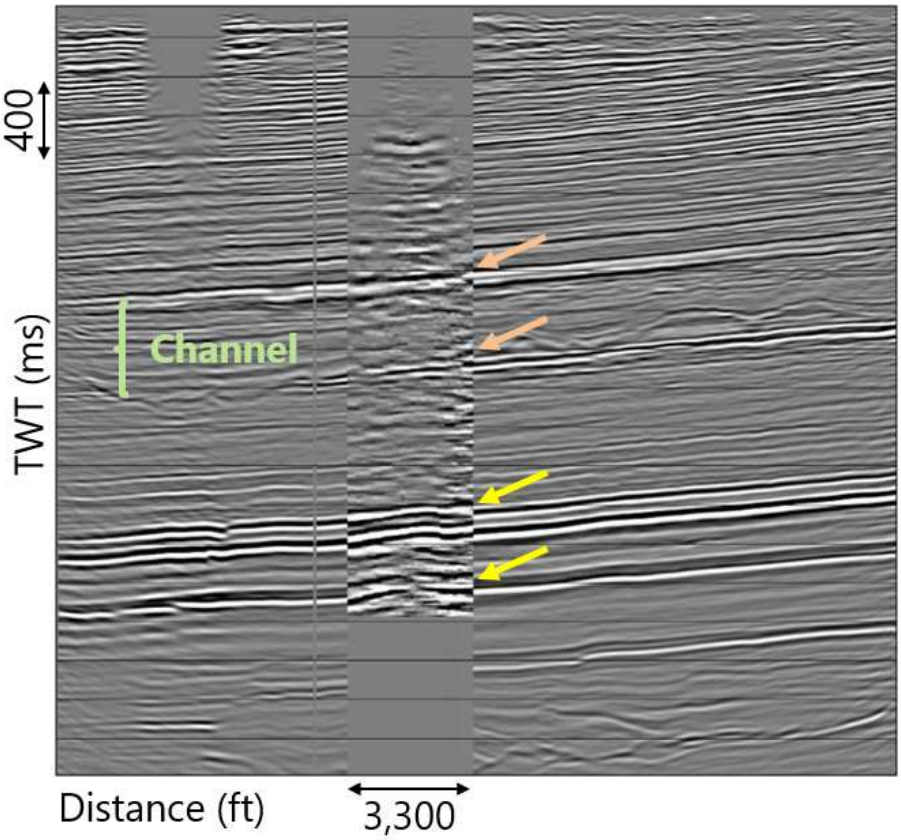

Figure 4.11 Crossline through Well A from the 3D VSP stack tied into surface seismic. A channel cutting across the section in indicated by the green bracket, orange arrows point to prominent reflections with good matches, and the yellow arrows point to prominent reflections with poor matches.

4.3 Analyzing Azimuthal Variations

It is possible that the channel mentioned previously in this chapter could contribute to lateral velocity variations within the study area. In order to determine whether the channel is affecting the ray tracing and if the 1-D velocity model holds up, shot gathers from three different offsets and 12 different azimuths are analyzed. Figure 4.12 illustrates the 12 azimuth sectors and the shots from each azimuth. The azimuths are labeled from 1 to 12 starting in the southwest sector. The shots were chosen to be as close to the center of the azimuth sector and offset circle as possible to insure consistency. Only the even azimuth sectors will be shown.

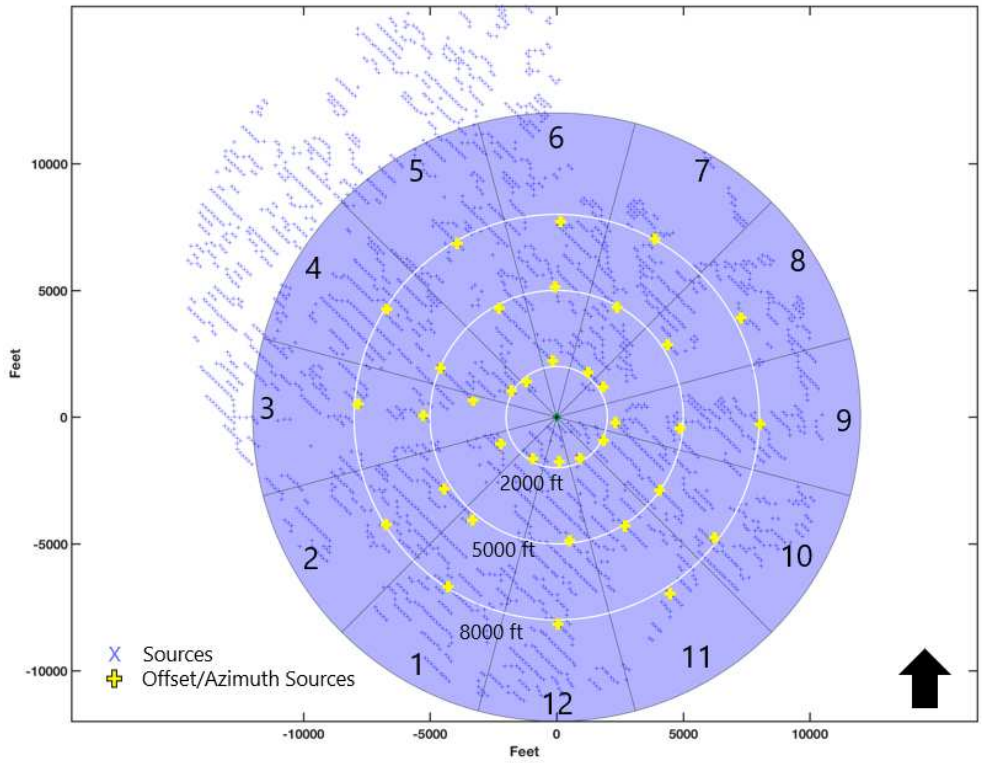

Figure 4.12 Azimuth sectors and chosen shots used to determine azimuthal variations in traveltime corrected shot gathers.

The shot gathers are displayed by offset and azimuth sector in Figure 4.13 and Figure 4.14. While there are slight variations from shot to shot, there is no distinguishable difference based on offset. The top of the Wilcox formation is highlighted in blue. The channel is located directly below this reflector. If there are significant velocity variations that affect the traveltime corrections, it should be noticeable on the reflections indicating the reservoir interval, highlighted in green. At the near and middle offsets the reflections are flattened well at every receiver depth. The reflection begins to dip downward at the far offsets but this is consistent at every azimuth. These results mean that there are no significant velocity variations from the channel that are affecting the ray tracing for the 3D VSP imaging.

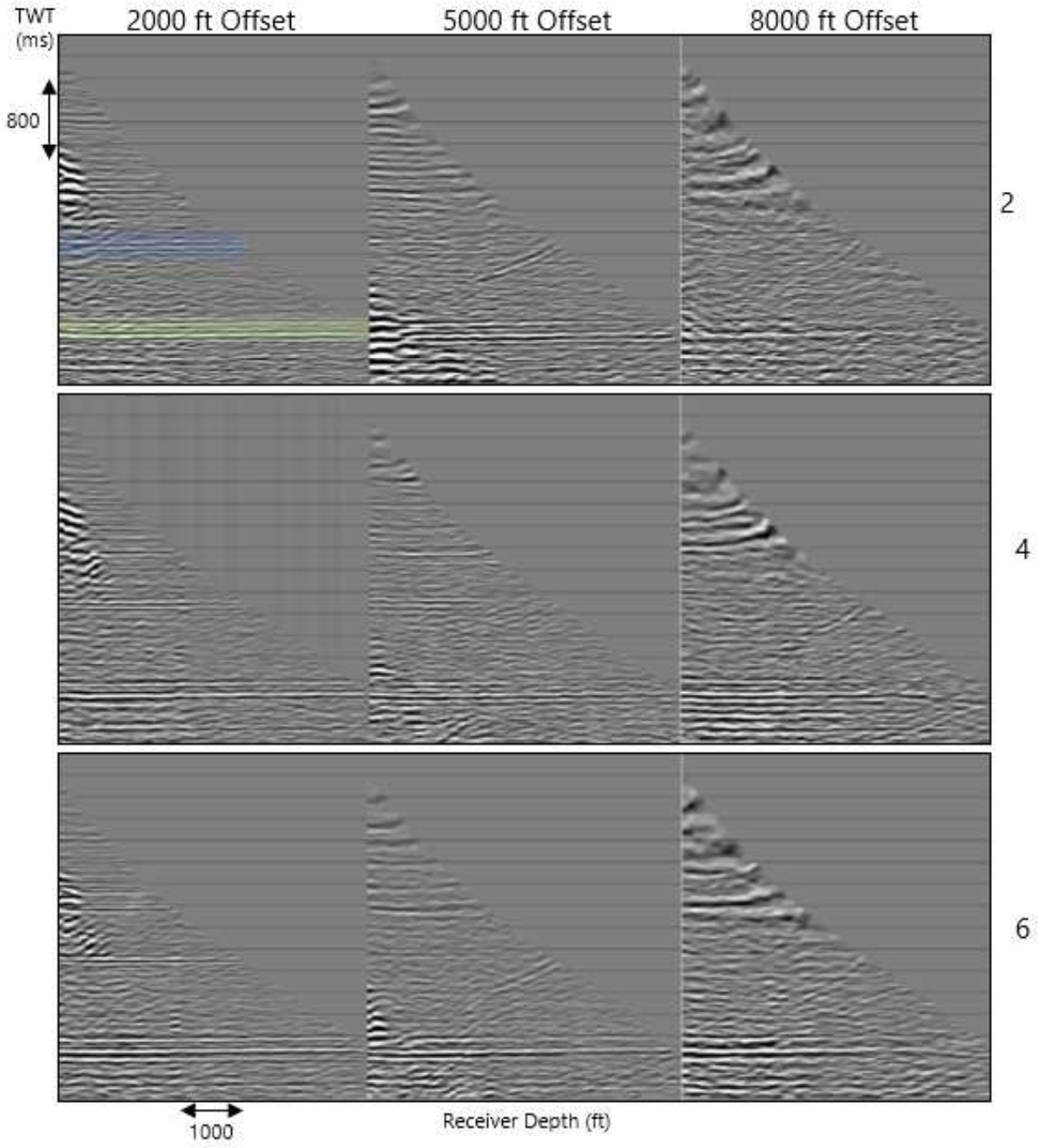

Figure 4.13 Shot gathers corrected for P-wave traveltime sorted by offset and azimuth sectors 2, 4, and 6. The top of the Wilcox is highlighted in blue and the reservoir interval is highlighted in green.

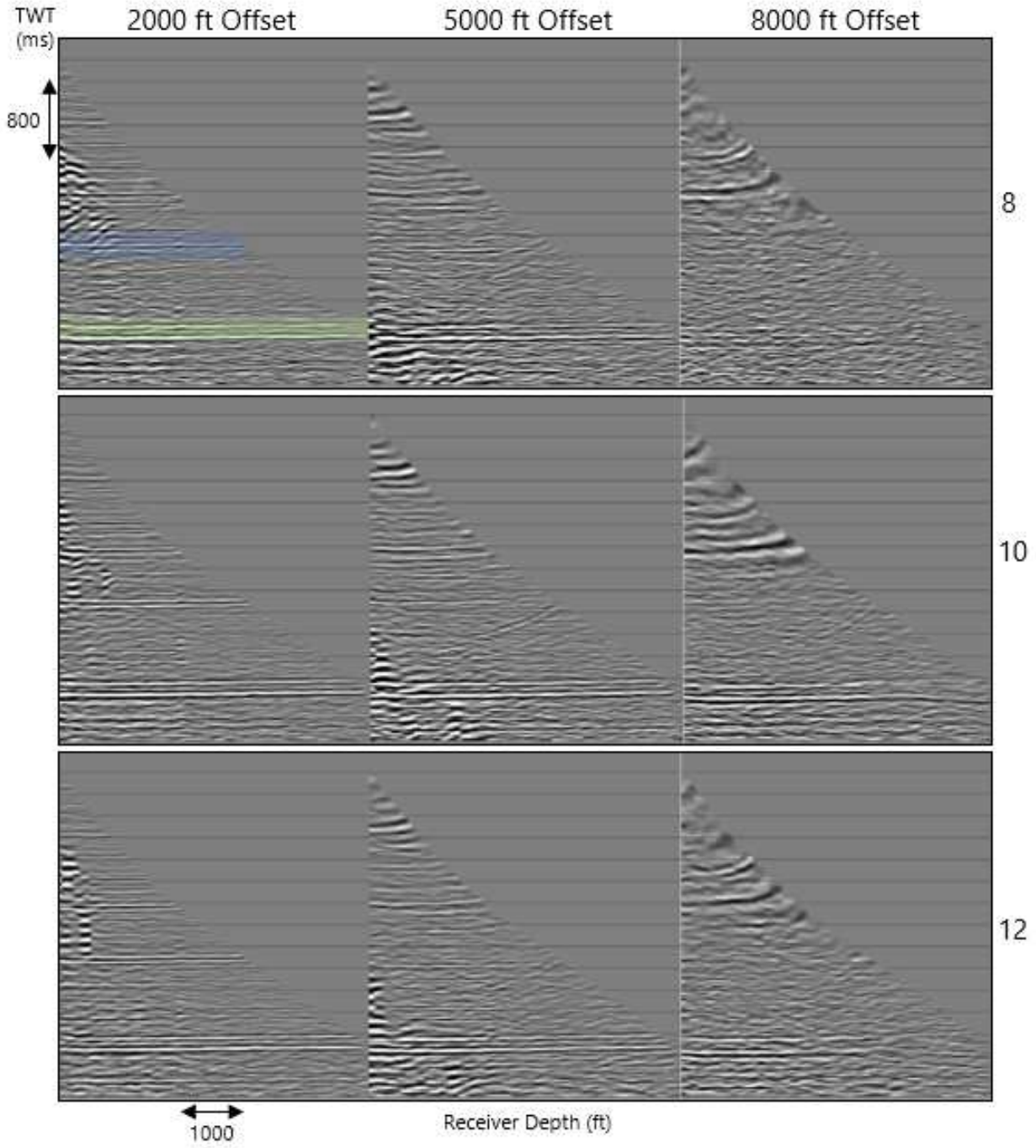

Figure 4.14 Shot gathers corrected for P-wave traveltime sorted by offset and azimuth sectors 8, 10, and 12. The top of the Wilcox is highlighted in blue and the reservoir interval is highlighted in green.

The same shots are also corrected using the PS-wave traveltimes (Figure 4.15 and Figure 4.16). As previously discussed, there is much lower PS-wave energy recorded on the DAS than the P-wave energy. The most PS-wave energy is recorded at the middle and far offsets. The PS velocity model is not perfect, indicated by the reflections not being perfectly flat, but there is no significant variations based on azimuth.

4.4 Migration

The ray tracing and CRP approach to VSP imaging is considered to be old technology (Dillon & Thomson, 1984). Virtues of this simple approach are that signal processing can be performed after traveltime moveout correction but before CRP imaging. In addition, gaps (holes) in reflection point coverage are exposed. Prestack depth migration of of 3D VSP data is very commonly used. Migration will be more accurate in the presence of geologic structure, assuming that the velocity model is accurate. Migration swings energy into reflection point gaps and inevitably shows "migration swings" along the edges of the imaged data. In addition, spikes and noise burst attenuation is more critical prior to the prestack migration than it is for CRP stacking. This section includes examples of prestack RTM and prestack elastic least-squares RTM provided by Dr. Ivan Lim (Lim, 2019). Note that these codes operate on DAS data as it is naturally recorded (Mateeva *et al.*, 2014).

The migration algorithms require significant computing power so they were computed along 2-D lines, illustrated in Figure 4.17, instead of on the full 3-D volume. These lines were made by specifying a small azimuth sector of 3°. The specific azimuths were chosen using the inline and crossline directions of the sources for Azimuths 2 and 4, and the other azimuth lines being 45°, from those lines. The inline and crossline directions also align with the minimum and maximum stresses. It is more obvious from these azimuth sectors that the source points were not designed for VSP. There is a lack of near offsets for most lines. Azimuth line 3 is the worst in this regard, there are no near offset sources, only middle and far. Azimuth line 2 has the best source spacing and is expected to have the best results from the migration.

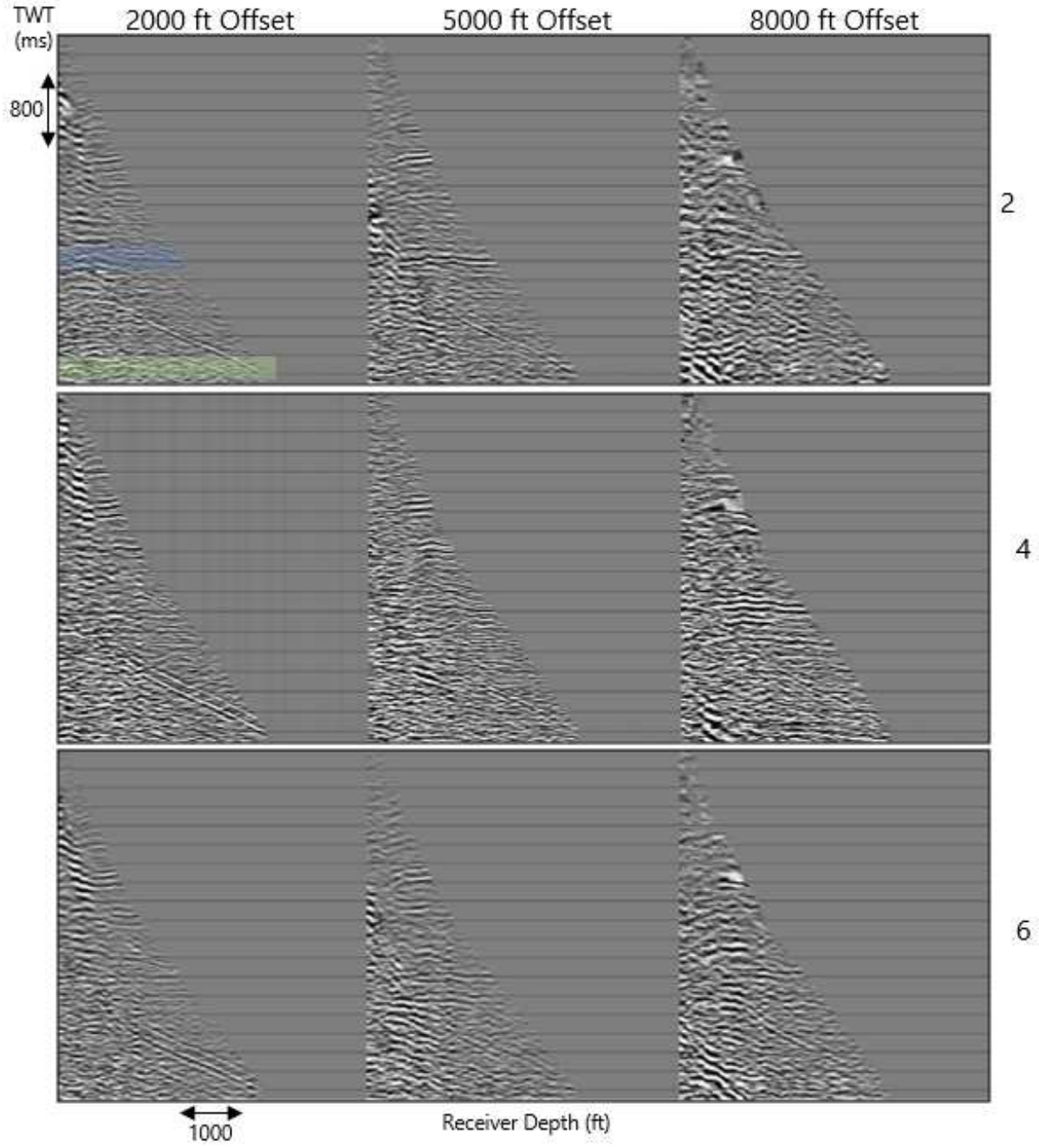

Figure 4.15 Shot gathers corrected for PS-wave traveltime sorted by offset and azimuth sectors 2, 4, and 6. The top of the Wilcox is highlighted in blue and the reservoir interval is highlighted in green.

The output of the migration algorithm are shot gathers for each shot point that went into the migration. Shots from near offsets are seen in Figure 4.18 and far offsets in Figure 4.19.

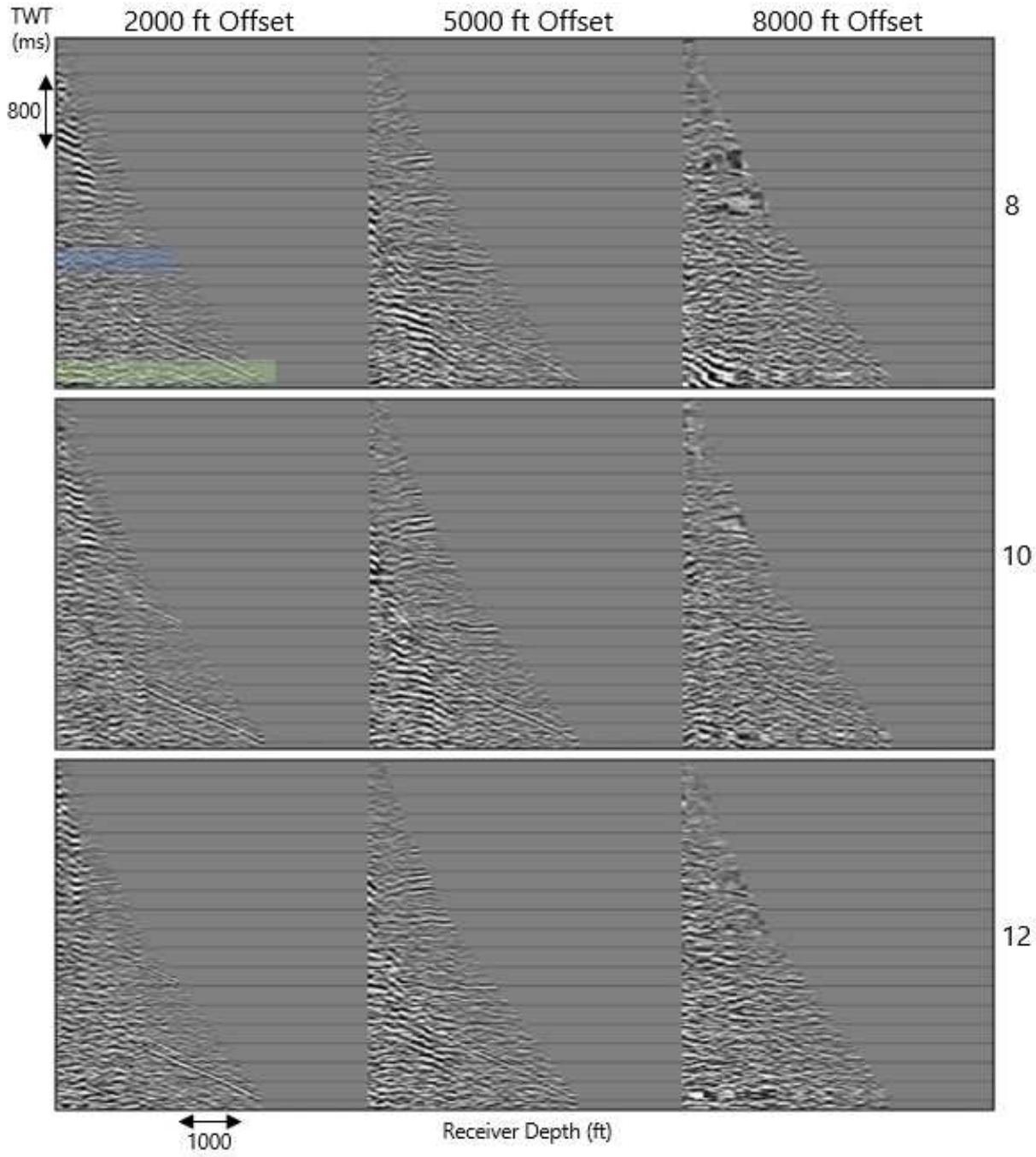

Figure 4.16 Shot gathers corrected for PS-wave traveltime sorted by offset and azimuth sectors 8, 10, and 12. The top of the Wilcox is highlighted in blue and the reservoir interval is highlighted in green.

These images depict shots from either side of the well for both RTM and the least-squares RTM (Lim, 2019). These are full wavefield inversions so, the elliptical wavefield is seen

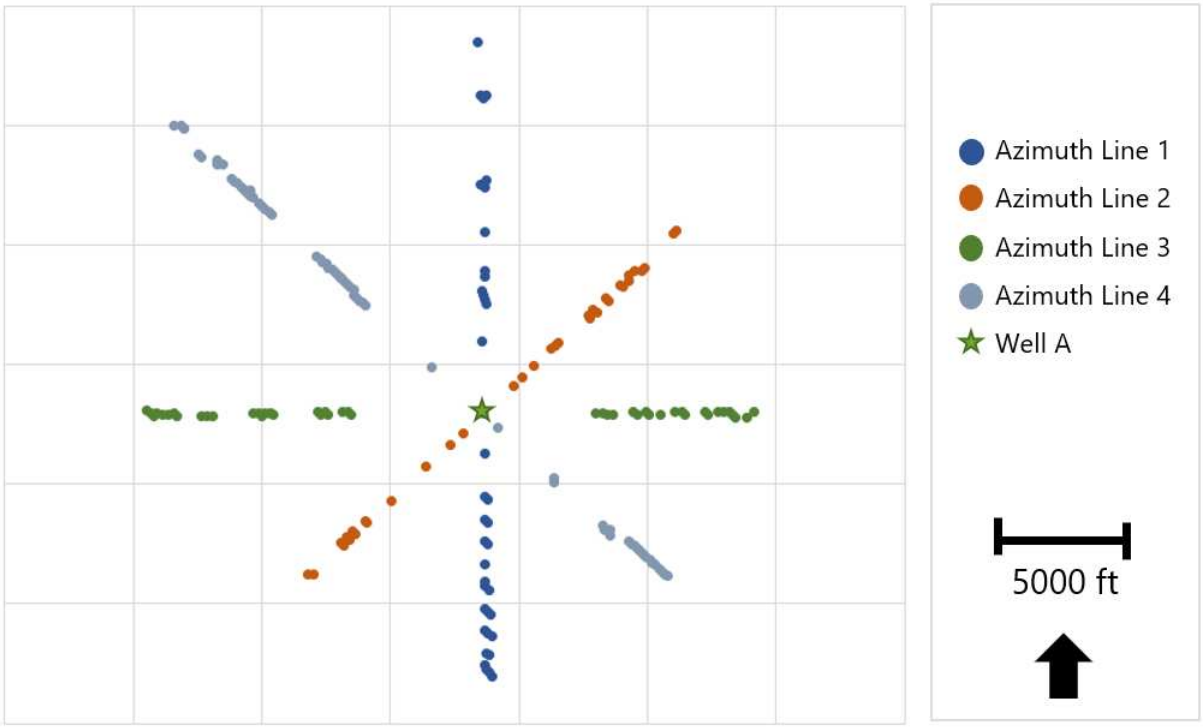

Figure 4.17 3D DAS CRP Azimuth lines

originating from the source location, traveling downwards, and warping and reflecting based on the input velocity model. The same model used for the ray tracing was used for to these migrations. There are small differences between the RTM and the least-squares RTM result. These differences are more apparent once the shots are stacked together.

These shots contain a considerable amount of steeply dipping artifacts and the edges of the wavefield itself has steep dips. An FK filter is used to remove this dipping energy before the shots are stacked together. A major concept behind these migrations is that when these shots are stacked together, the dipping energy negatively interferes with other shots and effectively cancels out. The reflection points positively interfere with one another and stack together to create the imaged reflection.

To create the final migrated image, the shot gathers are stacked together. Figure 4.20 shows the results of applying the FK filter to remove the dipping energy and artifacts before stacking. The images are largely improved, but there is still some shallow dipping energy that

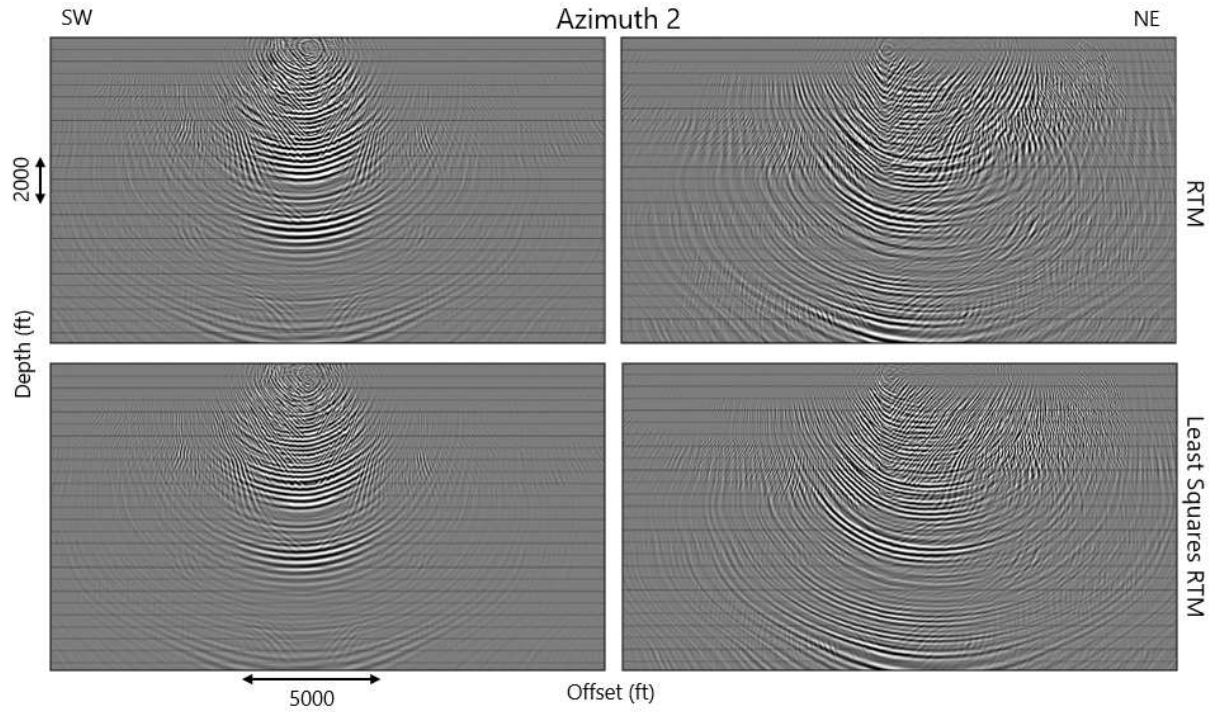

Figure 4.18 Near offset migrated shots.

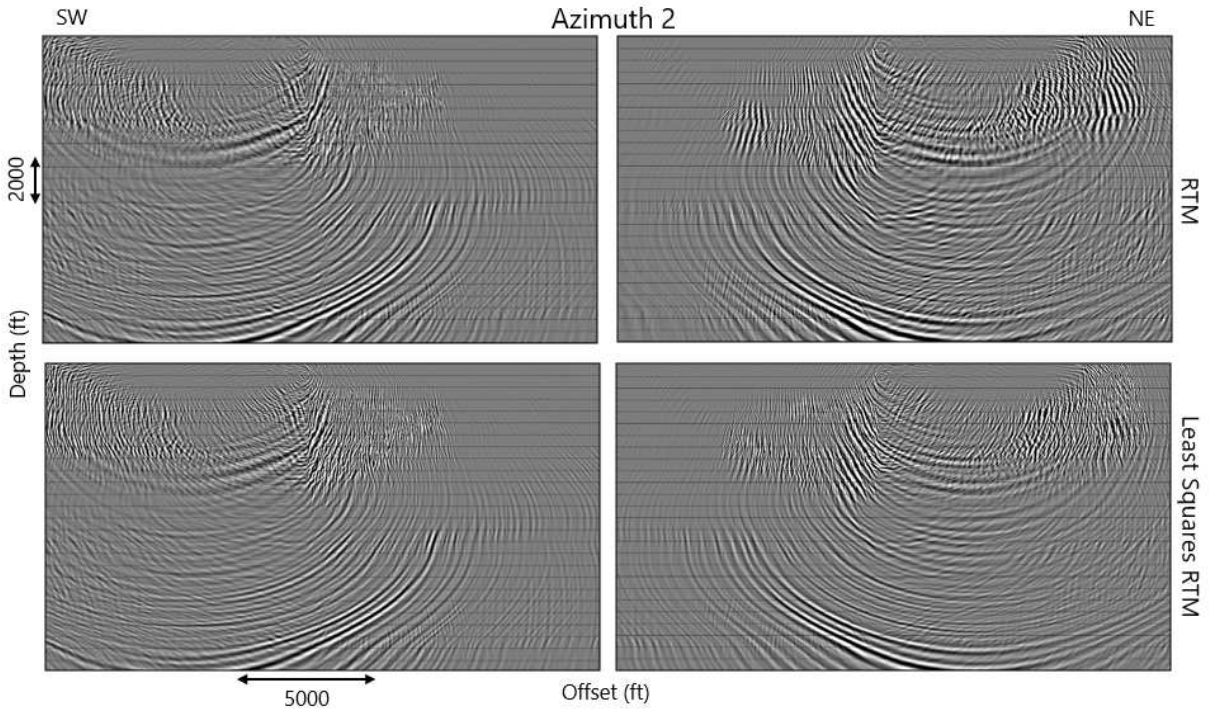

Figure 4.19 Far offset migrated shots.

is difficult to remove. The differences between the two types of migrations is more obvious now. The least-squares RTM migration extends the reflections laterally but also looks to contain lower frequencies than the RTM. The reservoir interval is at the very bottom of the image. The migration was not able to image deeper with the current velocity model. While the least-squares RTM migration seems to improve the image, it is still very difficult to interpret.

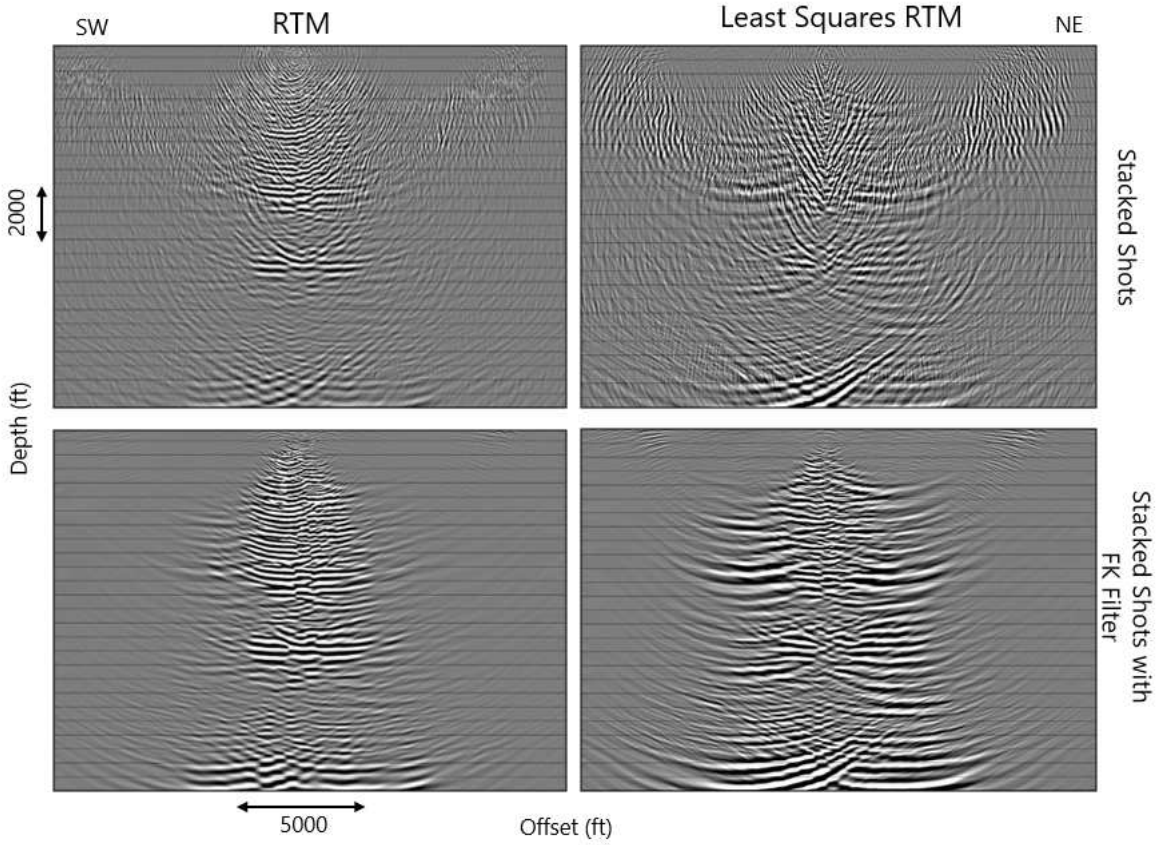

Figure 4.20 Before and after FK filter was applied.

4.5 Comparison Between Migration and Stacking

All of the migrations for the four azimuth lines are displayed in Figure 4.21. The prestack depth migration is suffering hugely from the gaps in shot point coverage. The variations are not due to differences in the subsurface, but rather, the source distribution. Azimuth 3, in particular, shows the result of having no near offset shots. The reflections are mapped

relatively well on the flanks, but in the center where the well is located, the image deteriorates. There are no near offset shots to contribute to the stack near the well, so the migration swings do not destructively interfere enough to cancel out. Azimuth 4 contains many densely spaced shots at middle and far offsets on the left side of the well. The result is well imaged reflections on that side of the well but a deterioration again closer to the well.

With these results, some conclusions can be made. First, is that near offset sources for this type of imaging is extremely important when the goal is to image close to the well. Many of these migrations are severely lacking in near offset sources so the image quality close to the well is poor. Second, consistent source spacing away from the well would improve the image. Consistent spacing relative to the well will lead to better stacking results. There will be fewer gaps in the imaged reflection points allowing for fewer migration swings. More shots could have been included by widening the azimuth sectors from 3° to 5° or 10° but the computing power needed to migrate all of those shots was not available.

For comparison between the migrations and the ray tracing method, the shots from the azimuth lines were traveltime corrected and CRP binned to create the images in Figure 4.22. The image quality is considerably better than the migrations. These stacked 2-D lines also further illustrate the impact of the lack of near offset sources. Azimuth 3, which contains no near offset sources, has a large gap in reflection points on the bottom half of the image. Azimuth 2, which has the best near offset sampling, has a much smaller reflection point gap.

4.6 Other Considerations for Migration Imaging

A common migration method used for VSP imaging is a prestack Kirchhoff depth migration which can limit the migration angular aperture and thus limiting the energy "swings" into the reflection point gaps. However, the same limitations of source offsets remains. These migrations presented also use a much smaller bin size than the CRP stacking (15 ft instead of 82.5 ft). Migrating to a larger bin size would have shown reduced migration artifacts.

Another way to significantly improve the migration results would be to weight the migrated stacks based on reflection point illumination using the method discussed in Wu *et al.*

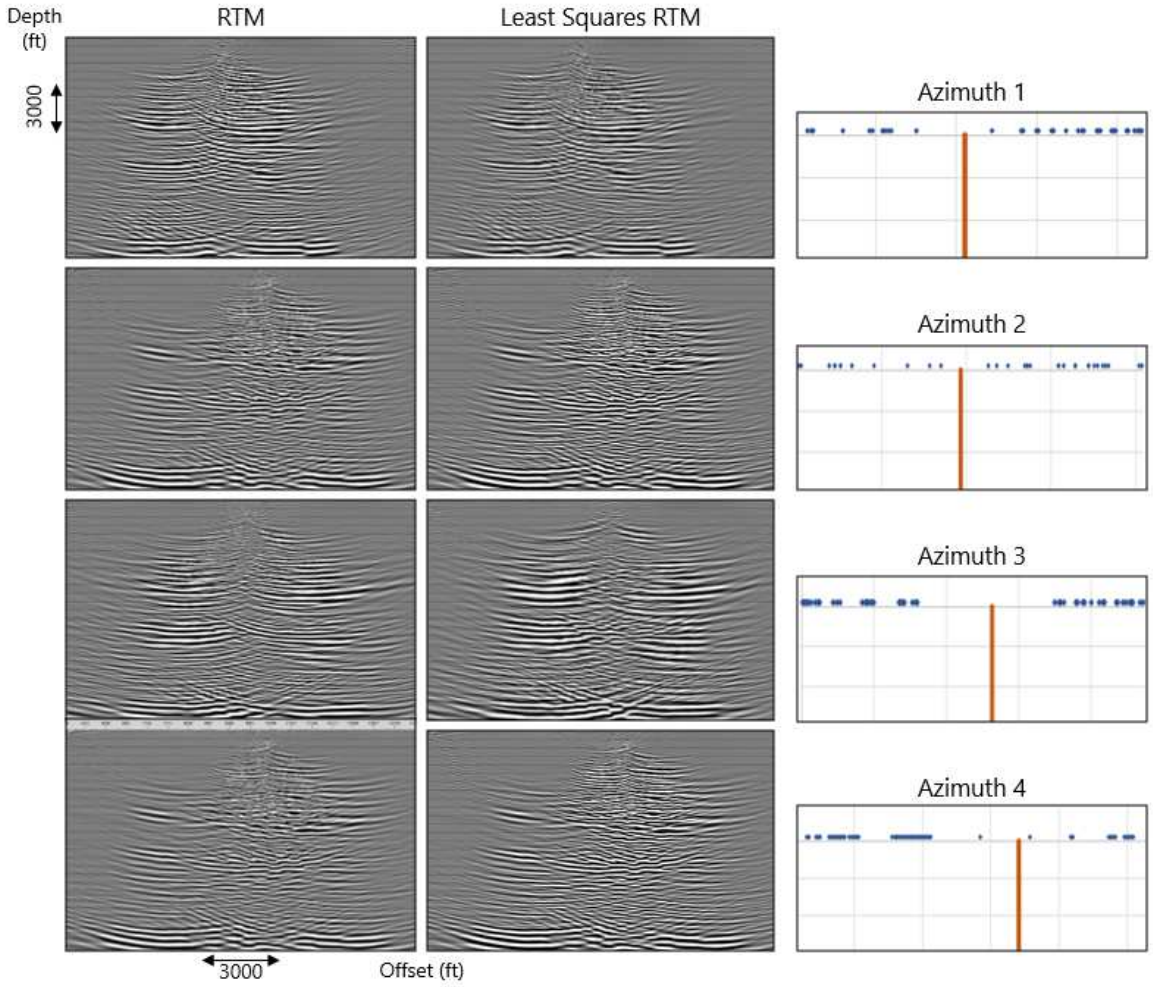

Figure 4.21 RTM and least-squares RTM compared for all four azimuths.

(2015). Applying the stacked VSP illumination compensation method could produce a final image which better represents the reflection points which are imaged and limit the migration swings in the gaps.

4.7 Summary

Using ray tracing on the 3D DAS VSP produces very good images even with a survey that was designed for surface seismic and not VSP. The P-wave reflections map out well and can be tied to the surface seismic. Even though the fiber only records one component of particle motion, the PS-wave imaging is very good once an inside mute is applied. The elastic

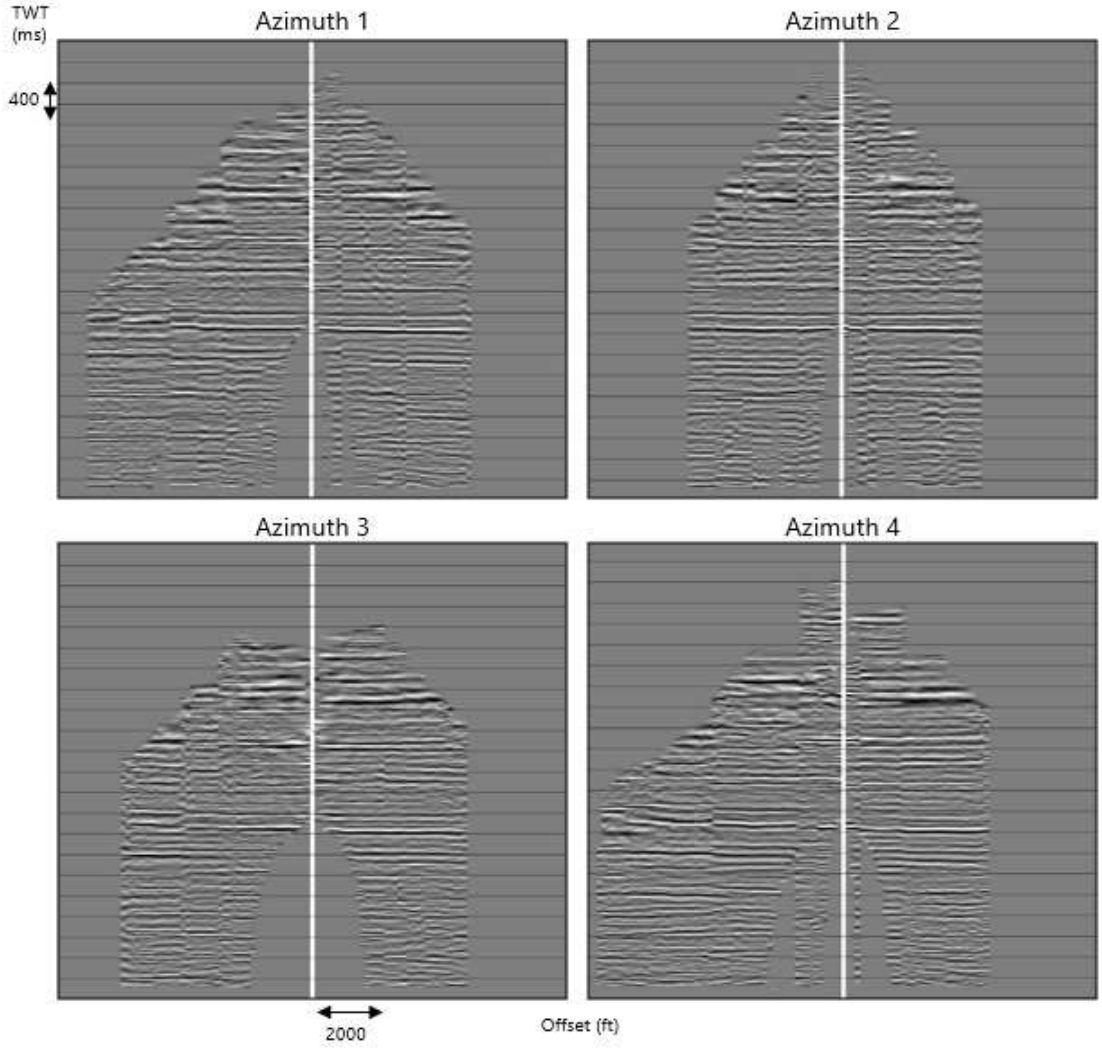

Figure 4.22 3D DAS CRP Azimuth lines.

least-squares RTM improves the image over RTM, but neither migration is as successful as the CRP stacks. The migrations are more susceptible to noise in the data, and irregular shot spacing. The migrations could significantly improve with a few additional processing steps, more near offset shots, and more regular shot spacing.

CHAPTER 5

WALKAWAY VSP TIME-LAPSE ANALYSIS

Results of the time-lapse analysis are discussed in this chapter. Both the zero-offset and walkaway surveys were acquired before and after the hydraulic fracturing of Well A. Unfortunately, the zero-offset survey design was not consistent, and so, could not be used for this analysis. The geophone and DAS walkaway surveys are analyzed in this chapter and the time-lapse results are compared to microseismic.

5.1 Theory

Time-lapse VSP seismic surveys are used for monitoring the changes in a reservoir due to a specific event. They have been used to analyze reservoir changes from hydraulic fracturing, CO2 and fluid injection, and production. Very small changes in properties such as time-shifts, amplitudes, scattered energy, and velocity are evaluated and interpreted in the context of the reservoir. Since the changes are very small, special attention must be paid when processing the data. The acquisition and processing flows must be identical, or as close as possible, in order to detect the differences. Even then some steps such as first break time alignment, match filtering, and gain equalization might be necessary to equalize the different datasets to make valid comparisons (Cheng & Huang, 2010).

5.2 Cross-equalization Workflow

The time-lapse datasets that are available include the zero-offset and walkway surveys. Both types of surveys were initially considered for time-lapse analysis, but the zero-offset survey had many differences between the baseline and monitor surveys. Neither the source nor receiver locations were replicated for the baseline and monitor surveys (Figure 5.1). The baseline sources were located at three different azimuths while for the monitor survey, the P-source was part of the walk-away survey and the shear-sources were located at the same

location. The geophone receivers for the baseline were located nearly the entire vertical length of the well. The monitor geophone receivers were limited to 3400 ft near the heel of the well. With all of these differences, the only repeated source and receiver pair is the S2XL source and the monitor receivers. Time-lapse analysis was not performed on this dataset.

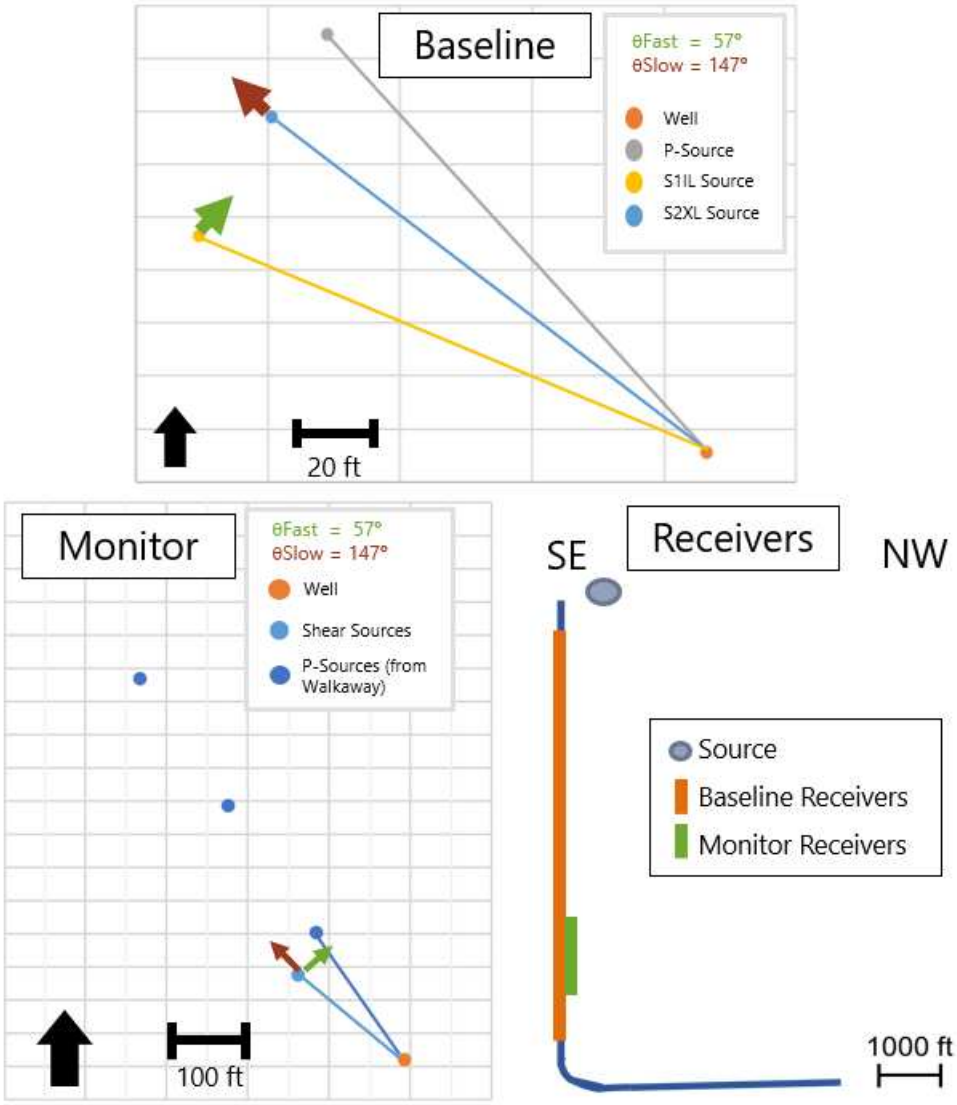

Figure 5.1 Diagrams, initially shown in Chapter 2, illustrating the source and receiver placements for the baseline and monitor zero-offset geophone VSP.

Both the geophone and DAS walkaway surveys are analyzed in this chapter. Each dataset went through the same processing flow under careful consideration to not perform time-varying filters or other processes that could affect the time-lapse signal. Most of the sources

were repeated with the exception of a few of the far offset sources towards the northwest (Figure 5.2). These shots do not contribute much to the over-all stack because of their distance away from the well. The geophone receiver locations, however, differ from baseline to monitor surveys. As seen in the diagram, the baseline receivers were located deeper than the monitor receivers. There is only 1500 ft of overlapping receiver locations which can be used in the time-lapse analysis.

The sources are located over Well B and the hydraulic fracturing took place in Well A. Due to this layout, and the distance between the wells, minimal to no time-lapse changes are expected. The only changes that would occur is if the fractures extended far enough towards Well B and caused a detectable change in velocities. The DAS survey has the same source locations so the reflection points do not lie directly over the well. Further offsets from the well are further from the horizontal section of the well and so are not expected to have time-lapse changes.

A simple approach to compute the time-lapse differences was used. Once the CRP binning was complete the cross sections were subtracted, baseline minus monitor. Cross-equalization of the CRP baseline to the CRP monitor minimized discrepancies in the amplitudes and timing between the two surveys. The cross-equalization is aimed at minimizing reflection energy above the fractured interval, where there should be no changes in signal. Then, the difference between the two surveys is calculated and the only changes should be those related to the hydraulic fracture. Reflections below the reservoir cannot be used because the wavefields travel through the stimulated rock and are similarly affected. The results of the geophone and DAS walkaway surveys are shown in the next section.

5.2.1 Time-lapse Differences

The cross equalization and time-shifts are necessary in order to get a good time-lapse response. Figure 5.3 is an example of the time-lapse response from the P-wave vertical component geophone survey without time-shifts and scaling. The amplitudes are very different between the two surveys so the difference between the two looks like another survey and not

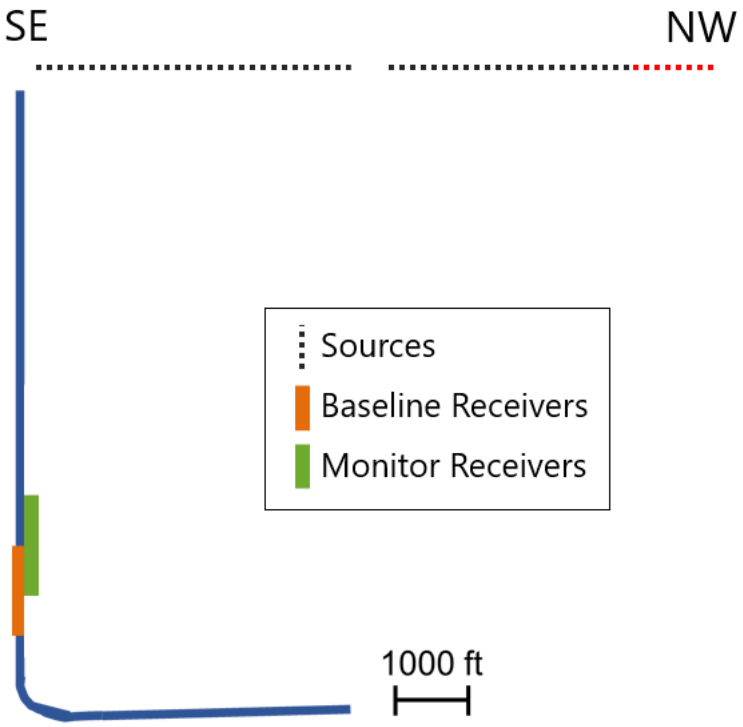

Figure 5.2 Cross section view of time-lapse walkaway survey design. The red sources were not shot for the baseline survey, but not the monitor survey. The orange and green receiver locations are for the geophones. The DAS fiber is located along the whole length of the well in blue.

a time-lapse response.

A single scalar was used to cross-equalize each geophone component. A scalar was calculated for the Z-component and then applied to Z, R, and T components. Unfortunately, with this dataset, there is not much recorded signal above the reservoir interval, and no strong reflection packages to help determine the scalar that minimizes those reflections. Instead, a thin reflection just above the reservoir interval was chosen as the reflection to calibrate the cross-equalization. Figure 5.4 shows the time-lapse results for the vertical (Z), radial (R), and transverse (T) geophone components. The orange circle indicates the location of the reflection that was minimized. The scalar used to equalize the datasets effectively minimizes this reflection. The reflections highlighted in the green circle are questionable time-lapse changes. This area of higher amplitudes is visible on both the monitor and baseline surveys

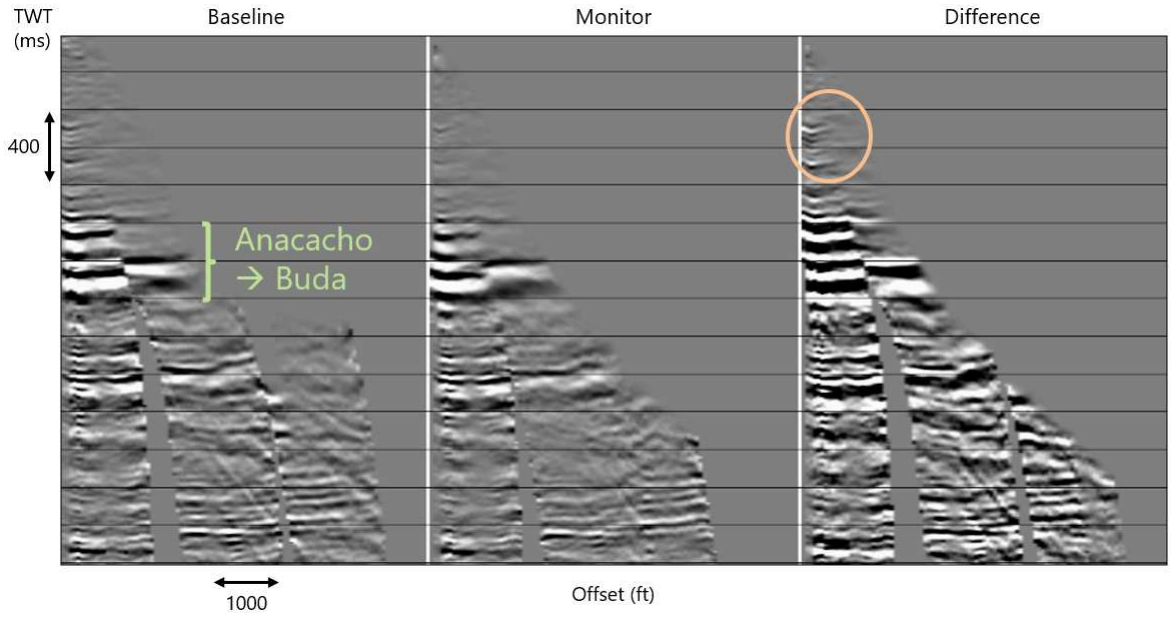

Figure 5.3 Time-lapse response of geophone walkaway surveys without cross-equalization.

and it is unclear what is causing these higher amplitudes. The shot gathers before ray tracing show no indications of having higher amplitudes at the near offsets. This is maybe a limitation in using a single scalar for cross-equalization. The reflections in the blue circle could potentially be real, and should be looked at closer alongside the microseismic data. This is done later in this chapter.

Time-lapse results for the PS-wave are shown in Figure 5.5. These are the Z, R, and T CRP images obtained from PS traveltime correction and CRP binning. The same scalar used to cross-equalize the P-wave images is used for the PS images. The scalar again minimizes the reflection energy above the reservoir interval. Unfortunately, there is a notch of no data right at the reservoir level. This significantly limits the lateral extent of the imaging. The notch is most likely caused by a combination of the source point gaps and the muting applied to remove the stretching which occurs when there is a relatively sudden velocity change with ray tracing.

The high amplitudes in the near offset, seen in the P-wave CRP images, do not appear in the Z-component for the PS data, nor any other component. The Z-component contains

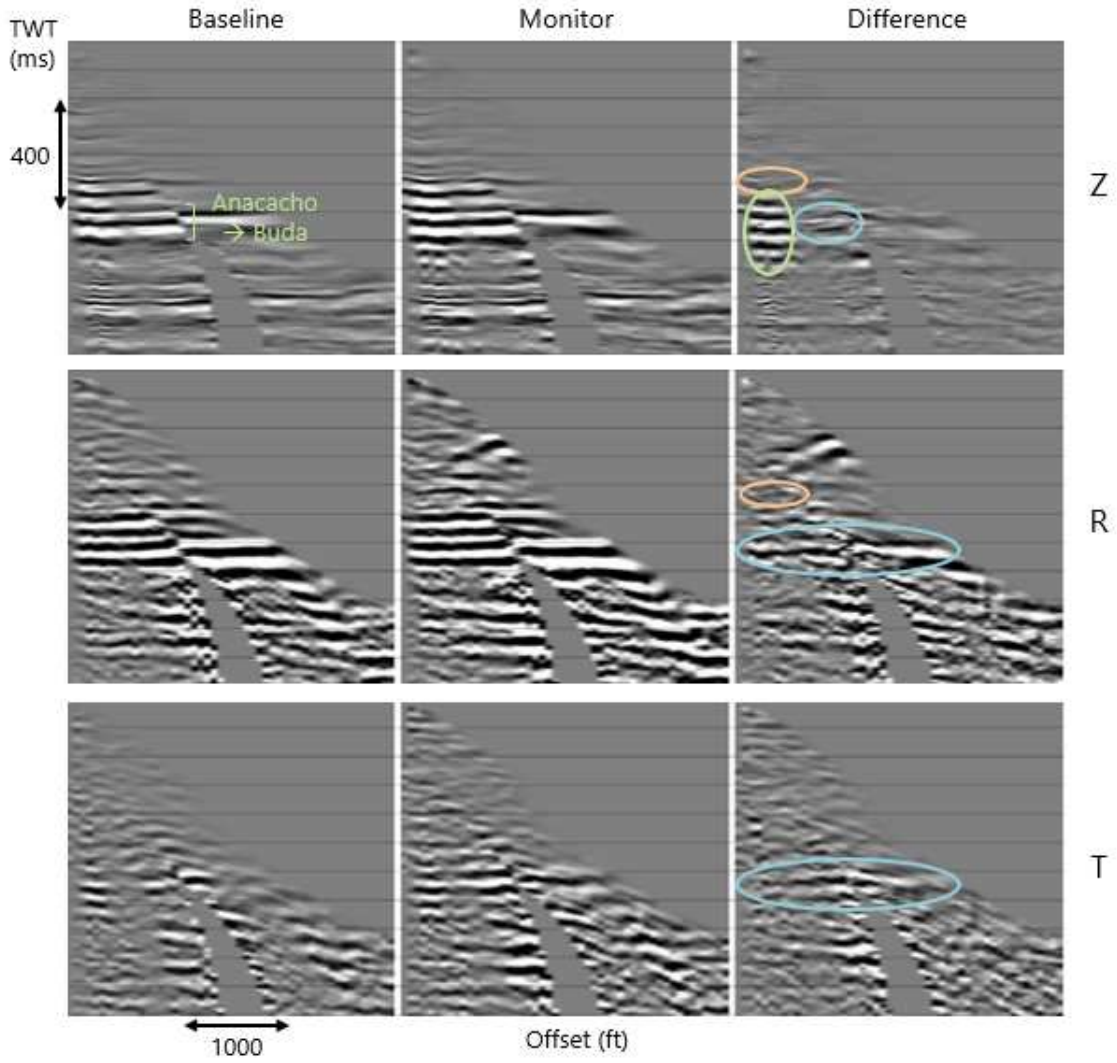

Figure 5.4 P-wave time-lapse responses for vertical (Z), radial (R), and transverse (T) geophone components. Orange circle indicates minimized reflection, green indicates a questionable time-lapse response, blue indicates a possible time-lapse response. All images are shown with the same gain.

so little energy, however, that no time-lapse response can be interpreted. The R-component contains some potential time-lapse changes highlighted in blue and the T-component is also difficult to interpret.

The same processes of scaling and time-shifts is applied to the DAS data. The baseline and monitor surveys, again, had very different amplitudes and the time-lapse response effectively demonstrates this (Figure 5.6). The orange circle indicates the reflection above the

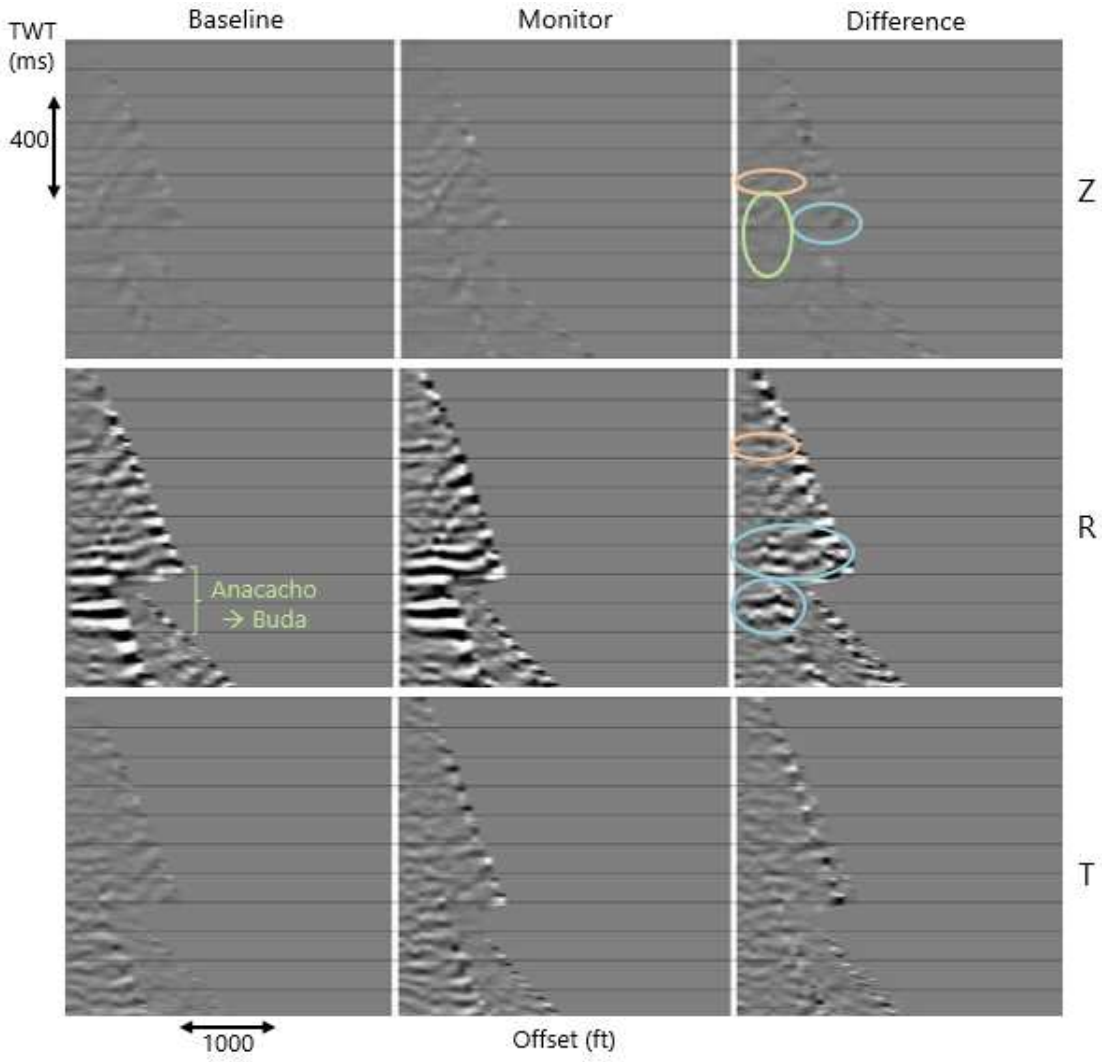

Figure 5.5 PS-wave time-lapse responses for vertical (Z), radial (R), and transverse (T) geophone components. Orange circle indicates minimized reflection, green indicates an untrusted time-lapse response, blue indicates a possible time-lapse response.

reservoir interval that is used to determine the scalar which minimizes the difference.

Figure 5.7 is the time-lapse response with the time-shifts and cross-equalization. The image is zoomed in to more closely analyze the reservoir interval and strong reflections above. The orange circle indicates the reflections that were used to cross-equalize the datasets. This reflection is minimized, but the time-lapse image appears to contain a significant amount of noise, mostly at the near and far offsets. It is unclear what is causing most of the noise at the near offsets, but there is a noisy trace which appears in the monitor survey and again in

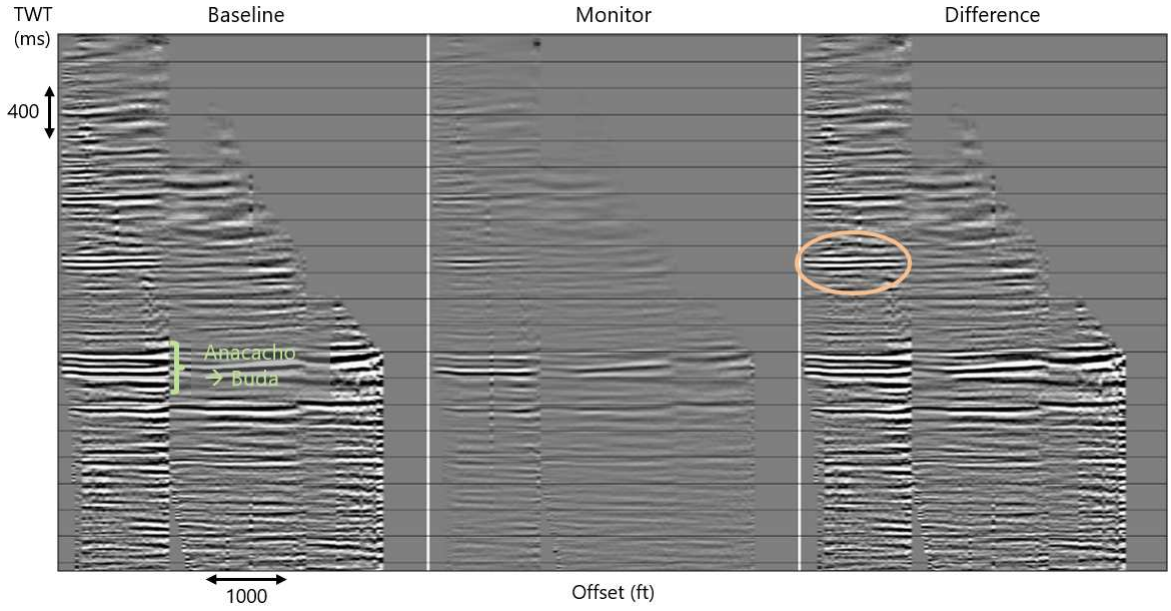

Figure 5.6 DAS walkaway P-wave time-lapse response without a time shift or scalar applied.

the difference. The noise at the far offsets is most likely effects of low fold. The blue circle indicates a area of a possible time-lapse response and should be looked at closely with the microseismic results.

5.2.2 P-wave Reflection Comparison to Microseismic

To tie the microseismic data to the VSP, the microseismic is converted to two-way-time using models discussed in Chapter 2. Then the VSP and microseismic points are plotted together in 3D. This section will contain various 2-D cross sections of the microseismic with the VSP. Figure 5.8 illustrates the map view of the microseismic distribution along with the well locations. Well A and B are seen in red and orange, respectively. The purple line is an estimation of the common reflection points mapped for the DAS walkaway survey. The reflection points are furthest away from the well near the toe, so time-lapse changes are expected to be weaker at the far offsets. Two different view points are indicated in this figure, View 1 and View 2. View 1 projects the microseismic points located to the southwest of the walkaway line and View 2 projects the microseismic events to the northeast onto the

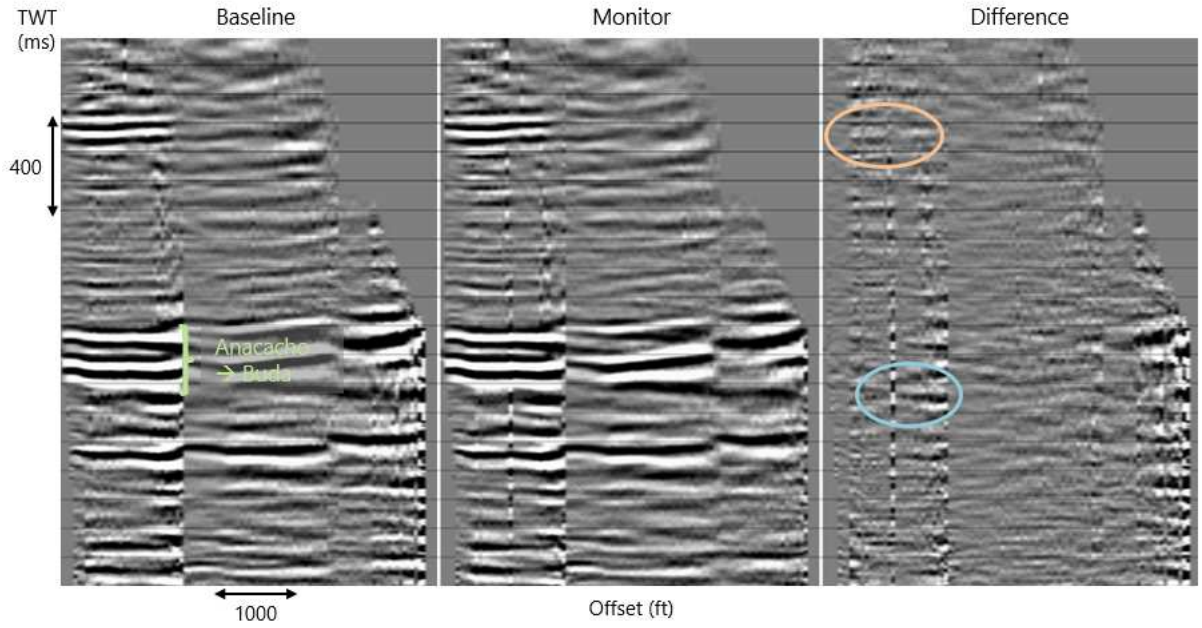

Figure 5.7 Das walkaway P-wave time-lapse response after cross-equalization and time shift. Orange circle indicates the strong reflector used to calibrate cross-equalization and blue circle highlights a potential time-lapse response.

walkaway line. These view points are used as the two view points for the 2-D cross-section views.

Induced fractures propagate in the direction of S_H max, but open perpendicular to this, S_h min. These directions are labeled on Figure 5.8. If simple HTI is assumed based on the direction of the hydraulic fractures, then the geophone walkaway line is oriented along the HTI symmetry plane. No shear wave splitting occurs, so no signal should register on the T-component, but velocities decrease.

Figure 5.9 shows the P-wave time-lapse response for all three geophone components (Z,R and T). Views 1 and 2 are shown as a comparison of where the events are located. These figures, and all following figures in this section, are gained individually to help with visualization. However, it is important to keep in mind the relative energy levels for each component depicted in the previous section. View 1 gives the most accurate representation of the events aligning with the VSP because most of the points seen in View 2 are located

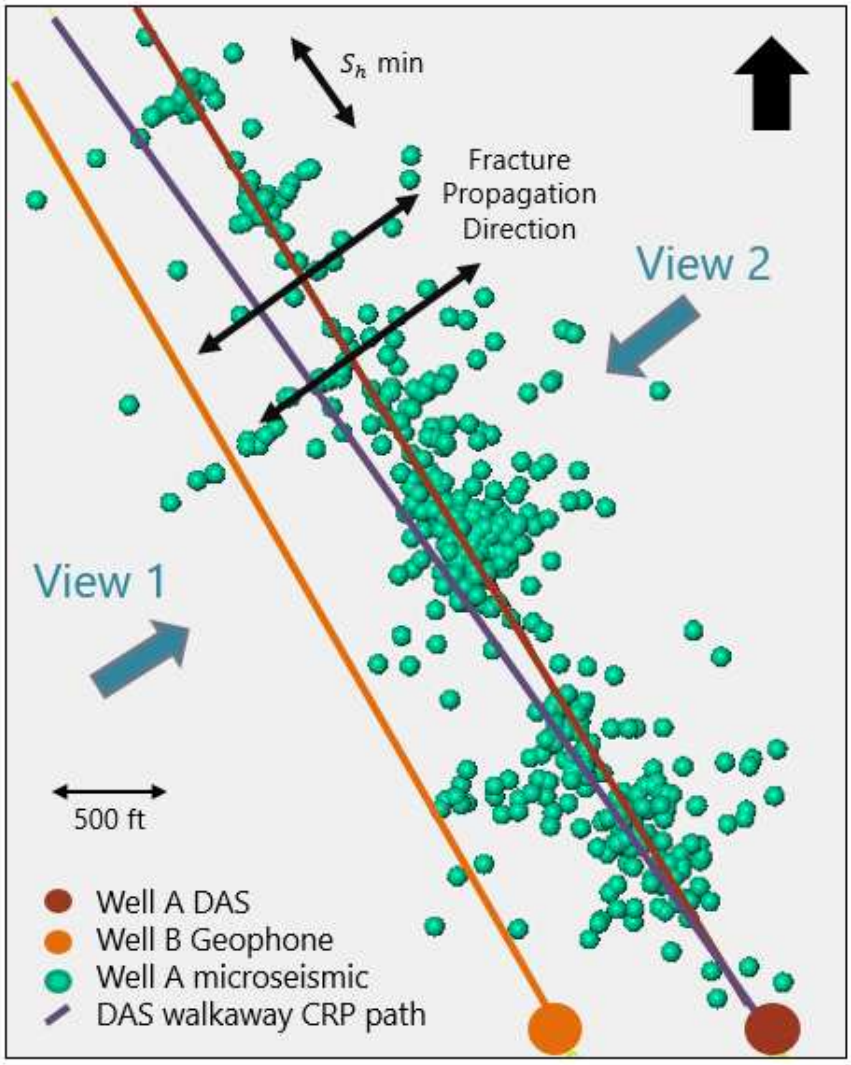

Figure 5.8 Map view of the horizontal well trajectories, the DAS common reflection point path and the microseismic for the Well A hydraulic fracture.

too far away to be recorded in this survey. This figure corroborates the previous assumption that the high amplitudes at the near offsets seen by the vertical component are not a time-lapse response. The R and T components seem to have a time-lapse response at the correct horizons, however, based on the horizontal distribution of the microseismic it is unlikely that such a strong time-lapse response would occur.

While the time-lapse response may be inconclusive, an important observation about the extent of the reflection points can be made. The CRP image does not extend far enough

to include the shallow section of the well. The reservoir interval is located near the top of the section with a significant portion of the image extending blow the area of interest. A possible way to improve this is to locate the geophone string higher in the well bore by a few thousand feet. This is just a speculation and to verify this claim, the DAS VSP data could be sectioned at various intervals, relating to possible geophone intervals, and reprocessed to determine what interval best images the reservoir. While this would be an interesting experiment to help improve the survey design, it is not part of the scope of this project.

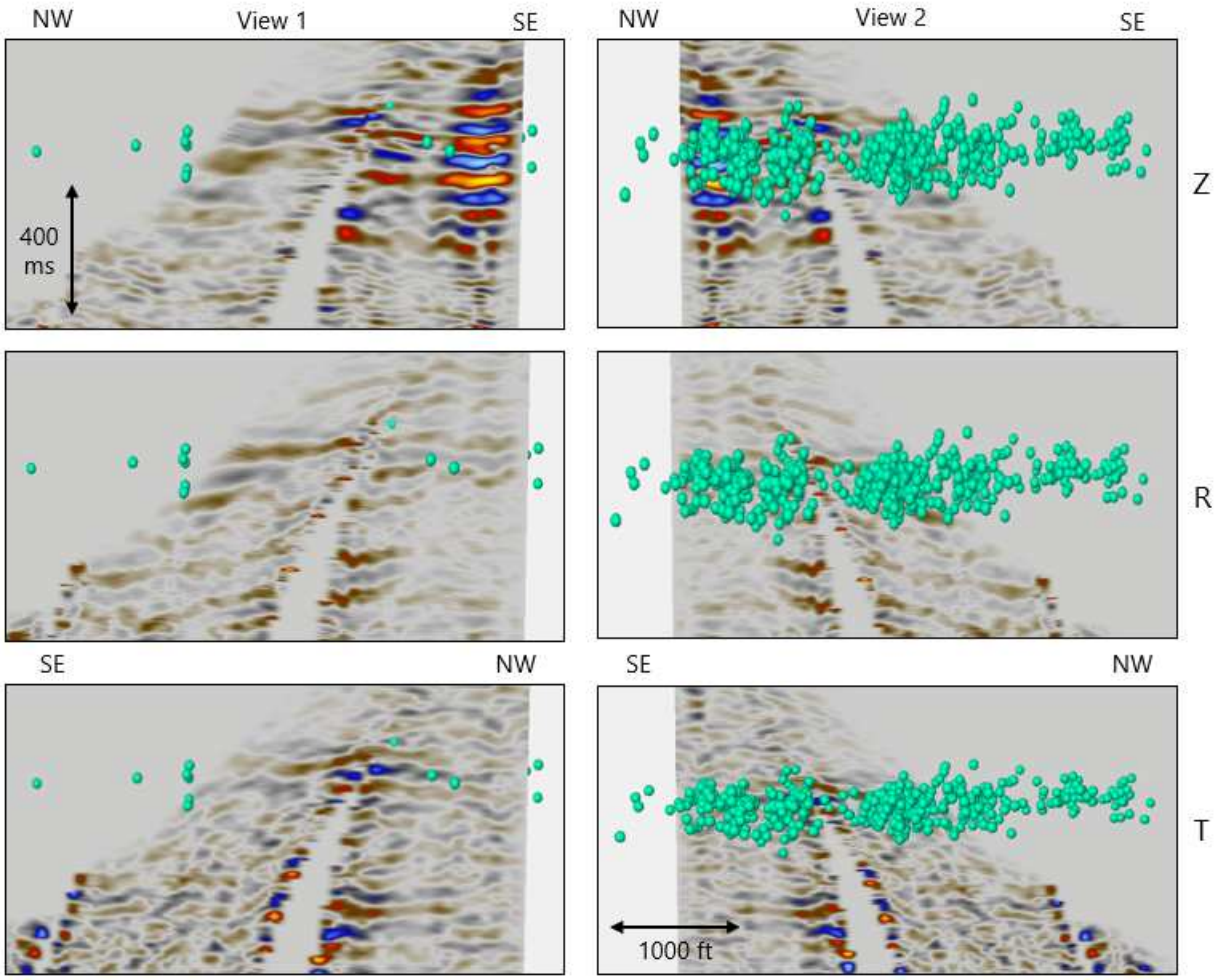

Figure 5.9 Geophone P-wave walkaway time-lapse response for all three geophone components (Z,R,T) compared with the microseismic event locations. View 1 projects the microseismic points located to the southwest of the walkaway line and View 2 projects the microseismic events to the northeast onto the walkaway line. Possible time-lapse response locations are circled in blue.

The P-wave time-lapse response from the DAS data is shown in Figure 5.10. With the larger receiver aperture of the fiber, the entire length of the well is imaged. The important horizons are indicated by the arrows (Green: Top Austin Chalk, Yellow: Eagle Ford, Red: Buda). Well A targets the lower Austin Chalk, and most of the microseismic events extend downwards into the Eagle Ford and Buda. Some of the higher amplitude areas in the time-lapse response align with large clusters of events. This is encouraging, but the image is noisy and for a more definitive result, more processing should be done to equalize the baseline and monitor surveys and remove some of the noise. The high amplitudes do not align with any microseismic events so the difference is most likely due to low fold for the CRP stack.

5.2.3 PS-wave reflection Comparison to Microseismic

Moving on to the PS time-lapse response, the geophone images for each component is seen in Figure 5.11 and the DAS images are seen in Figure 5.12. The main observation for both sets of images is that there is a notch with fewer reflection points right at the reservoir interval. This is highly unfortunate because this severely limits the imaged offsets as further evidenced by the microseismic data. A majority of the microseismic events extend well beyond the imaged reservoir interval. The specific cause of this notch is unclear, but could be attributed to a combination of the mutes applied and the high velocity contrast at this depth. Smoothing the velocity model across this interval could improve the results.

With this limited visibility of the reservoir interval, there are possible time-lapse responses seen in the geophone R and T components. Like with the P-wave responses, though, these results are difficult to interpret and more processing can be done to potentially improve these results.

5.2.4 Time-lapse Conclusions

In order to achieve more conclusive time-lapse results, more time-lapse processing is necessary. The single scalar used to minimize the reflections above the reservoir interval cannot handle variations across traces. It is also possible that minute time-shifts between

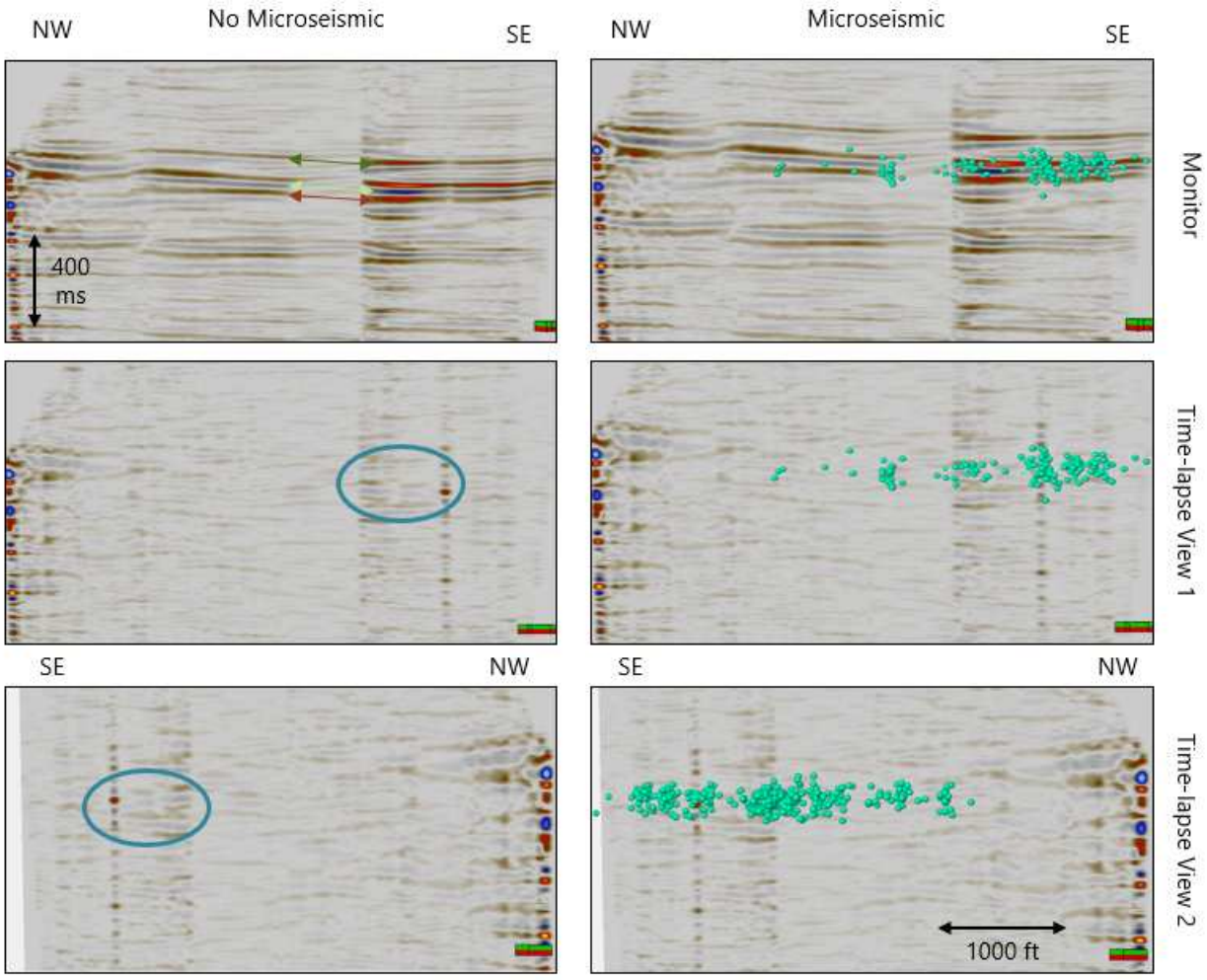

Figure 5.10 DAS P-wave reflection CRP walkaway time-lapse response. The monitor survey along with both view points are shown with and without the microseismic points. View 1 projects the microseismic points located to the southwest of the walkaway line and View 2 projects the microseismic events to the northeast onto the walkaway line. Possible time-lapse response locations are circled in blue. Important horizons are indicated by the arrows on the top left image. Green: Top Austin Chalk, Yellow: Eagle Ford, Red: Buda

the baseline and monitor surveys still needs to be corrected for. To look further at potential time-lapse responses, two shot gathers were analyzed as both the entire shot gather and just the horizontal section of the well. This analysis can be found in Appendix B.

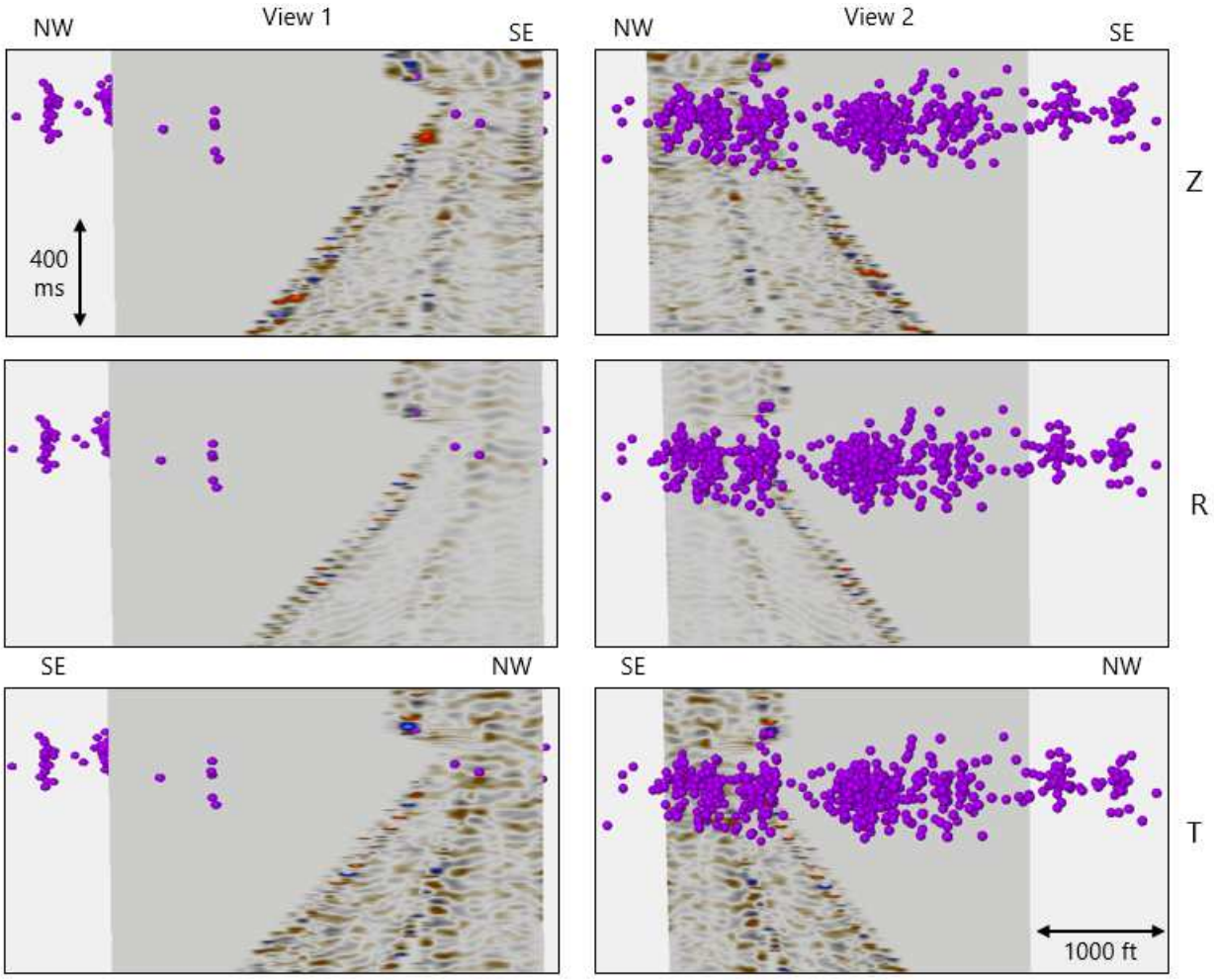

Figure 5.11 Geophone PS-wave reflection CRP walkaway time-lapse response for all three geophone components (Z,R,T) compared with the microseismic event locations. View 1 projects the microseismic points located to the southwest of the walkaway line and View 2 projects the microseismic events to the northeast onto the walkaway line. Possible time-lapse response locations are circled in blue.

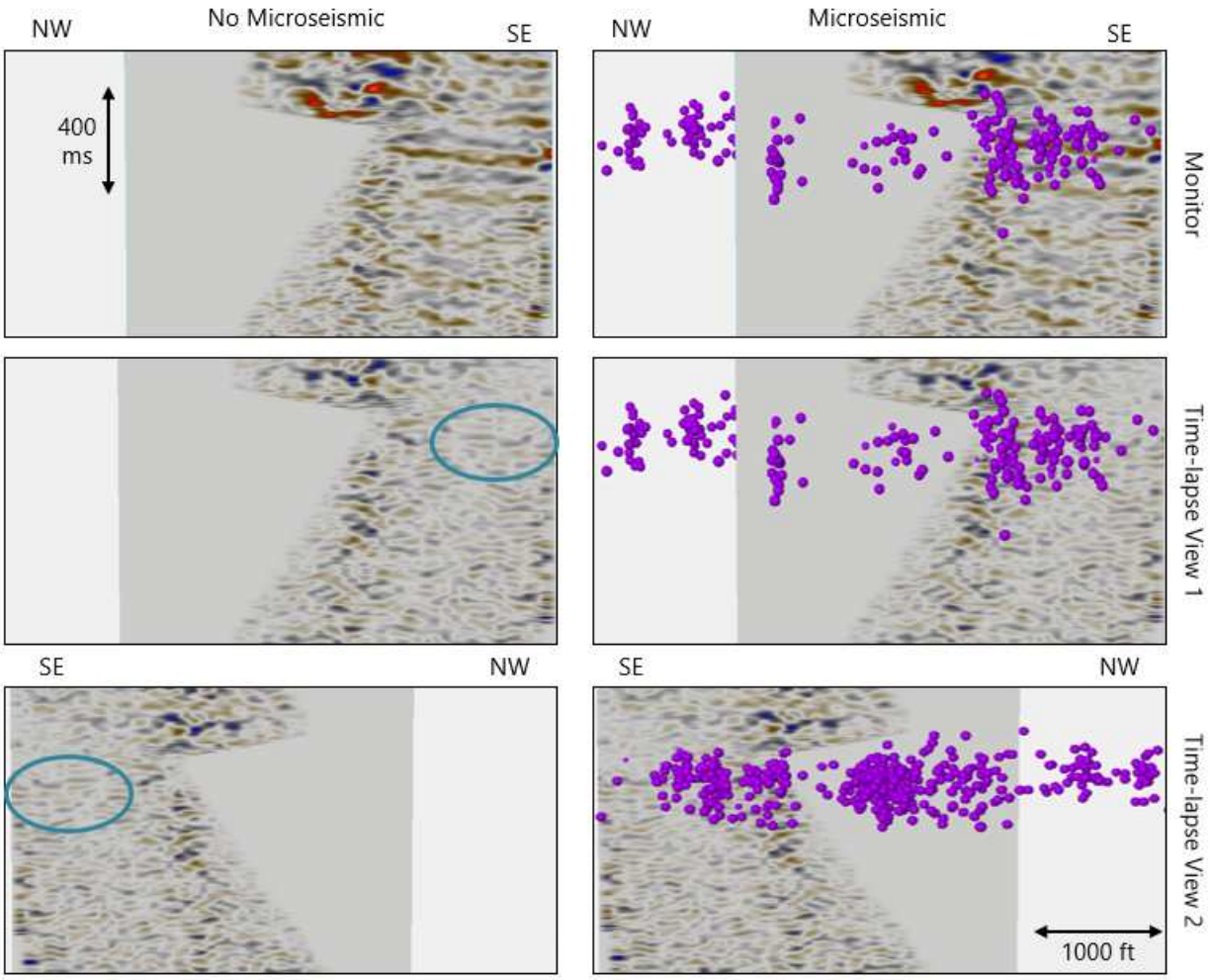

Figure 5.12 DAS PS-wave walkaway time-lapse response. The monitor survey along with both view points are shown with and without the microseismic points. View 1 projects the microseismic points located to the southwest of the walkaway line and View 2 projects the microseismic events to the northeast onto the walkaway line. Possible time-lapse response locations are circled in blue.

CHAPTER 6

CONCLUSIONS AND RECOMMENDATIONS

This last chapter will conclude the work which has been completed and recommend future work that could be done to further this study. Recommendations for improving future studies of this nature such as survey design is also included in this chapter.

6.1 Zero-offset VSP

The zero-offset geophone VSP survey was primarily used to calculate the P-wave velocities using the first arrivals. Processing steps which were used on the other datasets were also described using this dataset.

The biggest draw back to the baseline survey was the placement and orientation of the shear sources. Normally, the P, S1, and S2 sources are all at the same offset and azimuth from the well. There is also, usually, an offset P-source to help orient the horizontal geophone components. Instead the baseline survey offered three different source azimuths, no offset source, and shear shaking directions that were not radial and transverse to the well.

P-wave first arrival energy on the horizontal receivers (H1, H2) from the vertical vibrator was weak due to the small incidence angle of the P-wave arrival. Very little energy recorded on the horizontal geophone components made the rotation process difficult. In addition to this, the shear-source locations and shaking directions added complexities that could not be accounted for. The contractor who originally processed this data could not properly rotate these data either and no further processing was performed.

The monitor zero-offset survey had better geometry for rotating geophones. There were offset P-sources and the shear sources were at the same location. The geophones were easily rotated towards the P-source but this study could not account for the different azimuth of the shear-sources so further processing was not pursued. The previous processor applied Alford rotation and performed a shear-wave splitting analysis. The results of the shear-wave

splitting should be viewed with skepticism, though, because the RT and TR components are not identical, which is a requirement of proper Alford rotation (Alford, 1986).

The DAS zero-offset VSP was processed primarily as a comparison with the geophone zero-offset. As discussed, this is not really a zero-offset survey. The offset is large enough such that ray tracing should be done for the traveltime correction. The same processing flow as the geophone zero-offset was used and the results are promising. The DAS was converted to a geophone response by integrating along the depth axis. The datasets tie together well and the DAS response is comparable to the geophones. Integrating along the fiber amplifies any noise present and smears it across the gather so significant 2-D median filtering is needed to remove this noise and the result looses much of the high frequency energy.

6.2 Walkaway VSP

Walkaway surveys were processed for both DAS and geophone data. The survey design was such that the sources were located over Well B containing the geophones, with the DAS (Well A) recording at the same time. Implications of this design is that the sources are not directly over the lateral part of Well A, with the DAS, and the offsets are larger for the DAS recordings. This geometry also affects the common reflection points that are mapped. Instead of the reflection points inline with the well, they are offset. This geometry still allows for time-lapse responses to be recorded since the reflection points are still located near the horizontal part of the well. The mapped reflection points near the toe of the well, however, are further from the well and time-lapse responses are not expected.

The DAS fiber was able to image a much larger distance away because of its larger receiver-depth aperture. The PS-waves were recorded more clearly on the 3-C geophones, but the DAS still recorded enough PS energy to ray trace and map coherent reflections. Both the DAS and the geophone PS-wave CRP stacks have a notch of missing reflection points, the origins of which could be caused by rapid changes in the velocity model and can likely be removed with additional smoothing of the velocities. In this study, only the vertical section of the fiber was included in the processing, but signal from the far offset sources is recorded

on the horizontal section. This could be processed to gather information about traveltimes from the direct arrivals which could be analyzed in time-lapse as well and potentially record time-lapse PS-wave reflection differences.

A goal of this study was to tie in the walk-away surveys with the surface seismic, this was only done with the 3D VSP. The walkaway source line was oriented at a different azimuth than the surface seismic inline and crossline directions. These different azimuths require interpolation in order to match the CRP bins which could not be done for this project.

6.3 3D VSP

The results of the DAS 3D CRP stack is very promising. Reflections tied well to seismic at all depths. The section of the velocity model below the well had to be updated in order to better tie the deeper reflections. The initial velocity model calculated from the zero-offset VSP was slightly fast because the velocities had to be extrapolated past the last receiver depth and could not be directly calculated. The PS 3D stack also looked very good considering the significant portions of the shot gathers that have to be muted due to no PS energy or NMO stretch (Figure 4.7 and Figure 4.8).

The traveltime corrected shot gathers over different azimuths concluded that the 1-D velocity model is valid for the survey area, even with the channel potentially being the source of lateral velocity variations. There are multiple existing velocity models for other datasets in this project (microseismic, surface seismic). Future work in the Eagle Ford project hopes to merge these velocity models to a single unified 3-D velocity and anisotropy model. P-wave first arrivals from the 3-D DAS VSP can be inverted so solve for velocity variations across the survey.

Much more can be accomplished with this dataset. The quality of stacks can be improved by regularizing the sources on a grid, but it is probably better to design the acquisition with the 3-D VSP as the emphasis. This will lead to more consistent reflection point sampling and potentially fewer gaps in te final stacks.

The only migrations applied to these data were reverse-time depth migration and least-squares reverse-time depth migration. The least-squares migration improved the imaging result over the RTM by extending the reflections laterally, but neither migration resulted in interpretable images. A Kirchhoff migration is used more commonly in VSP processing but also has its limitations. With a Kirchhoff migration the aperture of the migrated shot can be specified, limiting the migration swings. The gaps in reflection points cannot be filled with the migration so the swings will still occur at the edges and gaps in the survey. The result is to hide the exact location of the gaps and deteriorate the image near the gaps.

6.4 Time-lapse

While this initially looked like a promising dataset for time-lapse analysis, a closer look indicates that the repeatability needed for time-lapse is severely limited.

The zero-offset was one such survey. Neither the source nor receiver locations were replicated for the baseline and monitor surveys. The baseline sources were located at three different azimuths, for the monitor survey, the P-source was part of the walkaway survey and the shear-sources were located at the same location. The receivers for the baseline were located over the whole vertical length of the well. The monitor receivers were limited to 3400 ft near the heel of the well. With all of these differences, the only repeated source and receiver pair is the S2XL source and the monitor receivers. Time-lapse analysis was not performed on this dataset.

Results for the the walkaway surveys were inconclusive. The datasets were noisy and further time-lapse processing is necessary to improve the result. Cross equalizing the geophone surveys is very difficult because there are no strong reflections above the reservoir available to use. The limited receiver coverage limited the reflection point coverage that could be mapped and the result was that the full length of the lateral was not imaged to compare with microseismic. The DAS data did not have this issue with the P-wave reflections. The PS time-lapse response is limited on both datasets because of the missing reflection points, the notch.

The wells are drilled in the direction of S_h min so that the induced fractures propagate away from the well in the direction of S_H max, perpendicular to the minimum stress. This propagation direction is seen on the microseismic event locations. The fractures then open towards S_h min direction. The geophone walkaway line is perpendicular to the induced fracture strike direction and the assumed HTI symmetry plane. No shear-wave splitting occurs along the symmetry plane, but the velocities decrease.

As a final conclusion, this project covered a broad range of work with the processing of multiple VSP datasets, with two different receiver types, and a time-lapse component. Important comparisons were made between the geophone and DAS datasets in the walkaway surveys, specifically, that the larger receiver offset of the DAS fiber improves the lateral extent that is imaged. Another contribution of this project is the 3D CRP stacks for both the P-wave and PS-waves. The good quality of the final stacks means that DAS is more practical and useful than geophones when acquiring a 3D VSP survey. Due to the breadth of this project and the time constraints, there are multiple aspects that are underdeveloped and could be researched more closely. To name a few, the zero-offset survey would benefit from a closer look at geophone rotations in order to analyze shear-wave splitting and the 3D survey could be processed to investigate the azimuthal variations which the DAS can record.

REFERENCES CITED

Alford, R.M. 1986. Shear Data in the Presence of Azimuthal Anisotropy: Dilley, Texas. *Chap. Seismic 9, pages 476–479 of: SEG Technical Program Expanded Abstracts 1986*. Society of Exploration Geophysicists.

Bakku, S. K. 2015. *Fracture Characterization from Seismic Measurements in a Borehole*. Ph.D. thesis, Massachusetts Institute of Technology.

Bóna, Andrej, Dean, Timothy, Correa, Julia, Pevzner, Roman, Tertyshnikov, K.V., & Van Zaanen, L. 2017 (06). Amplitude and Phase Response of DAS Receivers.

Cai, Zhidong, Yu, Gang, Zhang, Qinghong, Zhao, Yufeng, Chen, Yuanzhong, Jin, Yixin, & Zhao, Haiying. 2016. *Comparative Research between DAS-VSP and Conventional VSP Data*. Tech. rept. SEG Rock Physics and Borehole Geophysics Workshop.

Chalmers, Gareth R.L., & Bustin, R. Marc. 2017. A multidisciplinary approach in determining the maceral (kerogen type) and mineralogical composition of Upper Cretaceous Eagle Ford Formation: Impact on pore development and pore size distribution. *International Journal of Coal Geology*, **171**, 93–110.

Chen, Yuanzhong, Hu, Guangmin, Cai, Hanpeng, Wu, Junjun, Li, Yanpeng, Yu, Gang, & Li, Fei. 2018. *Fiber armor acquisition contrast experiment and noise suppression technique in DAS 3D-VSP*. Pages 5506–5510.

Cheng, Arthur, & Huang, Lianjie. 2010. Time-lapse VSP data processing for monitoring CO2 injection. *The Leading Edge*.

Correa, Julia, Egorov, Anton, Tertyshnikov, Konstantin, Bona, Andrej, Pavzner, Roman, Dean, Tim, Freifeld, Barry, & Marshall, Steve. 2017. Analysis of signal to noise and directivity characteristics of DAS VSP at near and far offsets-A CO2CRC Otway Project data example. *The Leading Edge*.

Craddick, Christi, Ryan, Sitton, & Christian, Wayne. *Texas Railroad Commission*.

Dai, Wei, & Schuster, Gerard T. 2013. Plane-wave least-squares reverse-time migration. *Geophysics*, **78**(4), S165–S177.

Daley, T.M., Miller, D.E., Dodds, K., Cook, P., & Freifeld, B.M. 2015. Field testing of modular borehole monitoring with simultaneous distributed acoustic sensing and geophone vertical seismic profiles at Citronelle, Alabama. *Geophysical Prospecting*, **64**(5), 1318–1334.

Dillon, P. B., & Thomson, R. C. 1984. Offset Source VSP Surveys and their Image Reconstruction. *Geophysical Prospecting*, **32**(5), 790–811.

Dyman, T S, & Condon, S M. 2006. *Volume Title Page Assessment of Undiscovered Conventional Oil and Gas Resources— Upper Jurassic–Lower Cretaceous Cotton Valley Group, Jurassic Smackover Interior Salt Basins Total Petroleum System, in the East Texas Basin and Louisiana-Mississippi Salt Ba*. Tech. rept. U.S. Geological Survey, Reston Virginia.

Harbor, Ryan L. 2011. *Facies characterization and stratigraphic architecture of organic-rich mudrocks, Upper Cretaceous Eagle Ford Formation, South Texas*. MS, The University of Texas at Austin.

Lim, Ivan. 2019. *Multicomponent Distributed Acoustic Sensing: Concept, Theory, and Applications*. PhD thesis, Colorado School of Mines.

Lines, L. R., & Ulrych, T. J. 1977. The Old and the New in Seismic Deconvolution and Wavelet Estimation. *Geophysical Prospecting*, **25**(3), 512–540.

Martin, Ron, Baihly, Jason, Malpani, Raj, Lindsay, Garrett, & Atwood, W Keith. 2011. Understanding Production from Eagle Ford–Austin Chalk System. *In: SPE Annual Technical Conference and Exhibition*. Denver: Society of Petroleum Engineers.

Mateeva, Albena, Lopez, Jorge, Potters, Hans, Mestayer, Jeff, Cox, Barbara, Kiyashchenko, Denis, Wills, Peter, Grandi, Samantha, Hornman, Kees, Kuvshinov, Boris, Berlang, Wilfred, Yang, Zhaohui, & Detomo, Rocco. 2014. Distributed acoustic sensing for reservoir monitoring with vertical seismic profiling. *Geophysical Prospecting*, **62**(4), 679–692.

Montgomery, S. 1991. Horizontal Drilling in the Austin Chalk Part1. Geology, drilling history and field rules. *Petroeum Fronteers*, **7**(3), 44.

Munn, Jonathan D., Coleman, Thomas I., Parker, Beth L., Mondanos, Michael J., & Chalari, Athena. 2017. Novel cable coupling technique for improved shallow distributed acoustic sensor VSPs. *Journal of Applied Geophysics*, **138**, 72 – 79.

Parker, Tom, Shatalin, Sergey, & Farhadiroushan, Mahmoud. 2017. Distributed Acoustic Sensing - A new tool for seismic applications. *First Break*, **32**(2), 61–69.

Phelps, Ryan M., Kerans, Charles, Loucks, Robert G., Da Gama, Rui O.B.P., Jeremiah, Jason, & Hull, David. 2014. Oceanographic and eustatic control of carbonate platform evolution and sequence stratigraphy on the Cretaceous (Valanginian-Campanian) passive margin, northern Gulf of Mexico. *Sedimentology*, **61**(2), 461–496.

Robison, C R. 1997. Hydrocarbon source rock variability within the Austin Chalk and Eagle Ford Shale(Upper Cretaceous), East Texas, U.S.A. *International Journal of Coal Geology C.R. Robison / International Journal qf Coal Geology*, **34**(34), 287–305.

Simmons, Jim, & Backus, Milo. 2001. Shear waves from 3-D-9-C seismic reflection data Have we been looking for signal in all the wrong places? *The Leading Edge*, 604–612.

Willis, Mark E, Erdemir, Cemal, Ellmauthaler, Andreas, Barrios, Oscar, & Barfoot, David. 2016. Comparing DAS and Geophone Zero-Offset VSP Data Sets Side-By-Side. 22–26.

Wu, Han, Wong, Wai-Fan, Yang, Zhaohui, Wills, Peter B., Lopez, Jorge L., Li, Yingping, Blonk, Bastian, Hewett, Ben, & Mateeva, Albena. 2015. Dual-well 3D vertical seismic profile enabled by distributed acoustic sensing in deepwater Gulf of Mexico. *Interpretation*, **3**(3), SW11–SW25.

APPENDIX A

UPDATING THE SHEAR-WAVE VELOCITY MODEL

In order to update the shear-wave velocities, PP-PS registration from the surface seismic was used. This method uses time-picks from the PP and PS surface seismic volumes at the location of the well to calculate the Vp/Vs ratio. The P-wave velocities are assumed to be correct. The time-picks are shown in Table A.1 below as T_p and T_s and the interval times are shown as ΔT_p and ΔT_s. The equations below are used to calculate the Vp/Vs ratios. The depths that correspond to the time-picks are calculated using a time-depth relationship derived from the zero-offset VSP.

The PS-wave CRP stack for the 3D DAS VSP is updated using these Vp/Vs ratios and is tied to surface seismic in Figure A.1. When using the initial shear-wave velocity model, the Eagle Ford horizon was shifted up relative to the surface seismic. This new model now corrects for this so the horizon is in the correct location in time. The PS-wave CRP stack is noisier than the P-wave image, so the tie is still not ideal and could be improved. However, major reflections do roughly correlate between the surface seismic and the VSP stack. As with the P-wave VSP, this image has not been corrected to geophone response so the phase is not expected to match. Overall, the PP-PS registration improves the PS-wave VSP tie to surface seismic.

$$\gamma_o RMS = 2 * (T_s/T_p) - 1$$

$$\gamma_o INT = 2 * (\Delta T_s/\Delta T_p) - 1$$

Table A.1 Values used to calculate the Vp/Vs ratios using PP-PS registration from the surface seismic. T_p and T_s are the time-picks at Well B from the PP and PS surface seismic, respectively. ΔT_p and ΔT_s are the time differences between the picked intervals. $\gamma_o RMS$ and $\gamma_o INT$ are the Vp/Vs ratios calculated for the RMS and interval velocities, respectively.

T_p (ms)	ΔT_p (ms)	T_s (ms)	ΔT_s (ms)	$\gamma_o RMS$	$\gamma_o INT$	Z (ft)
1306		2484		2.8	2.8	0-4600
2176	870	3780	1296	2.4	1.97	4600-9400
2686	510	4497	717	2.34	1.80	9400-12500
2783	97	4672	175	2.35	2.60	12500-30000

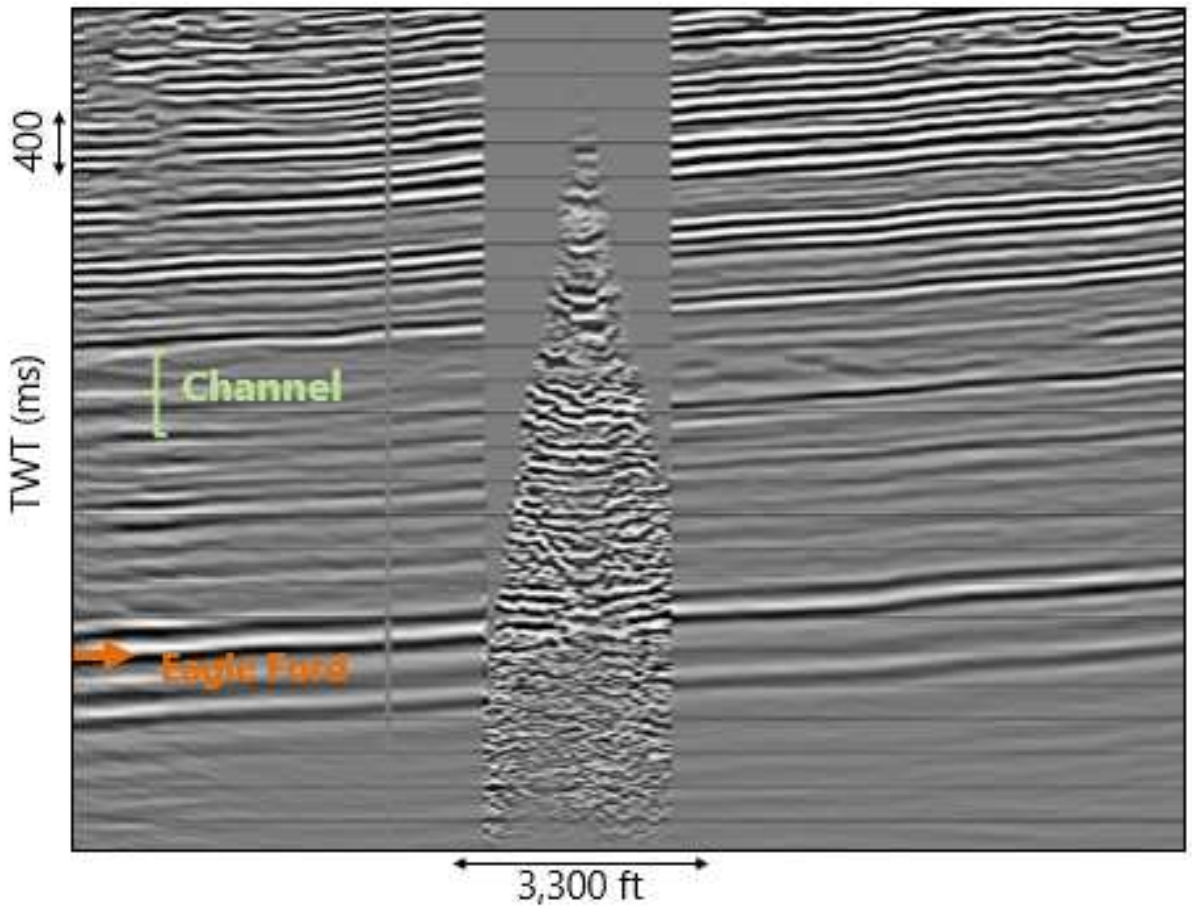

Figure A.1 Crossline through Well A from the 3D VSP PS-wave stack tied into surface seismic. A channel cutting across the section in indicated by the green bracket, an orange arrow indicates the Eagle Ford horizon.

APPENDIX B

ADDITIONAL TIME-LAPSE ANALYSIS

In an attempt to improve the time-lapse analysis discussed in Chapter 5, single shot gathers were analyzed. These shot gathers have had no processing other than a bandpass filter, so no processing could potentially interfere with the time-lapse results. Two shots were used from the further offsets (14,300 ft and 14,700 ft). These offsets record the direct P-wave arrival on the horizontal section of the well due to sufficient horizontal particle motion. Since the rocks around the horizontal wellbore were fractured, this is where the largest time-lapse response would occur. Figure B.1 shows the baseline, monitor, and difference images for both shot gathers. This shows the full length of the well, so the vertical and horizontal sections of the well are indicated with the orange and blue brackets, respectively. The baseline and monitor surveys were equalized by using a single scalar, as discussed in Chapter 5. Equalizing using a match filter was attempted, but the results were poorer than with the single scalar. Neither the match filter nor the scalar were able to completely equalize the shallow section of the well, but the rest of the well is better equalized. Some coherent energy can be seen on the horizontal section of the well and from the Eagle Ford reflection indicated by the green arrow.

To more closely analyze the time-lapse difference seen on the horizontal section of the well, those traces were sectioned off and the P-wave first-breaks were picked. Using the first-break picks, the wavefield is flattened and the difference is calculated (Figure B.2). Again, a match filter was attempted, but the single scalar produced the best results. The shot gather is very noisy so a bandpass filter and an FX-deconvolution was applied to reduce the random noise level. In the difference plots, there are small sections of more coherent signal, but they do not appear on both shots. If coherent signal appears on both shots, it is more likely to be a true time-lapse signal. However, this result does not show time-lapse signal. As discussed

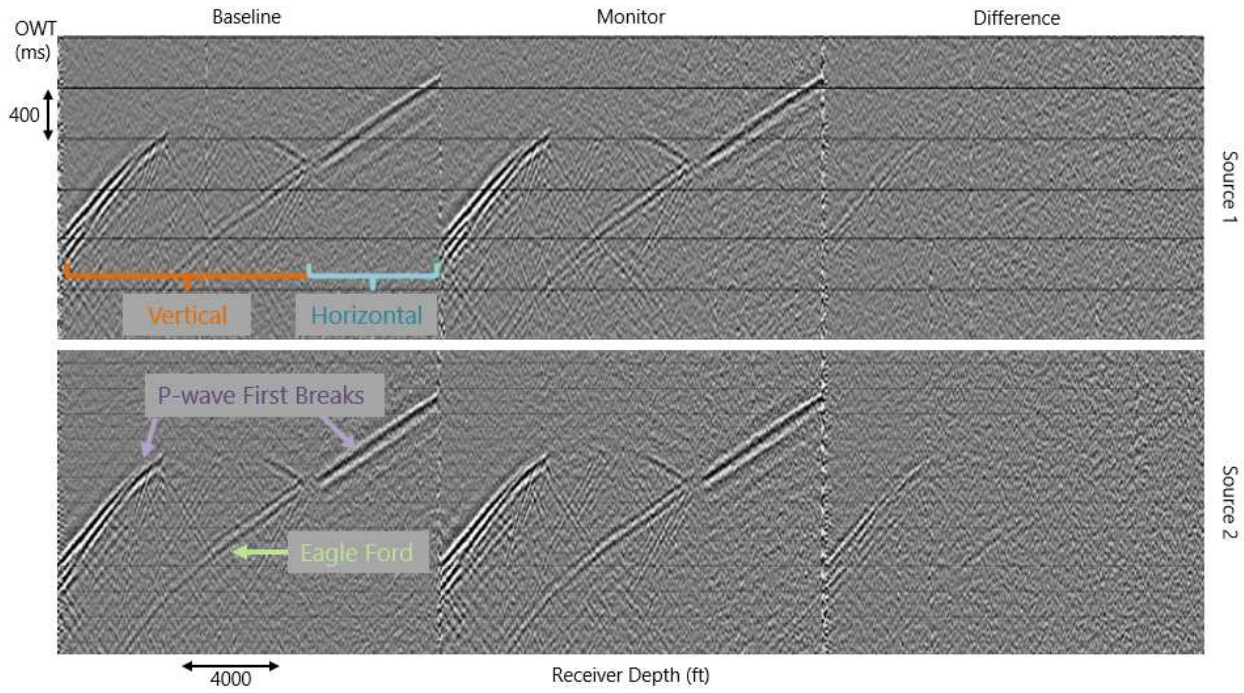

Figure B.1 Baseline, monitor, and difference images for two shot gathers. Source 1 offset = 14300, Source 2 offset = 14700.

previously in chapter 5, more time-lapse processing is needed in order to definitively prove whether or not there is a time-lapse signal.

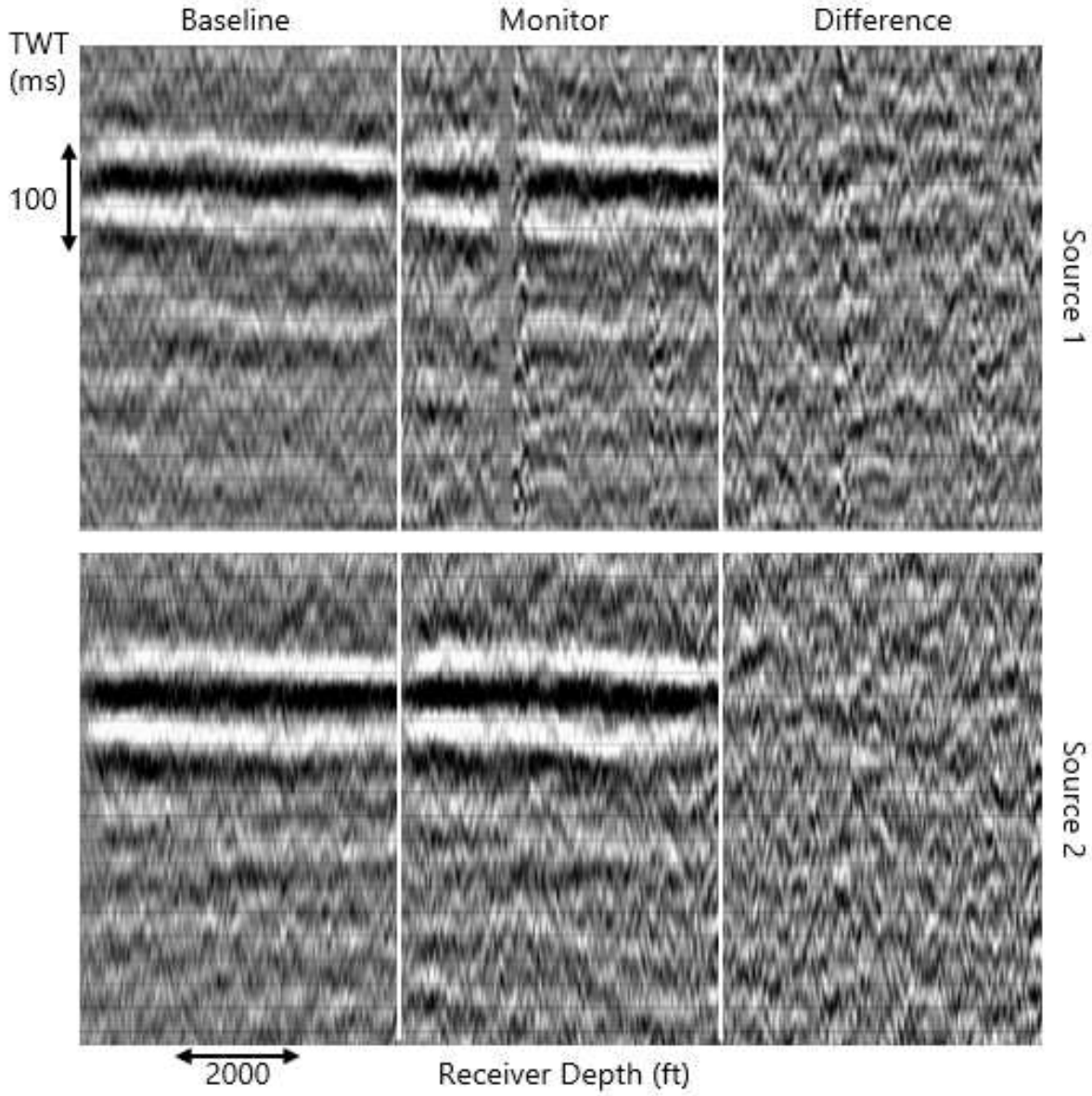

Figure B.2 Baseline, monitor, and difference images for the horizontal section of the well. Source 1 offset = 14300, Source 2 offset = 14700. The P-wave first-breaks are flattened.